Structure and dynamics of highly charged ions and pionic atoms

Martino Trassinelli

Université Pierre et Marie Curie, Sorbonne Universités, Paris, France

Habilitation à diriger des recherches

présentée par

Martino Trassinelli

Chargé de recherche CNRS (INP)

Structure and dynamics of highly charged ions and pionic atoms

Soutenue le 15 septembre 2017 devant le jury composé de :

Jean-Michel RAIMOND	Professeur (LKB, UPMC, Paris)	Président
Frédrich AUMAYR	Professeur (IAP, Vienne)	Rapporteur
José R. CRESPO LÓPEZ-URRUTIA	Professeur (MPI, Heidelberg)	Rapporteur
Xavier FLÉCHARD	Chercheur (CR1 avec HDR) (LPC, Caen)	Rapporteur
Eva LINDROTH	Professeure (Univ. de Stockholm)	Examinatrice

Preface

In this manuscript I present some of my research activities conducted during the past ten years starting from my hiring as researcher at the *Centre National de la Recherche Scientifique* (CNRS, National Center for Scientific Research) at the *Institut des NanoSciences de Paris* (INSP, Institute of NanoSciences of Paris). My research is carried out in the team *Agrégats et surfaces sous excitations intenses* (ASUR, Clusters and Surfaces under Intense Excitation) and also with external collaborations: the atomic physics group of GSI Helmholtzzentrum für Schwerionenforschung (GSI), and the *Pion Hydrogen and Pion Mass* collaboration.

The work presented in this manuscript is the result of a teamwork without which the results discussed here would not have been possible. Except in this preface and when my contributions are expressly specified, all topics are presented as impersonal.

Five chapters compose the manuscript. Chapter 1 is a general introduction. An overview of the different topics and the relationship between them in a general context are shortly presented. In the other chapters a selection of the most striking topics is detailed. Research activities on laser-cluster interactions [A11, C2, C8, C11, C13, C15], theoretical studies on ion–matter interaction [A10, C3] and plasma temperature measurements [A33] are not treated in this manuscript.

Chapter 2 is dedicated to the data analysis methods. Two multipurpose analysis programs I developed in the last years are presented in this chapter. The first is based on the χ^2 minimisation but with features that make it especially adapted for low-statistics spectra and where special functions can be included and employed for specific cases. The main feature of the second program is the possibility to compare different models describing the data and assign to them probabilities. This program is based on Bayesian statistics analysis methods that are introduced and presented as well in Ch. 2.

Chapter 3 is dedicated to the measurement of the negatively charged pion mass using high-accuracy X-ray spectroscopy of pionic nitrogen and using a muonic oxygen transition as reference. In this chapter, I present, in particular, two particular aspects of the data analysis. The first one is the study of the line profile determined by the de-excitation cascade processes that occur after the creation of the bound system and the radiative emission of interest. The second one is the investigation of the presence or not of satellite lines due to the non-complete electron depletion. The presence of one or more electrons in addition to the pion, may cause, in fact, a shift of the radiative transition energies leading to a systematic effect.

In chapter 4 I present the study of the collision of hydrogen-like argon with an atomic target at low velocity. Here, I focus on a particular aspect of the investigation: the atomic cascade processes and their comparison with theoretical predictions. The role of single- and multi-electron capture is revealed and the role of the presence of metastable states is evaluated.

The effect of heavy and slow ion impact on giant magnetocaloric thin films is discussed in Chapter 5. This new subject, quite different from the others described in chapters 3 and 4, deserves specific

introductions on the ion–matter interaction and on the magnetocaloric effect. The description and characterisation of modifications induced by the ion irradiation in specific samples as manganese arsenide thin films are given. The results are discussed in a thermodynamical point of view that highlights the key role of the phase transition type (of first or second order) associated to the giant magnetocaloric effect.

Finally, conclusions and perspectives of my future research projects are presented in the last part.

Except for the general introduction, each chapter starts with an introductory section that ends with a specific part labeled in **red** where my personal contributions are presented with reference to my publication list. Integral texts of the most relevant publications associated to the different chapters are proposed in the appendices, together with auxiliary subjects.

The manuscript is completed with my detailed curriculum vitae, the list of my oral contributions at conferences and workshops and the list of my publications. In the different chapters these publications are referred with a Latin letters and a progressive number: *A* for articles, *B* for book chapters, *C* for proceedings and *D* for patent. Other bibliographic references are indicated with simple numbers and can be found at the end of the document.

Contents

Chapter 1

General introduction

1.1 General presentation

The activities presented in this manuscript are centred on pionic atoms (hydrogen-like atoms where electrons are substituted with a negatively charged pion) and highly charged ions (HCI) (atoms with high atomic number Z and only one or a few electrons). These atomic systems, apparently very different, are sharing many common features and their investigation is carried out thanks to similar characterisation techniques. If we consider the typical level energies E_n and electric fields $\mathcal{E}$ of any

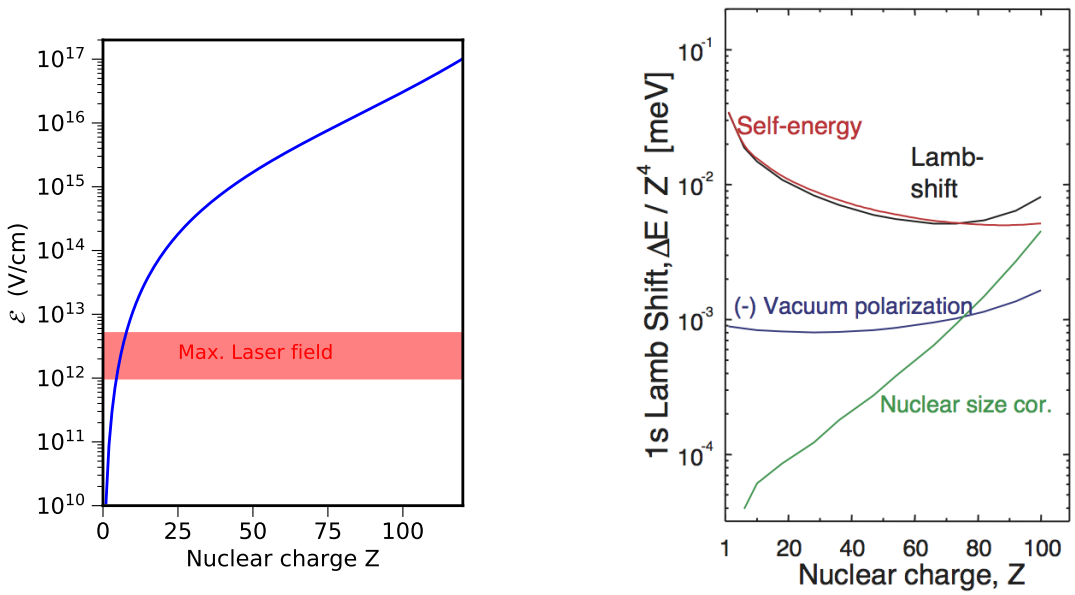

Figure 1.1 – Left: Average electric field relative to the $1s$ level as a function of the nuclear charge Z. As comparison, the value of the electric field of the most powerful available lasers is indicated in red. Right: Different QED and nuclear size effects as a function of the nuclear charge Z.

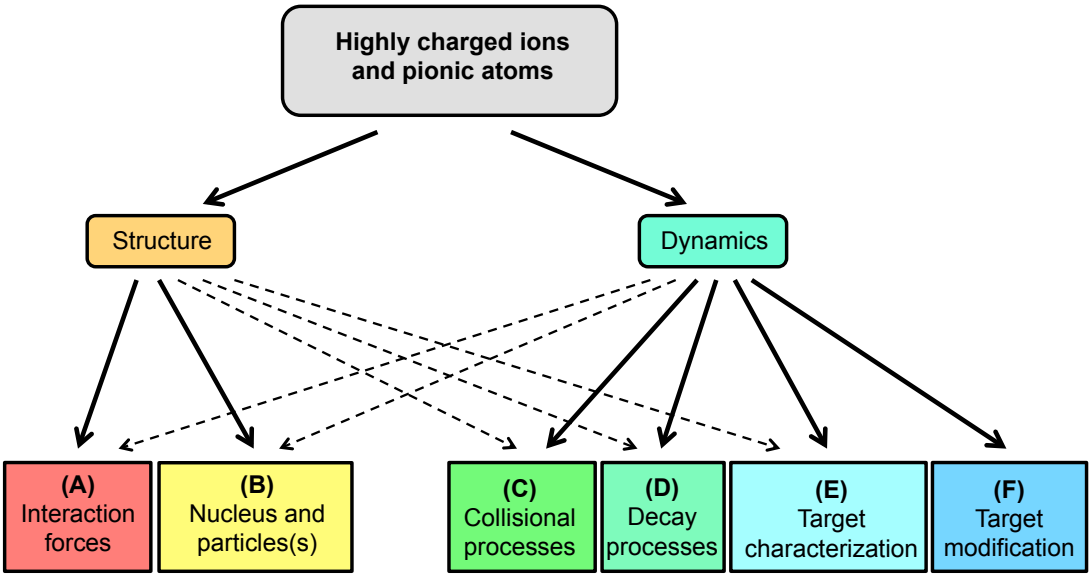

Figure 1.2 – Scheme of the research topics presented in the manuscript.

atomic system that are[1]

$$E_n = mc^2 \frac{(Z\alpha)^2}{2n^2} + \mathcal{O}\left[(Z\alpha)^4\right] \quad \text{and} \quad \mathcal{E} \sim \frac{m^2c^3}{e\hbar}(Z\alpha)^3, \tag{1.1}$$

(where m is the reduced mass of the system, c the speed of light, α the fine constant, e the electron charge, $\hbar$ the reduced Planck constant and n the principal quantum number) we see that a larger mass of the orbiting particle or a high of the nuclear charge causes a considerable increase of E_n and $\mathcal{E}$.

A negatively charged pion has a mass of about 250 times larger than the electron mass bringing the characteristics atomic transitions from the visible (few eV) to the X-ray range (2-100 keV). The same happens with hydrogen-like or helium-like ions because of the high value of Z. At the same time, the associated electric field increases enormously as shown in Fig. 1.1 (left). Already in neon ions and pionic hydrogen atoms, the electric field is higher than the field of the most intense available laser. This strong Coulomb field determines, on one hand, an enhancement of Quantum ElectroDynamics (QED) (see Fig. 1.1 right) and relativistic effects (represented in the $\mathcal{O}\left[(Z\alpha)^4\right]$ term in Eq. (1.1)) in their atomic structure, and, on the other hand, dynamical processes occurring during the collisions absent in light atoms. Due to the relative simplicity of these atomic systems, theoretical predictions on their structure and dynamical processes can be tested accurately.

The activities on pionic and HCI atoms are schematically resumed by the diagram in Fig. 1.2. The different investigations can be formally separated in two main categories: one about the study of the atomic structure and one about the dynamical processes involved in collisions. These two categories are not completely exclusive each other. As an example, transition line measurements for the structural studies have to take into account dynamical processes that lead to the atomic transition that characterise the emission spectrum. In the same way, the collisional processes investigated through the associated radiation emission require the knowledge of the structure of both the projectile and the

[1]No dependency on the nuclear mass is represented here other that the use of the reduced mass.

target atoms. Moreover, except for physical cases where laser spectroscopy can be used (not discussed in this manuscript), the only way to stimulate atomic transitions is via an initial collision with the creation of excited states and their subsequent decay. The different aspects are shortly described in the next sections following the diagram in Fig. 1.2.

1.2 Structure

(A) Interaction forces

The energy difference between atomic levels reflects directly the characteristics of the electromagnetic interaction between the nucleus and the orbiting particle(s). The theory of Quantum Electrodynamics (QED) describes this interaction and is tested successfully in low-Z atoms with extraordinarily high accuracy. However, in recent years spectroscopy measurements on muonic hydrogen have produced inconsistencies when compared with normal hydrogen and theoretical predictions for the evaluation of the proton size [1, 2]. Moreover, a very recent measurement of the hyperfine splitting in hydrogen- and lithium-like Bismuth shows a large disagreement with the QED [3]. From here comes the interest to continue to test QED in extreme conditions with the strong Coulomb field in exotic atoms and in high-Z ions.

In light atoms, QED and relativistic effects can be considered as perturbations with additional terms in Eq. (1.1) proportional to $mc^2(Z\alpha)^4$ and higher orders (see Fig. 1.1). In high-Z ions, where the classical velocity related to the level n

$$v_n \sim \frac{Z\alpha c}{n} \tag{1.2}$$

represent a considerable fraction of the speed of light c, relativistic effects can be taken into account in all perturbation orders by the use of the Dirac equation (for fermions like the electron) and the Klein-Gordon equation (for bosons like the pion) at the place of the non-relativistic Schrödinger equation (from which Eq. (1.1) is deduced). In high-Z ions QED corrections, as the self-energy and the vacuum polarisation (Fig. 1.1), have to be considered to all order of $\alpha\, Z$ but there are still a challenge for theory [4, 5]. In the same way in exotic atoms, the self energy contribution, sensitive to the typical orbiting radius

$$r_n \sim \frac{\hbar n^2}{mcZ\alpha}, \tag{1.3}$$

cannot be treated at the first order of perturbation only.

In this context, the author research activities of the last years were dedicated in particular to the study of two different atomic system: H-like gold and He-like uranium. Both experiments have been performed at the GSI Helmholtzzentrum für Schwerionenforschung (GSI) in Germany. In the case of H-like gold, QED effects are evaluated through the measurement of the Lamb shift of the fundamental level $1s$ by the measurement of $2p \rightarrow 1s$ Lyman$-\alpha$ lines with a high-accuracy X-ray spectrometer (transmission Bragg diffraction). The results of a series of challenging experiments, to which the author participated since 2003, have been finalised only this year 2017. The publications related to this topic are Refs. A2, A13, A39, A49, A50, B1.

QED effects in the interaction between two bound electrons in presence of the strong Coulomb field of the nucleus have been studied in He-like U in an experiment leaded by the author during a postdoc program at GSI (2006–7). Here, the high-accurate measurement of the $1s2p\ ^3P_2 \rightarrow 1s2s\ ^3S_1$ intrashell transition have been measured by Bragg spectroscopy (reflection diffraction in this case)

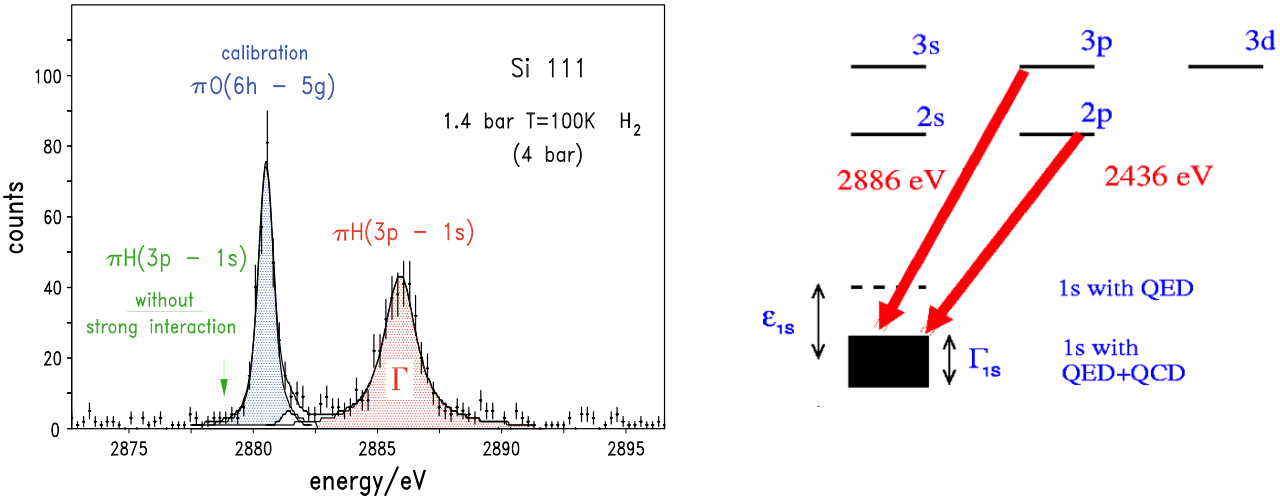

Figure 1.3 – Left: Spectrum from simultaneous measurements of the $\pi H(3p \to 1s)$ and the $\pi O(6h \to 5g)$ by crystal spectroscopy [A16]. Right: Atomic scheme of the πH transitions to the fundamental level.

[A30, A36, A44, B3, C22]. Experiments in He-like U represent the continuation of studies with medium-Z He-like ions performed during the author Ph.D. thesis and the years just after [A19, A40, A46, B2, C30]

In pionic hydrogen and deuterium, high-accuracy X-ray spectroscopy provides important information on the strong interaction force between the pion (formed by an anti-quark and a quark) and the nucleons (proton and/or the neutron, each formed by three quarks). In these bound systems, the strong interaction produces small perturbations in the atomic structure governed by the electromagnetic interaction. These effects are a shift of atomic levels and an additional broadening of transition lines to the fundamental level (see Fig. 1.3), which is in fact unstable due to the possible reaction between the nucleus and the pion [6–8].

The measurement of strong interaction effect in pionic hydrogen and deuterium is the goal of a long campaign, where the author started to contribute during his Ph.D. thesis and which is still in progress [A16, A18, A29, A32, A38, A51, A52, B4, C6, C17, C20, C21, C28].

Except for a short description of H-like U experiment in Sec. 2.2.6, the above topics are not detailed in this manuscript. More information can be found in the corresponding bibliography references.

(B) Nucleus and particles

When QED is taken for granted, information on the atomic nucleus and/or on the orbiting particle can be extracted. Charge and magnetic nuclear distributions of the nucleus can be deduced from the corresponding energy level corrections (included in the $\mathcal{O}\left[(Z\alpha)^4\right]$ terms in Eq. (1.1)). In this way, the root-mean- square charge radius of the proton is evaluated from spectroscopy of standard hydrogen [9] or muonic hydrogen [1, 2], as well as the energy shift due to isotopic effects in light or heavy few-electron systems [10, 11].

When the influence of the nucleus is negligible and/or well known, the mass of the bound particle can be measured from high-accuracy atomic transition spectroscopy via Eq. (1.1) (left). This is a

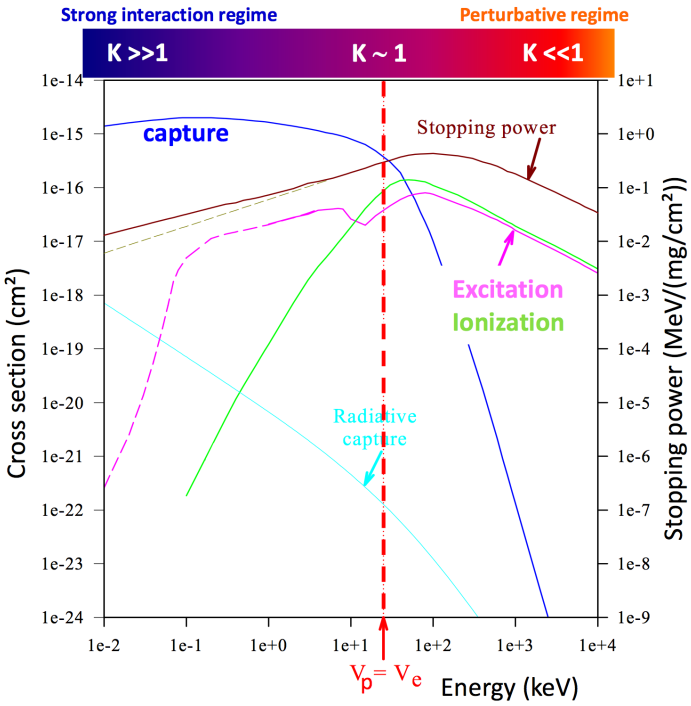

Figure 1.4 – Cross sections of elementary atomic collision processes for the system p → H. The vertical red dotted line indicates the proton energy where its velocity equals the hydrogen electron velocity. The brown line is the stopping power (refer to the right y-axis) for protons in aluminium.

very efficient method to measure with high accuracy the mass of short living particles with a negative charge as pions, kaons and Σ particle [12–15]. In this context, an experiment has been performed to measure the mass of the negatively charged pion by comparing the almost coinciding energies of $5g - 4f$ transitions in πN and μO with a high-accuracy spectrometer and using the muonic line as reference. This experiment is extensively presented in Ch. 3, in the publication in App. F [A7] and in Ref. C1.

1.3 Dynamics

(C) Collisional processes

The main processes involved in ion–atom collisions are electron (or exotic particle) capture, ionisation and excitation. Different dynamical channels play different roles depending on the collision velocity and on the asymmetry of the collision system. More precisely, we can define a parameter K_p (here relevant for processes that involves the projectile electrons) to distinguish the collision regimes:

$$K_p = \frac{Z_t}{Z_p} \times \frac{v}{v_p}. \tag{1.4}$$

Z_t and Z_p are the atomic numbers of the target and the projectile, respectively. v_p is the velocity of the projectile and v is the typical velocity of the active projectile electron.

When $K \gg 1$ the so-called *low velocity regime* or *strong interaction regime* is reached. The dominant process is then the electron capture. In this regime, the well know classical over-the-barrier

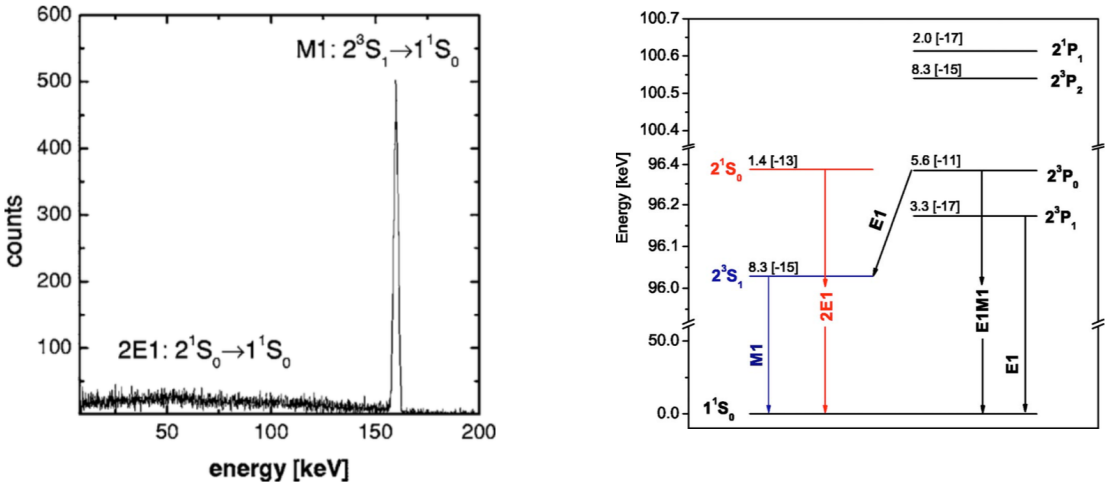

Figure 1.5 – Left: Projectile X-ray spectrum for 398 MeV/u $U^{89+} \rightarrow N_2$ measured in coincidence of U^{90+} detection (ionisation) [A47]. Right: Decay scheme of He-like uranium.

model [16,17] (presented also in App. B) and more sophisticated coupled state calculations using basis of either atomic or molecular orbitals [18–21] provide good predictions of cross sections.

When $K \ll 1$ the so-called *high velocity regime* or *perturbative regime* is reached. In this case the interaction with the target is seen by the projectile as a small perturbation. Ionisation and excitation have cross sections much larger than those for capture and relativistic effects may play an important role [22].

The research activity of the author on dynamical processes cover the both regimes with high-velocity experiments at the heavy ion facility GSI Helmholtzzentrum für Schwerionenforschung (Darmstadt, Germany) with $v_p \lesssim c$ and $Z_p \gg 1$, and low-velocity experiments with medium-Z ions at the ARIBE[2] installation at GANIL[3] (Caen, France) and SIMPA facility at INSP.

High-velocity regime

Studies in the perturbative regime are focused on the electron selective ionisation and on the electron and nuclear excitation processes. The selective ionisation is studied in the collision of a heavy and fast Li-like projectile (uranium or tin at 100-400 MeV/u) with a light gaseous target. A typical spectrum is presented in Fig. 1.5 together with the decay scheme. The dominant process is the ionisation of the projectile atom with the ejection of one K-shell electron and the creation of an excited He-like ion. From intensities and energies of the photons produced by the de-excitation of the $1s2s$ levels to the fundamental one ($1s2s\ ^3S_1 \rightarrow 1s^2\ ^1S_0$ via an M1 transition and $1s2s\ ^1S_0 \rightarrow 1s^2\ ^1S_0$ via a two-photon 2E1 transition), the selective populations of the $1s2s$ levels can be measured [A47] as well as the relativistic distribution of the two-photon emission [A31, A37, C12, C18, C25].

The role of excitation or ionisation from nuclei or electrons of target atoms is investigated varying the atomic number of the target Z_t. By performing measurements with H and N_2 targets at dif-

[2]French acronym for Accelerator for the Interdisciplinary Research with Low Energy ions
[3]French acronym for Large National Accelerator of Heavy Ions.

ferent collision energies, it is possible to distinguish the effect of electron-impact and nuclear-impact excitation processes in uranium ions [A12, A21, C16].

The above topics are not detailed this manuscript. More information can be found in the corresponding bibliography references.

Low-velocity regime

The strong coupling regime is investigated with the study of the collision between slow H-like Ar^{17+} ions with N_2 and Ar gaseous targets. Cross sections and selective populations of excited levels of the projectile are fully characterised by means of low- and high-resolution X-ray spectroscopy. The role of the single-electron capture and the multi-electron capture is highlighted as well as the influence of the presence of metastable states. This research activity is presented extensively in Ch. 4, in the publication in App. G [A26] and in Refs. C9, C10, C14, C22.

(D) Decay processes

As discussed above, the understanding of atomic decay processes is an essential ingredient for the study of dynamical processes. Moreover, de-excitation of unstable states can be itself the object of specific researches. Several experiment at the GSI have been dedicated to this topic and more precisely to nuclear decay processes where the atomic structure play a major role. More specifically, the capture of bound electron in H- and He-like ions of ^{140}Pr, ^{142}Pm and ^{122}I [A24, A25, A27, A34, A35, A45] is studied. The importance the atomic structure is evident as example in ^{140}Pr. Ions with one bound electron decay faster than neutral atoms with 59 electrons. This is due to the conservation of the total angular momentum, since only particular spin orientations of the nucleus and of the captured bound electron can contribute to the allowed decay.

These decays are observed by collecting in a storage ring unstable ions produced by collision with a solid target and by measuring the evolution of the Schottky noise produced by the ion revolution. Small changes of the ion mass due to the decay are detected here as change of the ion revolution frequency. From the intensities relative to unstable ions (parent ion) and decay products (daughter ion, kept stored in the ring), lifetimes of the order of few milliseconds up to several tens of minutes can be measured.

In the case of H-like ions, the bound electron capture is a purely two-body decay process where a monochromatic electron-neutrino is emitted. When single decays are recorded separately, a sinusoidal modulation is observed (Fig. 1.6) on the expected purely exponential decay probability for unit of time [A20, A41]. This modulation has not yet a clear interpretation but a possible connection with neutrino masses differences is speculated. The pertinence on the presence of such a modulation is tested by several methods. One of them is based on Bayesian methods and uses the program `Nested_fit` presented in Ch. 2. At present, an extended discussion on this controversial result is still open. The latest experimental data are still under analysis.

The above topics are not detailed in this manuscript.

(E) Target characterisation

When collisional and decay processes are well known, X-ray emission produced during collisions between highly charged ions and a target can be used to characterise the target itself. In this perspective, a series of experiments is performed to study the formation of argon clusters. These clusters are produced by adiabatic expansion in vacuum from a pressurised gas. The cluster jet is characterised by the X-ray emission induced by the collisions with an ion beam and an electron beam. The X-ray emission

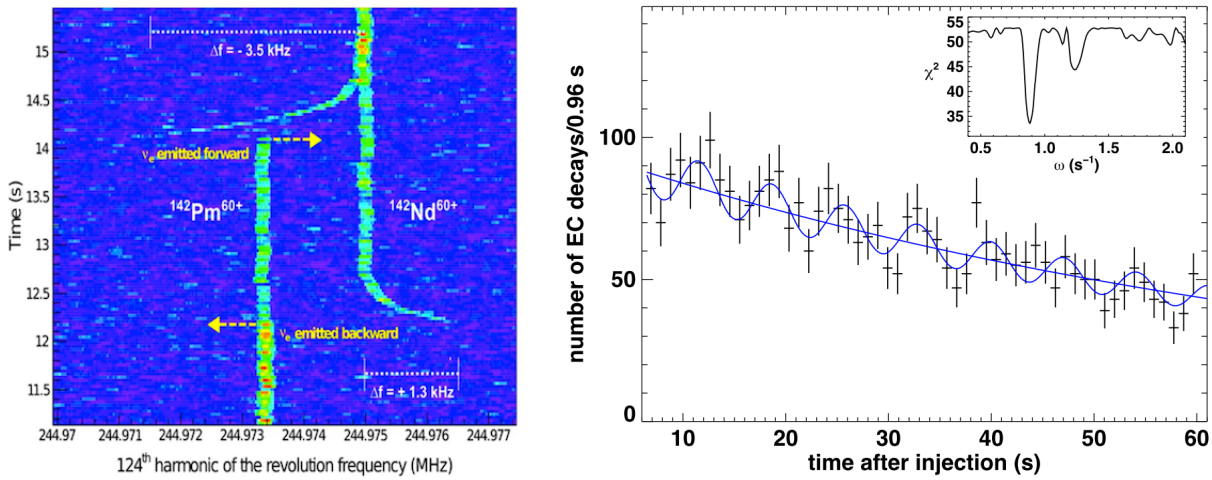

Figure 1.6 – Left: Traces of two cooled $^{142}Pm^{60+}$ parent ions, recorded at the 124th harmonic of the revolution frequency by the 245 MHz resonator vs. the time after injection. The yellow arrows indicate the true decay times, as unambiguously identified by a decrease of the intensity of the trace of the parent ions and the simultaneous onset of the trace of the recoiling daughter ion. The latter starts at a revolution frequency shifted with respect to the frequency after completion of electron cooling, which reflects the projection of the recoil velocity onto the beam direction axis immediately after the decay. Right: Number of electron capture decays per 0.96 s of H-like $^{142}Pm^{60+}$ ions vs. the time after injection of the ions into the ESR storage ring. Displayed are also a exponential fit and an exponential with a modulation fit. The inset shows the χ^2 values vs. the angular frequency ω [A20].

intensity produced by the collision with ions is proportional to the free atoms density, when the one associated to the collision with electrons is associated to the total density (condensed and free atoms) Preliminary results are published in Refs C10,C13. This topic is not detailed in this manuscript. More information can be found in the corresponding bibliography references.

(F) Target modification

The last aspect of dynamical processes treated here is about the permanent modifications of the target induced by the collisions with ions. In this context, research activities presented here are focused on the structural and magnetic properties modifications induced in thin films of Zn ferrites and giant magnetocaloric materials.

Zn ferrites are paramagnetic at room temperature, but nano-sized objects become ferrimagnetic[4]. It has been demonstrated that irradiation-induced defects produced by the bombardment with slow ions cause changes on the target atoms position that has an effect on the promotion of the ferromagnetic interaction and then increasing the global sample magnetisation [A9].

When giant magnetocaloric thin films are bombarded, the induced effects are more complex due to the presence of a first-order transition linked to the giant magnetocaloric properties. First-order transitions in magnetic materials are generally characterised by a magnetic phase change coupled to a solid-solid structural change and the presence of a thermal hysteresis. In this case, irradiation-induced defects act as nucleation seeds during the transition and reduce or suppress this thermal hysteresis.

[4]A ferrimagnetic material has populations of atoms with opposing magnetic moments, as in antiferromagnetism but where the opposing moments are unequal and a spontaneous magnetisation remains.

This last research activity in giant magnetocaloric thin films is presented extensively in Ch. 5, in the publication in App. H [A14] and in Refs. A1, A5, A22, C4, C5.

1.4 Investigation methods

Except for the nuclear decays in ions and irradiation-induced target modifications studies, the main instrument of investigation of all experiments presented here is the X-ray spectroscopy (low- and high-resolution), eventually coupled to other detectors (electrons, ions, etc.). Because of the relatively simple systems (H-, He-like atoms, etc.), atomic spectra are relative simple and all components can be unambiguously identified. However, because of the high-accuracy demand, these spectra have to be fully characterised. For this goal, in the last years a series of analysis program packages have been developed based on standard and Bayesian statistical data analysis methods. These tools and the theory behind are presented in Ch. 2.

1.5 Something completely different

In addition to the topics discussed above, in App. I is presented an original work not related to the others. It originates from simple physical considerations on the author's hobbies, freediving (constant weight freediving, more precisely). This study is more generally about the locomotion costs in breath-hold divers, human athletes or marine animals. Starting from basic mechanic principles, the work that the diver must provide through propulsion to counterbalance the action of drag, the buoyant force and weight during immersion is calculated. Compared to previous studies, the model presented here analyses accurately breath-hold divers which alternate active swimming with prolonged glides during the dive (as in the case of mammals). More details can be found in App. I [A8].

Chapter 2

Statistics and data analysis methods and applications

2.1 Introduction

2.1.1 Data analysis and developed programs

For the accurate analysis of the data of a large part of the experiments discussed in this manuscript, specific statistical methods have been employed and several programs have been developed. In particular two major program packages have been created and perfected in the past years. One, called `Minuit_fit`, is based to the common minimisation of the χ^2 to determine, for given data and model function, the best set of parameters and their correspondent uncertainties. The other one, called `Nested_fit`, is based on the Bayesian statistics. In addition to outputs similar to `Minuit_fit`, it calculates the complete probability distribution for each parameter. It also provides the Bayesian evidence, a quantity required to compare different models that could describe the data and affect them a probability.

Both programs have been developed in `Fortran90` with some `Python` complementary routines for visualising the output results and for doing automatic analyses of series of data. They use a common library of functions that can be selected by the user. Additional special functions can be developed for specific cases via simple programming of a dedicated subroutine. Both programs can treat several data sets (spectra) at the same time.

Each program accepts a similar input file and provides a series of outputs containing the information about the parameters of the model (best values, uncertainties, probability distribution, etc.).

Elements of basic statistics and data analysis that could facilitate the reading of next sections are presented in App. A.

2.1.2 Work context, personal contribution and associated publications

The both programs described here are entirely coded by the author. The core of `Minuit_fit` is the classic CERN library for which the author developed an user customisable and friendly interface and he added a library of functions and chi-square types. `Nested_fit` is based on the nested algorithm presented in the literature. The structure of the program is the same of the code developed by L. Simons [23] (who introduces the author to the Bayesian methods of data analysis) and other programs

existing in the literature. `Nested_fit` keeps the same modularity than `Minuit_fit` (structure of the input and output file, library of functions, etc.). Compared to similar codes, it implement a new core algorithm developed by the author that improve the robustness of the program. Both programs have grown continuously in the last years, pushed by the requirements for the analysis of the many different experiments described in Ch. 1 and more extensively in chapters 3 and 4.

The publication associated to this chapter is presented in App. E [A4], where the `Nested_fit` program is presented in details. No publications are associated to `Minuit_fit`. More details on the specific applications can be found at the end of the next section and Sec. 2.4.

2.2 A general fitting program: `Minuit_fit`

2.2.1 General features

The program `Minuit_fit` is based on the minimisation of the chi-square value with the implementation of the functions of the Minuit library. This library has been created by Fredric James at CERN [24] and it is implemented since the development of numerical data evaluation mostly by the physics community. It is now part of major data analysis environments (`R, Root, Python,` etc.).

Once the function that has to be minimised is defined, as an example a chi-square defined by a set of data and a selected function, Minuit library provides numerical subroutines to find the best function parameters and the corresponding uncertainties. The minimisation can be done using different strategies: (i) the simplex method, (ii) by the variable metric method and (iii) by a Monte Carlo minimisation (see Ref. [24] and reference therein for details). `Minuit_fit` act as interface to built such a function from (a) a selected data set, (b) a choice of function to model the data and (c) a choice of χ^2 function. The user determines these choices via an input file.

2.2.2 Selection of the data set

The data are provided in an additional input file in list mode. In addition to $\{x_i, y_i\}$ values, uncertainties σ_i on y_i values can be considered. If σ_i values are not provided, the standard uncertainty $\sigma_i = \sqrt{y_i}$ can be considered. Uncertainties on x_i values can also be considered and included via a transformation to the equivalent y-axis uncertainty via the procedure described in Ref. 25.

Several spectra can be considered at the same time considering different functions, one per spectrum, with eventual common parameters (the width of the peaks as an example).

2.2.3 Selection of the model function

Common functions are available: Gaussian, Lorentzian, Voigt profiles, etc. Models with several peaks are available as well, Relative differences and constraints can be considered between the parameters the different components, as well as common parameters as the peak width can be taken into account. For asymmetric profiles, several functions are also available, as the Weibull function, a Gaussian distribution convoluted with an exponential, etc. If the function cannot be simply calculated from basic principles but is coming from an external calculation (or measurement), the program can use an external data file provided by the user for interpolations. The external file is then fitted via splines and adapted to the data via few parameters (intensity, position and an eventual background function).

Function parameters can be fixed or determine by the χ^2 minimisation. Boundaries can also be applied to facilitate the convergence of the minimisation. N. B. these boundaries have no connections

to possible prior knowledge on the fitting parameter but are merely a stratagem to facilitate the calculation.

2.2.4 Selection of χ^2's

Compared to other available fitting programs, `Minuit_fit` provide a choice of different types of χ^2s or, more generally, norms to adjust a selected function $F(x)$ to the data $\{x_i, y_i\}$ (or $\{x_i, y_i, \sigma_i\}$) via the estimated values $f_i = F(x_i)$. As an example, when poor data sets are available, Poisson statistics has to be considered for the different channels instead of the normal distribution. This leads to a different expression for χ^2 than the standard one given in Eq. (A.5) (see App. A for more details). As another example, for data ranging over several orders of magnitudes, a lognormal distribution may be more adapted.

The possible choices of χ^2s proposed in `Minuit_fit` are:

Standard : the standard chi-square, $\chi^2 = \sum_{i=1}^{N}(y_i - f_i)^2/\sigma_i^2$, the only possible choice if $\{\sigma_i\}$ values are provided by the user.

L1-norm: A robust estimator based on the l1-norm (absolute value) $|y_i - f_i|$ values [26]. Compared to the standard χ^2 (a l2-norm), this is a very robust estimator, much less sensitive to possible noisy data. The corresponding chi-square is $\chi^2 = \sum_{i=1}^{N}|y_i - f_i|/\sigma_i$.

Lognormal: For data whose logarithm is expected to be normally distributed. This is the case for data varying several order of magnitude and/or where the relative change is more important the absolute value. In this case the corresponding chi-square is $\chi^2 = \sum_{i=1}^{N}[\ln(y_i/f_i)]^2/(\sigma_i/y_i)^2$ [26].

Poisson: A χ^2 derived from the maximum likelihood method for data following the Poisson distribution, i.e. well adapted to statistically poor data sets. This is applicable only with data where each y_i value corresponds to a number of counts. The associated chi-square is $\chi^2 = \sum_{i=1}^{N} 2[f_i - y_i + y_i \ln(y_i/f_i)]$ [27].

Pearson: The Pearson's approximation for Poisson distributed data. This is applicable only for data where each y_i value corresponds to a number of counts. $\chi^2 = \sum_{i=1}^{N}(y_i - f_i)^2/f_i$ [28].

Neyman: The Modified Neyman's approximation for Poisson distributed data. This is applicable only for data where y_i values corresponding to a number of counts. $\chi^2 = \sum_{i=1}^{N}(y_i - f_i)^2/\max(y_i, 1)$ [28].

Gamma: Another approximation for Poisson distributed data. This is applicable only for data where each y_i value corresponds to a number of counts. $\chi^2 = \sum_{i=1}^{N}(y_i + \min(y_i, 1) - f_i)^2/(y_i + 1)$ [29].

In addition, a mixture of L1-norm and Lognormal chi-squares can be implemented.

2.2.5 Outputs

After minimisation, the program provides two files:

- `output_par.dat` where the best parameter estimation, the associated uncertainty, the final value of χ^2, its reduced value and the probability to obtain it (from the χ^2 statistical distribution) are indicated,

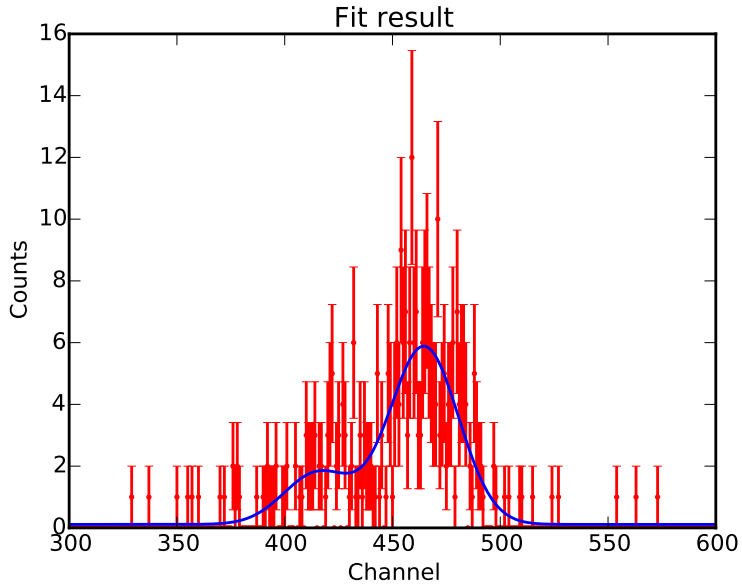

Figure 2.1 – High-resolution X-ray spectrum of $1s2p\ ^3P_2 \rightarrow 1s2s\ ^3S_1$ helium-like uranium intrashell transition from Ref. [A36] and the result of the fit considering two Gaussian peaks with common width. The best value found for the flat background is 0.11 counts per channel; the assumption of a Poisson distribution for the data is mandatory.

- `output_dat.dat` corresponding to the initial data input together with the best prediction of the fitted function, the residuals and the associated uncertainties (computed if not provided by the user).

To trace the different plots, special `python` routines have been written in an external library. Other routines from the same library can, if required, change systematically the input file `nf_input.dat` and read the output files for automated analysis of series of data sets.

An example of typical data and fitted model output is give in Fig. 2.1, where low-statistics data, coming from a X-ray crystal spectrometer, are fitted with a model with two Gaussian distributions and a flat background, using the "Poisson" χ^2.

2.2.6 Use in the different research topics

`Minuit_fit` has been started to be developed in 2007. Since then, different versions have been used for the analysis of different experiments: in the low-energy X-ray spectroscopy of He-like uranium [A30, A36, C22], the analysis of the ECR ion source bremsstrahlung emission [A33], the study of slow collision between ions and atoms [A26, C14] (Ch. 4), and the study of interaction between clusters with intense laser, ions and electrons [A11, C10, C11, C13, C15].

In particular, a specific version of `Minuit_fit` has been developed for the analysis of the data for the Lamb shift measurement of hydrogen-like gold [A2, A13]. In this experiment [A2, A13, A39, A49], the Lamb shift of the fundamental level is measured by the accurate X-ray spectroscopy of the Lyman-α transition using a transmission crystal spectrometer. The diffraction lines are detected by specially dedicated position-sensitive and time-sensitive detectors [30–32], specially sensitive to

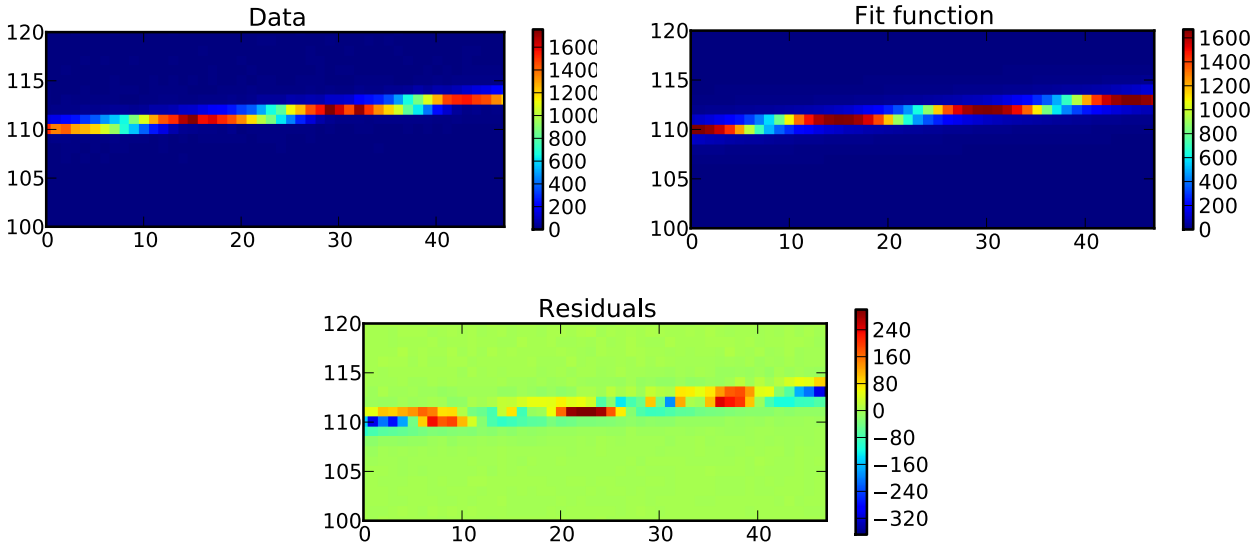

Figure 2.2 – Spectral line of the Lyman=α_1 $2p_{3/2} \rightarrow 1s_{1/2}$ transition of H-like gold (71.5 keV) obtained with Laue X-ray spectrometer equipped with special position-sensitive detectors. The three plots correspond to the recorded data (top-left), the modelled data (top-right) and the residuals (bottom). The position units are in strip numbers. Intensities are in counts.

10–100 keV photons. Each detector consists in a 11 mm thick germanium single crystal with both anode and cathode segmented into many strips. The cathode is divided into 128 strips, whereas the anode is segmented into 48 to have a position sensitivity equivalent to a 128×48 pixels segmented detector. The simple analysis of the one-dimensional spectrum obtained by the projection of the diffraction line intensity on the dispersion spectrometer axis implies a large loss of information due to the limited spatial resolution of the detectors and the slight slope of the spectral lines (due to the relativistic Doppler effect). Because of that, two two-dimensional data analysis have been developed independently by the author and T. Gassner [33]. Author's contributions were based on a modified version of `Minuit_fit` to compare model functions to data sets of the type $\{x_i, y_i, z_i\}$, where x_i and y_i correspond to detector strip numbers and z_i to the recorded number of counts.

Due to the relatively large size of each equivalent pixel, instead of comparing the number of counts z_i with the expected value of the model function $F(x_i, y_i)$, its integral over the dispersion direction y is considered:

$$\mathcal{F}(x_i, y_i) = \int_{y_i - \Delta y/2}^{y_i - \Delta y/2} F(x_i, \tilde{y}) d\tilde{y}, \tag{2.1}$$

where Δy is the "pixel" size along the dispersion axis of the spectrometer). There is no need for an integration over the x-axis due to the weak dependency of $F(x_i, y_i)$. As an example, a comparison between recorded data and data modelling with a Lorentzian profile with width Γ are presented in Fig. 2.2 with

$$F(x, y) = A \frac{1}{\pi\Gamma \left[1 + \left(\frac{y - a + bx}{\Gamma}\right)^2\right]}. \tag{2.2}$$

2.3 Bayesian approach for data analysis

Even if quite general and adaptable for a large part of cases, the methods of maximum likelihood or least-squares have some limitations and are affected by fundamental problems. Some of them are listed here.

Cause-effect inversion: First of all, one has to note that the maximum likelihood method is based on the probability $L(\boldsymbol{a}) = P(\{x_i, y_i, \sigma_i\}|\boldsymbol{a})$ to obtain certain data values for a given set of parameters $\boldsymbol{a}$ (Eq. (A.4)). But what is need is just the opposite; for given experimental data, one would like to obtain the probability for having certain parameter values (and find the most probable values and the correspondent uncertainties).

Constraints on the parameter values: Let's consider the case where one of the parameter of the considered function F represents a (physical) mass, called $a_1 = m$ as an example. In this case the parameter a_1 has a strong lower bound having to be positive. However, the minimisation of the likelihood function $L(\boldsymbol{a})$ could lead to values $a_1^{\text{best}} < 0$, which cannot be accepted for a mass. How can this prior knowledge ($a_1 \geq 0$) be included in the analysis?

Inference from past experiment data: If a past experiment reports a measured value $a_1' \pm \sigma_{a_1'}$, how can one include this knowledge in the analysis in a better way than a posterior weighted average?

Model testing: If there are two possible choices of models, one described by the function $F_1(x, \boldsymbol{a}^{(1)})$ and another by the function $F_2(x, \boldsymbol{a}^{(2)})$ with a different number of parameter $D_2 > D_1$, how the most probable model can be determined? If only the value of $L(\boldsymbol{a})$ or χ^2 is considered, one generally obtains a better value (higher or lower, respectively) for the model with more parameters, simply because there are more adjustable variables to fit the function F_2 to the data without any real indication of the plausibility of the different models.

For the last point, when certain conditions are satisfied, goodness-of-fit tests like the χ^2-test, the likelihood-ratio test, etc. [34–39], can be used to determine the relative pertinence of one model with respect to another. But how it is possible, for a given set of data, to assign a probability to a model selected from a pool of possible hypotheses? In the unfortunate case where there is no clear propensity to an unique model and one is interested on the value of a parameter common to all models (as the position of the a peak with undefined shape), no sort of weighted average can be computed from goodness-of-fit test outcomes. How can one overcome this problem? To answer these and other questions, a big step back has to be done and the definition of *probability* has to be discussed.

2.3.1 Probability definition and Cox's laws

The standard definition of probability required the infinite repeatability of some process. As an example a classical textbook may be cited:

> *"Suppose we toss a coin in the air and let it land. There is 50% probability that it will land heads up and a 50% probability that it will land tails up. By this we mean that if we continue tossing a coin repeatedly, the fraction of times that it lands with heads up will asymptotically approach 1/2, indicating there was a probability of 1/2 doing so."*
>
> *Data Reduction and Error Analysis*, Bevington and Robinson [36].

Because of the idea of repeatability, this classical point of view is often called "frequentist". To overcome the need of repeatability and other problems discussed in the previous section, a different approach has to be implemented with a new and more general definition of probability, This approach is the result of the work of Th. Bayes, P.-S. Laplace, H. Jeffreys and of many others [40–43] and is commonly called *Bayesian statistics*.

Bayesian methods are routinely used in many fields: cosmology [44–46], particle physics [47], nuclear physics, ... In atomic physics their implementation is still limited (e.g. in atomic interferometry [48, 49], quantum information [50], ion trapping [51], ion–matter interaction [52], etc.) with almost no use in atomic spectroscopy, even if in some cases it would be strongly required. For example, when the shape of a instrumental response function (Gaussian profile, Lorentzian profile, etc.) has to be determined by the data, one is actually testing hypotheses. In the same way, different hypotheses are tested when presence or no presence of a possible satellite line is evaluated (see Sec. 3.4.6).

A very general definition of probability can be built from the quantification of plausibility or believe [26, 43] considering all available information inherent in a phenomenon(experiment) studied. As analogy to the sentences above, one could state that

> *"If we are going to toss a coin in the air and let it land once, we have a probability of 50% that the sentence 'in the next toss, the coin will land with heads up' would be true."*

Similar statements could be formulated for a sentence referring to past events that one partially knows.

Because one usually would like to obtain a quantitative value for probability $P(X|I)$, the problem consist in assigning a real number to $P(X|I)$ that represent the degree of plausibility or believe that the assertions X would be true knowing the background information I.

With this general approach, which is the basis of "Bayesian statistics", the difficulty consists on quantifying the quantity probability, where the probability has the meaning of degree of plausibility or believe. This has been done in 1946 by Richard Cox who demonstrated that, pretending minimum requirement of consistency, the function probability $P(X)$ for having X true, a real number, has to respect simple rules. A minimum requirement is as example the transitive property. If $P(A) > P(B)$ and $P(B) > P(C)$ then $P(A) > P(C)$. Using Boolean logic rules, Cox demonstrate that the form of the probability P is ensured by the axioms [26, 43, 53–55]:

$$0 \leq P(X|I) \leq 1, \tag{2.3}$$

$$P(X|X, I) = 1, \tag{2.4}$$

$$P(X|I) + P(\bar{X}|I) = 1, \tag{2.5}$$

$$P(X, Y|I) = P(X|Y, I) \times P(Y|I). \tag{2.6}$$

In the equations above, $\bar{X}$ indicates the negation of the assertion X (not-X); the vertical bar "|" means "given" and where I represents the current state of knowledge. The joint probability $P(X, Y|I)$ means that both "X AND Y" are true (equivalent to the logical conjunction '$\wedge$'). The first three axioms are compatible with the usual probability rules. Here an additional axiom is present that plays a very important role.

From these axioms the following rule (sum rule) is deduced [55]

$$P(X + Y|I) = P(X|I) + P(Y|I) - P(X, Y|I). \tag{2.7}$$

Here the symbol '+' means here the logical disjunction ($X + Y \equiv X \vee Y \equiv$ "X OR Y is true").

The fourth axiom determines the rule for inference probabilities (product rule) for conditional cases. If X and Y are independent assertions, this is reduced to the classical probability property

$$P(X, Y|I) = P(X|I) \times P(Y|I). \tag{2.8}$$

When a set of mutual exclusive assertions are considered $\{Y_i\}$, with $P(Y_i|Y_{j\neq i}) = 0$, the *marginalization rule* can be deduced

$$P(X|I) = \sum_i P(X, Y_i|I) \tag{2.9}$$

that in the limit of continuous case $Y_{i+1} - Y_i \to dY$ becomes

$$P(X|I) = \int_{-\infty}^{\infty} P(X, Y|I)dY. \tag{2.10}$$

2.3.2 The Bayes theorem and other corollaries

Another important corollary can be derived from the fourth axiom (Eq. (2.6)) and the similar expression with exchange between X and Y:

$$P(X|Y, I) = \frac{P(Y|X, I) \times P(X|I)}{P(Y|I)}. \tag{2.11}$$

This is what is called the Bayes' Theorem, named after Rev. Thomas Bayes, who first [40] formulated theorems for conditional probabilities. It has been rediscovered in 1774 and further developed by Pierre-Simon Marquis de la Laplace [41].

For a better insight in the implication of this theorem, one considers the case where X represent the hypothesis that the parameter values set $\boldsymbol{a}$ truly describes the data (via the function $F(x, \boldsymbol{a})$) and where Y correspond to the recorded data $\{x_i, y_i\}$. In this case Eq. (2.11) becomes

$$P(\boldsymbol{a}|\{x_i, y_i\}, I) = \frac{P(\{x_i, y_i\}|\boldsymbol{a}, I) \times P(\boldsymbol{a}|I)}{P(\{x_i, y_i\}|I)} = \frac{L(\boldsymbol{a}) \times P(\boldsymbol{a}|I)}{P(\{x_i, y_i\}|I)}, \tag{2.12}$$

where I includes the available background information and where $P(\{x_i, y_i\}|\boldsymbol{a}, I)$ is by definition the likelihood function $L(\boldsymbol{a})$ for the given set of data (Eq. (A.1)). Differently from the common statistical approach where only the likelihood function is considered, there is here the additional term $P(\boldsymbol{a}|I)$ that includes the prior knowledge on the parameters $\boldsymbol{a}$ or possible boundaries. The denominator term $P(\{x_i, y_i\}|I)$ can be considered for the moment as a normalisation factor but it plays an important role when different hypothesis are considered and compared (see next section).

The use of prior knowledge lead historically to considerable critics concerning the Bayesian approach as it introduces a possible subjectivity into the method. On the other hand it offers a very much-needed possibility to represent prior knowledge or believe in a data analysis. If two scientists have different choices of priors, and use some common experimental data, the posterior probability distributions are generally not significantly different. If the posteriors are different because of the different choice of priors, this means that the data are not sufficient to analyse the problem.

From $P(\boldsymbol{a}|\{x_i, y_i\}, I)$, the probability distribution of each parameter $P(a_j|\{x_i, y_i\}, I)$ or joint probabilities $P(a_j, a_k|\{x_i, y_i\}, I)$ can be obtained from the marginalization (Eq. (2.10)), i.e. the integration of the posterior probability on the unconcerned parameters.

2.3.3 Hypothesis testing, Bayesian evidence and Bayes ratio

An important consequence of the Bayes' theorem is to have the possibility to assign probabilities to different hypothesis (models) with a simple and well-defined procedure. In this case, in Eq. (2.11) X represent the hypothesis that the model $\mathcal{M}$ describes well the observations and Y represent the

data, as in the previous section. From Bayes' theorem, the posterior probability of the model $\mathcal{M}$ is [26, 43, 45]

$$P(\mathcal{M}|\{x_i, y_i\}, I) \propto P(\{x_i, y_i\}|\mathcal{M}, I) \times P(\mathcal{M}|I), \tag{2.13}$$

where the first term of the right part is the so-called *Bayesian evidence* E of the model and the second term is the prior probability assigned to the model from the background knowledge. Using the marginalization rule to the parameter values and the probability properties (Eqs. (2.3–2.6)), one has

$$E \equiv P(\{x_i, y_i\}|\mathcal{M}, I) = \int P(\{x_i, y_i\}|\boldsymbol{a}, \mathcal{M}, I) P(\boldsymbol{a}|\mathcal{M}, I) d^J\boldsymbol{a} = \int L^{\mathcal{M}}(\boldsymbol{a}) P(\boldsymbol{a}|\mathcal{M}, I) d^J\boldsymbol{a}, \tag{2.14}$$

where J is the number of the parameters of the model considered, and where the likelihood function $L^{\mathcal{M}}(\boldsymbol{a})$ is explicitely shown relative to the model $\mathcal{M}$. The Bayesian evidence, also called *marginal likelihood* or *model likelihood*, is the integral of the likelihood function over the J-dimensional parameter space under the priors for a specific model choice. The evidence is also the denominator of Eq. (2.11). But from the considerations above it follows that it has a much deeper meaning than being a simple normalization factor. Considering equal priors, the probability of a model is higher if the evidence is higher, which means that the average of the likelihood function over the model parameter space is higher. To note, this does not implies that the maximum of the likelihood function is larger, as in the case of the likelihood ratio test used to compare the goodness of fit of two models (where however not assignment of probabilities is done to the models themselves but where only a criterion to choose between two models is provided). Models with higher number of parameters are generally penalised because of the higher dimensionality of the integral that corresponds to a larger parameter volume $V_{\boldsymbol{a}}$ (and then to a lower average value of the likelihood function). In fact, the calculation of the model probability via the Bayesian evidence includes, in some sense, the Ockham's razor[1] favouring simpler models when the values of the likelihood function are similar.

If one has to choose among only two different models $\mathcal{M}_1, \mathcal{M}_2$, the comparison between model probabilities is related to the calculation of the simple ratio

$$\frac{P(\mathcal{M}_1|\{x_i, y_i\}, I)}{P(\mathcal{M}_2|\{x_i, y_i\}, I)} = \frac{P(\{x_i, y_i\}|\mathcal{M}_1, I)}{P(\{x_i, y_i\}|\mathcal{M}_2, I)} \times \frac{P(\mathcal{M}_1|I)}{P(\mathcal{M}_2|I)}. \tag{2.15}$$

If there is no preponderance of one model with respect to the other, the prior probabilities $P(\mathcal{M}_i|I)$, and this probability ratio is given by the *Bayes factor* $B_{12} = E_1/E_2$, which is nothing else than the ratio of the evidences [26, 42, 45].

Values of B_{12} larger or smaller than one indicate a propensity for $\mathcal{M}_1$ or $\mathcal{M}_2$, respectively. In the literature several tables are available to assign, in addition to probabilities, degree of propensity of favour to one or other model [42, 56] with a correspondence to the p-value and the standard deviation [57].

For models with similar values of evidence, another criterion to decide between them is the Bayesian complexity $\mathcal{C}$, which measures the number of model parameters that the data can support [45]. This quantity is related to the gain of information (in the Shannon sense) and it is discussed in the next section. When E are similar, one should favour the simplest model, i.e. the model with the smallest value of $\mathcal{C}$.

The possibility to assigning probabilities to models has another important advantage. In the case one is interested to determine the probability distribution of a common parameter a_j without

[1] *"Non sunt multiplicanda entia sine necessitate"* , "Entities must not be multiplied beyond necessit" from William of Ockham's (1287-1347), which can be interpreted in a more modern form as "Among competing hypotheses, the one with the fewest assumptions should be selected".

the need to identify the correct model among the available choices $\mathcal{M}_\ell$, the probability distribution $P(a_j|\{x_i, y_i\}, I)$ can be obtained from the weighted sum

$$P(a_j|\{x_i, y_i\}, I) = \sum_\ell P(a_j|\{x_i, y_i\}, \mathcal{M}_\ell, I) \times P(\mathcal{M}_\ell|, I), \tag{2.16}$$

where $P(a_j|\{x_i, y_i\}, \mathcal{M}_\ell, I)$ are the probability distributions of a_j for each model and $P(\mathcal{M}_\ell|, I)$ are the probabilities of the different models.

2.3.4 Some consideration on information gain and Bayesian complexity

The gain of knowledge obtained from the analysis of experimental data can be quantified in terms of information $\mathcal{H}$, in the Shannon sense [58,59], that one gains in the process by the comparison between the posterior probability $P(\boldsymbol{a}|\{x_i, y_i\}, I)$ and the prior probability $P(\boldsymbol{a}|I)$. The information gain, in units of nat[2], is given by the so-called Kullback-Leibler divergence [60]

$$\mathcal{H} \equiv D_{KL} = \int P(\boldsymbol{a}|\{x_i, y_i\}, I) \ln \left[\frac{P(\boldsymbol{a}|\{x_i, y_i\}, I)}{P(\boldsymbol{a}|I)} \right] d^D\boldsymbol{a}. \tag{2.17}$$

Considering Eq. (2.12), D_{KL} can be written as

$$D_{KL} = -\ln E + \int P(\boldsymbol{a}|\{x_i, y_i\}, I) \ln L(\boldsymbol{a}) d^D\boldsymbol{a}, \tag{2.18}$$

which is nothing else that the negative logarithm of the evidence plus the average of the logarithmic value of the likelihood function.

From D_{KL} there is a interesting quantity can be derived that provides an additional criterion to compare models: the *Bayesian complexity* $\mathcal{C}$. $\mathcal{C}$ is calculated from the difference between the D_{KL}, i.e. the average of $\ln(L)$, and the "expected surprise" [45] from the data represented by the value $\hat{D}_{KL}$, where

$$\hat{D}_{KL} = -\ln E + \ln L(\hat{\boldsymbol{a}}), \tag{2.19}$$

where $\hat{\boldsymbol{a}}$ usually correspond to the posterior parameter mean values, or other possible estimators (ex. the likelihood function maximum or the posterior distribution medians) depending on the details of the problem[3]. The complexity is then defined as

$$\mathcal{C} = -2(D_{KL} - \hat{D}_{KL}) = -2\left[\langle \ln L(\boldsymbol{a}) \rangle - \ln L(\hat{\boldsymbol{a}})\right], \tag{2.20}$$

where the symbol $\langle\ \rangle$ indicates the mean value [39, 45]. $\mathcal{C}$ gives in practice a measurement of the number of parameters that the data can support for a certain model $\mathcal{M}$ for a defined set of data and parameter priors [39, 61].

For equiprobable models (similar evidence values), the comparison of Bayesian complexity could determine the choice in favour to one model or the other. Considering two different models $\mathcal{M}_1$ and $\mathcal{M}_2$ with $E_1 \approx E_2$ and different number of parameters $J_1 < J_2$, there are two cases [45]:

$\mathcal{C}_1 < \mathcal{C}_2$: The quality of the data is sufficient to measure the additional parameters of the more complicated model, but they do not improve its evidence by much. One should prefer model with less parameters.

[2] *nat* is the unit of information when the normal logarithm is used, similarly to the *bit*, the unit where the base-2 logarithm is employed.

[3] For multimode posterior probability distributions, the likelihood function maximum is more adapted. In fact the mean value can easily be far from the parameter region corresponding to high values of the likelihood function.

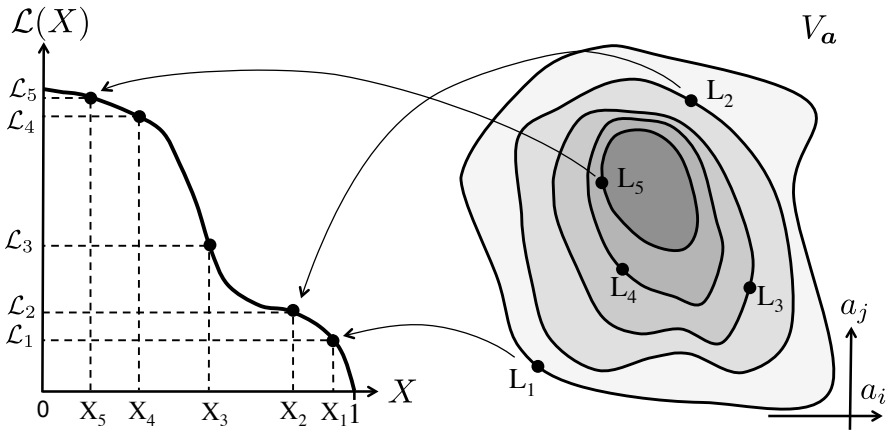

Figure 2.3 – Visualization of the integral of $\mathcal{L}(X)$ and corresponding volumes on the parameter space (two parameters only, a_i, a_j are considered with a 2D representation).

$\mathcal{C}_1 \approx \mathcal{C}_2$: The quality of the data is not sufficient to measure the additional parameters of the more complicated model and any conclusions cannot be drawn if whether extra parameters are needed.

2.4 The nested sampling for Bayesian evidence calculation

2.4.1 The basic idea

The major difficulty to calculate probabilities for hypothesis is the substantial computational power required for the evaluation of the Bayesian evidence. Contrary to the maximum likelihood method, where only the maximum of a function has to be found, one has to calculate here an integral over the J-dimensional space of parameters. Except in very few cases, there is not analytical solution of Eq. (2.14). The numerical integration by quadrature is not efficient due to the span of different order of magnitude of the likelihood function and the high dimensionality of the problem. The calculation of the evidence is generally done via the Monte Carlo sampling of the product $P(\{x_i, y_i\}|\boldsymbol{a}, \mathcal{M}, I)P(\boldsymbol{a}|\mathcal{M}, I)$.

A common approach to produce good sampling is the use of the Markov chain Monte Carlo (MCMC) technique. A Markov chain is a sequence of random variables such that the probability of the n^{th} element in the chain only depends on the value of the $(n-1)^{\text{th}}$ element. The purpose of the Markov chain is to construct a sequence of points $\boldsymbol{a}_n$ in the parameter space whose density is proportional to the posterior probability distribution. Different probabilistic algorithms are applied to build these chains like Metropolis-Hasting algorithm, Gibbs sampling, Hamiltonian Monte Carlo, etc. (see as example Ref. [62] and references their-in). Another method is the nested sampling where a subdivision of nested volumes in the parameter space is used to calculate the multi-dimensional integral. On this method is based the program `Nested_fit`.

The *nested sampling* algorithm is based on the subdivision of the parameters space volume $V_{\boldsymbol{a}}$, delimited by the parameters prior probabilities, into J-dimensional nested volumes that get closer and closer to the maxima of the likelihood function. With this method, the calculation of the evidence (Eq. 2.14) is reduced to one-dimensional integral from the original J-dimensional problem. This method has been originally developed by John Skilling in 2004 [26, 63, 64].

To reduce to an one-dimensional integral, the variable X (real and positive) is considered, which corresponds to the volume of the parameter space, weighted by the priors, for which the likelihood

function is larger than a certain value $\mathcal{L}$:

$$X(\mathcal{L}) = \int_{L(\boldsymbol{a})>\mathcal{L}} P(\boldsymbol{a}|I)d^J\boldsymbol{a}, \tag{2.21}$$

where I is the available background information. A schematic visualization of this relation is presented in Fig. 2.3. $X(\mathcal{L})$ is by construction monotonic and invertible, with $\mathcal{L} = \mathcal{L}(X)$. When $\mathcal{L} = 0$, the whole parameter volume $V_{\boldsymbol{a}}$ is considered and then $X = 1$ because of the prior probability normalization. When $\mathcal{L} \geq \max[L(\boldsymbol{a})]$, X is equal to zero. The infinitesimal volume dX is

$$dX = P(\boldsymbol{a}|I)d^J\boldsymbol{a}, \tag{2.22}$$

where $P(\boldsymbol{a}|I)d^J\boldsymbol{a}$ corresponds to the infinitesimal weighted volume of the parameter space where $\mathcal{L}(X) < L(\{x_i, y_i\}, \boldsymbol{a}) < \mathcal{L}(X + dX)$.

With the above definitions, Eq. (2.14) can then be rewritten as a simpler one-dimensional integral in X:

$$E = \int_0^1 \mathcal{L}(X)dX. \tag{2.23}$$

2.4.2 The evidence computation

The one-dimensional integral in the above equation and represented on the left part of Fig. 2.3 can be calculated numerically using the rectangle integration method subdividing the $[0, 1]$ interval in $M + 1$ segments with an ensemble $\{X_m\}$ of M ordered points $0 < X_M < ... < X_2 < X_1 < X_0 = 1$. Equation (2.23) is approximated by the sum

$$E \approx \sum_m \mathcal{L}_m \Delta X_m, \tag{2.24}$$

where $\mathcal{L}_m = \mathcal{L}(X_m)$ and $\Delta X_m = X_m - X_{m+1}$. The difficulty is now the determination of $\mathcal{L}_m$ and ΔX_m because a priori the relation between X and $\mathcal{L}$ is not known.

The evaluation of $\mathcal{L}_m$ values is obtained by the exploration of the likelihood function via a Monte Carlo sampling of K sets of parameter values $\{\boldsymbol{a}_k\}$ called *live points*. During the algorithm, these *live points* evolves to explore smaller and smaller parameter volume regions corresponding to higher and higher values of the likelihood function. In this way, values of $\mathcal{L}_m$ and ΔX_m can be calculated as well as the final value of the evidence. Details of the algorithm structure can be found in App. E.

2.4.3 Posterior probability distributions

The posterior probability distributions are built from the live points $\tilde{\boldsymbol{a}}_m$ determined during the nested sampling algorithm associated to the $\mathcal{L}_m, \Delta X_m$ values.

Once the evidence $E \equiv P(\{x_i, y_i\}|I)$ is determined, posterior inference can be easily generated from the $\{\tilde{\boldsymbol{a}}_m\}$ and $\{\boldsymbol{a}_k\}_M$ values. Each $\tilde{\boldsymbol{a}}_m$ is in the infinitesimal parameter volume $\Delta V_{\mathcal{L}_m < L(\tilde{\boldsymbol{a}}_m) < \mathcal{L}_{m+1}}$ that correspond to the interval ΔX_m. Considering the discrete form of Eq. (2.22) and Eq. (2.12), one can calculate the probability associated to the parameter values $\tilde{\boldsymbol{a}}_m$, in other words the step *weight* named in the previous sections:

$$P(\tilde{\boldsymbol{a}}_m|\{x_i, y_i\}, I) = P(X_m) \approx \frac{\mathcal{L}_m \Delta X_m}{E}. \tag{2.25}$$

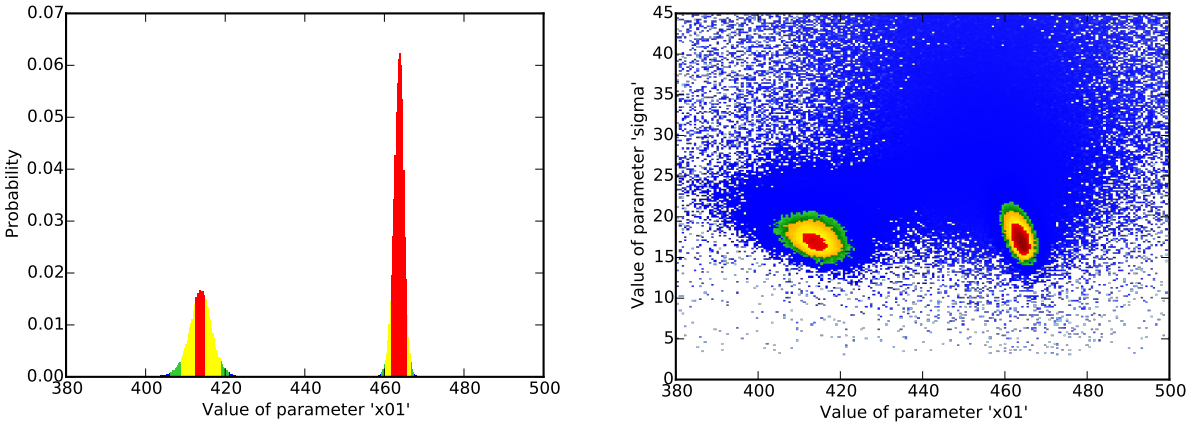

Figure 2.4 – Results from the nested sampling analysis of the data relative to the high-resolution X-ray spectrum of $1s2p\ ^3P_2 \rightarrow 1s2s\ ^3S_1$ helium-like uranium intrashell transition from Ref. [A36] when two Gaussian peaks with the same width are considered as model. On the left, the histogram relative to the probability distribution of position of one Gaussian peak ('x01') is presented. The presence of two solutions reflects the interchangeability of the two peaks. On the right, the two-dimensional histogram relative to the joint probability distribution of the position of one Gaussian peak and its width ('sigma'). Red, yellow and green regions indicate 68%, 95% and 99% confidence intervals (credible intervals).

From Eq. (2.25), the probability distribution of any single parameter a_j is obtained by marginalization (Eq.(2.10)), i. e. integrating of the posterior probability $P(\boldsymbol{a}|\{x_i, y_i\}, I)$ over the other parameters. In the case considered here, if the parameter of interest corresponds to the j^{th} component, its probability distribution can be built from $(\tilde{a}_m)_j$ values and their corresponding weights defined by Eq. (2.25).

As example, in Fig. 2.4 the histogram relative to the probability distribution of position of one Gaussian peak ('x01') relative to the data shown in Fig. 2.1 is presented on the left. On the right, the two-dimensional histogram relative to the joint probability distribution of the position of one Gaussian peak and its width ('sigma'). The presence of two solutions reflects the interchangeability of the two peaks.

2.4.4 Uncertainty of the evidence

As pointed by the Skilling, the main uncertainty of the final calculation of the evidence is related to the probabilistic determination of the terms ΔX_m [26, 64–66]. The choice of different integration methods of Eq. (2.23) (rectangle method, trapezoidal rule, etc.) does not influence very much the final result. Instead, the statistical glittering of X_m from Eq. (**??**) introduces an error.

The final value of the evidence is dominated by the region where the product $\mathcal{L}_m \Delta X_m$ is maximal, which is related to the amount of information that can be extracted from the data. In other words, E value is dominated by data inside a core in the parameter space corresponding to the X interval $[0, e^{-\mathcal{H}}]$, where $\mathcal{H}$ is the information defined in by Eq. (2.17).

The uncertainty associated to the evidence is given by [26, 64–66]

$$\delta(\ln E) \approx \delta \left[\ln \left(\sum_m \Delta X_m \right) \right] \approx \sqrt{\frac{\mathcal{H}}{K}}, \tag{2.26}$$

where K is the number of exploring set of parameters (*live points*) used for the computation.

A very pragmatic and practical way to evaluate the accuracy of E (used in `Nested_fit` program, see Sec. 2.5) is to calculate the evidence for different trials with different sets of *live points* an calculate then the average and the associated standard deviation from the different values of $\ln E$. From the consideration above, this is in fact the natural estimation to study the uncertainty of E [65,67]. More details on the origin of the evidence uncertainty can be found in App. E.

2.5 A data analysis program based on Bayesian statistics: `Nested_fit`

General considerations

`Nested_fit` has been developed for the calculation of the Bayesian evidence and posterior parameters probability distributions for a given set of data and selected model. The core of `Nested_fit` is the algorithm used for the calculation of the Bayesian evidence which is, as indicated by its name, the nested sampling presented in Sec. 2.4.

Similarly to `Minuit_fit`, the data has to be in the form $\{x_i, y_i\}$, where x_i are real numbers and y_i are necessarily counts detected at the positions x_i. y_i. Data with error-bars coming from other evaluations cannot be treated. The function to fit to the data can be chosen from the same function library than `Minuit_fit`. Outputs of `Nested_fit` are radically different and richer in information than `Minuit_fit` outputs. Not only the best parameter that maximise the likelihood (minimise the chi-square) is provided, but also the probability distribution of each parameter and the evaluation of the Bayesian evidence.

2.5.1 Computation algorithm of the Bayesian evidence

The calculation of the Bayesian evidence is made with the nested sampling method similarly to other program based to the same algorithm reported in Refs. [26, 46, 66, 68]. Even if the basic structure is practically identical to older programs, the algorithm for the search of new *live points* is substantially different. The searching algorithm is a Markov chain Monte Carlo method to explore the parameter volume $V_{L>\mathcal{L}_m}$ and it is an evolution of the *lawn mower robot* method, developed by L. Simons [23]. The maximum number of iteration M needed for the calculation of the evidence is determined by the comparison of the estimation of the error Err_M due to the truncation of the sum and the value of the suited accuracy δE. More details are presented in in App. E together with a simple example of analysis on the determination of the number of possible present peak contributions of the data presented in Fig. 2.1. Additional applications of `Nested_fit` can be found in Ch. 3.

2.5.2 Inputs

In addition to the function and data file names, common to `Minuit_fit` program input, `Nested_fit` requires in the input file `nf_input.dat` some more specific parameter. The most important are:

The maximum number of jumps N and the relative length of the jump f: These parameters are important for efficiency of the search of the new live points and for the non-correlated and efficient exploration of the parameter space. Higher values of f and N guarantee a better independence between sampling points of the Monte Carlo computation but a minor efficiency of the algorithm.

The number of live points K: The choice of K influence directly the expected accuracy of the evidence $\delta E \propto 1/\sqrt{K}$, and also provides a better sampling of the parameter volume. As counterpart, an increasing of K increases the computation time.

The required final evidence accuracy ΔE: A too large value of the accuracy will bias the evidence calculation. A too small value can make the evidence computation significantly long. For a given problem, the optimal value is obtained by looking a posteriori at the evolution of $\mathcal{L}_m \Delta X_m$. Good and efficient values are generally between 10^{-3} and 10^{-5} as also discussed in Ref. 66.

The number of trials sets of live points N_{LPS}: Besides theoretical considerations, the best strategy to estimate the evidence accuracy is to calculate E several times with different starting sets of live points (with different seed for the random generator) and to extract the mean and standard deviation of the logarithmic values of the computed evidence, which is the pertinent quantity for the uncertainty evaluation (Sec. 2.4.4).

The parameter priors Priors of the different parameters can be selected between two options: (i) an uniform prior where the parameter value boundaries have to be provided or (ii) a normal distribution where a main value and the associated standard deviation have to be provided (as example from a past experiment).

2.5.3 Outputs

The program provides four major files:

- `nf_output_res.dat` contains the details of the computation (n. of live points trials, n. of total iteration), the final evidence value and its uncertainty $E \pm \delta E$, the parameter values $\hat{\boldsymbol{a}}$ corresponding to the maximum of the likelihood function, and the mean, the median, the standard deviation and the confidence intervals (68%, 95% and 99%) of the posterior probability distribution of each parameter. Moreover, the information gain $\mathcal{H}$, the Bayesian complexity $\mathcal{C}$ and the theoretical minimal value of iteration deduced from the extracted information value are also provided. δE is calculated only if $N_{LPS} > 2$.

- `nf_output_data.dat` contains the original input data together with the model function values corresponding to the parameters $\hat{\boldsymbol{a}}$ with the highest likelihood function value, the residuals and the uncertainty associated to the data.

- `nf_output_tries.dat` is present only if $N_{LPS} > 2$. For each live points trial, it contains the final evidence, the number of iterations and the maximum value of the likelihood function.

- `nf_output_points.dat` contains all discarded and final live points values $\tilde{\boldsymbol{a}}_m$ and $\{\boldsymbol{a}_{M,k}\}$, their associated likelihood values $L(\boldsymbol{a})\}$ and posterior probabilities $P(\boldsymbol{a}|\{x_i, y_i\}, I) \approx \mathcal{L}_m \Delta X_m / E$. From them, the different parameter probability distributions or correlation diagrams, as that on Fig. 2.4, can be built from marginalization (Eq. 2.10) on the unretained parameter[4].

To built histograms, and trace the different plots, special `Python` routines have been written. These routines can, if required, change systematically the input file `nf_input.dat` and read the output files for automated exploration of input parameter values or priors, or models $\mathcal{M}$.

[4] In practice this consists to built histograms only from the parameter components of the *live points* one is interested on.

2.5.4 Use in the different research topics

`Nested_fit` has been employed mainly in the analysis of the pion mass experiments [A7, C1] described in Ch. 3. Additional analyses (still unpublished) have been performed on the data regarding the nuclear capture of the bound electron in H-like systems where an unexplained modulation of the exponential decay is observed [A20, A41]. Recently, `Nested_fit` has been used in the ASUR team at INSP for the determination of the presence or not of oxidation signature in photoemission spectra of gold nanoparticles.

Chapter 3

The measurement of the mass of the negatively charged pion

3.1 Introduction

3.1.1 Some history

The measurement of masses of unstable particles is mainly obtained by mass spectroscopy, if the particle lifetime is long enough, or by the measurement of the masses and of the kinetic energies of the decay producs. A negatively charged particle with a sufficiently long lifetime (more than a few ns) can form a bound system with an atomic nucleus. Here a third method is possible: precision spectroscopy of exotic atoms. Except for muonium ($e^- - \mu^+$ bound state) or positronium ($e^- - e^+$), atomic spectra of such atoms are in the X-ray domain due to the orbiting particle mass, orders of magnitude larger than the mass of the electron. In the past, the spectroscopy of exotic atoms successfully allowed for the determination of the mass of muons, pions, kaons and antiprotons [12–15, 69].

In the case of the pion, the 2014 official value from the Particle Data Group [70] is 139.57018 ± 0.00035 MeV/c^2 with an accuracy of 2.5 ppm. It is the result of an average of two values. One comes from the spectroscopy of pionic magnesium [71] (solution B) and the other comes from the spectroscopy of pionic nitrogen [14]. In the πMg experiment, a solid-state target was employed. In this case, electron capture from the pionic atom is unavoidable, leading to difficulties of the interpretation of the atomic spectra. Different assumptions on the K electron population lead to differences in the pion mass up to 16 ppm [71] and where one of the solutions (solution A) is in complete disagreement with evaluations obtained from pion decay measurements [72,73]. In the πN experiment the electron refilling is avoided. In this case, the experiment bottleneck was the calibration line, the Cu Kα fluorescence radiation, whose large width (4 eV) was limiting the final accuracy.

The experiment described here resumes the strategy of the gas target, but exploits (i) the high precision of 0.033 ppm for the mass of the positively charged muon being $m_{\mu^+} = (105.6583715 \pm 0.0000035)\,\mathrm{MeV/c^2}$ [70] and (ii) the unique feature that in πN and μO transition energies almost coincide. When using a gas mixture, the simultaneous measurement of πN and μO lines becomes possible with the muonic transition serving as an on-line calibration. Hence, systematic shifts during the unavoidably long measuring periods are minimised and a new accurate measurement of the charged pion can be performed.

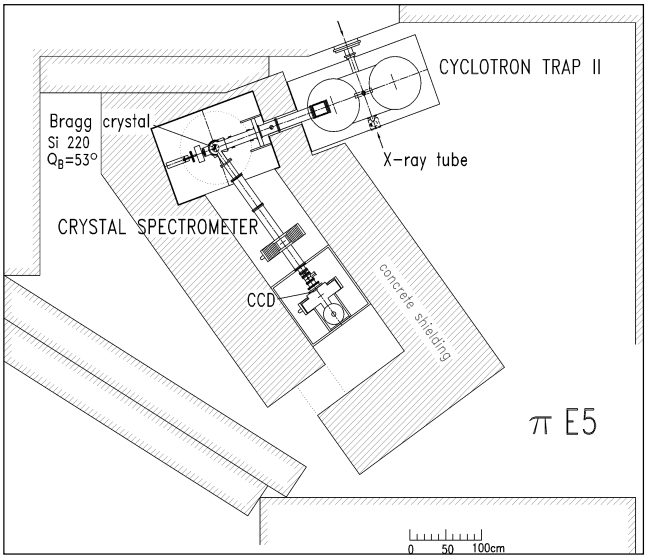

Figure 3.1 – Set-up of the experiment.

3.1.2 Work context, personal contribution and associated publications

This project for the new measurement of the negative pion mass started in an international collaboration based at the Paul Scherrer Institute (PSI, Villigen, Switzerland) in the '90s and the data were acquired in the year 2000. Part of the author's Ph.D. thesis (2002–2005) was dedicated to the analysis of those data providing a preliminary value of the pion mass as outcome. Due to the difficulties to describe accurately the response function of the X-ray spectrometer used for this measurement, the final analysis has been completed only in the years 2015–16 with the development and the implementation of Bayesian methods. Analysis of additional data, not exploited before, was also required to characterise the spectrometer response function for the energy range of interest. After a brief description of the experiment and previous developments, this last part of analysis, where the author mostly contributes with the use of the methods presented in Ch. 2, is presented.

The publication associated to this chapter is presented in App. F [A7]. Another related publication is Ref. C1.

3.2 Production of pionic and muonic atoms and detection of their radiative emission

3.2.1 Pionic and muonic atom production

Pionic atoms are obtained by stopping the intense pion beam (1.9 mA) at the πE5 beam line at the Paul Scherrer Institut in a gaseous target. The pions, with an initial kinetic energy of 112 MeV/u, are captured and slowed down in the so-called cyclotron trap [74, 75] constituted by a pair of superconducting magnets arranged to form a cyclotron-type field. The field has a maximum value of 4 T perpendicular to the pion trajectory. A series of plastic degraders is used to stop a maximum of pions in the centre of the cyclotron trap in a target chamber filled with the target gases. A general overview of the whole set-up is presented in Fig. 3.1. Between one and three percents of the initial pions produce pionic atoms. The large gap between the magnet coils guarantee an efficient recapture

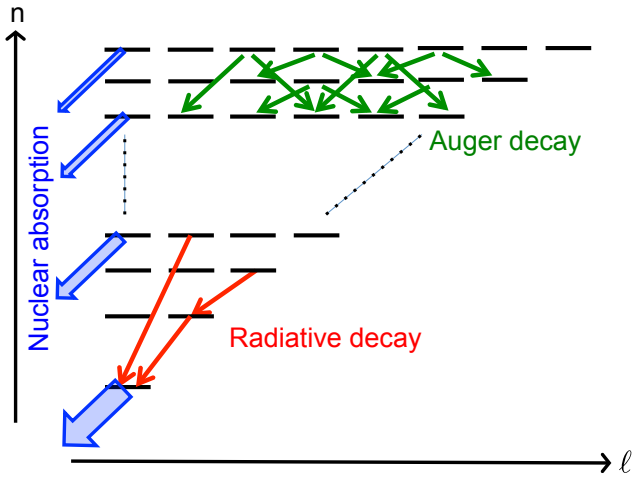

Figure 3.2 – Cascade processes after the formation of the pionic atoms. After the capture of the pion in a high-n state, the first decays are via the ejection of electrons (Auger emission). For low-n states, the dominant decay is radiative. Pion in ns states have a non negligeable probability to be absorbed by the nucleus .

of muons generated by pions decaying before stopping. In this way, a simultaneous stopping of muons and a production of muonic atoms is provided.

For the simultaneous measurement, comparable count rates for the πN and the μO lines are obtained by using a N_2/O_2 gas mixture of 10%/90% and by the installation an *ad hoc* set of polyethylene degraders inside the magnet gap to optimise the X-ray yield.

In the target cell, pions are captured by the atoms in highly exited states where the overlap of the outermost electron and pion wave-functions is maximal, i.e., where the characteristic radius (Eq. (1.3)) of the wavefunctions are similar [76]:

$$\frac{n_i^2\hbar}{m_{\mu,\pi}cZ\alpha} \sim \frac{n_e^2\hbar}{m_e cZ\alpha} \rightarrow n_i \sim n_e\sqrt{\frac{m_{\mu,\pi}}{m_e}} \sim n_e \times 16. \tag{3.1}$$

n_i is the initial principal quantum number of the captured pion,n_e is the principal quantum number of the most external electron of the atom with atomic number Z, α is the fine structure constant, $m_{\mu,\pi,e}$ are the muon, pion and electron masses and c the speed of light.

For exotic atoms with $Z > 2$, the first steps of the de-excitation proceed via Auger emission with the self-ionisation of the target atom or molecule. This quickly process leads to a high degree of ionisation acting at the femtosecond time scale. If the target is constituted by molecules, the fast ionisation causes the Coulomb explosion between the constituents with an acceleration of the molecule fragments and, consequently, a Doppler broadening of the emitted X–rays [77]. After the molecule fragmentation, the exotic atom continue its de-excitation by Auger and X–ray emission (see Fig. 3.2).

Auger transition probability W_A is in proportional to

$$W_A \propto 1/\sqrt{2\Delta E + 37.8\ \text{eV}}, \tag{3.2}$$

and increases more than exponentially with n [78].

Radiative transition probability W_X is proportional to [79]

$$W_X \propto \Delta E^3 |R^{n,\ell}_{n',\ell'}|^2. \tag{3.3}$$

$R^{n,\ell}_{n',\ell'}$ is an integral involving the radial part of the initial and final wavefunction states and

$$\Delta E \approx mc^2 \frac{(Z\alpha)^2}{2}\left(\frac{1}{n'^2} - \frac{1}{n^2}\right), \tag{3.4}$$

with m being the reduced mass of the system. For an initial level n, the radiative transition probability is[1] $W_X \approx n^{-5}$ [78,79] with the selection rule is $\Delta\ell = \pm 1$ and therefore in case of an electron free atom the states $(n, \ell = n-1)$ are efficiently populated.

For high-excited levels ($n \gg 1$

$$W_X \ll W_A. \tag{3.5}$$

The Auger emission dominates the upper part and it continues until the complete depletion of the electron shells if capture from neighbouring target atoms is avoided whereas radiative transitions are most probable for transition between lower levels.

If a low-density target ($\leq 1-2$ bar) is used, electron recapture from external atoms is unlikely because the probability for having a collision with another atom of the target is low even in the presence of the Coulomb explosion. The signature of the complete electron depletion is the appearance of X-ray lines at $n \geq 5$, which otherwise would be converted into Auger transitions [78, 80–83]. In the presented experiment, electron recapture during the cascade is not expected because of the use of a N_2/O_2 gas mixture with a pressure of 1.4 bar at room temperature. In the case of solid targets, however, electron refilling is unavoidable. More details on the atomic cascade in exotic atoms can be found in Refs. [76, 84–89].

The so-called circular transitions (yrast transitions in terms of nuclear physics) $(n, \ell = n-1) \rightarrow (n-1, \ell = n-2)$ are the most intense X-ray lines. Because of this, they are used for the measurement of the pion mass. In addition, for these transitions, strong interaction effects are small because of the reduced overlap between the pion wavefunction and the nucleus. The energy measurement of the πN and μO $5g-4f$ transitions are in particular chosen because (i) for the $6h-5g$ transition (2.2 keV) the absorption in target gas itself and windows significantly reduces the count rate and (ii) for the $4f-3d$ transition the $3d$-level energy in πN requires a already substantial correction due of the strong interaction effect.

3.2.2 The crystal spectrometer

The transition energies of the exotic atoms are measured using the Bragg diffraction spectroscopy. The crystal spectrometer is designed to be optimised to the needs of exotic-atom X-ray spectroscopy. It is set up in a Johann geometry [90] with a spherically bent Si(110) crystal [91] (see Fig. 3.3 left). Spherical bending (with a radius of curvature of about 3 m here) leads to a partial vertical focussing [91, 92] which increases the count rate. In the configuration considered here, the overall efficiency of the crystal spectrometer is $\approx 5 \times 10^{-8}$.

For the simultaneous detection of the pionic and muonic atoms lines, the spectrometer is equipped with a large position-sensitive detector, which is composed of an array of charge-coupled devices (CCDs) corresponding to a total sensitive area of about $48 \times 72\,\mathrm{mm}^2$ [93, A48]. About 85% of the reflected intensity is covered by the sensitive area of the detector. The CCD array is placed in proximity of the Rowland circle where X-rays are focused. The simultaneous measurement of two distinct lines implies that the focussing conditions are not fulfilled as show in Fig. 3.3 (right). Effects from defocussing have to be taken into account for the accurate determination of the line position.

[1] $W_X \approx n^{-3}\ell^{-2}$ for a specific angular quantum number.

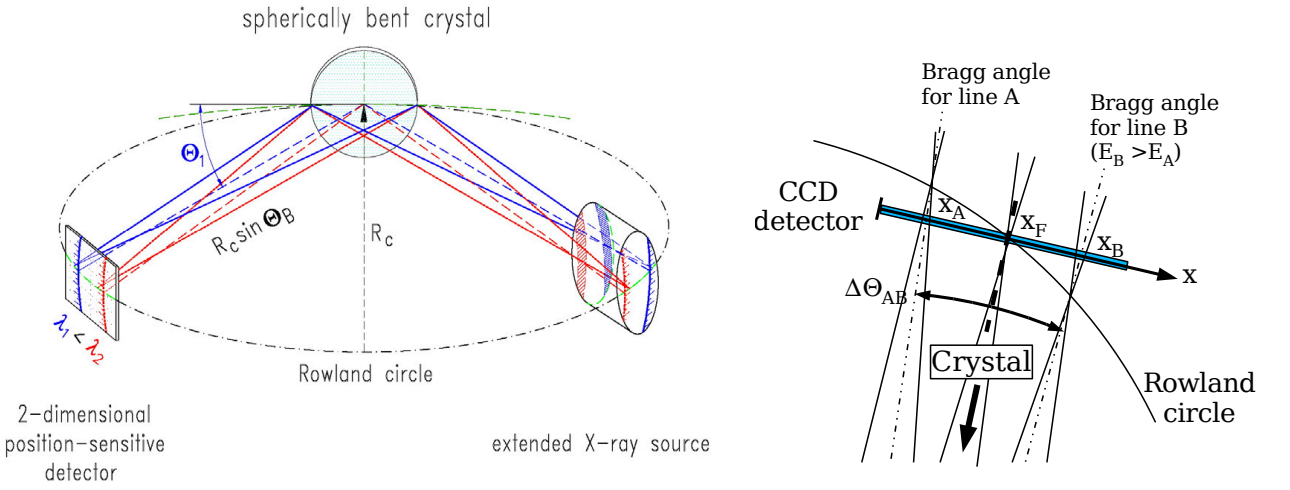

Figure 3.3 – Left: Schematic of the Bragg spectrometer in the Johann configuration. The crystal bending radius R_c is the diameter of the Rowland circle in proximity of which the position sensitive detector has to fulfil the focusing condition $R_c \sin\Theta_B$, where Θ_B is the Bragg angle. Right: Scheme of the X-ray detector position with respect to the Rowland circle (the focus location of the spectrometer) and two diffracted lines A and B with different energy $E_B > E_A$. The (small) displacements of the two lines from their individual focal conditions has to be taken into account in the calculation of the spectrometer response function.

3.2.3 Data acquisition and spectra

About 9000 events for each element are collected in each of the $(5g-4f)$ transitions during 5 weeks of data acquisition. The final spectrum is obtained from the projection of the two-dimensional spectral line distribution on the CCD (Fig. 3.4) to the dispersion axis (Figs. 3.4 and 3.5). Due to their diffraction nature, the lines are slightly curved. Before the projection, this curvature is fitted and the data are redressed. The count rates for the πN and μO transitions are about 15 events per hour each. During this period the temperature of the crystal and the spectrometer parts is monitored and the relative positioning of its components is checked by acquiring regularly X-ray spectra of Cu$K_{\alpha_{1,2}}$ fluorescence lines.

The focus of the μO and the πN transitions are 4.6 mm beyond and 14.2 mm before the CCD array plane, respectively. To correctly consider defocussing effects and and the general spectrum characteristics, additional data are recorded in addition to the simultaneous measurement of the πN and μO transitions. They different acquired spectra are summarised below.

Mix spectrum: The simultaneous spectrum of πN and μO transitions with the focus of μO and the πN lines 4.6 mm beyond and 14.2 mm before the CCD array plane, respectively.

Dispersion spectra: 6 spectra of the $5 \rightarrow 4$ πN transitions obtained by a 100% N_2 gaseous target for different angular positions of the detector. Except for the CCD angular position, the set-up of these measurements is the same than for the *mix* spectrum, i.e. with the focus of the πN line 14.2 mm before the CCD array plane.

πN focalscan spectra: 5 spectra of the $5 \rightarrow 4$ πN transitions obtained by a 100% N_2 gaseous target for different distances between the position sensitive detector and the crystal ($\pm$18 mm with respect to the focal position).

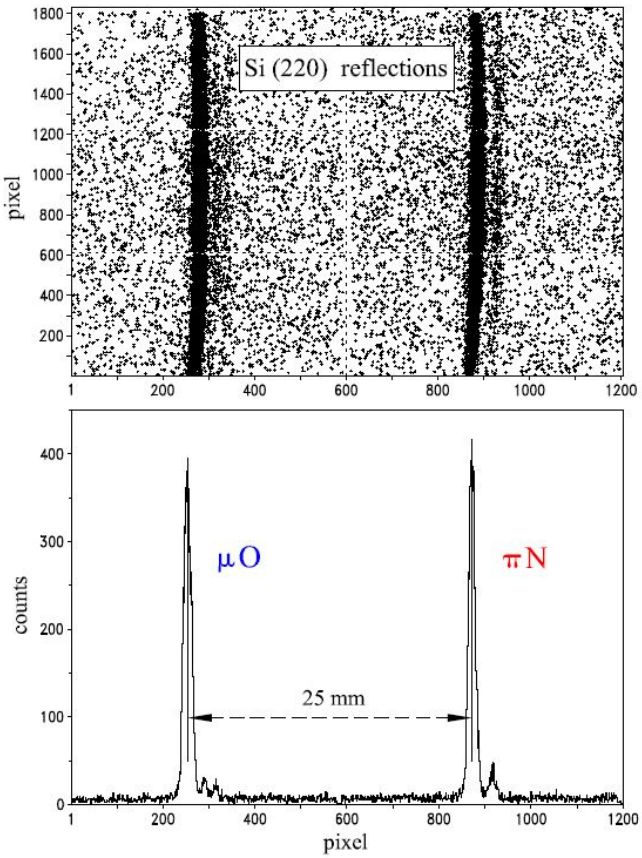

Figure 3.4 – Simultaneously measured $(5g - 4f)$ transitions in muonic oxygen (calibration) and pionic nitrogen. Top: Distribution of the Bragg reflections on the surface of the 2×3 CCD array. Straight dashed lines indicate CCD boundaries. Middle: Projection on the axis of dispersion after correction for curvature (see text).

πNe focalscan spectra: 7 spectra of the $6 \to 5$ πNe transitions (4.3 keV) obtained by a 100% Ne atomic gaseous target for different distances between the position sensitive detector and the crystal ($-27 + 18$ mm with respect to the focal position). Differently than in the case of πN and μO spectra, no Coulomb explosion occurs wheb neon, a monoatomic gas, is used as target.

3.3 Spectral line shape

3.3.1 General consideration

The mass of the charged pion is determined from the measurement of the distance between the πN and μO spectral lines [A7, C1]. The most complex part of the experiment is the extraction of a trustable value of such a distance. This requires the accurate determination of the spectrometer response function and of the characteristics of the atomic radiation (line composition, positions, intensities, widths, etc.). For each spectral line, the recorded intensity distribution function $F(x)$ is the result of the convolution of three main contributions:

$$F = F_{\text{spectr.}} \otimes F_{\text{cascade}} \otimes F_{\text{interaction}}. \tag{3.6}$$

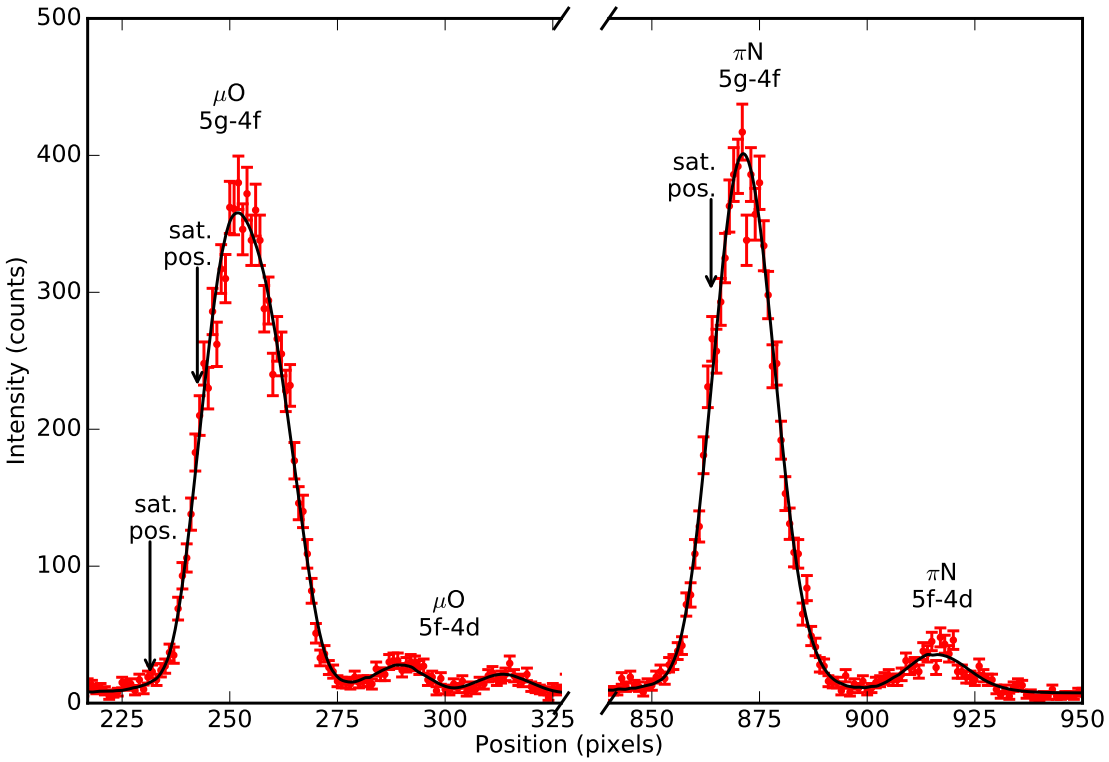

Figure 3.5 – Details of the fit to line patterns. The parallel transitions $5f - 4d$ and possible additional transitions from the presence of one remaining electron in the K shell are indicated ("sat. pos."). For μO, the larger width of the $5g - 4f$ transition is due to the non-resolved fine structure splitting, which is resolved for the $5f - 4d$ transition.

The first contribution is the response function of the instrument with respect to an ideal mono-energetic X-ray source. It depends on the characteristic of the crystal reflectivity curve (rocking curve), but also on the spectrometer aberrations and on the positioning of detector with respect the focal plane. The second contribution depends on the dynamics of the atomic cascade after the formation of the pionic atom, which generates a non-trivial broadening of the spectral lines. The last contribution is related to the natural width of the transition, which is negligible in the case considered here. The discussion about the evaluation of $F_{\text{spectr.}}$ and F_{cascade} is the object of the next sections.

In addition to the characterisation of each line profile, the different components of the atomic spectra, fine structure, parallel transitions, nuclear isotopes contributions, etc., have to be taken into account in the analysis. As an example, for the πN spectrum, in addition to the $5g - 4f$ transition, also the $5f - 4d$ and the $5d - 4p$ have to be considered as well as transitions of the ^{15}N isotope and possible satellite lines resulting from remaining electrons in the K shell. μO spectrum is even more complex due to the spin-1/2 of the muon (pion is a spin-0 particle), which produces a fine structure splitting of the lines. Different assumptions of the spectra composition are tested during the analysis as well as their influence on the pion mass final value.

3.3.2 Spectrometer response function

The spectrometer response function $F_{\text{spectr.}}$ is determine by means of a Monte Carlo simulation that takes into account the geometry of the spectrometer components (detector, crystal and source) and the characteristics of the crystal with

$$F_{\text{spectr.}} = F_{\text{geom.}} \otimes F_{\text{RC}} \otimes F_{\text{defects}}. \tag{3.7}$$

$F_{\text{geom.}}$ represents the contribution due to the spectrometer geometry, F_{RC} is the characteristic crystal reflectivity curve (rocking curve) and F_{defects} is an additional Gaussian broadening to take into account possible crystal imperfections.

The spectrometer geometry is defined by the position and spatial extensions of the X-ray source and the position-sensitive detector with respect to the Rowland circle, which defines the focus position of the employed Johann spectrometer (see Fig. 3.3). The crystal reflectivity is obtained by the code XOP (XCRYSTAL subroutine) [94, 95]. The additional Gaussian broadening has to be determined experimentally.

The reliability of the spectrometer simulation program has been tested by a series of measurements with X-ray lines with a very narrow natural width. In particular, a specially dedicated electron cyclotron resonance ion trap (ECRIT) has been built to produce intense X-ray narrow [91,96–99,C30]. In particular, $1s2s\ ^3S_1 \rightarrow 1s^2\ ^1S_0$ M1 transitions from He-like chlorine, sulphur and argon produced in the ECRIT plasma have been employed for this scope. These lines have in fact a natural width of few meV, much less than the resolution of the crystal spectrometer.

As an illustration of the reliability of the Monte Carlo spectrometer modelling and the effect of defocussing, in Fig. 3.6 the recorded and simulated spectra of the $6 \rightarrow 5$ transition in πNe are presented for different crystal–detector distances ("Pos." is the shift in mm with respect to the theoretical focal position on the Rowland circle). In the case of πNe lines, Coulomb explosion is not present and the width of the spectral line F is mainly due to $F_{\text{spectr.}}$. As one can see, the position of the detector with respect to the focal position plays an important role in the asymmetry of the spectral line that, if is not taken into account, can induce a systematic effect of the peak position.

3.3.3 Coulomb explosion, atomic cascade and strong interaction broadening

Several processes contributes to F_{cascade}: (i) the Coulomb explosion, (ii) the characteristic of the atomic cascade and, in the case of light pionic atoms not treated here, (iii) the strong interaction [A29,A32,C6]. F_{cascade} is studied and evaluate using Bayesian data analysis methods. Different hypotheses are considered (different characteristics of the Coulomb explosion and of the atomic cascade) and their correspondent probabilities are calculated via the computation of the Bayesian evidence, as described in Sec. 2.3.3.

The atomic cascade characteristics can influence the spectral line shape via collision-induced radiationless de-excitations. During the collision between the exotic atom and a normal target atom, the potential energy of the excited levels can be partially released in favour of an increase of the kinetic energy of the two atoms. The acquired velocity associated to the collision-induced de-excitations is isotropically distributed and it depends on the discrete energy difference between the involved atomic levels. The broadening due to the Coulomb explosion depends on the electrical charge of the molecule components. Both effects are approximated by simple kinetic energy distributions K^D (in the laboratory frame) and the relative Doppler broadening as shown in Fig. 3.7.

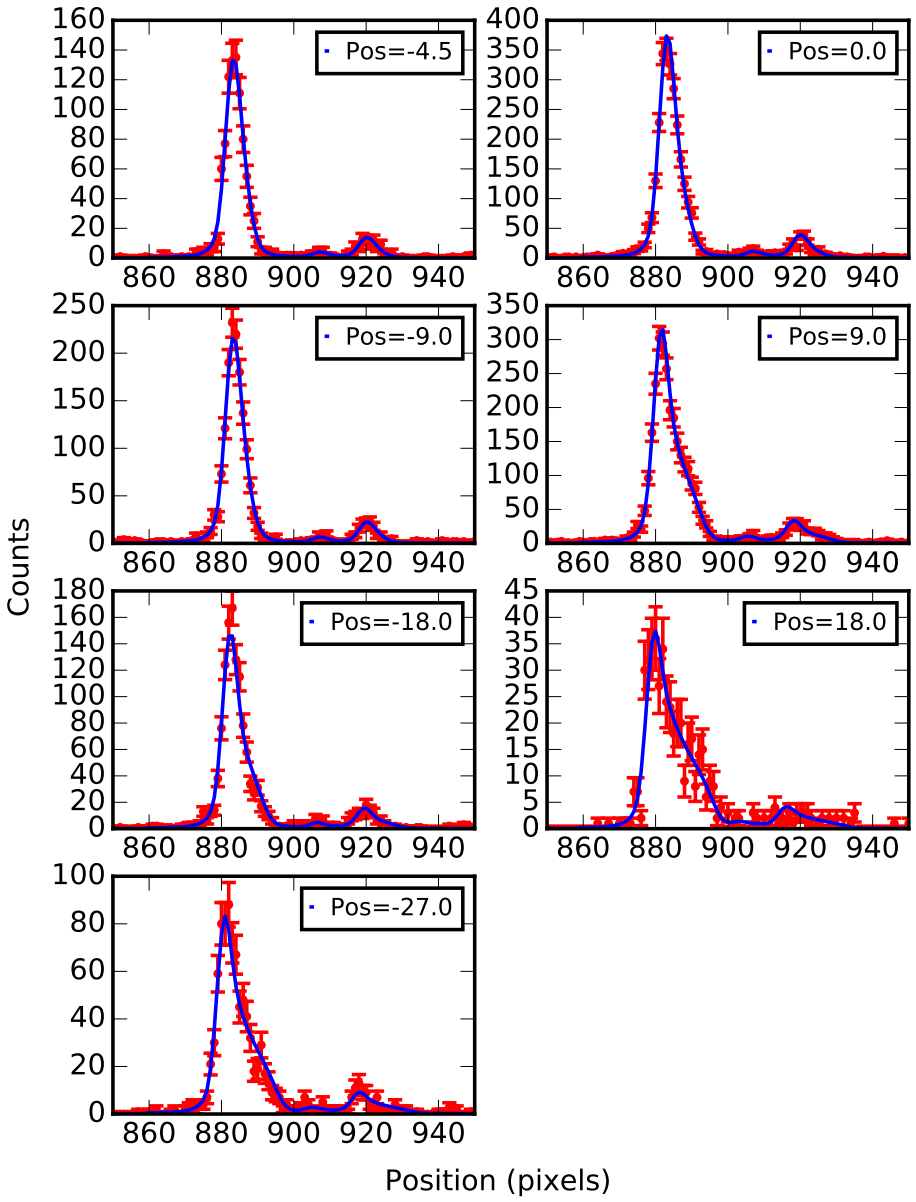

Figure 3.6 – Experimental data (red error bars) and fitted profile (blue lines) $F(x)$ for different spectra corresponding to different positions *Pos.* with respect the theoretical focal position (which does not corresponds to the real one as one can see from the width of the lines). The peak asymmetry on the high-energy side of the peak (right) is due to the typical aberration of Johann-type spectrometer from the X rays diffracted by the regions of the crystal far from its centre.

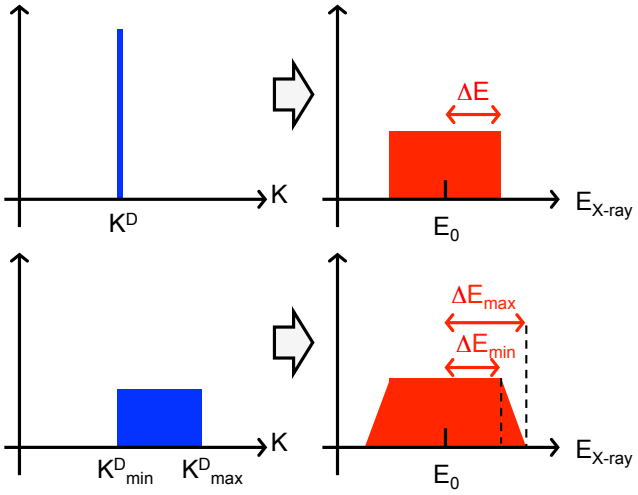

Figure 3.7 – Effect of the kinetic energy distribution of the pionic atoms on the energy spectra of the emitted photons of energy E_0 in the laboratory reference frame.

The transition energy observed in the laboratory reference frame E_{lab} depends on the transition energy E_0 and on the acquired velocity v via the Doppler shift formula

$$E_{\text{lab}} = E_0\gamma(1 - \beta\cos\theta_{\text{lab}}), \tag{3.8}$$

where $\beta = v/c$, $\gamma = 1/\sqrt{1-\beta^2}$ and θ_{lab} is the observation angle in the lab with respect to the velocity direction. Considering an isotropic emission, a non-relativistic kinetic energy gain K^D corresponds to a rectangular broadening[2] of $2\Delta E$, where $\Delta E/E_0 = \gamma(1+\beta)$. If a flat kinetic energy gain distribution between K^D_{min} and K^D_{max} is considered, a trapezoidal X-ray line broadening is expected (see Fig. 3.7).

A realistic kinetic energy distribution is much more complex than the distributions represented in Fig. 3.7. It reflects in fact the structure of the exotic atom and the atomic cascade processes. To describe the Coulomb explosion in πN, rectangular distributions of K^D are however sufficient. More details on this topic can be found in Refs. 23, A38, C6.

3.4 Analysis of the data and discussions

3.4.1 Analysis methods

Each spectrum, or series of spectra, are analysed by the `Nested_fit` program package described in Sec. 2.5 using the multi-spectra analysis option, particularly essential for sets of spectra corresponding to different focal positions.

[2]The spectrum distribution can be decomposed in $\frac{dI}{dE_{\text{lab}}} = \frac{dI}{d\Omega}\frac{d\Omega}{dE_{\text{lab}}}$, where Ω is the solid angle in the source reference frame. For an isotropic emission $\frac{dI}{d\Omega}$ is constant and proportional to $\frac{dI}{d\cos\theta}$. Then one can rewrite $\frac{dI}{dE_{\text{lab}}} = \frac{dI}{d\cos\theta}\frac{d\cos\theta}{d\cos\theta_{\text{lab}}}\frac{d\cos\theta_{\text{lab}}}{dE_{\text{lab}}}$. From Eq. (3.9) and the relativistic transformation between $\cos\theta = \frac{\beta-\cos\theta_{\text{lab}}}{\beta\cos\theta_{\text{lab}}-1}$ [100] one has

$$\frac{dI}{dE_{\text{lab}}} \propto \frac{1}{\gamma^2(1-\beta\cos\theta_{\text{lab}})^2} \times \frac{1}{E_0\gamma\beta} = \frac{E_0}{\beta\gamma E_{\text{lab}}^2} \tag{3.9}$$

and where E_{lab} is bound by the values $E_0\gamma(1\pm\beta)$. For non-relativistic cases, the distribution can be approximated as flat. The first term in Eq. (3.9) tend to a constant value when $\beta \to 0$.

For each line contribution, the spectral line is modelled by a function F^{fit} obtained by the convolution of the different contributions and an adjustable amplitude A and position x_0

$$F^{\text{fit}}(x) = A \times [F_{\text{MC}} \otimes F_{\text{Doppler}} \otimes G]\,(x - x_0). \tag{3.10}$$

F_{MC} includes the spectrometer geometry and crystal rocking curve ($F_{\text{geom.}}$ and F_{RC}) and it does not contain adjustable parameters. F_{Doppler} represents the contributions due to the Coulomb explosion and atomic cascade (F_{cascade}). It is modelled by a series of uniform distributions kinetic energy K^D distributions (called Doppler boxes) with variable boundaries, as described in Sec. 3.3.3. Its adjustable parameters are the positions and extensions of the K^D distribution boxes and their relative intensity. The diffraction crystal imperfections are modelled by a Gaussian distribution G with the characteristic angular dispersion variance σ_{cry} as unique adjustable parameter.

Due to the complexity of the calculation of the effects of the kinetic energy distributions, their boundaries $(K^D_{min})_1, (K^D_{max})_1, (K^D_{min})_2, (K^D_{max})_2, \ldots$ cannot be adjustable parameters of the function used by `Nested_fit` but they are fixed at priori. The relative populations of the different distribution regions are on the contrary free parameters of the profile functions (with the constraint that their sum is equal to 100%). The estimation of the best choice of the kinetic energy boundaries is done by the calculation of the Bayesian evidence E that provides the probability of the chosen model.

Each line of the spectra uses the same peak profile but adjustable intensities and positions (plus a flat background). For the analysis of a set of X-ray measurements, the Doppler boxes intensity, σ_{cry}, the relative intensities and angular relative line positions are common parameters between the different spectra. The background level, the amplitude and the position of the main line are adjusted for each spectra.

3.4.2 Strategy of the analysis

Except for the *mix* spectrum, the different data sets described in Sec. 3.2.3 are used to determine different characteristics of the spectra that depend on the apparatus and the atomic cascade.

Focalscan spectra from $6 \to 5$ πNe transitions are mainly used to check the correct reproducibility of the crystal spectrometer response function and the evaluation of the contribution due to the Bragg crystal imperfections via the value of σ_{cry} in G.

In *Focalscan* spectra from $5 \to 4$ πN transitions, the kinetic energy distribution boxes are reliably studied, together with the evaluation of relative positions and intensities of the different lines.

Differently to *mix* and *dispersion* spectra, in the set of *Focalscan* spectra from $5 \to 4$ πN transitions, there are few acquisitions that correspond to detector positions very close to the focal position of the crystal spectrometer. Due of the consequent better instrumental resolution of these spectra, the kinetic energy distribution boxes are in particular reliably studied, together with the other parameters.

Dispersion spectra of πN are analysed together with the *mix* spectra for (i) an additional evaluation of the Doppler boxes and relative line position and intensity values and (ii) the final position of the $5g \to 4f$ πN transition for the pion mass evaluation. The position of the πN line in the mix spectrum is more accurate than the μO line because it benefits from the much better determination of the other parameters (relative line positions and amplitudes, etc.) from the *dispersion* spectra. These spectra, obtained with a 100% N_2 target, are in fact characterised by a much better statistics (60000 counts) than the mix spectrum (9000 counts in each main line).

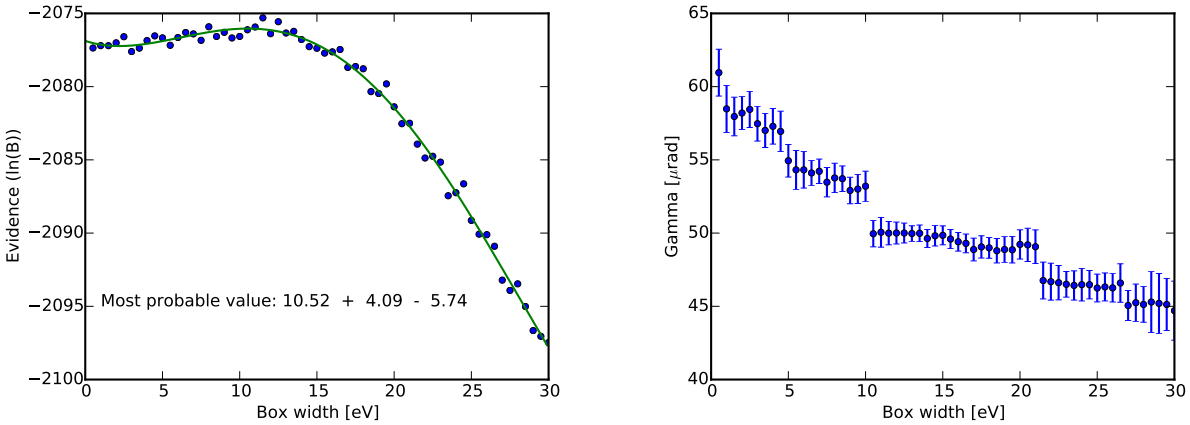

Figure 3.8 – Logarithm of the evidence)left) and value of the Gaussian width σ_{cry} (right) for different end values $(K^D_{max})_1$ of the kinetic distribution box for the πNe spectra.

3.4.3 Measurement of the Gaussian broadening of the crystal from πNe data

Unfortunately, due to the X-ray energy range of interest (around 4 keV), no characterisation with highly charged ions emission could be done (limited to 2.5–3 keV energy range) to extract the Gaussian broadening of the crystal σ_{cry} at these energies. For this reason, the analysis of πNe spectra is particularly valuable. Due of the monoatomic nature of the neon gaseous target, no Coulomb explosion occurs during the formation of πNe atoms. X-ray emission from the $6 \rightarrow 5$ transitions are then used for the characterisation of the response function of the spectrometer.

σ_{cry} is estimated together with effect of collision-induced radiationless de-excitations (terms F_{Doppler} and G, respectively of Eq. (3.10)) as described in Sec. 3.4.1. More precisely, the procedure developed for the first time to study πD spectra [23] is applied, which consist in two steps:

1. the analysis of a kinetic energy distribution K modelled by an single flat distribution (a Doppler box) with $K^1_{min} = 0$ and $(K^D_{max})_1$ that is varied, and

2. the analysis a kinetic energy distribution K modelled by two flat distributions, one similar to that one of the step (1) and a second one localised at the position $(K^D)_2$ (± 1 eV).

For each step, the posterior probability distribution of σ_{cry} is given as output from the analysis program. The probabilities $P(K^D)$ of the preselected K^D values are determined from the Bayesian evidence calculation E with $P(K^D) \propto E$. For the step (1), the values of E and σ_{cry} are reported in Fig. 3.8 for the different $(K^D_{max})_1$ upper bounduary. The most probable value of $(K^D_{max})_1$ and its associated uncertainty are calculated considering the maximum values of E and the boundaries values corresponding to a relative drop of 0.9 of $\ln E$, which correspond to a confidential level of 95% [23,57]. With this method, $(K^D_{max})_1 = 10.5^{+4.1}_{-5.7}$ eV (and at the fixed value $(K^D_{min})_1 = 0$) is obtained, which correspond to a value of σ_{cry} between 48 and 55 μrad[3].

[3] A more rigorous calculation should consider the posterior probabilities $P(\sigma_{\text{cry}}|K^D)$ and calculate the final posterior distribution

$$P(\sigma_{\text{cry}}) = \sum_{K^D} P(\sigma_{\text{cry}}|K^D) \times P(K^D)$$

following Eq. (2.16).

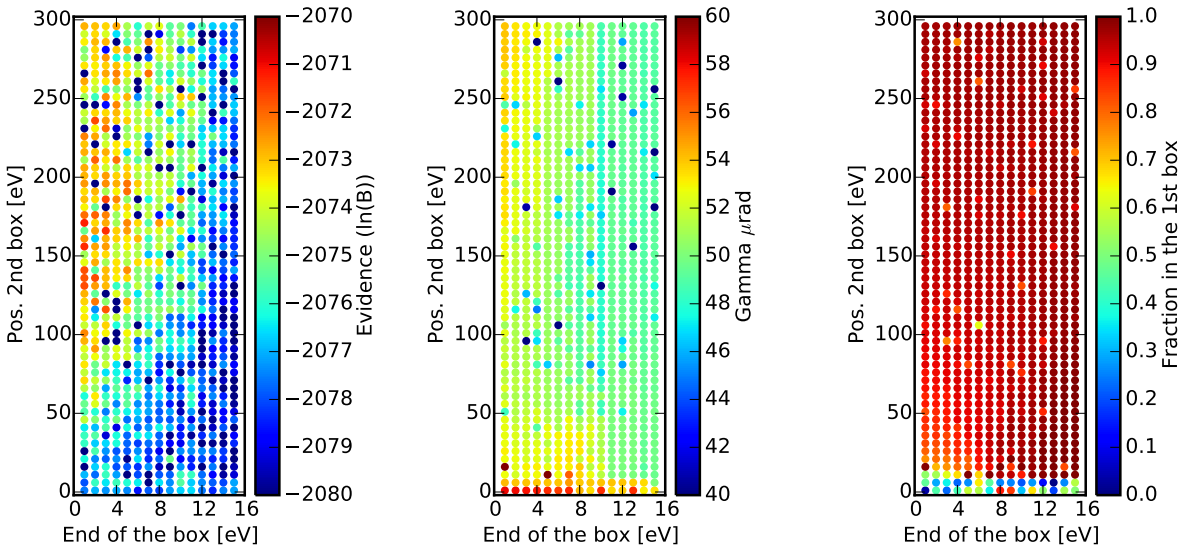

Figure 3.9 – Logarithm of the evidence (left), value of the Gaussian width σ_{cry} (centre) and relative filling of the fist kinetic distribution box (right) for different values $(K^D_{max})_1$ the position of the second kinetic distribution box position $(K^D)_2$.

When two kinetic distribution boxes are considered, the analysis is more difficult because of the larger scattering of the evidence values[4]. From the results of the second step, which agrees with the results of the first step, one can conclude that the value $\sigma_{\text{cry}} = 50 - 54$ μrad is due to the characteristics of the crystal for 4.5 keV X rays, which however is 0.5 keV higher than the $5 \rightarrow 4$ μO and πN transition photon energy . The values of $(K^D_{max})_1 = 10.5$ eV or $(K^D_{max})_1 = 0 - 2$ eV and $(K^D)_2 \approx 170$ eV are due to the atomic cascade following the capture of the pion. To note that, as expected, the main contribution of the radiationless de-excitation broadening is due to the low energy box (more than 90% occupation), which contribution can hardly be disentangled from the spectrometer response function.

3.4.4 Doppler boxes and Gaussian width from πN data

Differently to the case of πNe, πN and μO X-ray emission is affected by the Coulomb explosion of the target molecules during the formation of the pionic atoms and the first steps of their de-excitation. Details of the atomic cascade are not visible and only one large kinetic energy distribution box can be used. For the deduction of K^D_{max}, two different sets of data, *focalscan* πN spectra and *dispersion* spectra, are considered, which correspond to two slightly different set-ups with different crystal–detector distances (see Sec. 3.2.3 for details).

The results are presented in Figs. 3.10 and 3.11. For the both sets of data, the upper limit of the kinetic energy distribution box is around $K^D_{max} = 146$ eV. This value is in agreement with previous observations [77] and corresponds to two molecular fragment with a total charge $q_1 q_2 \approx 11$ in unit of elementary charge.

[4]Here only 200 *livepoints* are used to make faster the evidence calculation that have to be repeated over a large set of $\{(K^D_{max})_1, (K^D)_2\}$ values.

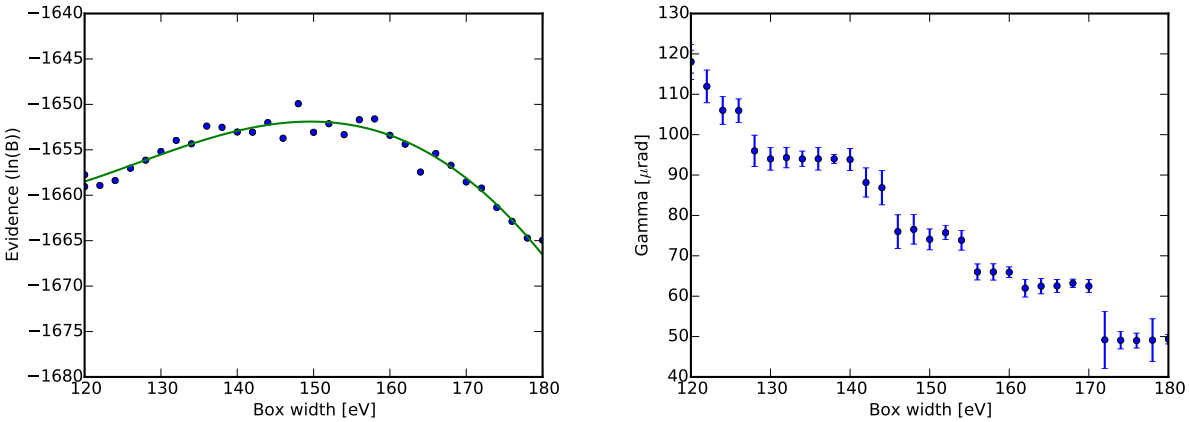

Figure 3.10 – Logarithm of the evidence (left) and value of the Gaussian width σ_{cry} (right) for different end values $(K^D_{max})_1$ of the kinetic distribution box for the πN *focalscan* spectra.

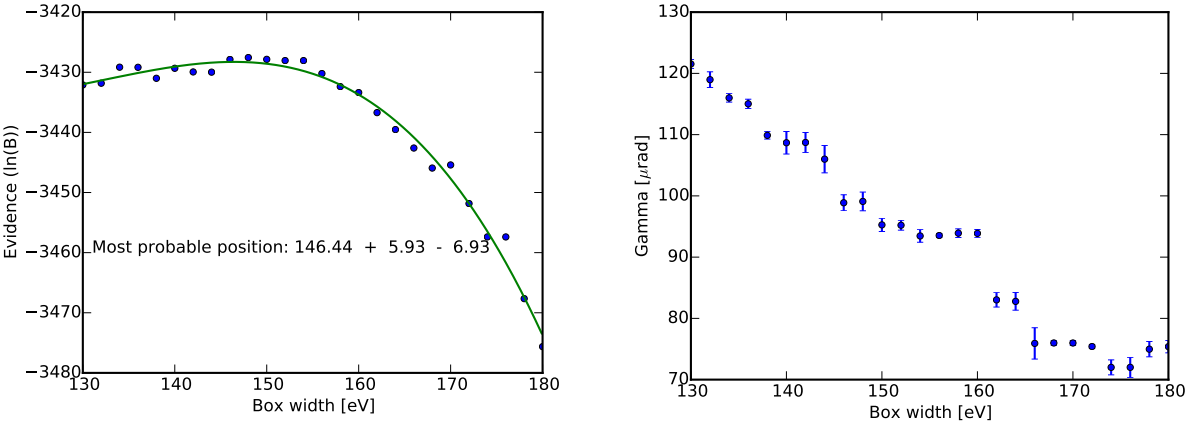

Figure 3.11 – Logarithm of the evidence (left) and value of the Gaussian width σ_{cry} (right) for different end values $(K^D_{max})_1$ of the kinetic distribution box for the πN *dispersion* spectra.

The values of the Gaussian broadening are $\sigma_{\rm cry} = 70 - 80$ eV for the *focalscan* spectra and $95 - 100$ eV for the *dispersion* spectra, significantly different between each other and from the πNe values. These differences can have different reasons:

- the slightly different set-ups can have slightly different spectral line curvature on the CCD and then influence the final line width after curvature correction and projection procedure (see Sec. 3.2.2);
- the different nature of the data sets. *Focalscan* data set is obtained for different crystal–detector distances and it may be more sensitive to $\sigma_{\rm cry}$ (and to the Doppler box boundaries);
- a partial compensation of the Coulomb explosion effect from the Gaussian component (i.e. $\sigma_{\rm cry}$);
- in the case of the comparison with πNe values, the different energy of the diffracted photons (4.0 and 4.5 keV) may imply different values of $\sigma_{\rm cry}$.

These differences are taken into account to evaluate a possible influence of the line position determination of the the μO – πN lines relative positions, and then, to the pion mass. For the final evaluation, the common value of *dispersion* and *mix* spectra is used. The associated systematic uncertainty is calculated assuming the value obtained from the *focalscan* πN spectra analysis instead that *dispersion* spectra. The difference amounts to $^{+0.023}_{-0.027}$ pixels corresponding to $^{+0.29}_{-0.34}$ part per million (ppm) of the pion mass value.

The uncertainty related to the curvature and effect of the curvature correction of the diffracted line on the CCD is considered separately and contributes to ± 0.23 ppm.

3.4.5 Lines modelling and tests

For the accurate determination of relative position between the $5g - 4f$ lines of μO and πN, also the other $5f - 4d$ and $5d - 4p$ transitions are considered. For the case of μO, due to the spin-1/2 of the muon, the fine structure has to be taken into account. The relative position of the secondary lines with respect to the main transition $5g - 4f$ is fixed by the theory prediction except for the $5d - 4p$ line where the strong interaction induces an important shift via the $4p$ level. Similarly, the position of the fine-structure components of the μO spectrum are fixed. Their intensities are also fixed by the assumption of a statistical population of the sub-levels.

A different Gaussian width is considered between the main line and the other transition because of the different history of the atomic cascade. The two Gaussian widths are very similar, however, with a ratio of $r_G = 0.80 \pm 0.05$. The systematic uncertainty related to the line modelling is estimated from the comparison of the results of thee cases: (i) when r_G is fixed to unity, (ii) when r_G is fixed to the value extracted from the *focalscan* spectra analysis and (iii) when r_G is a free parameter. Its value is $^{+0.014}_{-0.022}$ pixels corresponding to $^{+0.19}_{-0.29}$ ppm of the pion mass value.

3.4.6 Possible contribution from remaining electrons

The possible presence of remaining electron(s) in the exotic atom may induce an important systematic energy shift of the X-ray energies and, consequently, of the pion mass. One (or two) remaining electron(s) in the K shell in pionic nitrogen can generate satellite lines having energies 0.45 eV (0.81 eV) lower than the main transition $5g-4f$ (Calculation from MCDF code developed by P. Indelicato [101, 102]). Such weak satellite lines cannot be resolved from the main transition (see Fig. 3.4).

Table 3.1 – Bayes factor (in logarithmic scale) and the average P_0 of the model M_0 from the analysis of the different spectra. The possible range of P_0 is presented tanking into account the uncertainty of $\ln B_{01}$.

Spectrum	$\ln B_{01}$	P_0	P_0^{min}	P_0^{max}
high-stat. πN	6.6 ± 1.8	99.98%	99.86%	100%
low-stat. μO	-0.3 ± 0.4	42.52%	32.70%	52.98%

As discussed in Sec. 3.2.1, for light pionic atoms produced in low-pressure gaseous target, the possibility that residual electrons are present is very small when X rays are emitted. However, it cannot be excluded beforehand that small fractions of pions or muons may arrive at the $5g$ level by $\Delta n \gg 1$ transitions from low-angular momentum states immediately after capture.

To estimate the probability for the occurrence of satellite lines, the evaluation of the Bayes factor (see Sec. 2.3.3 is employed for two different hypotheses, presence or no presence of satellite lines. The first hypothesis is associated to the model M_0 of the spectra without additional satellite lines. In the model M_1 associated to the second hypothesis, the presence of additional satellite lines is considered with additional spectral contributions with fixed positions with respect to the main transition and keeping the (relative) intensities as a free parameter (two lines in the case of muonic oxygen, one per each fine structure main component).

For the calculation of B_{01}, two data sets were analysed: the high-statistic *dispersion* spectra of πN, and the *mix* spectrum of μO (shown in Fig. 3.4). The results obtained by `Nested_fit` for these sets are summarised in Fig. 3.12 and Table 3.1. Due to the too low statistics, the results from muonic oxygen cannot be used as valuable test against one of the two models due to the too large uncertainty of $\ln B_{01}$ with respect to its value. For the high-statistics pionic nitrogen spectra, the Bayes factor is significantly different from unity and the probabilities of the two models can be reliably calculated. The value $\ln B_{01} = 6.6$ indicates a decisive support for the M_0 hypothesis for any Bayes factor scale considered ("decisive" for Jeffreys scale [42], "very strong" for the Kass scale [56] or "strong" for the Gordon-Trotta scale, equivalent to a p-value of about 10^{-5} for M_1 [57]). Model M_0 and M_1 relative probabilities are 99.98% and 0.02%, respectively. Though being small, the effect of such a non-zero probability for M_1 on the pion mass can be evaluated.

When the model M_1 is considered, a satellite amplitude of about 1% of the main line (see Fig. 3.12) is found for both sets. As expected and clearly visible in Fig. 3.12, πN satellite amplitude is strongly correlated to the main line position, from which the pion mass value directly depends. The most probable value of the satellite amplitude corresponds to a shift of the main line of $(\delta x)_1 = 0.08$ pixels with respect to the case where satellite lines are not taken into account. This is equivalent to about 1 ppm of the pion mass. The shift value that has to be considered for the possible systematic effect is the weighted value considering the probability of the two models using the values of Table 3.1 and where $(\delta x)_0 = 0$ in analogy to Eq. (2.16). One has

$$\delta x = 0 \times P_0 + (\delta x)_1 \times P_1 = 1.8 \times 10^{-5} \text{ pixels}, \tag{3.11}$$

which corresponds to a systematic uncertainty of $^{+0}_{-0.0002}$ ppm. When the uncertainty of Bayes factor is taken into account (Table 3.1), the probability of M_0 drops to $P_0^{min} = 99.86\%$ and the systematic uncertainty increases to $^{+0}_{-0.0014}$ ppm, which is still completely negligible with respect to the statistical error and other systematic effects.

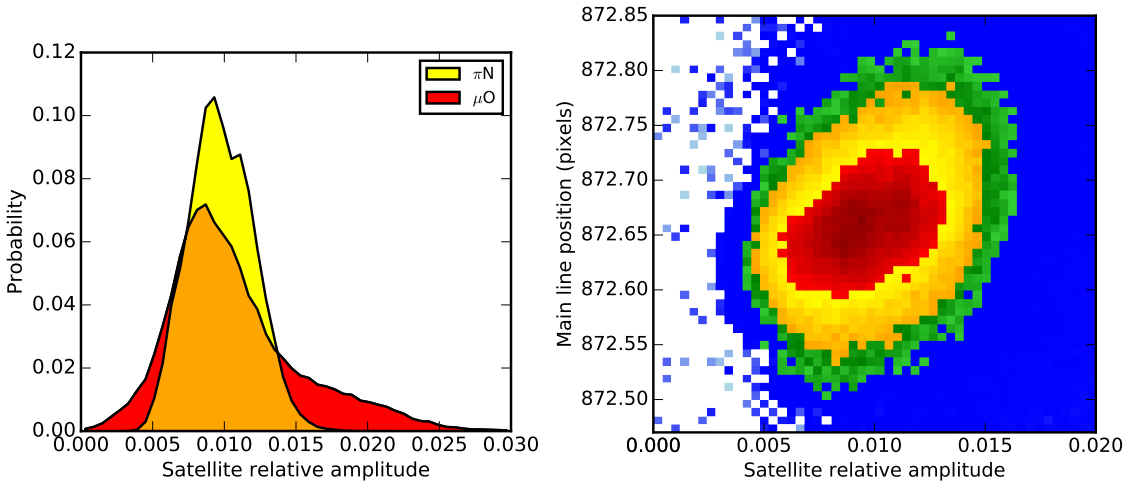

Figure 3.12 – Left: Probability distribution of the amplitudes relative to the main line intensity of the possible satellite line due to the presence of one remaining electron in the K shell. Right: Joint probability distribution of the relative satellite amplitude and the position of the main line $5g \rightarrow 4f$ in pionic nitrogen. The accumulation on the diagonal shows the correlation between satellite intensity and main line position. Assuming no satellite line, the position of the main line for this set of data is 872.58 ± 0.04 pixels.

3.5 The new value of the charged pion mass

3.5.1 The final value of the negatively charged pion mass

The final distance between the πN and μO lines has an accuracy of 0.064 pixel. This uncertainty, which correspond to 0.82 ppm, represents the statistical contribution for the pion mass measurement.

The mass value is obtained from the spectral line distance in two steps: (i) the evaluation of the $5g \rightarrow 4f$ πN transition energy using the μO transition as reference line and (ii) the extraction of the pion mass value from the pionic nitrogen transition energy.

In the first step, the angular difference of the two spectral lines is evaluated from their spatial separation:

$$\Delta\Theta_{AB} = \arctan\left(\frac{x_B - x_c}{D}\right) - \arctan\left(\frac{x_A - x_c}{D}\right), \tag{3.12}$$

x represent the position on the CCD as indicated in Fig. 3.3, D is CCD–crystal distance, A represent the μO transition used as reference and B the πN transition. From the Bragg law $n\ hc/E = 2d\sin\Theta$, one obtains E_B as a function of E_A and their angular separation Θ_{AB}:

$$E_B = E_A \frac{1}{\cos\Delta\Theta_{AB} - \cot\Theta_A \sin\Delta\Theta_{AB}}. \tag{3.13}$$

To note, the only dependency on the crystal lattice d (and diffraction order n) is now in $\Theta_A = \arcsin(n\ hc)/(2dE_A)$.

From the equations above, the spatial separation of the spectral line and the theoretical prediction of the μO transition, the energy of the $\pi\mathrm{N}(5g-4f)$ transition is found to be $(4055.3970 \pm 0.0033_{stat} \pm 0.0038_{sys})$ eV. From this energy measurement, the pion mass is extracted considering the theoretical dependency of E_B in m_{π^-} and the expected energy E_B^{PDG} obtained using the reference mass $m_{\pi^-}^{PDG}$ of the Particle Data Group [70].

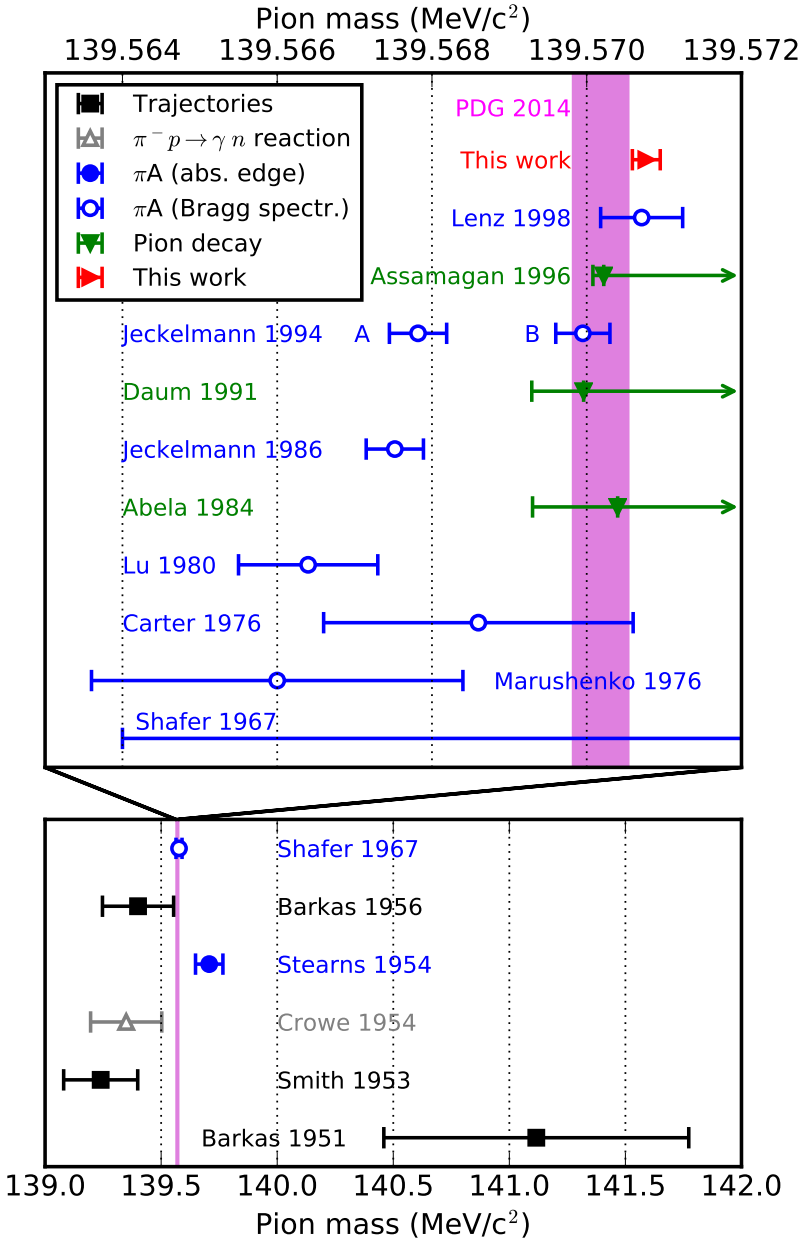

Figure 3.13 – Results of for the mass of the charged pion from various experimental methods since its discovery (Figure from Ref. C1). The world average value "PDG 2014" [70], indicated by the magenta region, is calculated from "Lenz 1998" [14] and solution B of "Jeckelmann 1994" [103]. Other results are taken from Refs. 72, 103–114.

The relation between E_B and m_{π^-} requires relativistic calculations via Klein-Gordon equation with, addition of QED and recoil corrections [A43]. Due to the expected small difference between m_{π^-} and $m_{\pi^-}^{PDG}$, the relation is considered linear with

$$E_B = \mu_{\pi^-} C, \tag{3.14}$$

where the constant C derived by the theory.

For the comparison between the expected transition energy E_B^{PDG}, obtained considering $m_{\pi^-}^{PDG}$, and the measured energy E_B, the new value of the pion mass m_{π^-} is extracted

$$m_{\pi^-} = \frac{\mu_{\pi^-}^{PDG} \dfrac{E_B}{E_B^{PDG}}}{1 - \dfrac{\mu^{PDG}}{M}\dfrac{E_B}{E_B^{PDG}}}, \qquad \text{with} \qquad \mu_{\pi^-}^{PDG} = \frac{m_{\pi^-}^{PDG}}{1 + \dfrac{m_{\pi^-}^{PDG}}{M}}, \tag{3.15}$$

where M is the Nitrogen nuclear mass. To explicitly separate the uncertainty contribution coming form QED calculations (via the constant C), M and $m_{\pi^-}^{PDG}$, the equation above can be rewritten as

$$m_{\pi^-} = \frac{E_B}{C} \frac{1}{1 + \dfrac{m_{\pi^-}^{PDG}}{M} - \dfrac{E_B}{CM}}. \tag{3.16}$$

Finally, the new value of the pion mass is evaluated to be

$$m_{\pi^-} = 139.57077 \pm 0.00018 \text{ MeV/c}^2. \tag{3.17}$$

3.5.2 A short discussion on the uncertainties

The larger systematic error is due to the uncertainty of the distance between the detector and the crystal, which contributes with 0.67 ppm, followed by the uncertainty due to the QED calculations (Dirac equations for the reference line and Klein-Gordon to extract the pion mass) with 0.35 ppm. Additional relevant sources are the uncertainties, partially discussed in the previous paragraphs, are: the response function and Doppler broadening ($^{+0.29}_{-0.34}$ ppm), the 6 CCDs reciprocal alignment (0.32 ppm) and the line modelling ($^{+0.19}_{-0.29}$ ppm). To note, the muon mass accuracy determines a systematic uncertainty of only 0.03 ppm via the energy of the reference transition.

The asymmetric uncertainties $+\Delta_+^i, -\Delta_-^i$ of the different contributions are summed together observing the recommendations of the Joint Committee for Guides in Metrology [115] following the recipe described in Refs. [116,117]. The final systematic accuracy Δ_{sys} is calculated by the quadratic sum from the different contributions $\Delta_{sys} = \sum_i \bar{\Delta}_i$, where $\bar{\Delta}_i = (\Delta_+^i + \Delta_-^i)/2$. The shift δ due to the uncertainty asymmetry is calculated by the different terms $\delta = \sum_i \delta_i$, with $\delta_i = (\Delta_+^i - \Delta_-^i)/2$.

A complete and exhaustive list of all systematic contributions and uncertainties can be found in Ref. A7 (App. F) and C1.

3.5.3 Final considerations

As it can be observed in Fig. 3.13,the new value of the pion mass has a final uncertainty of 1.3 ppm, half of the previous best measurement, it is 4.2 ppm larger than the present world average [70]. It is in good agreement with the mass obtained by [14], but 5.4 ppm above the result of the pionic magnesium

experiment (solution B [71]) where a solid target was employed instead of a gaseous target. At present, the present measurement is included in the new reference value of the mass the negatively charged pion provided by the Particle Data Group [47, 118].

When the value of the pion mass is combined with the measurement of the muon momentum after pion decay at rest [73], a value for the muon neutrino mass is obtained of $m_{\nu_\mu} = 183\,^{+62}_{-83}$ keV/c^2 (c.f. 90%). This value is obtained using the statistical approach of Ref. 119 (orthodox and Bayesian unified method recommended by the Particle Data Group). The result is far above the cosmological limit (11 eV/c^2 for the sum of all neutrino flavours) [70]. However, extending the error limits to 3σ either for the pion mass or the muon momentum yields values for m_{ν_μ} consistent with zero.

Chapter 4

Slow collisions between ions and atoms

4.1 Introduction

4.1.1 General considerations

The interaction between low-velocity ions and atoms or molecules is one of the most common atomic collisional processes in nature. This interaction is in fact responsible for X-ray emission during the collision of solar wind with comet comas [120–125], with planets, satellites [126, 127], but also with galactic and intergalactic medium [128–130]. In artificial plasmas, radiation from ion–atom interaction is commonly used as diagnostic as for tokamak plasmas [4, 131–134].

At this low velocity regime, 0.4–1 atomic unit[1] (a.u.), the dominant process is the electron capture from the neutral atom to the selective excited states of the projectile, the collisional system behaving like a quasi-molecule. This leads to an energy gain of the projectile ion and the populated excited states decay by emission of photons and/or electrons, both carrying information on the collision dynamics.

The basic processes involved in ion–atom collisions have been extensively investigated in the past using low-charged ion beam interacting with gaseous targets [135–141] and, more recently, with the advent of new ion sources with heavier projectile ions of higher charge states [142–157]. At the same time, extended theoretical investigations have been developed as the simple Classical Over-the-Barrier (COB) model [16,17] (presented in detail in App. B), the reaction window within the Landau-Zener model [158], couple state calculations using basis of either atomic or molecular orbitals [18–21], time-dependent Schroödinger equation resolution [159–161] and the classical trajectory Monte Carlo method [162–164].

X-ray measurements performed in well defined conditions in laboratories provide important insights to understand the collisional process involved and to interpret X-ray spectra from natural or artificial plasmas [124, 125, 146, 157, 165]. More precisely, values of differential electron capture cross sections for different atomic levels can be evaluated. Several low-resolution X-ray detection experiments have been performed in the past [143, 144, 147–149, 157]. In these experiments, no information of selective electron capture in $n\ell$ states is accessible because of the low-resolution X-ray detectors employed (solid state detectors), insufficient to resolve $n \to 1$, and to distinguish the effect of single and multiple

[1] 1 a.u. corresponds to the classical velocity of an electron in the fundamental level of an hydrogen atom. $v = 1\text{a.u.} = \alpha c$. In a generic hydrogen-like atom with nuclear charge Z, the characteristic velocity for an electron in the n shell is $v = Z/n$.

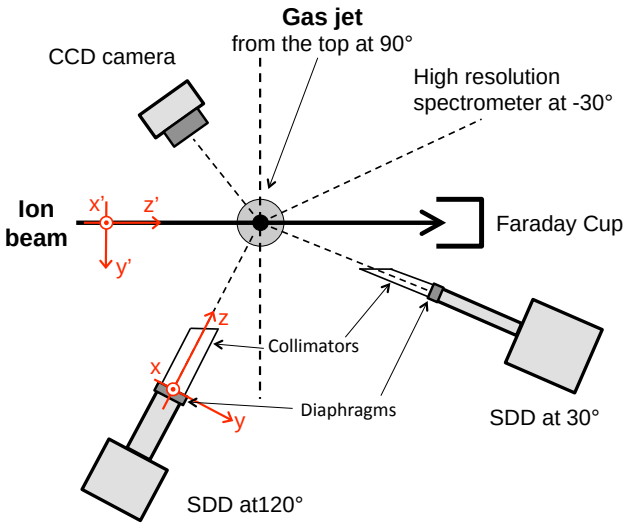

Figure 4.1 – A schematic view of the experimental set-up showing the localisation of the two solid-state detectors, the high resolution X-ray spectrometer, the CCD camera and the gaseous jet target.

electron capture processes, as discussed recently in [154,166]. Some measurements with high-resolution detectors are available but limited to few specific cases [146, 151, 156, 164, 167, 168].

In this chapter, the advantage of using high-resolution X-ray spectroscopy will be discussed. In particular, the study of the collision of low-velocity (0.53 a.u.) Ar^{17+} ions with a gaseous Ar and N_2 jet is presented. By resolving the whole Lyman series $1snp \rightarrow 1s^2$ up to $n = 10$, the preferential level n_{pref} and n-distribution $\{\mathcal{P}_n\}$ of the selective-state single-electron capture is determined. Thanks to the accurate knowledge of the detection spectrometers, the single-electron capture cross section is also extracted. Moreover, the contribution from the multi-electron capture is evaluated. Finally the importance of the emission from metastable states is pointed out for the comparison between laboratory and astronomical observations.

4.1.2 Work context, personal contribution and associated publications

The experiment described here has been conceived, executed and analysed by the ASUR team at the INSP. In the same experimental campaign, in addition to ion–atom systems, studies of the collision between highly charged ions with thin carbon membranes and noble gas clusters [A11, C2, C10, C13] have been performed but they are not presented here. In addition to participate to the preparation and data acquisition, the author mainly took care of the analysis of the high-resolution X-ray data. This chapter is focussed on this part of the data analysis, and on the related results.

The publication associated to this chapter is presented in App. G [A26]. Other related publications are Refs. A11, C10, C22.

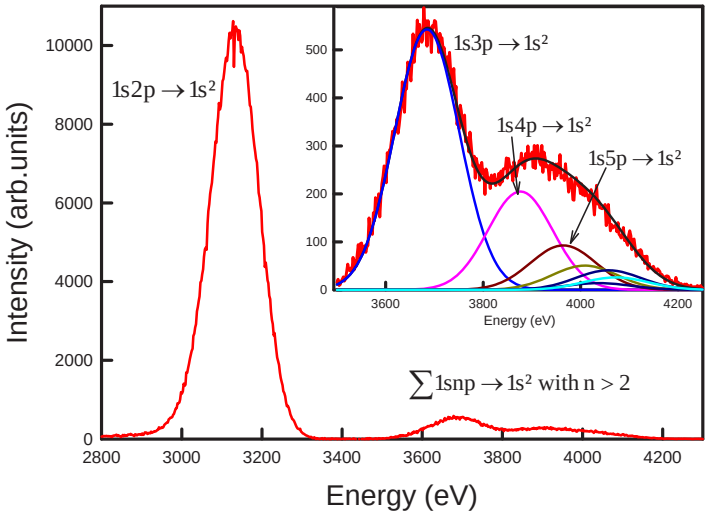

Figure 4.2 – Typical spectrum recorded by one of the solid-state detectors exhibiting transitions from Ar^{16+} ions produced after collision with the argon gaseous target. Experimental data are in red and the solid black line represents the fit result. The different $n > 3 \rightarrow 1$ transition contributions are shown in the zoom.

4.2 Experimental set-up and methods

4.2.1 Set-up and data acquisition

The experiment has been performed at the low energy ion installation ARIBE[2] [169] at GANIL[3] where 255 keV $^{36}Ar^{17+}$ ions (with a current of 2 nA) are directed onto a gaseous jet of neutral Ar and N_2.

A schematic view of the experimental set-up is presented in figure 4.1. The beam profile is regularly monitored with a high-sensitivity CCD camera that recoreds the fluorescence light from the ion impact on a stainless steel or alumina target; its current is measured regularly with a Faraday cup.

Lyman lines (in the 3.1–4.1 keV energy range) from the ion projectile are recorded by two Silicon Drift Detectors (SDD) [170] and by a high-resolution high-transmission Bragg crystal spectrometer [A33]. The typical accessible energy range of the Bragg spectrometer for a given setting is about 160 eV with a resolution of a few eV for a few keV photons, compared to 190 eV for SDD detectors. All the He-like $1snp \rightarrow 1s^2$ transitions generated during the collision are then resolved as well as the fine structure of $n = 2 \rightarrow 1$ transitions from He- and Li-like ions. More details can be found in the App. G (Ref. A26).

4.2.2 Low-resolution spectra analysis and discussion

A typical X-ray spectrum from the SDD is presented in Fig. 4.2. Two major peaks are clearly visible in the energy region from 3 to 3.8 keV. They are assigned to the $1s2p \rightarrow 1s^2$ (high-intensity line) and $1s3p \rightarrow 1s^2$ transitions. The broader peak at higher energy is due to $1snp \rightarrow 1s^2$ transitions with $n > 3$.

[2] Accélérateurs pour les recherches avec les ions de basses énergies
[3] Grand Accélérateur National d'Ions Lourds, Caen, France.

For the extraction of the absolute value of the X-ray emission cross section, the ion beam and the gas-jet profiles are considered to evaluate precisely the target-projectile overlap, together with a complete efficiency characterisation of the SDD detectors [170]. For gas-jet pressures where single collision condition is fulfilled, the absolute value of the X-ray emission cross section, σ^{X-ray}, is evaluated with great accuracy: $11.4 \cdot 10^{-15}\text{cm}^2$ $\pm 15\%$. Compared to the only previous experiment performed on this type of system, where the value $11.6 \cdot 10^{-15}\text{cm}^2 \pm 35\%$ was found [147]. The uncertainty is reduced by a factor of more than two and without referring to any external calibration. No noticeable differences, within the error bars, are observed when using argon or molecular nitrogen gaseous targets. Additional information can be found in Ref. A26 and in App. G.

As underlined by Tawara and co-workers [147], due to the presence of metastable states, the value of the X-ray emission cross section can be influenced by the measurement set-up configuration. This issue is discussed in more detail in the next sections.

4.2.3 High-resolution spectra results

With the high-resolution spectrometer, the whole set of $n \rightarrow 1$ transitions are well resolved from $n = 2$ to 10. At lower energy, for $n = 2$, the He-like $1s2p\ ^3P_{1,2} \rightarrow 1s^2\ ^1S_0$ and $1s2p\ ^1P_1 \rightarrow 1s^2\ ^1S_0$ transitions are observed and well separated. M1 $1s2s\ ^3S_1 \rightarrow 1s^2\ ^1S_0$ and Li-like $1s2s2p\ ^4P_{1/2,3/2} \rightarrow 1s^2 2s\ ^2S_{1/2}$ transitions, from the capture on metastable states formed before the interaction chamber, are also observable.

Quantitative values of the transition intensities are obtained from fits of the different spectral components using `Minuit_fit` (described in Sec. 2.2) and modelling the data with a series of Voigt profiles (plus a polynomial background) that reproduce well the response function of the crystal spectrometer over the whole considered energy range.

As for the low-resolution spectra recorded by the SDD detectors, no significant difference is observed between Ar and N_2 targets. Therefore only the case of argon target is considered for the discussions of the detailed analysis that follows.

To extract valuable information from the high-resolution spectra, a modelling of the atomic cascade processes after the ion–collision is mandatory; see next section.

4.3 Atomic cascade characteristics and modelling

4.3.1 Characteristics of radiative decay cascade of He-like atoms

After an electron capture of Ar^{17+}, one has an excited He-like atom that can de-excite only via radiative transitions. The combination of the spin of two electrons can be combined in triplet states, with the total spin $S = 1$, and in singlet states, with the total spin $S = 0$. In the decay cascade, the most probable transitions are of E1 type (electric dipole transition) that implies a change of the quantum angular momentum number $\Delta\ell = 1$ or -1 and their probability is proportional to ΔE^3. Transitions with maximal difference of the principal quantum number n are favoured. These two rules imply that (i) all P-states ($\ell = 1$, any n) decay preferentially to the fundamental level and (ii) $(n, \ell = n-1)$ states are efficiently populated and decay subsequently via yrast transitions $(n, \ell = n-1) \rightarrow (n-1, \ell = n-2)$. Transitions between triplet and singlet states are generally forbidden because they imply an electronic spin-flip, which is much less probable with respect to transitions with the same type of state of spin S. Considering that the fundamental level $1s^2\ ^1S_0$ is a singlet, this implies that $n \geq 3 \rightarrow 1$ X-ray transitions are exclusively due to singlet states $S = 0$ as indicated in Fig. 4.4. $n \geq 3$ triplet states

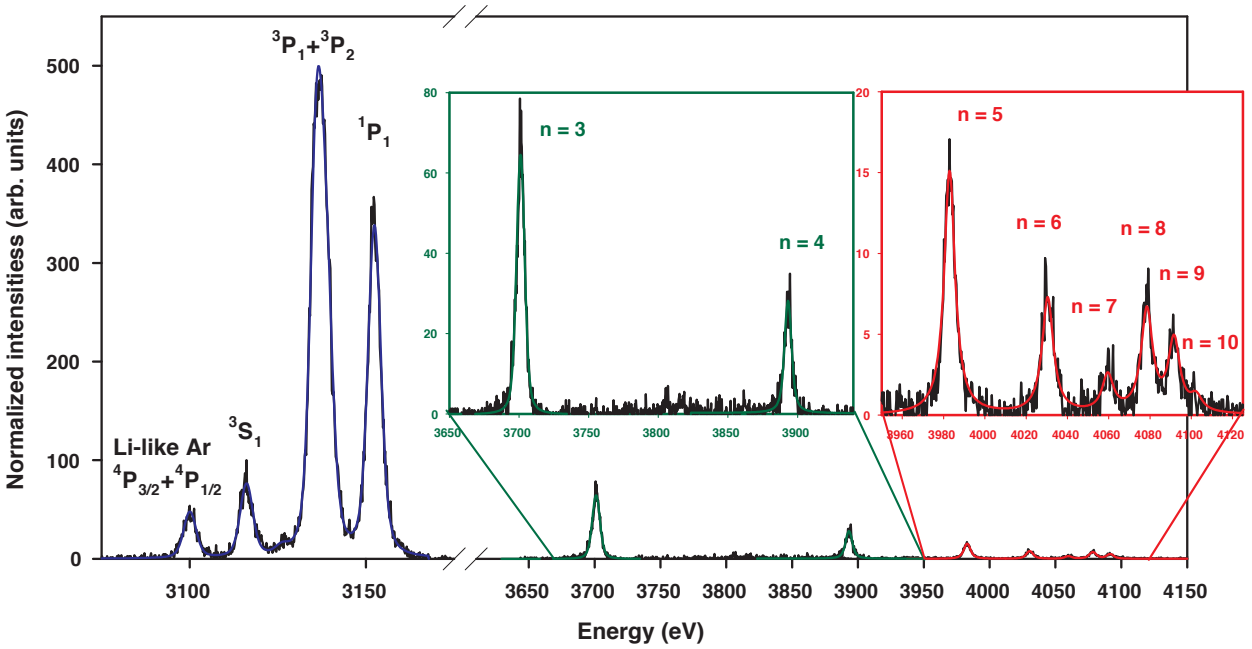

Figure 4.3 – High resolution spectra (background subtracted) of Ar^{16+} X-ray transitions observed with an argon target (p=1.5 mbar). The He-like Ar $1snp \rightarrow 1s^2$ with n up to 10 are visible. For $n = 2$, transitions from $1s2p\ ^3P_1$,$^3P_2$,$^1P_1$ and $1s2s\ ^3S_1$ to the ground level are partially resolved. In addition, M1 $1s2s\ ^3S_1 \rightarrow 1s^2\ ^1S_0$ and Li-like Ar $1s2s2p\ ^4P_{1/2,3/2} \rightarrow 1s^22s\ ^2S_{1/2}$ transitions are observed and well resolved from the $1s2p$ He-like transitions. The continuous colored lines represent the fit using a series of Voigt profiles. Intensities are normalized to the counts recorded by the SDD at 30° (see text).

($S = 3$) decay preferentially to $1s2s\ ^3S_1$ and $1s2p\ ^3P_{0,1,2}$ levels, which subsequently decay to the fundamental level via spin-flip electric dipole and forbidden transitions (see Fig. 4.5).

4.3.2 Calculation of the expected transition intensity

To compare experimental records with theoretical predictions the atomic cascade have to be modelled to link the predictions on the capture cross sections $\sigma_{n,\ell}$ and recorded X-ray transition intensities. Only the atomic cascade of excited levels $1sn\ell$ of He-like systems is considered here.

Three major items have to be computed:

(A) the branching decay ratio from different states (n, ℓ) and $(n', \ell \pm 1)$ via radiative decay,

(B) the probability to populate a state $(n', \ell \pm 1)$ from an initial state (n, ℓ) via a series of radiative decays of intermediate levels.

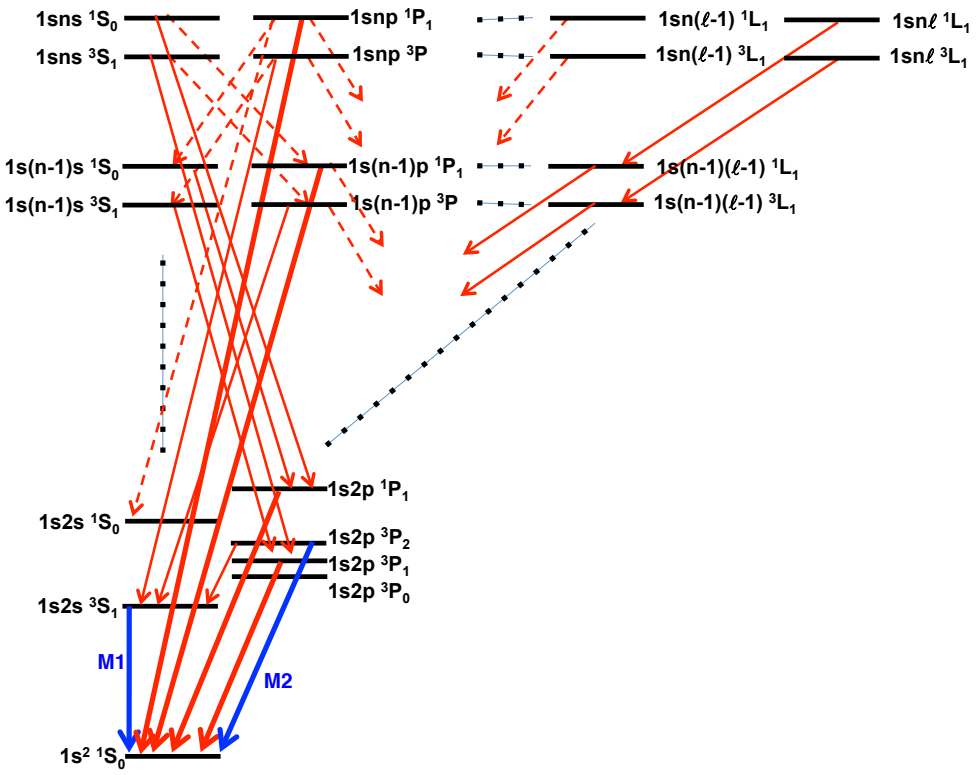

Figure 4.4 – One-photon radiative transitions in the atomic cascade of He-like excited atom. Continuous or dashed lines correspond to dominant or secondary allowed transitions (E1 transitions in red). The transition corresponding to the radiation recorded by the X-ray spectrometer are indicated by thick arrows.

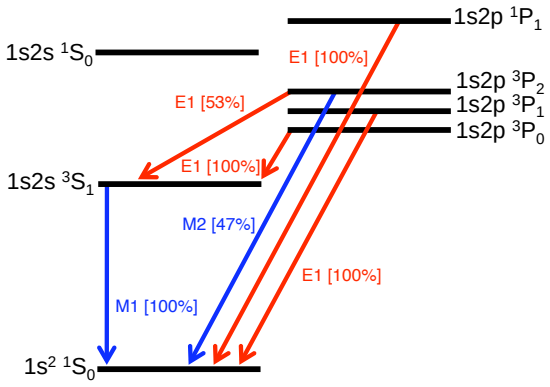

Figure 4.5 – Level scheme of $n = 2$ helium-like argon and major one-photon decay branches. The corresponding branching ratio are in bracket [171, 172].

(C) for a given set of capture cross sections $\sigma_{n,\ell}$, the intensity of a particular transition $(n', \ell') \rightarrow (n = 1, \ell' \pm 1)$.

The second and third steps are obtained via a homemade simple Fortran90 code (`Cascade_He` presented in App. D); the first one, is accomplished by a simple code described below and using external data.

(A) Branching ratio calculation

Except for the $n = 2 \rightarrow 1$ transitions, branching ratios are calculated considering only the dominant transitions (E1) with probabilities for an hydrogen-like atom in the non-relativistic framework.

Within this approximation the probability $W^{n,\ell}_{n',\ell'}$ for a transition $(n, \ell) \rightarrow (n', \ell')$ is, as for pionic atoms (see Eq. (3.3)), given by [79]

$$W^{n,\ell}_{n',\ell'} \propto \Delta E^3_{n,n'} |R^{n,\ell}_{n',\ell'}|^2, \tag{4.1}$$

where $\Delta E_{n,n'}$ is the energy difference between levels

$$\Delta E_{n,n'} = mc^2 \frac{(Z\alpha)^2}{2} \left(\frac{1}{n'^2} - \frac{1}{n^2} \right) \tag{4.2}$$

and $R^{n,\ell}_{n',\ell'}$ is the integral

$$R^{n,\ell}_{n',\ell'} = \int_0^\infty R_{n,\ell}(r) R_{n',\ell'}(r) r^3 dr \tag{4.3}$$

with $R_{n,\ell}(r)$ the radial parts of non-relativistic wavefunctions of the hydrogen-like atom. The different transitions are calculated by a simple Mathematica [173] script. From them, the branching ratios are deduced:

$$B^{n,\ell}_{n',\ell'} = W^{n,\ell}_{n',\ell'} \Bigg/ \sum_{\substack{n''<n \\ \ell''=\ell\pm1}} W^{n,\ell}_{n'',\ell''}. \tag{4.4}$$

For $n \geq 3$ states, the same branching ratios are used for singlet and triplet states and no spin-flip transitions are considered. For $n = 2 \rightarrow 1$ transitions, the branching ratios are computed from the fully relativistic two-electron predictions probabilities of all relevant level decays (including spin-flip, M1, M2 transitions) [171, 172] represented in Fig 4.5.

(B) Generalised branching ratio calculation

The probability to populate a state $(n', \ell' = \ell \pm 1)$ from an initial state (n, ℓ) via a series of radiative decays in intermediate levels is calculated via a *generalised branching ratio* $G^{n,\ell}_{n',\ell'}$ defined here and deduced by the different branching ratio values. This is actually not a real probability and it is defined as, considering a population of 100% of the level (n, ℓ), the fraction of this population that reach the level (n', ℓ') after an undefined number of transitions through other levels $(\tilde{n}, \tilde{\ell})$ with $n > \tilde{n} > n'$ with

$$G^{n,\ell}_{n',\ell'} = \sum_{\tilde{\ell}_1} \sum_{\tilde{\ell}_2} \cdots \sum_{\tilde{\ell}_i} B^{n,\ell}_{\tilde{n}_1,\tilde{\ell}_1} B^{\tilde{n}_1,\tilde{\ell}_1}_{\tilde{n}_2,\tilde{\ell}_2} \cdots B^{\tilde{n}_i,\tilde{\ell}_i}_{n',\ell'}. \tag{4.5}$$

$G^{n,\ell}_{n',\ell'}$ are calculated as a "water flow" of probabilities starting from the high-excited levels through lower levels via different B values. Different possible paths to go from (n, ℓ) to (n', ℓ') are considered and added together.

(C) Line intensities calculation

From a given set of capture cross sections $\sigma_{n,\ell}$, the population of the initial excited levels is deduced by considering a statistical distribution between triplet and singlet atomic levels giving rise to a ratio 3:1 for $1s\,n\ell\,^3L : 1s\,n\ell\,^1L$ states. From this initial population, from the generalised branching ratios $G^{n,\ell}_{n',\ell'}$ and from the branching ratio of the level (n',ℓ'), the expected intensity of the transitions $(n',\ell') \rightarrow (n'',\ell'')$ is calculated.

4.4 Discussions on the high-resolution spectra and comparison with theory predictions

4.4.1 General considerations

To interpret the experimental data and compare them with the theory, firstly some basic considerations on the simple- and multi-electron capture processes have to be done. At low velocity, the single capture preferentially populates high-excited n levels while multi-electron capture populates multiple excited states with $n', n'', n''' \ldots < n$ [174] that decays mainly by Auger emission. Taking into account COB model predictions for the single-electron capture process, $n_{pref} = 7 - 9$ are populated in the collision system Ar^{17+} (0.5 a.u.) $\rightarrow$ Ar or N_2. From that, with the above considerations and the discussions in Sec. 4.3.1, one can assume that

- the $1s\,np\ ^1P_1 \rightarrow 1s^2\ ^1S_0$ radiative decays with $n = 7 - 10$ are due to the single-electron capture,
- the $1s\,2p\ ^{1,3}P_{0,1,2} \rightarrow 1s^2\ ^1S_0$ and $1s\,np\ ^1P_1 \rightarrow 1s^2\ ^1S_0$ radiative decays with $3 < n < 7$ are influenced by the multi-electron capture.

These assumptions, checked *a posteriori*, permit to separate the data analysis in two parts: one where only single-electron capture can be considered and one where multi-electron capture has to be included.

4.4.2 The contribution of the single capture

From the analysis of the X-ray emission intensities of $1s\,np\ ^1P_0 \rightarrow 1s^2\ ^1S_0$ with $n = 7 - 10$ one can extract

- the n-levels population distribution,
- the cross section of the single-electron capture.

Quantitative values of those both items is the starting point of the discussion on the multi-electron capture.

The n-levels population distribution

The population probability $\mathcal{P}_n$ in n-levels is easily extracted from the observed relative transition intensities (Fig. 4.3), assuming different ℓ-population distributions $\{\mathcal{P}_\ell\}$ and taking into account the atomic cascade. At an ion velocity of 0.53 a.u. the ℓ-sublevel distribution is most likely of statistical-type [161,175,176]. Nevertheless to probe the sensibility on $\mathcal{P}_n$, two ℓ-distribution has been considered: a flat distribution and a statistical $(2\ell+1)$ one. The results are presented in Fig. 4.6. As expected from the COB model, the single-electron capture is observed to occur in a reaction window that populates preferentially $n = 8-9$ states with a relative narrow distribution, in agreement with the Landau-Zener

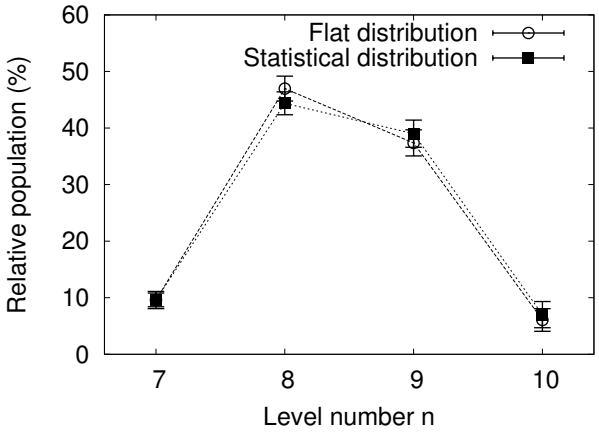

Figure 4.6 – $\{\mathcal{P}_n\}$ distribution of the single-electron capture population for Ar target, assuming different ℓ-distributions on the $n = 7 - 10$ levels. Note that here $\sum_{n=7}^{10} \mathcal{P}_n = 100\%$.

model [158] and with observation by Knoop et al. in [150] where the COLTRIM technique for Ar^{17+} on He at $v = 0.4$ a.u has been used. Different assumptions on $\mathcal{P}_\ell$ do not affect significantly the results, which stay compatible within the error bars.

The single-electron capture cross section

In addition to the assumptions on $\mathcal{P}_\ell$, a statistical population is considered between triplet ($S = 1$) and singlet states ($S = 0$), which correspond to a ratio 3:1, as already discussed in Sec. 4.3. Contrary to $\mathcal{P}_n$, the extracted value of σ^{single} strongly depends on the choice of the ℓ-distribution. Indeed the extracted cross section value ranges from $\sigma^{single} = 12.8 \cdot 10^{-15}$ cm^2, with a statistical ℓ-distribution, down to $4.6 \cdot 10^{-15}$ cm^2 when an improbable flat distribution is assumed.

The result is satisfactorily in good agreement with the experimental value $8 \cdot 10^{-15}$ cm^2 obtained by Ali et al. [142] from coincidence measurements of projectile-target charge exchange for Ar^{17+} on Ar at $v = 0.6$ a.u. and with the COB model that predicts $\sigma^{single} \approx 6.6 \cdot 10^{-15}$ cm^2 (see Eq. (B.2) in Sec. B).

4.4.3 The contribution of the multi-electrons capture

Multi-electron capture [136,142] processes in slow ion collision have been detected since long time from the measurement of final charge state and/or kinetic energy gain of projectile and target atoms. Their influence on X-ray spectra has been discussed and estimated in the past [147,154,166] but it has been precisely measured only recently in the work presented here and other recent studies [155,177,178].

In the presented work, to quantify the role of the multi-electron capture, two different approaches are presented. The first one is based on the results of the previous section and the use of the cascade model presented in Sec. 4.3. The second method is based on theoretical predictions of the partial cross sections $\sigma_n^{app.single}$ provided by Kirchner et al. [177] and implementing them in the same cascade code. These theoretical predictions include multi-electron capture processes and take into account Auger decays to provide values of the *apparent* single-electron capture cross sections. Recent calculations from Otranto et al. [178] are also considered.

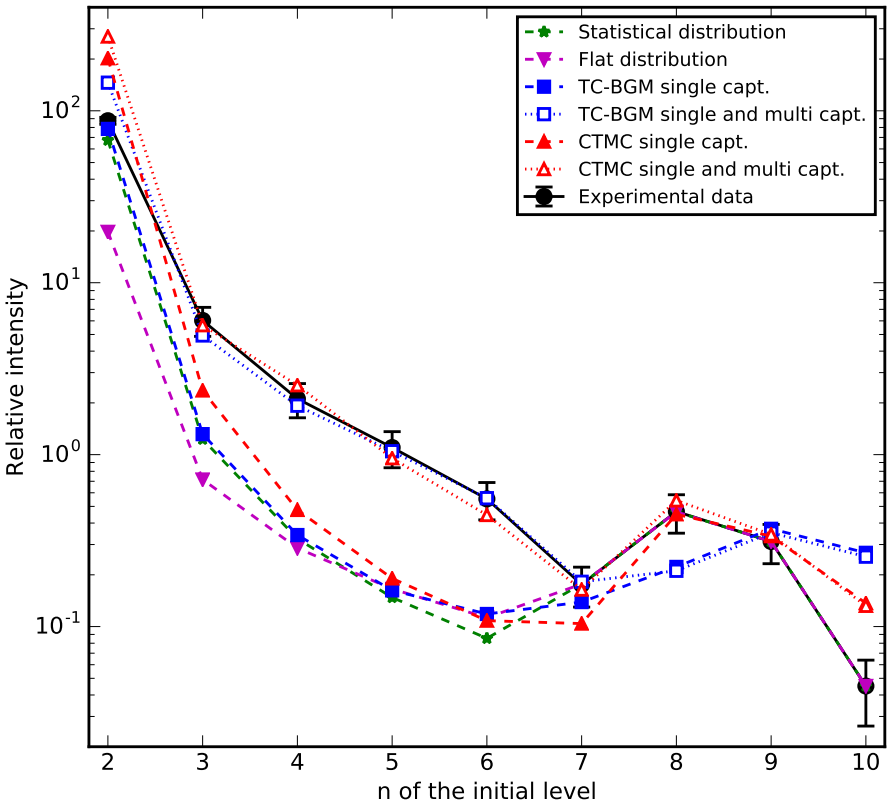

Figure 4.7 – Comparisons between experimental $1s\,np \rightarrow 1s^2$ intensities and theoretical predictions: two centre basis generator method (TC-BGM) [177] and classical trajectory Monte Carlo (CTMC) [178]. For $n \neq 2 \rightarrow 1$, only $1s\,np\ {}^1P_1 \rightarrow 1s^2\ {}^1S_0$ transitions are considered. For $n = 2$ both triplet and singlet transitions are taken into account. In addition, an empirical prediction of the contribution of the single-electron capture is presented (see text for more details).

Single-to-multiple capture comparison

The first method does not require theoretical predictions as input. Taking into account that the multi-electron capture affects only X-ray transitions involving atomic levels with $n < 7$, the probability population distribution $\mathcal{P}_n$ obtained in the previous section can be used to calculate the expected intensities of all X-ray transitions assuming that only single capture occurs. These intensities are then compared to the experimental data and the contribution of the multi-electron capture is evaluated. This estimation strongly depends on the assumption of the ℓ-sublevels population distribution. This comparison is presented graphically in Fig. 4.7. For both statistical and flat $\mathcal{P}_n$ assumptions, the intensities of $(n = 7 - 10) \rightarrow 1$ transitions are equal to the experimental ones by construction and normalisation. From $n = 6$, expected intensities are much lower than the measured ones indicating already a non-negligible influence of the multi-electron capture. More quantitatively, the total influence on the X-ray emission is estimated to be 29% when a $\mathcal{P}_\ell$ statistical distribution is considered and 88% for a flat distribution. This large difference is mainly due to the comparison of the intensity of

$1s\,2p \rightarrow 1s^2$ transitions, which represent, alone, the 88% of the total recorded $1s\,np \rightarrow 1s^2$ X-ray emission.

Experiment-to-theory comparison

A comparison with the theoretical predictions is obtained by considering the expected values of the partial cross sections $\sigma_{n,\ell}$ for single and multi-electron capture and the use of cascade code. In this case, Auger decays have to be considered and modelled. This has been done for the first time in slow ion collisions by Ali and collaborators [142]. The same model has been more recently reapplied by Kirchner et al. [177] and Otranto et al. [178].

The basics concepts of the Auger decay modelling are shortly presented. Starting from an initial multiple-excited level population distribution, the Auger decay scheme of Ali et al. consists in a series of simple rules reflecting the complex Auger transition probability values. The most important rules are that radiative decay is dominant over Auger emission when (i) the state is singly-excited and when (ii) the electrons in the excited states n and n' have a too high value $|n - n'|$.[4] Additional rules are considered for the decay order of the possible Auger transitions. More details can be found in Refs. 142, 177, 178.

Starting from the theoretical predictions of the multi-electron capture $\sigma_{n,\ell}^{multi}$, the Auger decay scheme is considered to calculate a resulting population of excited levels that decay subsequently by a purely radiative emission[5]. From these predictions, the apparent (from the point of view of the X-ray emission) cross section $\sigma_{n,\ell}^{app.single} = \sigma_{n,\ell}^{multi+Auger} + \sigma_{n,\ell}^{single}$ is considered as input for the atomic cascade code of singly excited ions.

Kirchner et al. predictions are based on the time-dependent Schroödinger equation resolution using the two centre basis generator method (TC-BGM) [159–161]. This method provides only the partial cross section σ_n and assumptions on the ℓ-distribution have to be done. For simplicity, one considers here only a statistical distribution of $\mathcal{P}_\ell$. The predictions of Otranto et al. are based on the classical trajectory Monte Carlo method (CTMC) [162–164] and ℓ-sublevels cross sections are computed.

Both theoretical predictions are presented in Fig. 4.7. When only single electron capture is considered, TC-BGM predictions do not reproduce well the experimental observations. CTMC calculations fit better for the levels $n = 7$ and 10. For both set of theoretical predictions, $\sigma_{n,\ell}^{app.single}$ reproduces very well the effect of the multi-electron capture contribution in the characteristic X-ray emission [177, 178] for $n \leq 7$. In particular, the comparison of CTMC predictions with experimental data indicates a possible multi-electron capture contribution already for the $n = 7$ level.

The disagreement with the measured intensities of the $n = 2 \rightarrow 1$ lines is partially due to the presence of metastable states that in fact can explain an underestimation of the experimental evaluation of about 50%. This issue is discussed in the next section.

To summarise the results presented in this section, one can conclude that the simple model of Ali et al. for the Auger decay results is very reliable and efficient, independently on the implemented multi-electron cross section. This indicates that the X-ray intensities of $1s\,np\ ^1P_1 \rightarrow 1s^2\ ^1S_0$ transitions with $n = 3 - 7$ are almost exclusively determined by Auger processes and not by $\sigma_{n,\ell}^{multi}$ values.

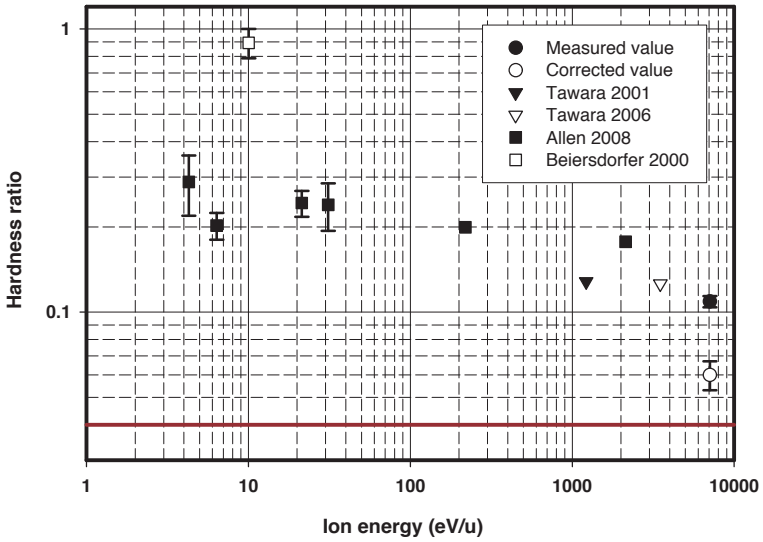

Figure 4.8 – Measured hardness ratio H values (with one-sigma error bar) for Ar^{17+}+ Ar as function of the collision energy from different experiments: Tawara 2001 [147], Tawara 2006 [148], Allen 2008 [149], Beierdorfer 2000 [143]. The values of Allen 2008 at $E_{ion} = 6.4$ eV/u and Beierdorfer 2000 correspond to measurements obtained in magnetic trapping experiments. The others are obtained with extracted ion beams. The empty circle correspond to H_{corr}, the corrected value of H taking into account the partial detection of the $1s2s\ ^3S_1 \rightarrow 1s^2\ ^1S_0$ M1 transition (see text). The horizontal solid line corresponds to a H value expected assuming a statistical population $\{\mathcal{P}_\ell\}$.

4.4.4 Metastable states

The presence of the $1s2s\ ^3S_1$ metastable state strongly influences the flux of detected X rays in proximity of collision location. This means that radiative emission intensities of atomic systems with metastable states should be compared with precautions between each other because of this dependency on the experimental set-up. In particular, it has a strong impact on the total intensity of $n = 2 \rightarrow 1$ transitions as anticipated in the previous paragraph and as discussed by Tawara [147] and in Refs. 155, 179.

As all ion–atom collision experiments with an extracted ion beam, X-ray detectors can see only a small spatial region (about ± 1 cm) corresponding to several tens of ns (with $v \sim 1$ a.u., which is much larger than the typical de-excitation cascade time ($10^{-(10-13)}$ s) excepted when metastable states are involved. Due to the long lifetime of the $1s2s\ ^3S_1$ state (0.2 μs), most of the X rays emitted by its decay to the fundamental level (95%) are on the contrary not detected. Thanks of the high-resolution of the spectrometer, X rays from the decay of the $1s2s\ ^3S_1$ metastable state is detected and resolved, and its influence can be evaluated.

To quantify the set-up dependent effect due to the metastable states, the hardness ratio parameter

[4] This last rule is obtained from similar considerations already developed for pionic atoms and discussed in Sec. 3.2.1 (Eqs. (3.2)–(3.5)).

[5] This is the case when (i) only one electron in the excited state remains and (ii) when one or more electrons act as spectator during the radiative decay.

H is considered, commonly used as parameter in X-ray astronomy. The hardness ratio is defined as

$$H = \sum_{n>2} I_n \Big/ I_2 \tag{4.6}$$

with I_n the intensities of $(n > 2) \rightarrow 1$ transition and I_2 the $(n = 2) \rightarrow 1$ transitions. H serves as a reference to determine abundance of elements when interpreting astrophysical X-ray spectra. It is used to deduce also the velocity of the colliding atoms in space environment. Reference values of H are then required with good accuracy. We have to keep in mind that no directly comparable values can be obtained in ion–atom experiments with extracted beam, where only a limited region around the collision zone is visible, and in astronomical measurements where a very large region is visible.

Different measured values of H for Ar^{17+}+ Ar collisions at different velocities are presented in Fig. 4.8. Here, data obtained with ion traps and ion beams are reported as well as the expected value of H assuming a statistical population of the ℓ-sublevels (horizontal line).

Without considering the effect of metastable states, a value of $H = 0.109 \pm 0.005$ (solid circle) is extracted from the experiment discussed here. When the partial detection of the $1s2s\ ^3S_1$ decay emission is considered, a value of 0.060 ± 0.007 is obtained (empty circle), almost half of the previous value wrongly estimated. The corrected H value is much closer to the statistical distribution prediction as expected for high velocity collisions. When ions with smaller atomic number Z are considered, e.g. C, N, O, Ne, Mg and Si, even more attention has to be paid since the correction factor depends on the metastable state lifetime that increases exponentially with $1/Z$.

4.5 Final considerations

In this chapter, it has been shown how to extract from high-resolution X-ray spectroscopy measurement important information on the dynamic of the collision between slow ions and atoms. No additional measurements of emitted electron, recoil or projectile charge exchange have been used but only the intensities of the resolved $1sn\ell \rightarrow 1s^2$ transitions. From $n \geq 7 \rightarrow 1$ X-ray line intensities, the single electron capture is characterised. From $(2 \leq n < 7) \rightarrow 1$ X-ray line intensities, the multi-electron capture is studied. Thanks to the high resolution power, the forbidden $1s2s\ ^3S_1 \rightarrow 1s^2\ ^1S_0$ transition is also clearly identified and the effect of the population of the metastable $1s2s\ ^3S_1$ state is also evaluated.

An interesting development of this kind of measurement is the coupling of X-ray detection to ion detection to determine clearly the number of exchange electrons during the collision. This has been partially done in recent experiments where a low-resolution X-ray spectroscopy is coupled to the measurement of the final projectile charge state [179] and with both projectile and recoil target atom charge state [155]. A measurement with high-resolution X-ray spectroscopy coupled to measurements of charge states of projectile ions and/or target atoms after the collision remains challenging.

Chapter 5

Modification of properties of magnetocaloric thin films by ion irradiation

5.1 Introduction

5.1.1 Target properties modification induced by collisions with ions

Differently from the previous chapters dedicated to the dynamic and structure of isolated atomic systems, the main topic treated here is the study of the properties modifications of solid targets, more specifically of thin films, induced by the collisions with slow heavy ions. By 'slow' one means ions with energy of a few keV/u. In this case, ions efficiently produce atomic displacements in the solid target. The defects induced by the ion interaction may change the properties of the target material. We may even tune the material properties with an appropriate choice of irradiation parameters. To efficiently determine these parameters, the ion–solid interaction have to be deeply understood.

The goal of the research activity presented in this chapter is to understand the specific case of slow heavy ions interacting with thin films having giant magnetocaloric properties. This investigation is carried out thanks to a series of systematic studies where the ion characteristics (kinetic energy, mass, etc.) and target samples are varied. Before to present the major results, a review of the basic processes involved in ion–solid collisions and an introduction of the giant magnetocaloric effect are presented.

5.1.2 Work context, personal contribution and associated publications

This project has been started by the author within the ASUR team at the INSP in 2010 from scratch. The first results on the suppression of the thermal hysteresis in thin MnAs films [A14, A22] have been obtained in 2012-2014. They permit to obtain a financial support from the Labex MATISSE for a Ph.D. Thesis (S. Cervera). The Ph.D. topic is on the characterisation of the processes responsible for the thermal hysteresis suppression in MnAs and the extension of these investigations to other giant magnetocaloric materials.

Related to this topic, a research on the slow heavy ion irradiation effects on zinc ferrite thin films and powders have been developed in the context of the E.V. Gafton's Ph.D. thesis (University of Iasi,

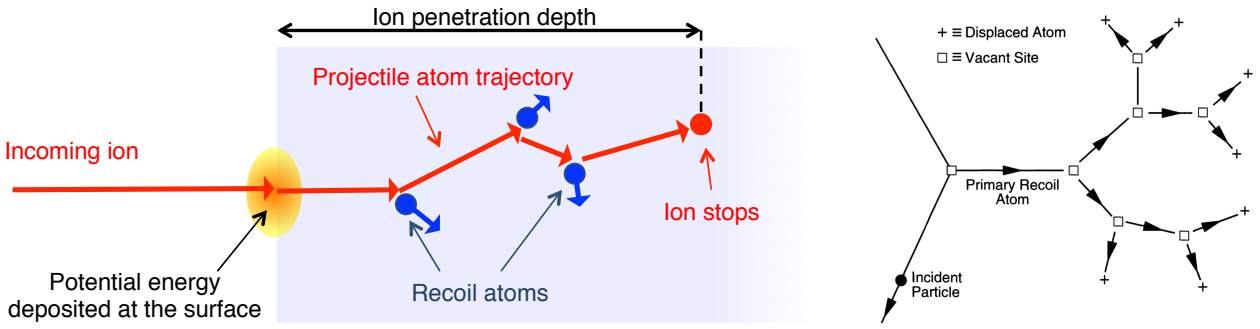

Figure 5.1 – Right: scheme of the basic processes of ion–matter interaction. Ions interact with the solid matter principally by two ways until it stops (if the target is thick enough): (i) by elastic scattering with target atom nuclei that deviate considerably the ion trajectory and (ii) by kinetic energy loss resulting from the interaction with the target electrons with no noticeable variation of the ion trajectories (strait lines in the figure). Left: Scheme of the secondary cascade generated by a target atom accelerated by a collision with the incoming ion [185].

Romania). Part of the results of this research activity is published in Ref. A9 and is not presented in this chapter. The publication associated to this chapter is presented in App. H [A14]. Other related publications are Refs. A1, A5, A22, C4, C5.

5.2 Ion – matter interaction

5.2.1 Basic processes

The study of the ion–matter dynamics is old as the construction of the first ion accelerators, and it has been extensively studied [180–184]

During the interaction with a solid, the ion transfers its kinetic and potential energy to the target atoms by a series of collisional processes. These collisions determine the energy loss of the ion and, in other words, the ion stopping power in the target. The involved processes can schematically separated in two categories, one due to the interaction with the target nuclei and the other due to the interaction with the electrons.

At the kinetic energies considered here (less than 1 MeV), the interaction with the target nuclei (and eventual surrounding electrons) is due to the Coulomb repulsion only. This can be generally treated as a two-body elastic collision. The mean free path between two collisions is then much greater than the interatomic spacing as schematised in Fig. 5.1. Nuclear collisions are dominant at low energy and for heavy ions. They are responsible for the production of lattice disorder due to the displacement of atoms and they cause large changes of the ion trajectory and kinetic energy.

The interaction with the electrons is also due to the Coulomb interaction and is generally inelastic because during the collision electrons can be ejected from target atoms, captured by the ion or put in an excited level (see Sec. 1.3). Electronic collisions are dominant at high velocity and light ions with a negligible deflection of the ion trajectory and target lattice distortion. The interaction with the target electron medium results in an average energy loss that corresponds to an energy transfer to the solid with a temperature increasing that can be modelled with a thermal spike approach [181, 186].

The ion energy loss rate in the solid dE/dx can conveniently be separated in two distinct contributions: one due to the nuclear collisions and the other due to the electron collisions. One then can

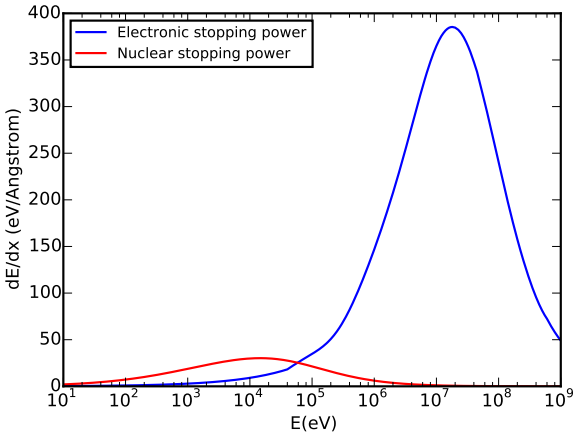

Figure 5.2 – Electric and nuclear stopping power of Ne ions of MnAs as function of the ion kinetic energy obtained by SRIM [182, 187].

write:

$$\frac{dE}{dx} = \left(\frac{dE}{dx}\right)_n + \left(\frac{dE}{dx}\right)_e . \tag{5.1}$$

An example of sopping power dependency on the ion energy ins presented in Fig. 5.3.

During the binary collision with the incoming ion, accelerated recoil atoms can also interact with other target atoms via nuclear and electronic collisions. If the energy transfer to the recoil atom is sufficiently large, this can generate a cascade of binary collisions between target atoms with important distortion of the target lattice, as schematically represented in Fig. 5.1. To note, collisional cascades close to the surface are responsible for sputtering, a process extensively studied in the past [188–190].

If the ion is highly charged, it can bring a non-negligible potential energy E_p related to the ionisation energy of the lost electrons. Because of the fast capture processes occurring in proximity to the target surface, the potential energy of the ion is deposited in the first layers and is transformed in heat with a localised temperature rise. In insulators, this thermal spike can give origin to additional sputtering processes [189, 191–193] and to the creation of local defects or nanostructures [194–199].

For the cases considered here, $E_p \lesssim 5$ keV. Because of this small value and of the metallic nature of the irradiated samples, no defects associated to the ion potential energy are expected [198]. Additionally, no defects have been detected (with AFM measurements at atmospheric pressure). Consequently, the pertinent parameters to characterise the irradiation are only the ion mass and the ion kinetic energy only. In the following sections, possible marginal dependencies on the ion charge are ignored. Additional considerations on the interaction of highly charged ions and dependencies with their charge state can be found in App. C.

5.2.2 Collisional cascades, simulations and defect clustering

Collisional cascades are generally simulated by Monte Carlo techniques assuming the binary collision approximation. This approximation consists in considering a series of uncorrelated elastic nuclear collisions i) between the ion and the target atoms, and ii) between the recoil atoms accelerated by the

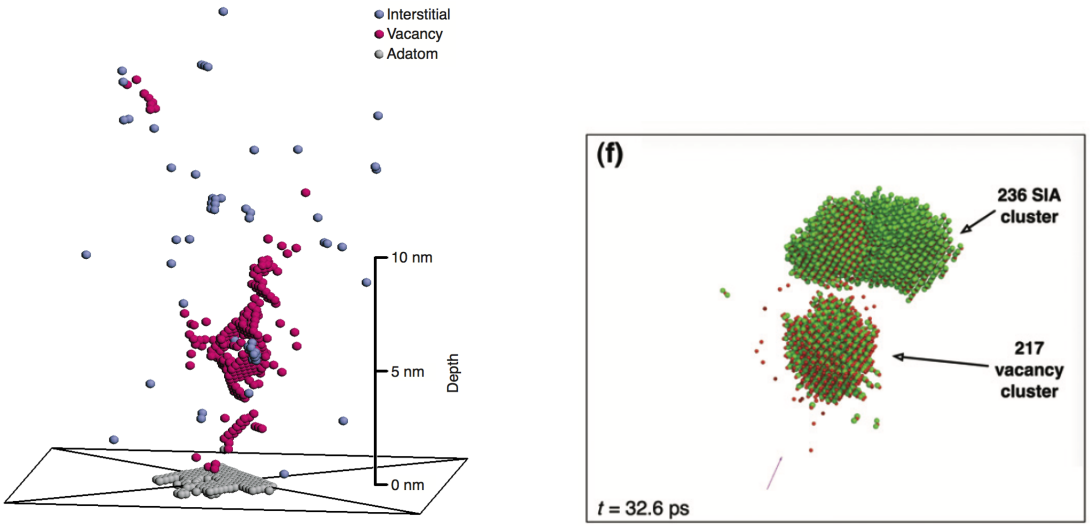

Figure 5.3 – Production of vacancy and interstitial atoms (SIA) clusters calculated by a molecular-dynamics simulation for 50 keV Cu in collision with a Cu target [200] (left) and for 30 keV Bi_2 in iron [201] (right).

primary collision (collision with the incoming ions) and the other target atoms. Between each collision, the atoms are assumed to travel in a straight path loosing their energy via electronic stopping power.

Many codes are based on this approximation and in particular, the SRIM/TRIM code [182, 187]. Nuclear and electronic stopping powers used by SRIM are obtained by interpolation of a large ensemble of ion–solid collision data. In addition to numerical values of the nuclear and electronic stopping power (where Fig. 5.3 is an output example), SRIM can simulate ion implantation and target atoms displacements and other quantities. Displacements are calculated considering a zero absolute temperature of the target; auto-healing processes due to the thermal movement are not then considered. The eventual target ordered structure (as in a crystal) is not taken into account neither and each incident ion experiences the same target characteristics (no memory of the defects produced by previous simulated tracks). Due to these approximations, SRIM (and other binary collision codes) has some limitations, particularly on the induced defects properties. It is however quite reliable to calculate the distribution of the implanted ions and it provides a distribution of collisional processes (atom displacement and deposited energy).

More accurate simulations require many-body molecular dynamics calculations to take into account collective behaviour and temperature effects. These calculations consider nuclear and electronic processes at the same time and the same footing. Then, they account for the enhanced mobility and self-healing of point-like defect due to the irradiation-induced temperature rise. Many studies have been done with this approach and are compared and competed by experimental observations [183, 200–204]. In particular, from studies in metals irradiated with heavy ions, the formation of cluster of defects (vacancies or interstitial atoms) emerges inducing specific local modifications in the material. In the following sections it will be show that these collective processes play a key role in the present investigations.

5.2.3 Modification of magnetic thin film properties by ion irradiation

Irradiation induced changes in the material propertiescan be resumed in:

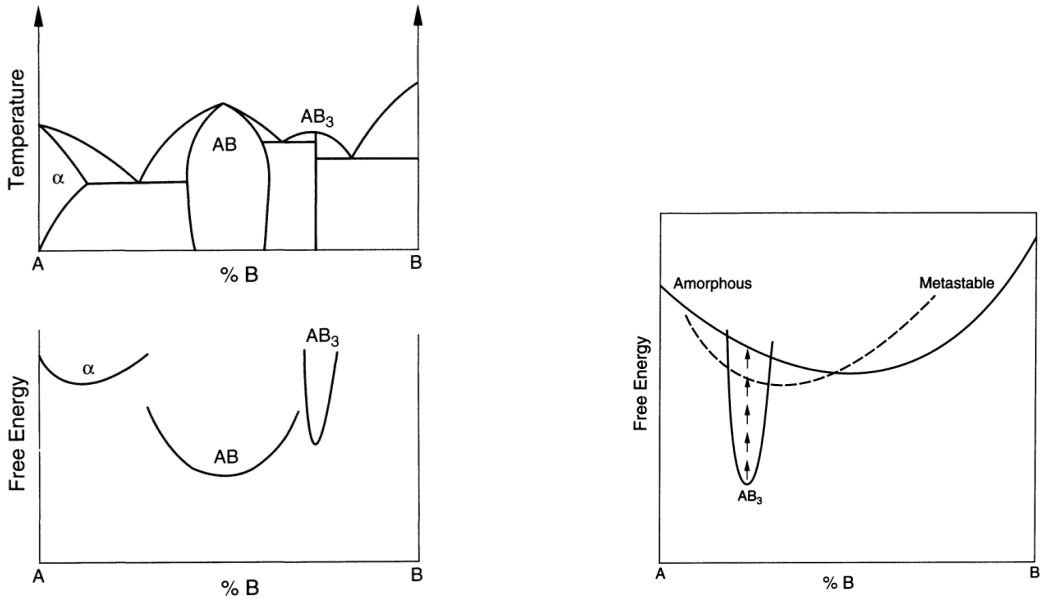

Figure 5.4 – Left: Schematic of the equilibrium phase diagram (up) and free energy diagram (down) for an $A-B$ binary system with an fcc solid solution α, an AB CsCl structure with wide phase field and a line-compound AB_3 [183]. Right: Zoom of free energy region close to the AB_3 compound phase. Adapted from Ref. 183.

- local energy deposit by heat,
- disordered dislocation of target atoms,
- implantation of projectile ions in the target.

Properties modifications and radiation resistance depend on the structural phase of the target sample. As an example, let consider a A–B binary composition material and the associated phase diagram in Fig. 5.4 (left, top). For different percentage of one element with respect to the other, we have different structures. For almost pure A material, we have a phase α (a face centred cube). For %A $\sim$ %B we have a CsCl structure and we have a vertical line corresponding to the compound AB_3. The stability of the different phases depends on several parameters [183] as the local composition that modify the Gibbs free energy[1] G. The stability of a particular phase depends on G values as a function of the A/B concentration. In the example presented in Fig. 5.4 (left, up and down), the AB compound is expected to be more radiation-resistant than the AB_3 compound due to the larger minimum of the free energy. Moreover, as suggested in Fig. 5.4 (right), irradiation can provide locally additional energy (small arrows in the figure) to induce a transformation to a metastable ordered phase or to an amorphous one [183]. The local deposit of heat can also induce the decay of possible

[1]The Gibbs free energy is a thermodynamic potential that can be used to calculate the maximum of reversible work that may be performed by a thermodynamic system at a constant temperature and pressure (isothermal, isobaric). Just as in mechanics, where the decrease in potential energy is defined as maximum useful work that can be performed, similarly different potentials have different meanings. The decrease in Gibbs free energy is the maximum amount of non-expansion work that can be extracted from a thermodynamically closed system. Minimising G for the system maximise the total entropy (system plus thermal bath). For this reason, at equilibrium the system assumes minima values of G.

metastable phases of the material and/or induce a local annealing bringing to the creation of ordered structures in amorphous materials [205, 206].

Many studies have been done in bulk materials using fast ions and in thin films with slow and fast ions. In particular, since the late '90s, irradiation-induced properties modifications have been deeply studied in magnetic materials. Since the first application in Co/Pt multilayers [207], where the coercivity is increased by collision with an He^+ beam, this technique has been successfully employed to create magnetic patterns in thin magnetic films for potential applications in micro and nano-electronics. At the same time, many more fundamental studies have been performed to characterise the modifications of thin film properties as magnetic saturation, coercivity, anisotropy, lattice spacing, etc. as a function of the irradiation conditions [208–222].

All past studies on magnetic thin films were performed with materials exhibiting second-order transitions between magnetic phases (ferromagnetic –paramagnetic as an example) where the properties modifications are mainly related to the induced disorder that disturb the ferromagnetic interaction and change the domain wall mobility after a high-fluence irradiation ($\geq 10^{13}$ ions/cm^2).

In this chapter original results are presented on the irradiation-induced properties modifications in magnetic thin films exhibiting first-order transitions. Magnetic first-order transitions are commonly associated to an enhancement of the magnetocaloric effect (common to all magnetic materials, see next section) due to the large entropy change occurring during this type of transition. Differently from second-order transition materials, even small ion fluences can drastically change the features of first-order transitions and, at the same time, still slightly perturb the properties of the material far from the transition conditions. This interesting feature is the object of the study presented in the next sections where irradiation-induced modifications in thin films exhibiting giant magnetocaloric properties are presented. The impact of these studies on the development of the magnetic refrigeration is also discussed.

5.3 Giant magnetocaloric effect and thin films

5.3.1 The magnetocaloric effect and magnetic refrigeration

Before to present the effect of ion irradiation in giant magnetocaloric thin films, a short introduction of the magnetocaloric effect and the magnetic refrigeration is mandatory.

The MagnetoCaloric Effect (MCE) consists in the common properties of magnetic materials. When an external magnetic field is applied to a magnetic material, the atomic spins are oriented and consequently the associated entropy $\mathcal{S}_m$ decreases. If the field application is done under adiabatic condition (no exchange of heat, horizontal line in Fig. 5.5 left), the total entropy

$$\mathcal{S} = \mathcal{S}_{\text{lattice,el}}(P,T) + \mathcal{S}_m(P,H,T) \tag{5.2}$$

is constant. $\mathcal{S}_{\text{lattice,el}}(P,T)$ is the entropy associated to the movement of the lattice atoms and electrons. As $\mathcal{S}$ is constant, a decrease of $\mathcal{S}_m$ produces then an increase of $\mathcal{S}_{\text{lattice,el}}(P,T)$ accompanied by a temperature rise. Similarly, when isotherm (and isobar) transformations are considered, only $\mathcal{S}_m(P,H,T)$ changes as a function of the applied field H (vertical line in Fig. 5.5 left). Considering the elementary spin J associated to the magnetic material, one expects that the variation of entropy $\Delta\mathcal{S}_m$ does not exceed the theoretical value

$$\Delta\mathcal{S}_m^{max} = n_m R \ln(2J+1), \tag{5.3}$$

where R is the gas constant and n_m the number of moles of considered material.

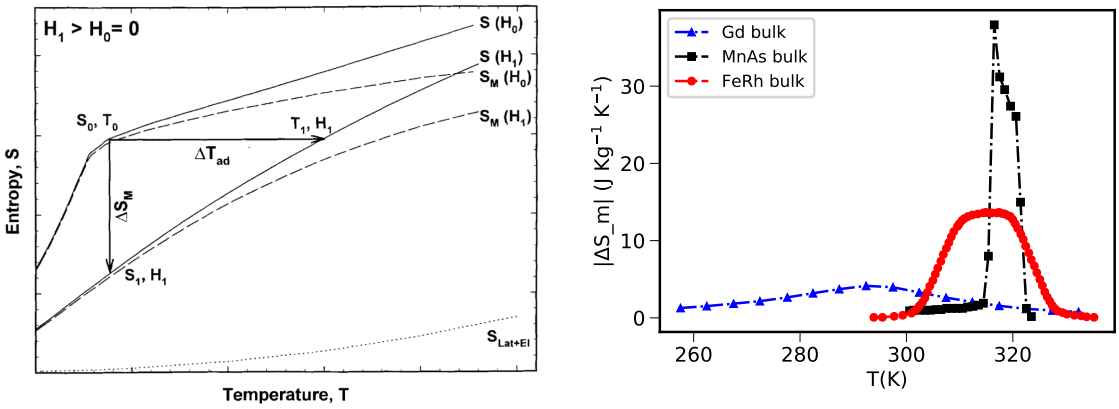

Figure 5.5 – Left: Different entropy components as a function of the temperature in proximity of a second-order ferromagnetic–paramagnetic transition [223]. Right: Variation of the magnetic entropy ΔS_m of Gd, MnAs and FeRh for a variation of applied fields from 0 to 2 T at different temperatures (data from Refs. 224–226). For Gd and MnAs $\Delta S_m = S(H = 2\ T) - S(H = 0\ T) < 0$ and for FeRh $\Delta S_m > 0$ (inverse magnetocaloric effect).

The magnetocaloric effect has been discovered by Weiss and Picard in 1917 [227] (and not Warburg in 1881 [228] as claimed in some publications) during caloric measurements in proximity of the ferromagnetic–paramagnetic transition of Nickel (354°C) when an external magnetic field (1.5 T) was applied or removed.

Few years later in 1926-7, a refrigeration method based on the magnetocaloric effect has been proposed by Debye and Giauque [229, 230]. From the definition of the Gibbs free energy for magnetic systems

$$G(P, H, T) = U - T\mathcal{S} + PV - \mu_0 H\mathfrak{M} = G_{\text{lattice,el}}(P, T) + G_m(P, H, T), \tag{5.4}$$

they built thermodynamic cycles based on the variation of the applied magnetic field H instead of the variation of the pressure P. In the above equation, $\mathfrak{M}$ indicates the magnetic moment of the system, G_m is the free energy associated to the magnetic components (spins) and $G_{\text{lattice,el}}$ is associated to the lattice and electrons (this subdivision does not apply to the case of itinerant-electron magnetism and in giant magnetocaloric phenomena, see next section). A typical magnetic refrigeration cycle based to adiabatic transformations (Brayton cycle) is presented in Fig. 5.6 and it is put into perspective of the gas compression/expansion cycle commonly employed.

The practical demonstration of the magnetic refrigeration has been done in 1933 by Giauque himself with $Gd_2(SO_4)_3 \cdot 8H_2O$ paramagnetic salts, with which the record temperature of 0.25 K [231] was reached. For this discovery he won the Nobel price in 1949.

At higher temperatures, magnetic refrigeration is found to be inefficient, except the in presence of a phase transition [232, 233] (see Fig. 5.5), as in the Nickel transition at the origin of the discover of the magnetocaloric effect [227]. In the first scientific article on magnetic refrigeration at room temperature, Brown [232] clearly explains why: *"the ordering influence of the exchange interaction and the disordering effect of thermal agitation are in approximate balance near T_c. In this neighborhood, applying a field under isothermal conditions produces a greater increase in magnetization (decrease in entropy) than at a higher temperature T where only a paramagnetic response could be produced or at much lower T where the spontaneous magnetization approaches saturation and cannot be increased to any great extent".*

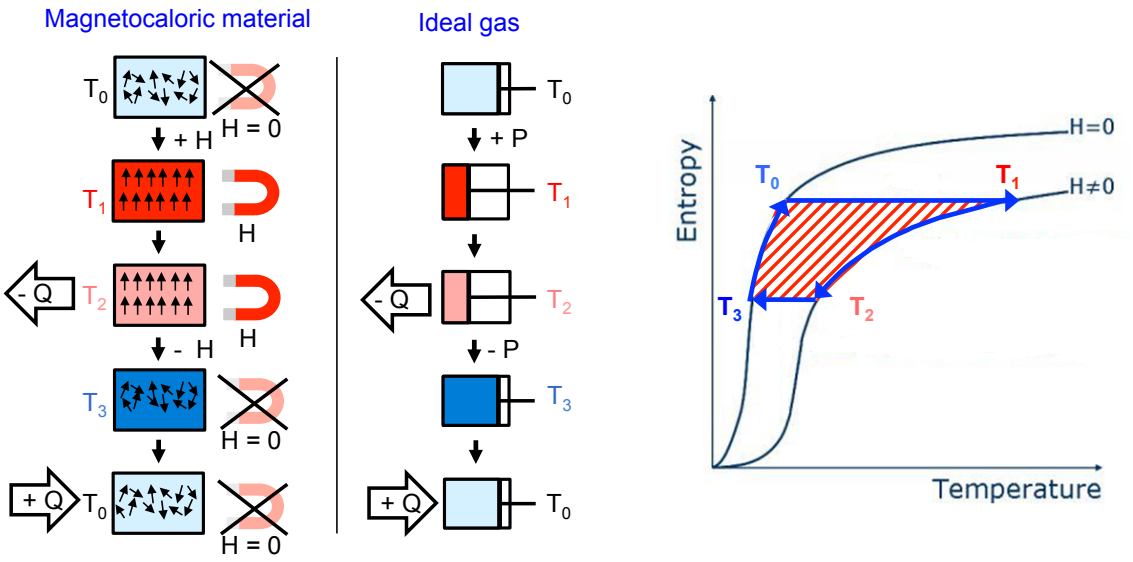

Figure 5.6 – Left: a magnetic refrigeration cycle (Brayton cycle) compared to the typical gas compression/expansion thermic cycle [223]. Right: a Brayton cycle (with adiabatic transformations) visualised in the entropy–temperature diagram.

The ferromagnetic metal gadolinium, which has a phase transition at room temperature, discovered by Urbain, Weiss and Trobe already in 1935 [234], was not used during many years for magnetic refrigeration systems. Two patents appeared only in 1952 [235, 236] and magnetic refrigeration was proposed in a scientific publication by Brown only in 1976 [232]. The first prototype based on Gd came in 1978 [237] with additional important developments (the invention of the active magnetic regenerator) in 1982 [238, 239]. Since then, many magnetic refrigerator prototypes based on Gd have been developed [240, 241].

A breakthrough of magnetic refrigeration came in the 1996-7 years [242–244] with the discovery of the giant magnetocaloric effects, based on materials with first-order transitions (see following section). Today, a commercial wine refrigeration prototype, based on LaFeSi [245] is in production [246].

Magnetic refrigeration is at the centre of interest of many studies in the last years. This large interest lies on the fact that magnetic refrigeration is in principle more efficient than technology based in gas compression/expansion and it is environmental-friendly due to absence of gases.

Reviews of magnetocaloric effect and materials and magnetic refrigeration can be found in Refs 225, 233, 240, 247–259. Additional historical insights can be found in Ref. 228.

5.3.2 The giant magnetocaloric effect and the role of the transition order

The Giant MagnetoCaloric Effect (GMCE) is related to first-order phase transitions. These transitions are characterised by a discontinuity in physical properties (volume, magnetisation, conductivity, etc.) due to a transition between phases of different symmetries (in the atomic arrangement, in valence electron bands, etc.) with a large change of the associated entropy [260–262]. This is due to the fact that, for certain temperature values T the Gibbs free energy (see note 1 at page 65 for its definition) can have two distinct minima corresponding to different system symmetries. An example of presence of two possible minima is illustrated in Fig. 5.7 for a magnetic material corresponding to two possible

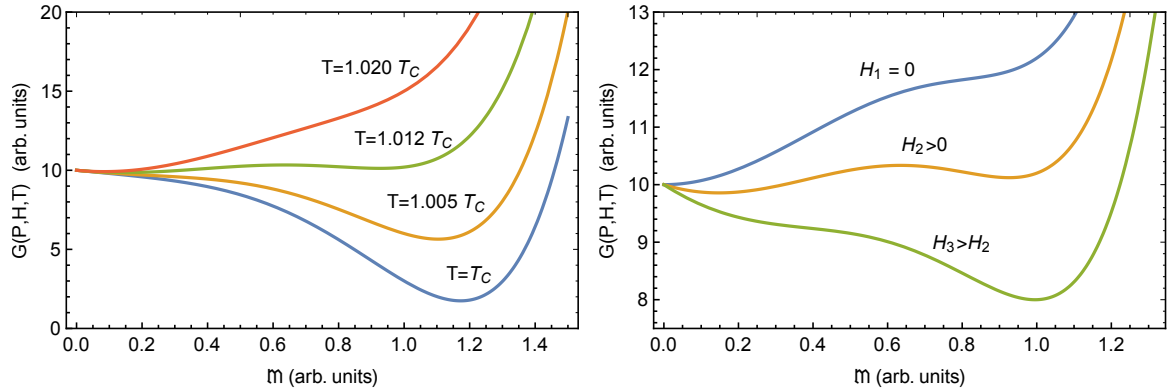

Figure 5.7 – Gibbs free energy of a first-order transition material as a function of the temperature T and $H \neq 0$ (left) and applied magnetic field H at $T = 1.012\ T_c$ (right) for different values of the magnetic moment $\mathfrak{M}$, which is an internal parameter of the system.

magnetic moment states $\mathfrak{M} \sim 0$ or $\mathfrak{M} > 0$ for certain values of T and H. For given external conditions of applied magnetic field H and temperature T, the value of the Gibbs free energy, more precisely its value at equilibrium, is absolute minimum with respect to magnetic moment $\mathfrak{M}$ value, which is an internal parameter of the system.

When the external conditions are varied, T or H as example as in Fig. 5.7, G changes continuously. For different temperatures, G pass from one local minimum to another other, with a sudden change of an internal symmetry of the system (the magnetic moment $\mathfrak{M}$ in Fig 5.7) accompanied by a large change $\Delta\mathcal{S}$ of the associated entropy $\mathcal{S} = -\partial G/\partial T$ as shown in Fig. 5.8. $\Delta\mathcal{S}$ variation at the critical temperature T_c is associated to a latent heat L to pass from one phase to another, as in the liquid–solid transition, with $\Delta\mathcal{S} = LN/T_c$, where N is the number of the particle involved and T_c is the transition (critical) temperature. The discontinuity of $\mathcal{S} = -\partial G/\partial T$ is at the origin of the name *first-order transitions*, in comparison to transitions without abrupt changes, as paramagnetic–ferromagnetic transition, called *second-order transitions*.

Because of the presence of several minima in the Gibbs free energy, as suggested by Figs. 5.7 and 5.8, first-order transitions are related also to phenomena of phase coexistence, of metastability and, more generally, of a dependency on the past history of the material. Metastability is at the origin to the common phenomena of supercooling or superheating of liquid water with a temperature below 0 and 100°C, respectively. Another common example of such phenomena can be found in a glass of champagne or beer, at room temperature (or better fresh): while the equilibrium state corresponds to the vapour state, one can have the presence of supersaturated dissolved CO_2 molecules in the liquid. Similarly, in clouds, supercooled water vapour well below the condensation temperature is present.

In the case of magnetic materials, Gibbs free energy is modelled in the framework of Landau theory by [253, 263–266]

$$G(P, H, T) = G_0 + a(T - T_c)\mathfrak{M}^2 + b\mathfrak{M}^4 + c\mathfrak{M}^6 - \mu_0\mathfrak{M}H + \dots, \tag{5.5}$$

where a, c are positive constants, b negative, T_c is the critical temperature of the material, $\mathfrak{M}$ is its magnetic moment and where additional dependencies with external pressure and strain have been omitted.

In the case of second-order transitions, $b > 0$ for which there is always only one solution of $\mathfrak{M}$ that

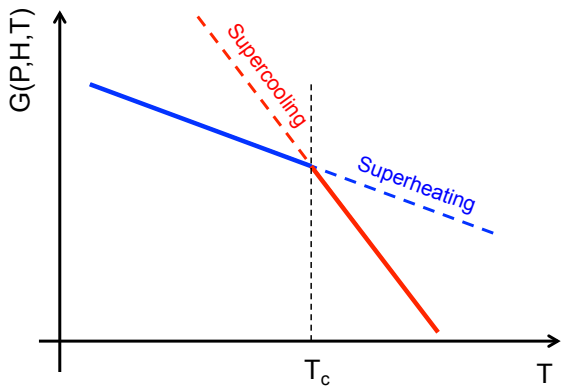

Figure 5.8 – Gibbs free energy for different values of temperatures T. At $T = T_c$, the equilibrium value of G (the absolute minimum) pass from one internal symmetry to another (from one local minima to another), with a large change of the entropy $\mathcal{S} = -\partial G/\partial T$. Due to the coexistence of local minima of G, metastable states can be present with the corresponding phenomena of supercooling or superheating and/or thermal hysteresis.

minimise G. In opposite, as visible in Fig. 5.7, when $b < 0$, two solutions solving

$$\frac{\partial G}{\partial \mathfrak{M}}(H,T) = 0 = 2a(T - T_c)\mathfrak{M} + 4b\mathfrak{M}^3 + 6c\mathfrak{M}^5 - \mu_0 H \tag{5.6}$$

are possible. Differently than in second-order transitions, when T or H is continuously changed, a jump between the magnetisation solution $\mathfrak{M}$ of Eq. (5.6) is present corresponding to a discontinuity of $\mathfrak{M} = \mu_0^{-1}\partial G/\partial H$. As in the general case, the presence of two possible values $\mathfrak{M}$ for a certain range of H and T values implies the presence of thermal and magnetic hystereses, and, more generally, metastability and phase-coexistence as anticipated at the beginning of the section.

The large entropy change due to the abrupt passage from one minimum to another of the free energy is larger than the expected maximal entropy variation $\Delta\mathcal{S}_m^{max}$ (Eq. (5.3)). We are then in presence of the so-called Giant MagnetoCaloric Effect (GMCE). Magnetic transitions of giant magnetocaloric materials are often associated to structural phase transitions as in MnAs where the large $\Delta\mathcal{S}_m$ is related to a lattice–magnetic moments coupling, represented in the free energy G by an additional term $G_{\text{lattice,el–spin}}$ with respect to Eq. (5.4):

$$G(P,H,T) = G_{\text{lattice,el}}(P,H,T) + G_m(P,H,T) + G_{\text{lattice,el–spin}}(P,H,T). \tag{5.7}$$

An overview of the compared behaviour of magnetisation and entropy of first- and second-order transitions in magnetocaloric materials are presented in Fig. 5.9.

In experiments, the specific magnetisation M is considered instead of the magnetic moment $\mathfrak{M}$. In addition, instead of the total entropy of the system $\mathcal{S}$, the entropy per mass unit S is generally reported. Consequently, they are no longer extensive variables. From now on, only the specific variables are considered in the text.

5.3.3 Past and present studies on GMCE

Historically, GMCE has been discovered in the '90s. In 1996 Annaorazov and colleagues noticed a *"anomalous high entropy change"* associated to the magnetocaloric effect in iron-rhodium (FeRh) [242]

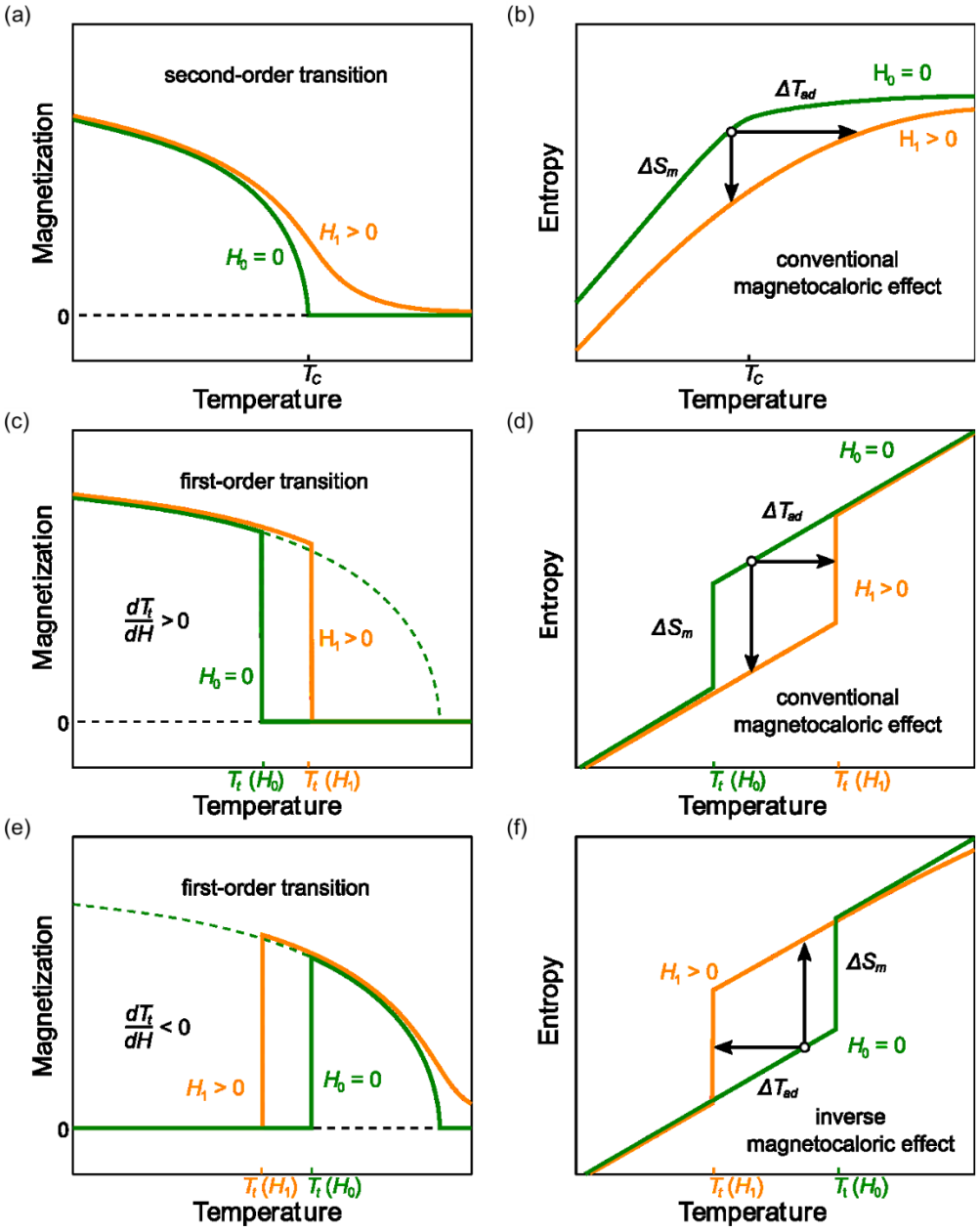

Figure 5.9 – Summary of the main characteristics of conventional magnetocaloric effect associated to second- or first-order transitions and of the inverse magnetocaloric effect (associated to first-order transitions). Figure from Ref. 258.

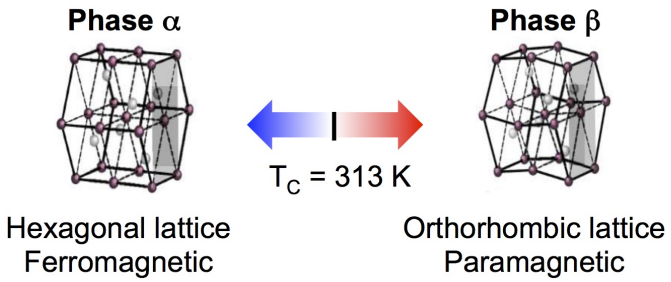

Figure 5.10 – Magneto-structural phase transition of MnAs metallic compound close to room temperature (adapted from Ref. 275).

(discovery of giant magnetorestriction in 1994 [267]), and in 1997 Pecharsky and Gschneidner claim the evidence of the *"giant magnetocaloric effect"* in GdSiGe compounds [243,244]. Since then, many other materials exhibiting GMCE have been discovered; all characterised by first-order phase transitions associated to normal or inverse magnetocaloric phenomena. Among them, it has to be mentioned the discovery of giant magnetocaloric effect in manganese arsenide (MnAs) metallic compound in 2001 [224] and in MnFePAs compounds [268] that, together with FeRh, are irradiated here with ions and discussed in the next sections.

In the last years, many efforts have been spent on this materials in particular to find ways (i) to change the characteristic critical temperature T_c (for which the magnetocaloric effect is maximal) and (ii) to elimination of the hysteresis phenomena connected to the phase transition nature associated to the peak of the magnetocaloric effect. The first point is important for having efficient thermal machines working close to room temperature. The second point is equally important because thermal or magnetic hystereses induce energy losses in the thermal cycle. For both points, many studies have been done to search new materials doping of existing ones [225,233,240,247–259] and cited references. Studies of the effect of external pressure or strain are also explored in bulk materials [269, 270] or in thin films [271–273].

5.3.4 A particular giant magnetocaloric material: manganese arsenide

Bulk material properties

Manganese arsenide metallic compound (MnAs) is one of the more promising GMCE materials for the development of magnetic refrigeration. As shown in Fig. 5.5, it exhibits a large change of magnetic entropy (typically [224, 274] $\Delta S(T = \text{cst}) \approx -30$ J Kg^{-1} K^{-1} for a variation change $\Delta H = 2$ T) in proximity of its transition close to room temperature ($T_c = 313$ K) corresponding to a large refrigeration power (that depends on the ΔS integral over a temperature interval) up to 200 J Kg^{-1}.

This ferromagnetic–non-ferromagnetic transition is associated to the first-order magneto-structural phase transition from hexagonal (α-phase, NiAs-type) to orthorhombic (β-phase, MnP-type) [276], as schematically presented in Fig. 5.10 and in the composition phase diagram in the line corresponding to stoichiometric MnAs in Fig. 5.11.

The phase transition can be triggered by temperature or external magnetic field changes [277]. Because of the different cell volume of the two phases, Gibbs energy strongly depends on the applied external pressure P and the phase transition can be induced also by a variation of it [278–282].

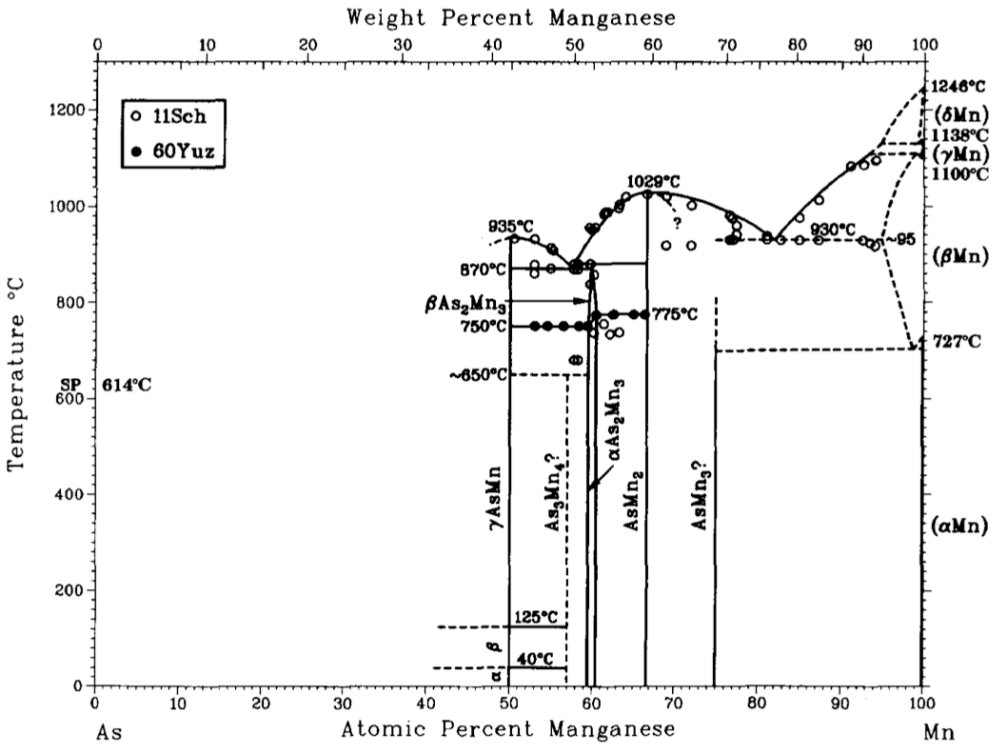

Figure 5.11 – Composition phase diagram of manganese arsenide from Ref. 276. The metallic compound MnAs studied here correspond to the stoichiometric MnAs.

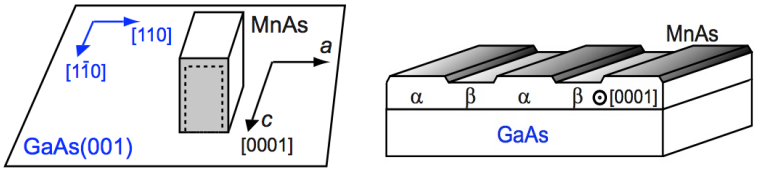

Figure 5.12 – Left: Orientations of MnAs think films on a GaAs(001) substrate. Rigth: self-organizations of $\alpha - \beta$ phases regions on a GaAs(001) substrate. Figures from Ref. 275.

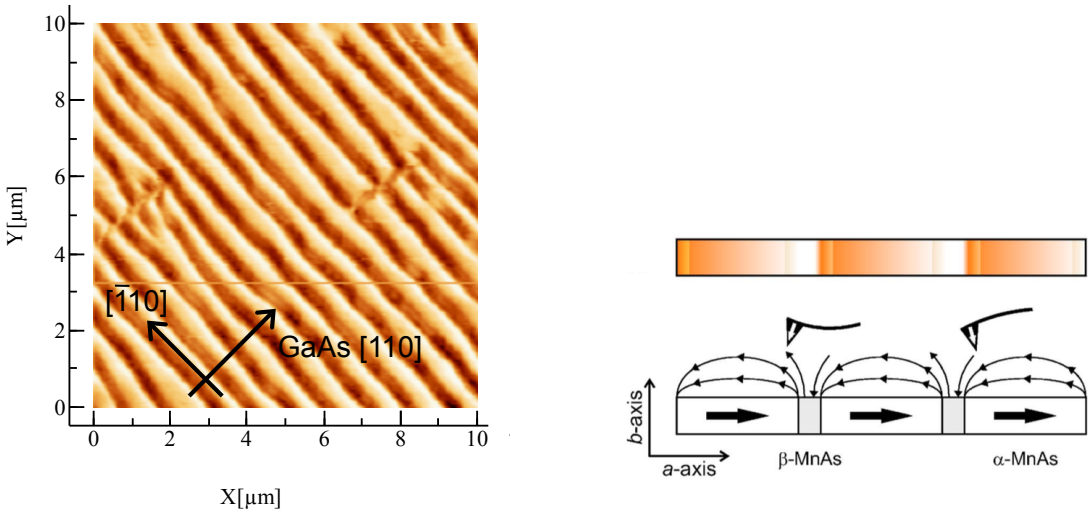

Figure 5.13 – Left: Sketch of the MFM contrast formation (below) and the resulting MFM contrast (above) (from Ref. 283). Right: Typical image of the MFM MnAs thin film samples (150 nm thickness). The regular spacing due to the GaAs substrate constrains is visible in all images.

Thin films properties

The possibility of epitaxial growth on standard semiconductors such as GaAs makes MnAs thin films interesting also for spintronic research [284] and magneto-elastic applications [272, 273]. Compared to bulk, MnAs thin films epitaxially grown on a substrate have a phase transition disturbed by the strain of the substrate leading to the $\alpha - \beta$ phases coexistence, absent in the case of bulk material.

When a gallium-arsenide GaAs(001) is used as substrate, the coexistence of $\alpha - \beta$ phases (290–320 K) is accompanied by a self-organisation with longitudinal alternating regions (Figs. 5.12 and 5.13). The regular patter is the result of the effect of the substrate strain on the internal elastic energy of the thin film [285, 286]. The period λ of the self-organization depends linearly on the MnAs film thickness t with the relationship [275, 286, 287] $\lambda \approx 4.8\ t$.

The alternating regions of α-phase (ferromagnetic) and β-phase (paramagnetic) can be easily visualised in magnetic force microscopy as a subsequence of ordered stripes due to the alternation of the out-of-plane magnetic field in proximity of the β phase regions as shown in Fig. 5.13.

The richness of MnAs thin films properties results in a complex dependency of the magneto-structural properties with the external temperature, applied magnetic field and constraints. Thanks to this richness and application interests, many studies have been dedicated to the characterisation of epitaxial MnAs films [275, 283–304].

About the magnetocaloric effect of thin films with respect to bulk, the phase coexistence reduces the maximum value of $\Delta S_m(T)$ without, however, reducing the refrigeration power (proportional to the integral of $\Delta S_m(T)$ over a temperature range). Modifications of S_m behaviour due to the epitaxy constraints are linked to modifications of the magnetisation visible in Fig. 5.14. Indeed the ΔS_m per mole of material portion passing from one phase to another is still very high [271], which characterises the giant MCE materials.

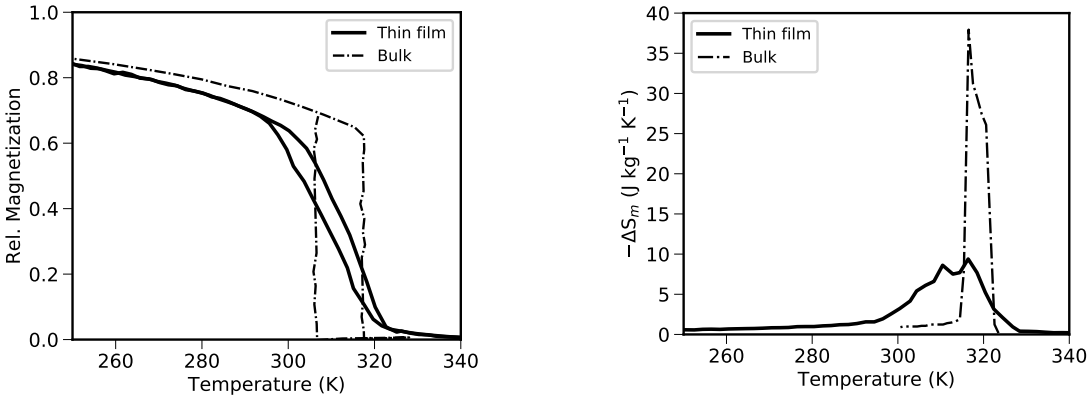

Figure 5.14 – Relative magnetisation (left) and magnetic entropy variation (right) of bulk (dot-dash line) and thin film (solid line) MnAs as a function of the temperature. The magnetisation measurement corresponds to an applied magnetic field of $H = 1$ T. The magnetic entropy variation is relative to the variation of the magnetic field between 0 and 2 T. Bulk material data are extracted from Refs. 224, 281. Thin film data are from the sample with a thickness of 150 nm discussed in the text.

5.4 Experimental methods

5.4.1 Film production

MnAs epilayers investigated here are grown by molecular beam epitaxy (MBE) on GaAs(001) substrate. The deposed MnAs is oriented with the α-MnAs[0001] and β-MnAs[001] axis parallel to GaAs[$\bar{1}$10]. The different samples, with a surface of a few mm^2, are obtained from the same wafer, At the end of the growth process, 150 ± 10 nm thick samples are capped in situ with an amorphous As layer in order to prevent the MnAs oxidation. More details on the growth process can be found in Ref. 275.

5.4.2 Ion irradiation

The ion irradiation is performed at the SIMPA facility [A33] (French acronym for highly charged ion source of Paris) that includes an electron-cyclotron resonance ion source coupled to a dedicated ultra-high vacuum beam line. Samples are irradiated in different conditions varying the angle of incidence, the ion energy and ion species. The pioneering studies [A14, A22] have been performed with a beam of Ne^{9+} ions with a kinetic energy of 90 keV (4.5 keV/u). The incidence angle between the ion beam and the sample surface is set at 60°, for having an average penetration depth of the ions corresponding to the half-thickness of the MnAs film [187] leading to a consequent maximisation effect of the ion irradiation [213].

Irradiations with different ions are done keeping the average penetration similar, except in specific cases. Only a negligible fraction of ions is deposited in the GaAs substrate excluding the possibility of MnAs-GaAs mixing [215].

During the irradiation, the ion–sample collision zone is continuously monitored with a visible-light sensitive CCD camera coupled to an array of micro-Faraday cups [305, 306] to obtain the spatial ion current intensity. A standard Faraday cup monitors the total ion current. From these measurements, the fluence is deduced with an accuracy down to 5%.

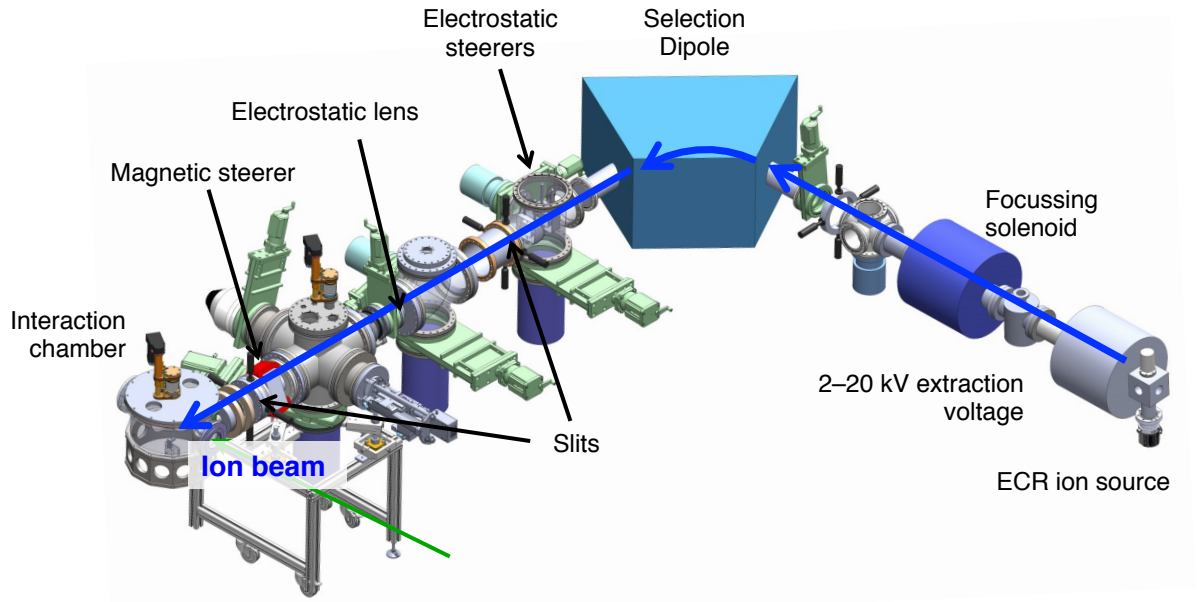

Figure 5.15 – Scheme of the SIMPA (Source d'Ions Multichargés de Paris, i.e. highly charged ion source of Paris) platform.

Different ion beam bombardment durations with ~ 0.5 μA beam intensities, from 5 to several thousands of seconds, and corresponding to a fluence between $\Phi = 10^{12}$ and 10^{15} ions/cm^2, are applied on different samples. The potential energy E_p of the ions, which depends on their charge state and ion type, contributes marginally ($E_p \lesssim 5$ keV) making the dependency with the ion charge insignificant in the bombardment (see also Appendix C). More details about the irradiation process can be found in Ref. A22.

5.4.3 Characterisation

Magnetic properties of the samples and their dependency with the ion fluence are studied using different techniques, namely: magnetic force microscopy (MFM) and sample magnetometry (with a vibrating sample magnetometer, VSM, and a superconducting quantum interference device, SQUID magnetometer). Due to their thermal reliability, SQUID magnetometer is used mainly to study the dependency of the magnetisation with the temperature ($M(T)$ measurements). Complementarily, VSM magnetometer is employed for magnetisation dependency with the applied magnetic field ($M(H)$ measurements), thank to its ability to change H rapidly.

Quantitative information on the entropy variation $\Delta S(T, \Delta H)$ are obtained by a series of $M(T)$ measurements at different values of H following a procedure similar to that one described in Ref. 271: i) each sample is initially brought to 350 K with $H = 0$; ii) a magnetic field H (with a starting value equal to 2 T) is applied; iii) the sample is cooled down to 150 K; iv) the magnetic moment is recorded continuously during the temperature variation from 150 to 350 K with a sweep rate of +2 K/min; v) at $T = 350$ K, the magnetic field is decreased with a step of 0.2 T; and then the procedure from ii) to

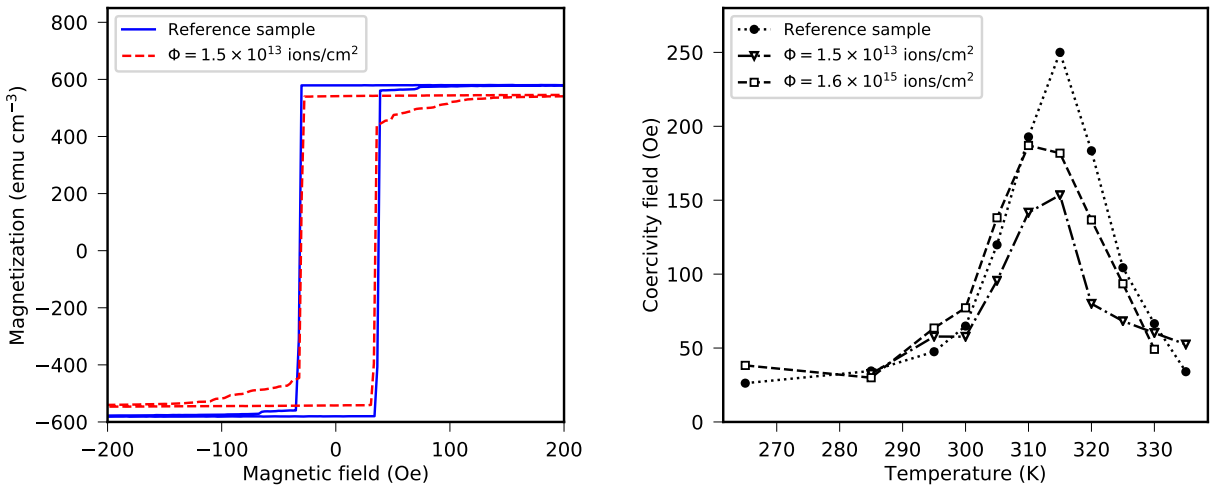

Figure 5.16 – Left: Magnetic cycle of reference and irradiated samples at $T = 285$ K. At this temperature, only the ferromagnetic α phase is present. Right: Coercivity field values at different temperatures for the reference sample and two samples irradiated with different fluences. Figures adapted from Refs. A5 and C4.

v) is repeated until $H = 0$. The entropy variation is then obtained by the integral

$$\Delta S_m = \int_{H_i}^{H_f} \left(\mu_0 \frac{\partial S_m}{\partial H}\right)_T dH = \int_{H_i}^{H_f} \frac{\mu_0}{\rho} \left(\frac{\partial M}{\partial T}\right)_H dH \approx \sum_j^N \frac{\mu_0}{\rho} \left(\frac{\partial M}{\partial T}\right)_{H_j}^{\text{num}} \delta H, \tag{5.8}$$

where ρ is the specific density of the material. Here the Maxwell's relations of thermodynamics are used[2] $\partial S_m/\partial H = \partial M/\partial T$ and the derivative $\partial M/\partial T$ is obtained by numerical evaluation. We remember that S is given per unit of mass. The use of Maxwell's relations is not completely justified for first-order transition materials because of the discontinuity of $\partial M/\partial T$. However, by varying continuously the temperature instead of the magnetic during the measurement, artefact effects like the so-called *colossal magnetocaloric effect* [307,308] are avoided via the material history erase at high temperature for each $M(T)$ cycle.

Additional characterisation with X-ray diffraction are performed and reported partially in Ref. A14; they are not discussed here.

5.5 Results and discussions of the ion irradiation effects

5.5.1 Some first considerations

Because of the relative fluence used here, lower than 10^{15} ions/cm^2, and the relative robustness of MnAs, a metallic compound, the impacts of the ions do not alter significantly the properties of the thin films. For a first comparison between pristine and irradiated samples, a sample irradiated with a

[2]Maxwell's relations of thermodynamics derive from the assumption of the continuity of the Gibbs free energy and its derivatives. More specifically one has $S(T,H) = \left(\frac{\partial G}{\partial T}\right)_H$ and $M(T,H) = \left(\frac{\partial G}{\partial H}\right)_T$. Maxwell's relations derive from the assumption that $\frac{\partial^2 G}{\partial T \partial H} = \frac{\partial^2 G}{\partial H \partial T}$.

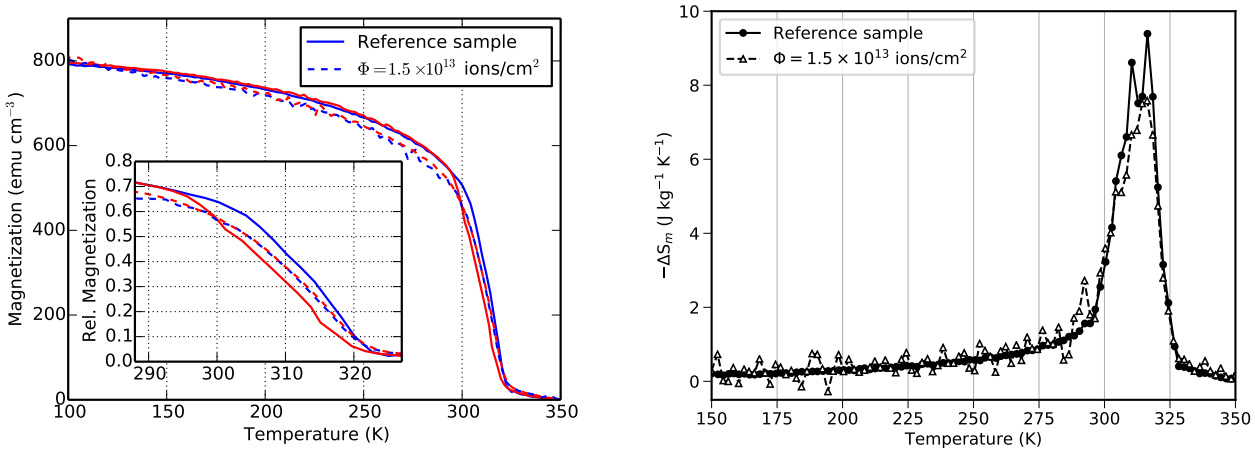

Figure 5.17 – Left: Magnetization of the reference and irradiated ($\Phi = 1.5 \times 10^{13}$ ions/cm^2) samples as function of the temperature with an applied magnetic field of 1 T. Right: ΔS_m behaviour with the temperature. Figures from Refs. A5.

fluence of $\Phi = 1.5 \times 10^{13}$ ions/cm^2 is considered. As visible in Fig. 5.16 (left), the magnetic cycle of the ferromagnetic phase at low temperature (here T=285 K) is only slightly altered. The coercivity is practically the same at low temperature also for higher fluences ($\Phi = 1.6 \times 10^{15}$ ions/cm^2, Fig. 5.16 right). It does not vary neither significantly for higher temperatures during the phase transition, where the characteristic coercivity peak [309, 310] is well visible.

In Fig. 5.16 (left) it is worthwhile to mention that the irradiation-induced defects produce some additional pinning on the mobility of the magnetic domains, leading to the presence of "wings" on the magnetic cycle. An additional feature of the irradiated sample is the slightly lower magnetisation with respect to the reference sample. This magnetisation reduction is present not only at $T = 285$ K as in Fig. 5.16 but also for an extended region of temperatures as visible in Fig. 5.17 (left). However at lower temperatures ($T = 100$ K), the magnetisation of the irradiated samples equal to the value of the pristine.

The most astonishing and interesting modification due to the ion bombardment visible in Fig. 5.17 (left) is the suppression of the thermal hysteresis. Even if the transition temperature is practically unchanged as well as the associated variation of S_m (Fig. 5.17 right), the hysteresis is cancelled.

In view of the above observations, questions are rised: what is the nature of defects responsible for the hysteresis suppression? Is it due to the implanted ions or to the defects caused by their collision with the target atoms? To answer to these and other questions, a series of systematics studies is carried out by varying the ion collision conditions (energy, type of ions, etc.), the nature of the irradiated samples and using additional characterisation techniques.

5.5.2 Dependency with the implanted ion and collisions numbers

A first simple systematic investigation is obtained by varying the number of ions that collide with the samples, keeping the other quantity constant. As visible in Fig. 5.18 relative to Ne ion irradiations, the hysteresis is quickly suppressed already for a fluence of 10^{13} ions/cm^2. For high fluences, the shape of the $M(T)$ curve starts to change significantly with a significant reduction of the magnetisation (even at low temperature) for a fluence of $\Phi = 9 \times 10^{14}$ ions/cm^2. This reduction is related to the appearance

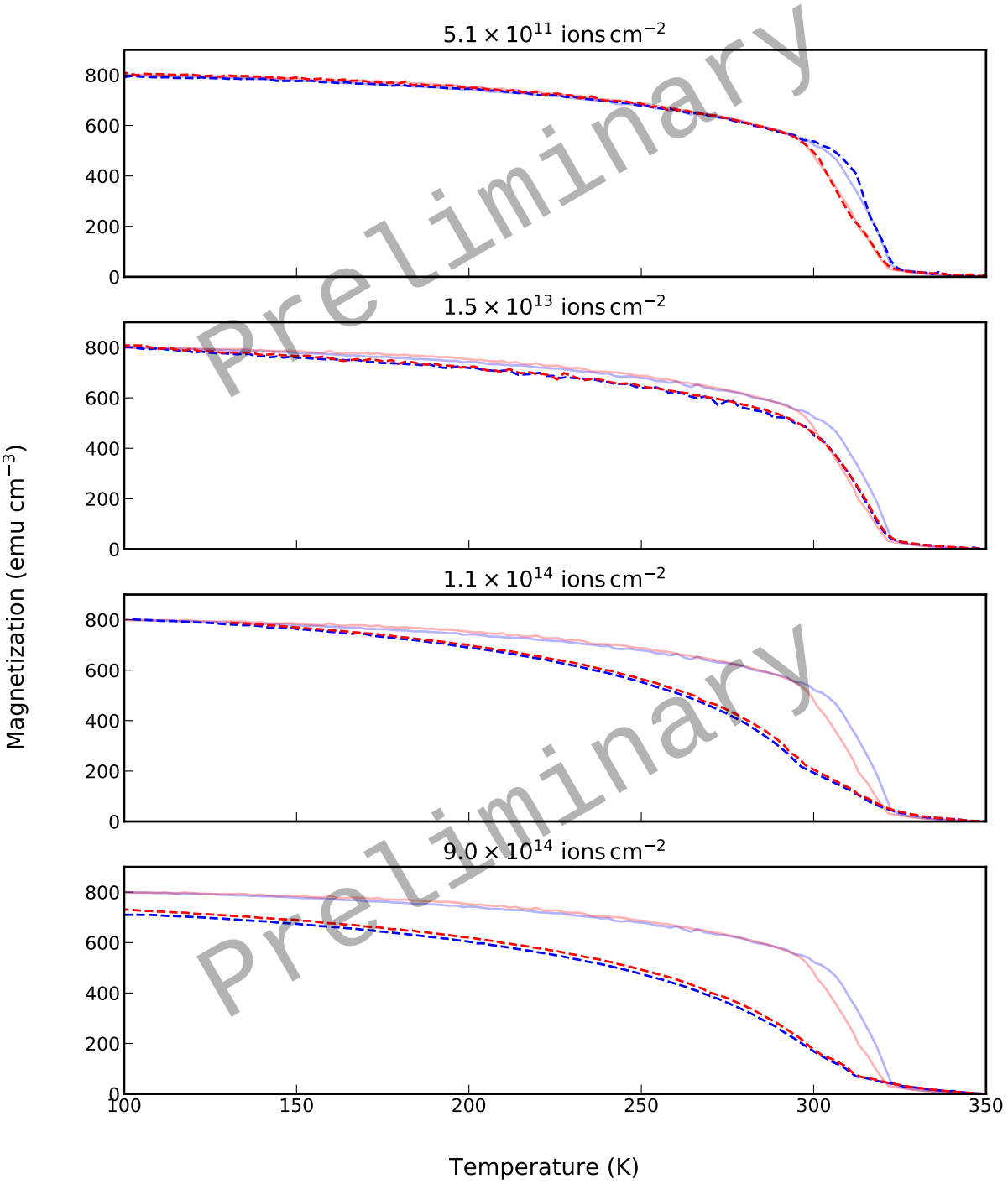

Figure 5.18 – Magnetisation as a function of temperature for the reference (solid lines) and for the irradiated samples (dashed lines) for different fluences with Ne ions. Data obtained by a temperature increase (from colder temperatures) and decrease (from hotter temperatures) are presented in blue and red, respectively (preliminary results).

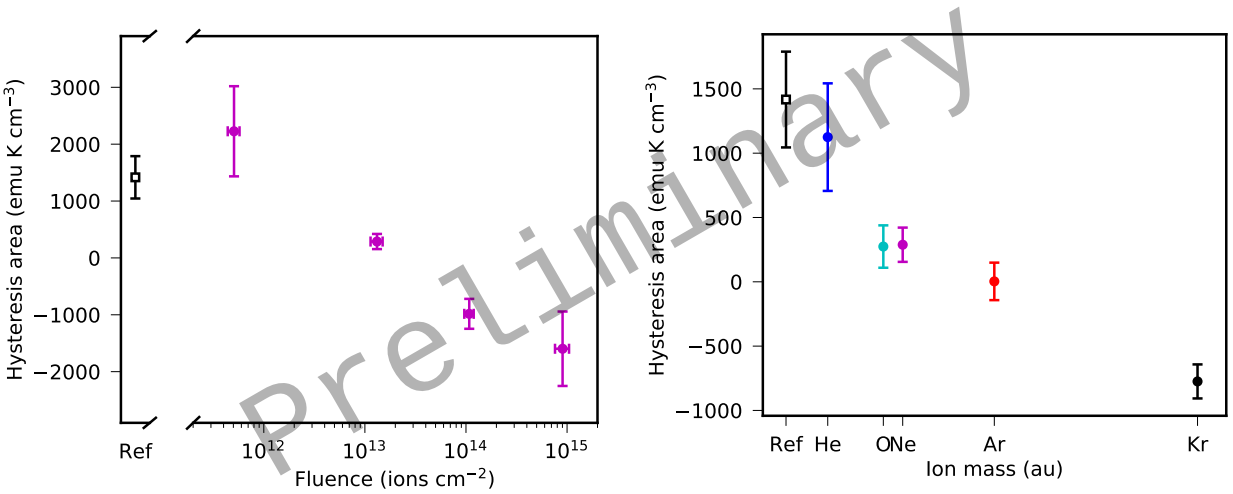

Figure 5.19 – Left: Thermal hysteresis area dependency with the fluence for samples irradiated with neon ions with the same kinetic energy. Right: Thermal hysteresis area dependency with the ion mass keeping constant the fluence ($\Phi \sim 10^{13}$ ions/cm^2) and the average penetration depth of the ions in the sample. Thermal hysteresis area of the non-irradiated sample ('Ref') is also reported (preliminary results).

of a metastable phase in the sample (as in Fig. 5.4 right) and not by an amorphisation of the samples (as deduced by X-ray diffraction data not presented here bus shown in App. **??** [A14]) while an amorphisation has been observed in the past in other ferromagnetic thin films [207, 209, 211, 215, 216] irradiated with high values of fluence.

To quantify the hysteresis reduction, the hysteresis area A_{hyst} is measured for the different fluences. The corresponding values are plotted in Fig. 5.19 (left) as a function of the ion fluence. A logarithmical dependency is visible. It can be also noted that the hysteresis assumes negative values. This is related to the nature of the measured signal (magnetisation in this case) – see discussion in Sec. 5.5.4.

The influence of the ion mass is investigated by irradiating the different samples with the same fluence ($\sim 10^{13}$ ions/cm^2) of different species of ion and where the kinetic energy of the ions is adjusted to the penetration depth constant (equal to half the sample thickness, $\sim 150/2$ nm). As for the fluence, a linear dependency of the hysteresis area with the ion mass is observed (Fig. 5.19 right). This is a first indication that the hysteresis reduction is not proportional to the density of the implanted ions. Another point is that the A_{hyst} reduction seems to be related to the number of collisions produced by each ion. At this energy regime in fact, an increase of the ion mass can drastically increase the total number of collision due to the larger momenta transfer to target ions, which can produce additional collisional cascades. In the experimental conditions discussed here (same average penetration depth) He ions produces in average 84 collisions in the MnAs film, 800 for O, 1000 for Ne, 2700 for Ar and 5000 for Kr ions.

A more complete and general picture is obtained by plotting the different hysteresis area A_{hyst} values as a function of the implanted ion density and of the total density of collisions induced by the ion irradiation, independently on the ion nature and irradiation conditions. The fraction of ions that stop in the samples, and then the average value of the implanted ion density, is calculated by SRIM

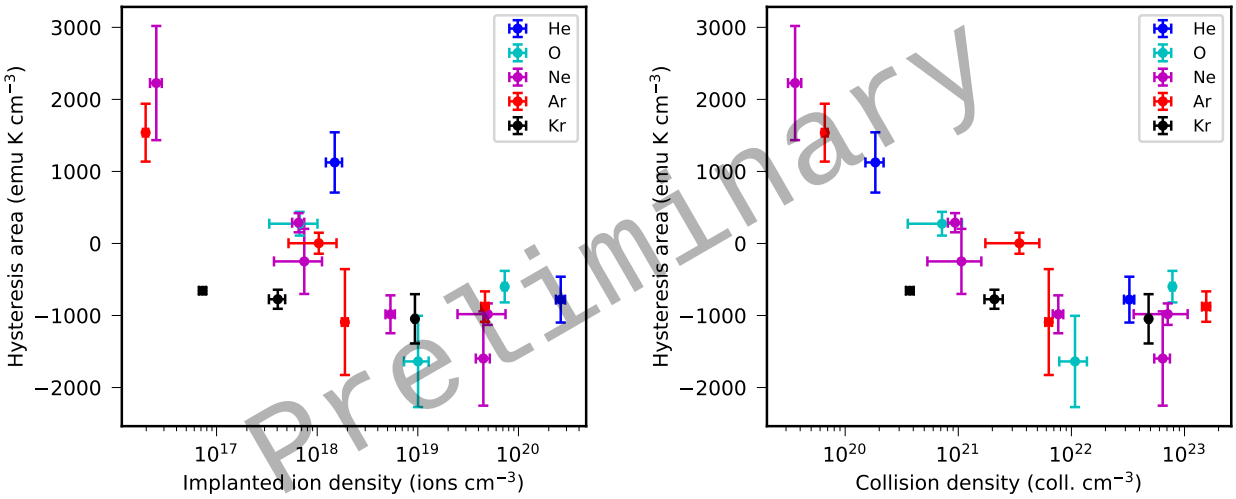

Figure 5.20 – Thermal hysteresis area dependency with the average density of implanted ions (left) and with the collision density (right). The data correspond to irradiation conditions with different type of ions and different fluences keeping constant the average penetration depth of the ions in the sample (preliminary results).

(see Sec. 5.2.2). In the same way, the density of elastic nuclear collisions is deduced by SRIM outputs. As discussed already in Sec. 5.2.2, the number of binary collisions does not correspond to the number of induced defects because of the threshold energy required to move a target atom from its place and of to the defect auto-healing at a finite temperature. However one expects, and assumed here, that these two quantities are proportional.

When A_{hyst} is plotted as a function of the density of implanted ions, Fig. 5.20 left, no particular tendency can be deduced. On the contrary, when the hysteresis area values are plotted as a function of the collision density (i.e. irradiation-induced defects), a clear logarithmic dependency is present, with a saturation behaviour for densities higher than $\sim 10^{22}$ collisions per cm^3. This is not completely true for the irradiations with krypton that seems deviate from the main stream for low fluences.

The dependency with the irradiation-induced density indicates without too many ambiguities that the hysteresis suppression is related to the presence of vacancies and interstitial atom defects produced by the ion bombardment. The details of how this process acts are still unclear and their characterisation requires additional complementary measurements as magnetic force imaging presented in the following section.

5.5.3 Local magnetization studies and related measurements

To investigate the effect of irradiation-induced defects at the micrometric scale, images of the local magnetisation at different temperatures are obtained by a magnetic force microscope (MFM).

In Sec. 5.3.4 it has been shown that when α and β phases of MnAs coexist they auto-organise in stripes perpendicular to the easy magnetisation axis of the ferromagnetic phase. If the sample is prepared from cooling in presence of an external magnetic field, MFM images as in Fig. 5.13 (left) are obtained. They correspond to the alternation of paramagnetic and ferromagnetic regions with the same magnetisation orientation. When the sample cooling is done with $H = 0$, magnetic macro-

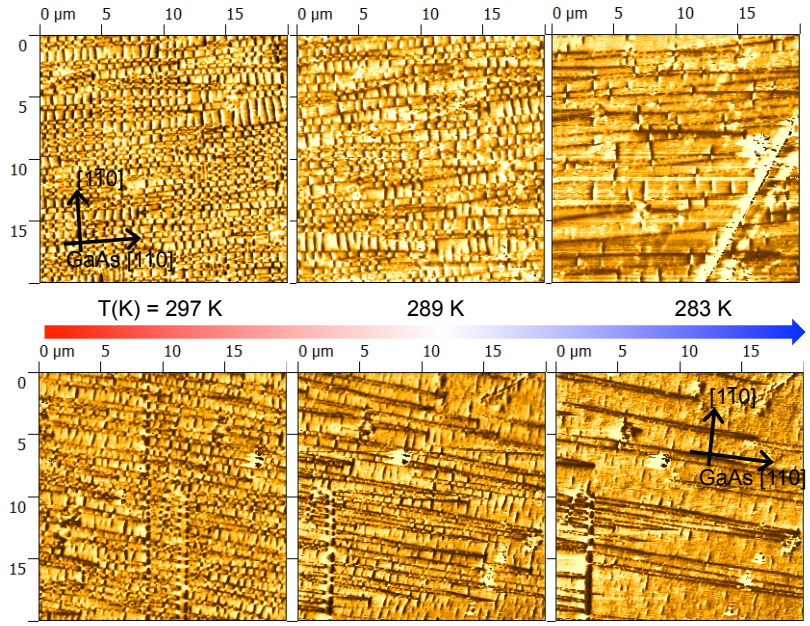

Figure 5.21 – MFM images at different temperatures of the reference sample (up) and a sample irradiated with a fluence of 1.5×10^{13} ions/cm^2 of Ne ions (down). The diagonal line in the right of the reference sample images is due to a topological defect. In contrast, the diagonal and vertical lines in the images of the irradiated sample have no correspondence with the topography images and are purely due to magnetic features [A5].

domains with different orientation are present (along the easy magnetisation axis perpendicular to the stripes, parallel to the GaAs[110] axis) and images like the upper row of Fig. 5.21 are obtained. Here, the horizontal lines correspond to borders of macro-domains with different orientations.

The ion irradiation introduces irregularities in the stripe pattern (but not in their periodicity [A14]) as observed in images in the lower row of Fig. 5.21. For both pristine and irradiated samples, at low temperature, β phase regions almost disappear and the stripe structure with it.

Among the different features of these MFM images, discussed extensively in Ref. A5, one can notice in Fig. 5.21 that vertical lines, more and more visible at low temperature, are present in the irradiated samples and not in the reference. These structures are produced by a sudden variation of the MFM phase. In fact it can be noticed that the phase variation has a sign changing (from dark-to-light to light-to-dark) when a structure crosses different macro-magnetic domains. This indicates the presence of a paramagnetic region (see also Fig. 5.13 right). This effect is even more evident when the sample is cooled from a high temperature with an external field of about 5000 Oe before imaging it with the MFM. As shown in Fig. 5.22, where the irradiated sample at the temperature of 298 K is prepared in this way, a β-phase diagonal region is visible in the MFM image together with a corresponding depression (of about 5 nm) in the topography image (down) expected for the β phase (smaller volume cell than α phase). When the temperature is increased, this β-phase region is less and less contrasted with respect to the surrounding area in both MFM and topography images due to the global transition to the β phase.

Both series of images show the presence of β-phase regions that anomaly persist at a temperature lower than the characteristic transition temperature ($T_c = 313$ K). The link between the presence of

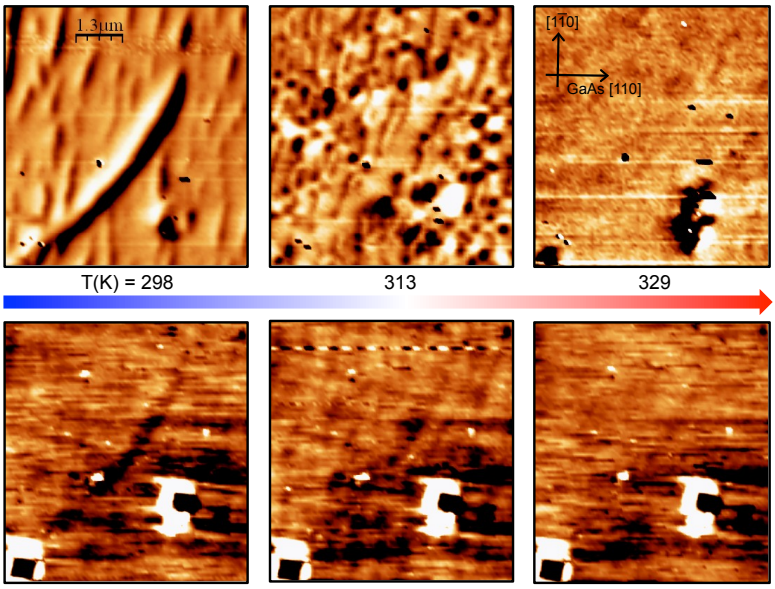

Figure 5.22 – MFM (upper row) and AFM (bottom row) images at different temperatures for a sample irradiated with Ne ions with a fluence of 1.5×10^{13} ions/cm^2 and cooled in presence of a persisting magnetic field ($H \sim 5000$ Oe) [A5].

these regions and the suppression of the hysteresis is discussed in the next section.

5.5.4 The hysteresis suppression mechanism revealed

Seeding from the irradiation-induced defects

The presence of the β phase at this low temperature may be due to local constraints induced by the ion irradiation. As discussed in Sec. 5.2.2, past experimental and theoretical studies on ion–matter interaction show that, at this ion energy regime, collision cascades can lead to the formations of spatially localised regions rich in interstitial atoms or vacancies [200, 202–204]. Interstitial-rich regions could cause an increase of the local high internal pressure favouring the presence of the β phase that is characterised by a volume 2% larger than the α phase. In connection to the persistence of small β-phase regions, the sample magnetisation is expected to be reduced with respect to the reference sample, which is the case, as visible in the magnetometry measurements in Figs. 5.16, 5.17 and 5.18. Except for very irradiated samples, at very low temperature ($T = 100$ K) not monitored with the MFM, irradiated samples have practically the same saturation magnetisation than pristine samples (Fig. 5.18) suggesting that these "frozen" β-phase regions are thus suppressed.

Similarly in proximity to vacancies-rich regions, a local low internal pressure is expected that can favour the presence of the α phase. The presence of surviving α-phase regions at high temperatures seems plausible, but difficult to observe in MFM images due to the complex magnetic images caused by the transition between different types of magnetic domains (type-I and type-II) and the reduced size of α-phase regions. Another possible sign of the presence of persisting α-phase regions could be a magnetisation at high temperature, expected to be higher than in the reference sample. This is actually the case as visible in $M(H)$ curves at $T = 330$ K shown in Fig. 5.23. The presence of these out-of-equilibrium regions is deduced to be at the origin of the hysteresis suppression.

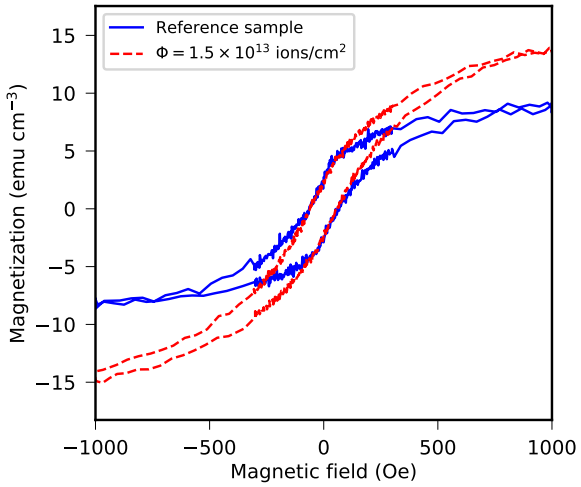

Figure 5.23 – Magnetic cycle of reference and irradiated samples at the $T = 330$ K. At this temperature, the paramagnetic β phase should be dominant [A5].

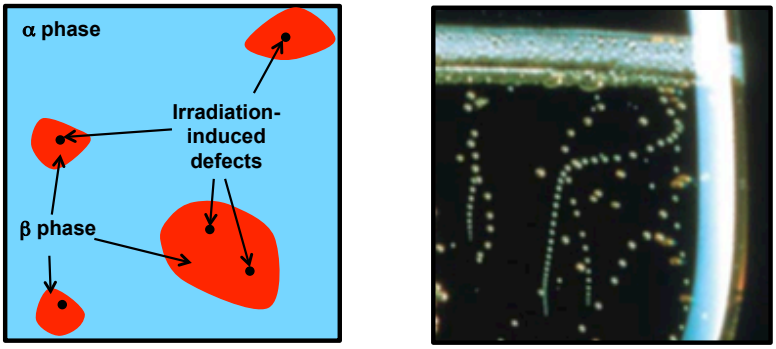

Figure 5.24 – Left: Analog artistic view of the nucleation of MnAs β phase in α phase in proximity of the irradiation-induced defects. Right: Chains of CO_2 vapor bubbles in proximity of glass defects [311].

Generally, the suppression of hysteresis phenomena in first-order transitions, and especially in structural phase transitions like liquid–solid or liquid–vapour, is related to the presence of defects in the system.

In the case of a glass of champagne or beer, the recipient surface defects or small grains of dust facilitate the creation of CO_2 vapour bubbles from the supersaturated molecules dissolved in the liquid [311,312] with the creation of typical chains of small bubbles arising from a precise point in the glass (Fig. 5.24 right). In the same way, the silver iodine smoke particles are used for the nucleation of ice or water drops formation in supercooled clouds (cloud seeding) [313]. The local small radii of surface defects or dust grains lower the structure energy barrier facilitating the nucleation.

Similarly, interstitial-rich or vacancy-reach regions induced by the ion impact in MnAs could favour the presence of local regions of α and β, which are persisting at a temperature respectively higher and lower than the transition temperature. These regions act then as seeds during the transition for the nucleation of one phase into the other as in Fig. 5.24 (left), with a consequent suppression of the

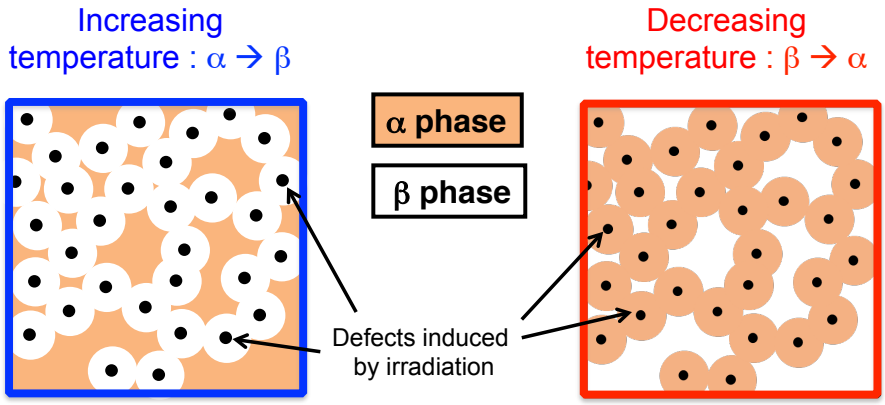

Figure 5.25 – Fractionated or clustered ferromagnetic regions produced by nucleation of the different phases (paramagnetic β and ferromagnetic α) in proximity of irradiation-induced defects. When both phases are present, the sample average magnetisation is expected to be lower when the ferromagnetic regions are fractionated (left) with respect when they form connected clusters (right).

hysteresis.

Recent studies on nanoindentation in NiMnGa Heusler alloy films [314] corroborate this hypothesis showing that local constrains can favour the nucleation of one phase into the other for the characteristic first-order phase transition.

The new seeds density is expected to be proportional to the irradiation-induced defects (and then to the collision number) and to the reduction of the hysteresis area. Once the hysteresis is completely eliminated, additional irradiation-induced defects does not contribute significantly. This is in agreement with the saturation effect on the hysteresis area values visible in Fig. 5.20 This saturation value is actually negative and not close to zero. The reason of this behaviour is discussed in the next section.

On the inverted hysteresis

From the observations discussed previously, the inversion of the hysteresis can now be easily interpreted. It is not related to a violation of causality but to the type of measurement employed to characterise MnAs thin films. To determine the presence or not of α phase, samples magnetisation is measured, as in Figs. 5.17 and 5.18. Here the fraction of α phase with respect to the β phase is not directly measured, but simply the resulting magnetic response when an external magnetic field is applied. But the samples cannot be considered homogeneous and their magnetisation depends on the nucleation and growing of the different phases and their disposition, and not only on T and H values.

Let consider as an example the magnetisation of an irradiated sample with 50% of α phase and 50% of β phase. In a first case, this ratio is reached by warming up the sample. This means that β-phase regions nucleate around irradiation-induced defects creating fractioned regions of α phase (Fig. 5.25 left). In a second case, the same ratio is reached by cooling down the sample. Here α-phase regions nucleate around irradiation-induced defects creating clusters of ferromagnetic regions (Fig. 5.25 right). In this last case, when a magnetic field is applied, the magnetisation is higher than in the first case because of the enhancement field effect due to the close presence of other ferromagnetic regions (that produces a different demagnetisation field). Considering the magnetisation cycles like in Figs. 5.17 and 5.18, this results on an apparent inversion of the hysteresis which is nothing else

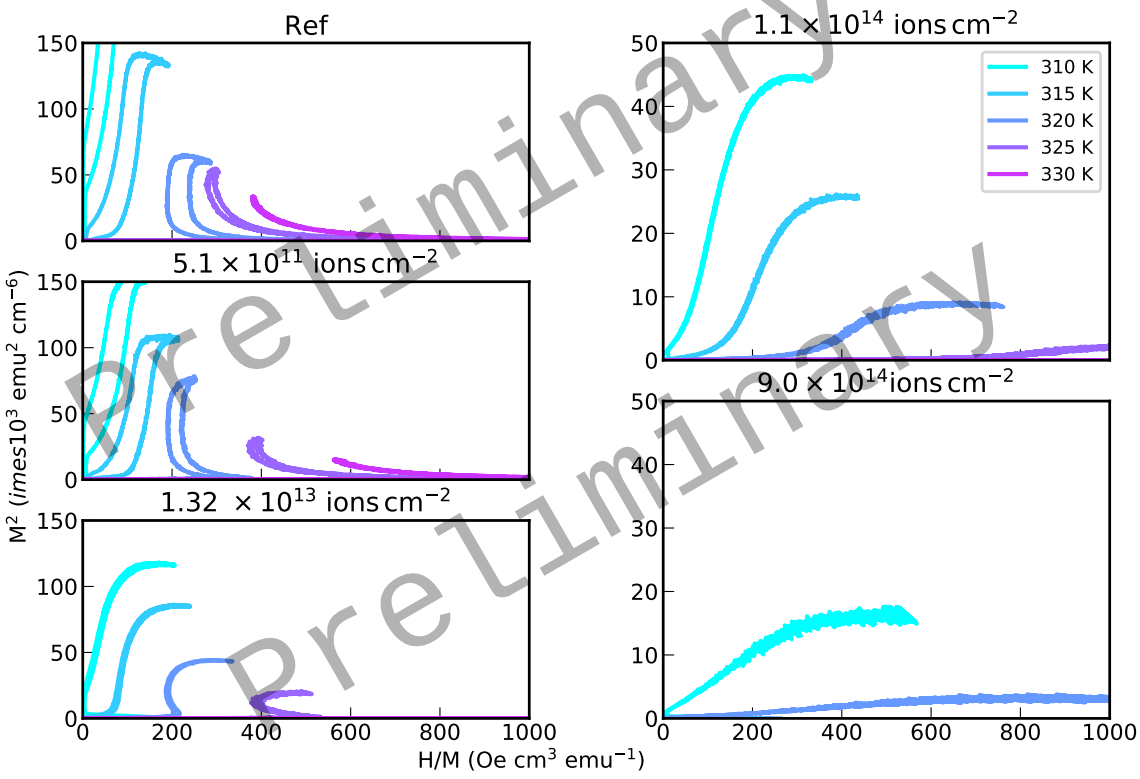

Figure 5.26 – Arrott's plots of the reference and Ne ion irradiated samples obtained from $M(H)$ measurement by the VSM magnetometer (preliminary results). From the dependency between M^2 and H/M, the sign of the term b of the Gibbs free energy can be determined (Eq. (5.5)) and the order of the transition is then established ($b < 0 \rightarrow$ first-order transition).

that the asymmetric magnetic response of the paramagnetic and ferromagnetic regions caused by their different spatial repartition during the cooling and heating processes of the sample.

Similar cases of inverted hysteresis are in fact observed in relation of resistivity of materials exhibiting an insulator–metal transition [315–319], where the presence or not of connected conducting regions can change significantly the conductivity, and in catalysis processes [320,321]. The presence of the hysteresis inversion actually confirms the creation by ion irradiation of new defects that facilitate the nucleation of one phase into the other.

Arrott's plots and transition order

A practical way to establish if one has a first-order or second-order transition consists in determining the sign of the factor b in Eq. (5.5) by plotting M^2 as a function of H/M. The equilibrium condition of Eq. (5.6) imposes that $H/M \propto bM^2 + \mathcal{O}(M^4)$. This means that a negative slope in $(H/M, M^2)$ plot obtained from $M(H)$ measurements, called Arrott's plot [322], corresponds to a negative values of the term b in Eq. (5.5) and then to a presence of a first-order transition. As visible in Fig. 5.26, this is the case for the reference and samples irradiated with moderated fluences. For $\phi = 10^{13}$ ions/cm^2 the transition is clearly of the first type but the characteristic hysteresis is completely gone due to the

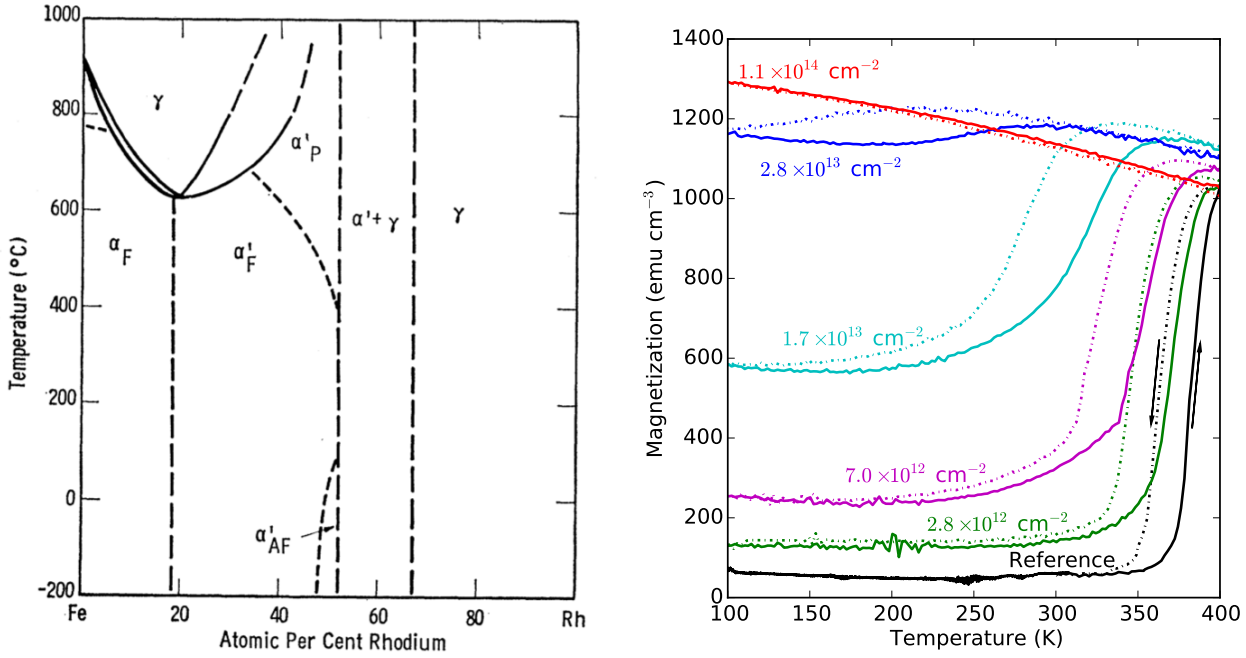

Figure 5.27 – Left: Composition phase diagram of iron-rhodium alloy from Ref. 323. Right: FeRh thin film magnetization as a function of temperature for irradiated and reference samples. Data obtained, at 1 T, by a temperature increase (solid lines) and decrease (dash-dotted lines) [A1] (preliminary results).

seeding effect of the irradiation-induced defects.

It is not the case for fluences $\gtrsim 10^{14}$ ions/cm^2 where the magnetisation behaviour is strongly disturbed. For these cases, no first-order transition signature is present ($b < 0$), there neither is a clear trace of a second-order transition for which, accordingly to Eq. (5.6), for sufficiently large M, a liner relation between M^2 and H/M is expected.

The observation of the hysteresis suppression together with the negative slope of first-order transitions in Arrot's plots has never been saw in other giant magnetocaloric samples, where doping treatments or external pressures are applied. This is a clear indication of the unicity of the properties changes induced by the irradiation with slow ions.

5.6 Other samples and general discussion

From the discussion on the results with MnAs thin films, it emerges that the ion irradiations create new local defects that make easy the nucleation of one phase with respect to the other one during the transition. This facilitated nucleation seems to be related to interstitial- or vacancy-reach regions that, due to the free energy dependency with the pressure, favour the local presence of one phase or the other. This is related to the characteristics of the first-order transition of MnAs, which is a magneto-structural transition.

The MnAs transition is only an example of first-order transition associated to the giant magnetocaloric effect. The metallic alloy iron-rhodium (FeRh) present a antiferromagnetic–ferromagnetic transition with a large entropy change, a large hysteresis, a significant change of volume but without structural changes [323–326]. FeMnPSi, a compound with the same structure than Fe_2P, present

also a giant magnetocaloric effect associated to first-order magnetic transitions associated to itinerant electron metamagnetism [327, 328] but without changes of structure and volume.

To proof or disproof the connection between the hysteresis reduction mechanism and the structural change, FeRh thin films are irradiated with slow neon ions. As visible in Fig. 5.27 (right), three features have to be noted: (i) the transition temperature is shifted to lower values when increasing fluence is applied, (ii) the antiferromagnetic phase is gradually destroyed resulting with a non-zero magnetisation at low temperature ($T = 100$ K) and the (iii) the thermal hysteresis increases.

The destruction of the antiferromagnetic phase is related to the nature of FeRh. FeRh is a metallic alloy that, compared to the more robust metallic compounds like MnAs, is very sensitive to the local composition as visible in Fig. 5.27 (left).

Indications of a transition temperature shift induced by ion irradiation have been partially seen in previous works with fast ions [218, 329]. With the measurement presented here, it has been clearly observed and correlated to the ion fluence and other thin film characteristics (one publication is in preparation [A1]). The evidence of the relation between the ion fluence and the T_c shift opens new perspectives for magnetic refrigeration. As pointed out already in 1952 by Chilowsky [235, 236], a gradient of Curie temperature of the cooling magnetocaloric material can considerably improves the performances of magnetic refrigerators. For this reason, these studies gave rise to a patent [D1] to produce an unique material with different values of transition temperature located at different spatial positions by smartly manipulating the irradiation conditions.

The increase of the thermal hysteresis shown in Fig. 5.27 (right) confirms the hypothesis presented here about the relation between thermal hysteresis suppression and the structural change of the transition associated to the giant magnetocaloric effect. This relation is however under study and additional investigations with other materials and irradiation conditions are at present considered. In particular, preliminary experiments with FeMnPSi show indications of reduction of the associated thermal hysteresis in a system where no structural and neither volume changes occur during the transition.

Appendix A

Some recall on maximum likelihood and least-squares methods

A.1 The likelihood function

A large portion of data analysis methods is based on the maximum likelihood method or other techniques based on it (ex. least-squares method) [36, 357]. In this method, for a given set of data $\{x_i, y_i, \sigma_i\}$, where σ_i is the uncertainty associated to y_i and a selected function $F(x, \boldsymbol{a})$ used to describe the data, the best choice of the parameter values $\boldsymbol{a}$ is assumed to be the values that maximise the likelihood function.

The likelihood function consist in the product of the single probability p_i for having a certain value y_i at the coordinate x_i with respect to the model prediction $f_i = F(x_i, \boldsymbol{a})$. Per each channel, $p_i = p(x_i, y_i|\mathcal{M}, \boldsymbol{a})$ where we indicates with the symbol "|" the conditional probability for having the data x_i, y_i for a given choice of model $\mathcal{M}$ associated to the function F, and parameter values $\boldsymbol{a}$. Considering the entire set of N observation $\{x_i, y_i, \sigma_i\}$, the total probability P is given by the product of the single probabilities:

$$P(\{x_i, y_i, \sigma_i\}|\mathcal{M}, \boldsymbol{a}) = \prod_{i=1}^{N} p(x_i, y_i, \sigma_i|\mathcal{M}, \boldsymbol{a}). \tag{A.1}$$

which is by definition the *likelihood function* $L(\boldsymbol{a})$.

In the particular case we have a normal distribution for the y_i single values, we have

$$p_i = \frac{1}{\sigma_i\sqrt{2\pi}} e^{-\frac{(y_i - f_i)^2}{2\sigma_i^2}} \tag{A.2}$$

and then

$$L(\boldsymbol{a}) \propto \exp\left(-\sum_{i=1}^{N} \frac{[y_i - F(x, \boldsymbol{a})]^2}{2\sigma_i^2}\right). \tag{A.3}$$

One could then expect that the best choice of parameters $\boldsymbol{a}^{\text{best}}$, should maximise the probability $P(\{x_i, y_i, \sigma_i\}|\mathcal{M}, \boldsymbol{a})$, i.e. the likelihood function L. The best estimation of parameters $\boldsymbol{a}$ is reduced to the search of the maximum of the function $L(\boldsymbol{a})$. In other words, *the maximum likelihood method*

is based on the assumption[1] that the likelihood function gives us a good estimator for calculating the parameter probability distributions and

$$P(\boldsymbol{a}|\{x_i, y_i, \sigma_i\}, \mathcal{M}) \equiv P(\{x_i, y_i, \sigma_i\}|\mathcal{M}, \boldsymbol{a}). \tag{A.4}$$

The probability distribution and uncertainties of each parameter can then be calculated from $L(\boldsymbol{a})$.

A.2 Least-squares method and evaluation of parameter uncertainties

The maximisation of L is strictly equivalent to the minimisation of its exponent, which in the specific choice of probability distribution given by Eq. (A.2) it becomes (once multiplied by a factor 2)

$$\chi^2 = \sum_{i=1}^{N} \frac{[y_i - F(x, \boldsymbol{a})]^2}{\sigma_i^2}. \tag{A.5}$$

This is nothing else that the standard chi-square definition on which is based the method of the *least squares* for standard fit procedures. This specific name is due to the presence of the square terms in the above equation. Different assumptions on the probability distribution bring to different forms of χ^2, as discussed in Sec. 2.2.

Once found the best values $\boldsymbol{a}^{\text{best}}$ that minimise Eq. A.5, the associated uncertainties has to be estimated. For this, the likelihood function dependencies on the different parameters has to be evaluated around its maximal value (eventually with a Monte Carlo sampling) or one can determine them analytically using some approximations. For a general case, the probability distribution associated to a parameter a_j is expected to be a gaussian distribution with standard deviation σ_{a_j} and centred on a_j^{best}:

$$P(a_j) \approx Ae^{-\frac{(a_j - a_j^{\text{best}})^2}{2\sigma_{a_j}^2}}. \tag{A.6}$$

This assumption corresponds to an approximation of the χ^2 distribution with a parabola near its minimal value $\chi^2(a_j^{\text{best}}) = \chi^2_{min}$. In fact

$$\chi^2(a_j) = \ln[P(a_j)] \approx \chi^2_{min} + \frac{(a_j - a_j^{\text{best}})^2}{\sigma_{a_j}^2}. \tag{A.7}$$

The value of $1/\sigma_{a_j}^2$, can obtained by the second derivative of $\chi^2(a_j)$ evaluated for $a_j = a_j^{\text{best}}$

$$\frac{\partial^2 \chi^2}{\partial a_j^2} = \frac{2}{\sigma_{a_j}^2} \quad \Rightarrow \quad \sigma_{a_j} = \left(\frac{1}{2}\frac{\partial^2 \chi^2}{\partial a_j^2}\right)^{-1/2}. \tag{A.8}$$

For more details see as ex. Ref. [36].

[1] For a discussion of this crucial assumption see Sec. 2.3.

Appendix B

Classical over-the-barrier model

A simplified but effective schematization of the capture process at low velocity is given by the Classical Over-the-Barrier (COB) model [16,17]. At the low velocity collision regime, the velocity of the outmost target electron is much faster than the relative motion between the projectile ion and the target atom. In this case, we can consider a quasi-static picture of the Coulomb potential of the two atoms as shown in Fig. B.1, where the electrons have discrete potential energies in the Coulomb well. When the two atoms approach, the potential barrier between them go down and a capture of electrons is possible when the Coulomb barrier height is lower than the ionization energy I_0 of the target atom outmost electron. This scenario correspond to the internucleus distance R_C that is the electron capture radius with

$$R_C = \frac{2\sqrt{q}}{I_0}, \tag{B.1}$$

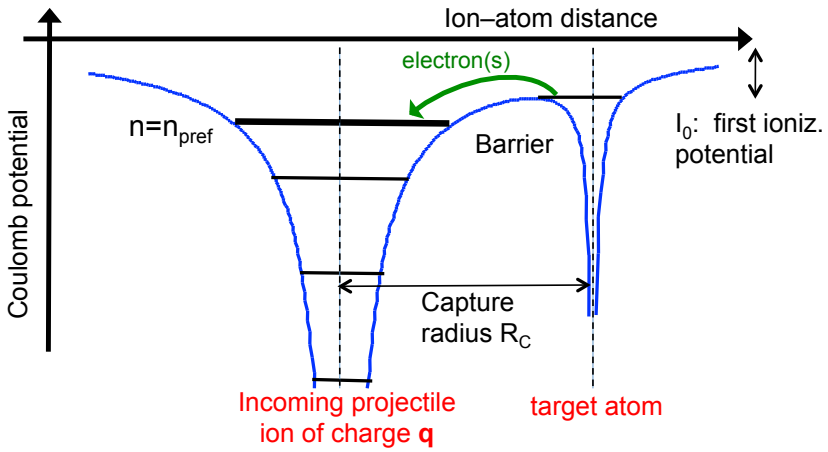

Figure B.1 – Scheme of electron capture at low energy of the over-the-barrier model. The electron(s) capture occurs when the barrier between the two atomic Coulomb well is lower than the ionization energy of the outmost electron of the target atom. The electron(s) is (are) then captured in an excited level n_{pref}.

where all units are in atomic units and where q is the charge of the incoming ion. The value of R_C defines geometrically the expected cross section equal to

$$\sigma_{COB} \approx 0.5\ \pi R_C^2 \tag{B.2}$$

(in atomic units) where the factor 0.5 is an empirical adjustment.

The projectile atomic level n_{pref} where the electrons are captured is also determined by the Coulomb barrier (in atomic units):

$$n_{\text{pref}} \approx \frac{q^{3/4}}{\sqrt{I_0}}. \tag{B.3}$$

In the simple model, no predictions of the distribution of the sublevels ℓ is predicted and only some consideration on its average and its dependency on the projectile velocity can be done [175].

In this simple scenario, not only the single electron capture is possible but also the multiple capture [174]. Also in this case, a dependency on the ion velocity (i.e. the time spent at short distance with the target atom) is expected with an enhancement of multiple capture at low velocity.

Appendix C

Highly charged ion–surface interaction and other ion–matter processes

When collisions between solid targets and highly charged ions are considered, in addition to the initial kinetic energy of the incoming ion, also its potential energy has to be considered. The potential energy is related to the Coulomb potential of the electrons token away from the ion and it is released as soon as the highly charged ion can recapture new electrons from the target. This happens in proximity of the target surface as soon as the depth of the Coulomb barrier of the target is lower than the working function W of the solid (see Fig. C.1), the equivalent of the ionization energy I_0 of the target atom in ion–atom collision discussed in App. B. As in the ion–atom collision, the electrons are normally captured in exited levels of the projectile ion, with a fast de-excitation via radiative and Auger emission. Because of the high atomic density of the target, many electrons are captured and quickly ejected already above the surface due to the large radius capture [358–361] $R_C \approx \sqrt{8q}/(2W)$, similarly to Eq. (B.1) for slow ion–atom collisions, and populates high-excited projectile levels with $n_{\mathrm{pref}} \approx q/\sqrt{2W}$.

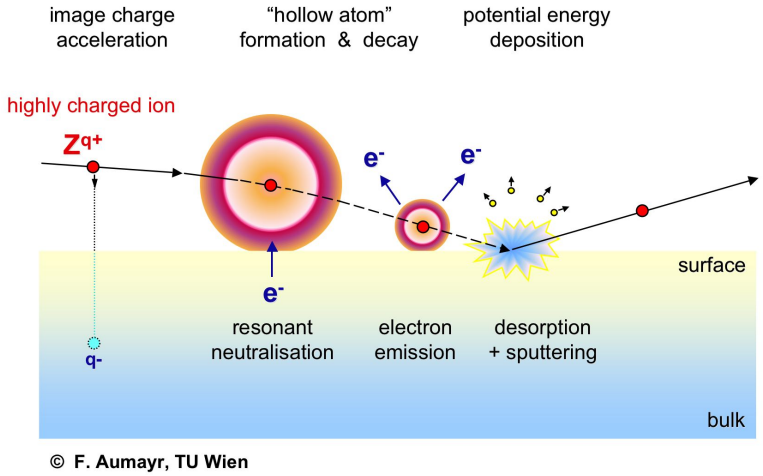

Figure C.1 – Basic processes of highly charged ion interacting with a surface (see text for details).

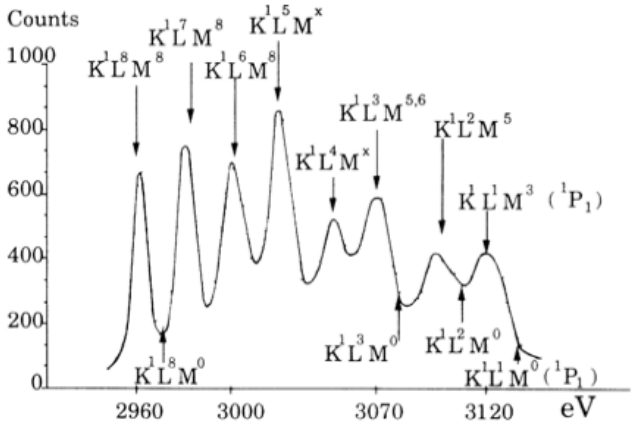

Figure C.2 – Typical high-resolution "hollow atom" X-ray spectrum from Ar^{17+} ions colliding with a Ag surface from Ref. 362. Characteristics X-ray transition energies correspond to different numbers of electrons in the L and M shell during the one-electron $n = 2 \rightarrow 1$ transition.

The involved processes are so fast that when a highly charged ion encounter a solid surface, one can have X-ray emission from the radiative decay to the K-shell with an important presence of electron in the excited levels L and K from the capture from the surface. The presence of electrons in the L significantly change the energy of the $n = 2 \rightarrow 1$ transition. As shown in Fig. C.2, the resulting high-resolution spectra is characterized by the presence of different spectral components corresponding to a different number of electrons in the L shell. We are in presence of a so-called "hollow atom", deeply investigated since its discover in the '90s [**?**, 361–363].

The potential energy of the ion is dissipated by the emitted photons and electrons that are in part absorbed by the neighbour target atoms and then transformed in heat with a thermal spike. This thermal spike can give origin to additional sputtering [189, 191–193] and the creation of local defects or nanostructures [194–199]. This is particularly effective in insulating materials where the heat cannot easily dissipate.

Some ion-induced features have been observed also in gold surfaces irradiated with $Xe^{25,44+}$ by in-vacuum STM [196] but the origin of impact marks has been found to come by the ion kinetic energy rather than their potentials. No sign of impacts have been observed in similar irradiation conditions but by AFM imaging in ambient conditions [195, 364].

For metallic surfaces it is worth mentioning that a charged particle is additionally accelerated by its image charge. This causes an additional gain of kinetic energy of about $Wq^{3/2}/(3\sqrt{2})$ [361], which can contribute with fews hundreds of eV in addition to the initial kinetic energy (as ex. 200 eV for I^{30+} of 150 keV on a gold surface).

After the first target layers, the charge of the incoming ion is stabilized by ionization/capture processes in the solid that depends on the ion and target atoms nature and on the ion velocity [365–368, A11]. The effects of these processes are summarized by the electronic stopping power. However phenomenon as polarization of the target medium ("wake field") [369–371] and resonant coherent excitation of the ion from the regular structure of a crystalline target [372–374] can additionally occur.

Appendix D

Atomic cascade code for He-like ions

```
PROGRAM CASCADE_HE
   ! Automatic Time-stamp: <Tuesday, September 11, 2012, 11:00:06 cest martino>
   ! Program for the calculation of atomic cascade.
   ! Input files:
   ! i)  initial population of the atomic levels
   ! ii) transition probabilities or branching ratio of the transitions
   !
   ! tp = transition probabilities
   ! ip = initial population
   ! br = brancing ratio
   ! gbr = generalized branching ratio
   ! pp  = population values for the line intensity calculation
   ! fpp = final population of the n=1 or 2 levels
   !
   ! NOTE: li, lf: from 0 to ni-1 or nf-1
   !       l -> position in the table -> l+1 (l:[0:n-1]
   !
   ! Version for He-like ions that take into account the fact that
   ! triplet states can almost not reach the foundamental level
   ! due to the spinflip
   ! For he-like version the variables mentioned above are distinguished
   ! in Singlet "_S"  and triplet "_T"

   IMPLICIT NONE
   INTEGER(4) :: i, n, m, ni, li, nf, lf, nm, lm, nli, nlf
   INTEGER(4) :: nimax, nfmax, nit, lit, nft, lft
   INTEGER(4), PARAMETER :: imax=285, nmax = 11
   REAL(8), DIMENSION(nmax,nmax,nmax-1,nmax-1) :: tp_S, br_S, gbr_S, ti_S
   REAL(8), DIMENSION(nmax,nmax,nmax-1,nmax-1) :: tp_T, br_T, gbr_T, ti_T
   REAL(8), DIMENSION(nmax,nmax) :: ip
   REAL(8), DIMENSION(nmax,nmax) :: ip_S, pp_S, tisum_S
   REAL(8), DIMENSION(nmax,nmax) :: ip_T, pp_T, tisum_T
   REAL(8), DIMENSION(2,2) :: fpp_S, fpp_T
   REAL(8), DIMENSION(nmax-1,nmax-1) :: ptmp
   REAL(8) :: tptmp, tpsum
   CHARACTER :: yn_n2*1

   ! Variable initialization
   ip = 0.
   tp_S = 0.
   br_S = 0.
   gbr_S = 0.
   ip_S = 0.
   pp_S = 0.
   ti_S = 0.
   tisum_S = 0.
   tp_T = 0.
   br_T = 0.
   gbr_T = 0.
   ip_T = 0.
   pp_T = 0.
   ti_T = 0.
   tisum_T = 0.
   tptmp = 0.
```

```
yn_n2 = 'y'
fpp_S = 0.
fpp_T = 0.


! Choose if you want activate the intrashell and spinflip transitions
WRITE(*,*) 'Do you want activate the n=2->2 and 1 transitions? [y/n]'
READ(*,*) yn_n2


! Read transition probabilities file for H-like levels
! mathematica generated files, with foundamental levels
! i.e., imax=285
OPEN(UNIT=12,file='cascade_mat.dat', status='old')
DO i=1, imax
   READ(12,*) ni, li, nf, lf, tp_S(ni,li+1,nf,lf+1)
END DO
CLOSE(12)
!
! A different treatment is reserved to 3P states that
! cannot reach the foundamental level directly
tp_T = tp_S
tp_T(:,2,1,1) = 0.
! ... except for the 3P1 spinflip transitions
!
! Activate n=2->2,1 and intrashell transition on demand.
! (and desactivate otherwise)
IF(yn_n2.EQ.'y') THEN
   ! This allow to compare better the results
   ! Quantum mechanics treatment for the spinflip transitions 1snp 3P1->1s2 1S0 transitions
   ! 22.5% value found from Safranova ADNDT 85, page 83 (2003)
   !tp_T(3:nmax,2,1,1)=0.225*3/12*tp_T(3:nmax,2,2,1)
   !tp_T(3:nmax,2,2,1)=(1-0.225)*3/12*tp_T(3:nmax,2,2,1)
   ! For the moment there are not working -> I changed the branchig
   !
   ! Quantum mechanics treatment for the 3P  n=2->1 transitions:
   ! 1s2p 3P0 -> 1s2s 3S1
   ! 1s2p 3P1 -> 1s2 1S0
   ! 1s2p 3P2 -> 1s2s 3S1 53%
   !          -> 1s2 1S0 47%
   tp_T(2,2,1,1)= (0.47*5+3)/9
   tp_T(2,2,2,1)= 1-tp_T(2,2,1,1)
END IF

! Write the read data in a file to check that everythink is good
OPEN(UNIT=66,file='trans_prob_S.dat', status='unknown')
DO ni=1,nmax
   DO li=0,ni-1
      DO nf=1,nmax-1
         DO lf=0,nf-1
            IF(tp_S(ni,li+1,nf,lf+1).GT.0.) THEN
               WRITE(66,*) ni, li, nf, lf, tp_S(ni,li+1,nf,lf+1)
            END IF
         END DO
      END DO
   END DO
END DO
CLOSE(66)
OPEN(UNIT=666,file='trans_prob_T.dat', status='unknown')
DO ni=1,nmax
   DO li=0,ni-1
      DO nf=1,nmax-1
         DO lf=0,nf-1
            IF(tp_T(ni,li+1,nf,lf+1).GT.0.) THEN
               WRITE(666,*) ni, li, nf, lf, tp_T(ni,li+1,nf,lf+1)
            END IF
         END DO
      END DO
   END DO
END DO
CLOSE(666)

! Calculation of the branching ratio via normalization
! Only Delta l = +-1 are admited.
! Intrashell transitions are allowed
! Singlet
DO n=0,nmax-1
   ni=nmax-n
   nfmax=ni
```

```
   DO li=0,ni-1
      tpsum=0
      DO m=0,nfmax-1
         nf=nfmax-m
         IF (li.EQ.0) THEN
            tpsum = tpsum+tp_S(ni,li+1,nf,li+2)
         ELSE IF (li.GT.0.AND.li.LT.(ni-1)) THEN
         tpsum = tpsum+tp_S(ni,li+1,nf,li)+&
            tp_S(ni,li+1,nf,li+2)
         ELSE IF (li.EQ.(ni-1)) THEN
            tpsum = tpsum+tp_S(ni,li+1,nf,li)
         END IF
      END DO
      ! Normalization
      br_S(ni,li+1,:,:)=tp_S(ni,li+1,:,:)/tpsum
   END DO
END DO
! Triplet
DO n=0,nmax-1
   ni=nmax-n
   nfmax=ni
   DO li=0,ni-1
      tpsum=0
      DO m=0,nfmax-1
         nf=nfmax-m
         IF (li.EQ.0) THEN
            tpsum = tpsum+tp_T(ni,li+1,nf,li+2)
         ELSE IF (li.GT.0.AND.li.LT.(ni-1)) THEN
         tpsum = tpsum+tp_T(ni,li+1,nf,li)+&
            tp_T(ni,li+1,nf,li+2)
         ELSE IF (li.EQ.(ni-1)) THEN
            tpsum = tpsum+tp_T(ni,li+1,nf,li)
         END IF
      END DO
      ! Normalization
      br_T(ni,li+1,:,:)=tp_T(ni,li+1,:,:)/tpsum
   END DO
END DO



! Write into a file the branching ratios
OPEN(UNIT=33,file='br_ratio_S.dat', status='unknown')
DO ni=1,nmax
   DO li=0,ni-1
      DO nf=1,nmax-1
         DO lf=0,nf-1
            IF(br_S(ni,li+1,nf,lf+1).GT.0.) THEN
               WRITE(33,*) ni, li, nf, lf, br_S(ni,li+1,nf,lf+1)
            END IF
         END DO
      END DO
   END DO
END DO
CLOSE(33)
OPEN(UNIT=333,file='br_ratio_T.dat', status='unknown')
DO ni=1,nmax
   DO li=0,ni-1
      DO nf=1,nmax-1
         DO lf=0,nf-1
            IF(br_T(ni,li+1,nf,lf+1).GT.0.) THEN
               WRITE(333,*) ni, li, nf, lf, br_T(ni,li+1,nf,lf+1)
            END IF
         END DO
      END DO
   END DO
END DO
CLOSE(333)

! Calculation of the generalized branching ration between two different levels
! i.e. a composed decay with several transitions with intermediate levels
!
! Calculate for each level the generalized branching ratio
DO ni=2,nmax
   DO li =0,ni-1
      DO nf = 1,ni-1
         DO lf=0,nf-1
            ! Generalized branching ratio like a population waterflow from each of the ni,li level
            ptmp = 0
```

```
               ! Initial virtual population in the starting level
               ptmp(ni,li+1) = 1.
               ! Virtual population to the other levels (n,lm) only from levels with lm+-1
               ! and arbitrary n=[nf:nm].
               ! The loop is in from the level just after ni to nf level .
               ! Step by step the population of the nm+1 levels is propagated to the lower levels
               ! following the possible transitions.
               DO n=1,ni-nf
                  nm=ni-n
                  ! s-state cases
                  lm =0
                  ptmp(nf:nm,lm+1) = ptmp(nf:nm,lm+1) + ptmp(nm+1,lm+2)*br_S(nm+1,lm+2,nf:nm,lm+1)
!                  write(*,*) ni,li,nm, lm, nf,lf,ptmp(nm,lm+1),ptmp(nf,lf+1)
                  ! other cases
                  DO lm=1,nm-1
                     ptmp(nf:nm,lm+1) = ptmp(nf:nm,lm+1) + ptmp(nm+1,lm+2)*br_S(nm+1,lm+2,nf:nm,lm+1) &
                        + ptmp(nm+1,lm)*br_S(nm+1,lm,nf:nm,lm+1)
!                     write(*,*) ni,li,nm, lm, nf,lf,ptmp(nm,lm+1),ptmp(nf,lf+1)
                  END DO
               END DO
               gbr_S(ni,li+1,nf,lf+1) = ptmp(nf,lf+1)
            END DO
         END DO
      END DO
   END DO
   DO ni=2,nmax
      DO li =0,ni-1
         DO nf = 1,ni-1
            DO lf=0,nf-1
               ! Generalized branching ratio like a population waterflow from each of the ni,li level
               ptmp = 0
               ! Initial virtual population in the starting level
               ptmp(ni,li+1) = 1.
               ! Virtual population to the other levels (n,lm) only from levels with lm+-1
               ! and arbitrary n=[nf:nm].
               ! The loop is in from the level just after ni to nf level .
               ! Step by step the population of the nm+1 levels is propagated to the lower levels
               ! following the possible transitions.
               DO n=1,ni-nf
                  nm=ni-n
                  ! s-state cases
                  lm =0
                  ptmp(nf:nm,lm+1) = ptmp(nf:nm,lm+1) + ptmp(nm+1,lm+2)*br_T(nm+1,lm+2,nf:nm,lm+1)
!                  write(*,*) ni,li,nm, lm, nf,lf,ptmp(nm,lm+1),ptmp(nf,lf+1)
                  ! other cases
                  DO lm=1,nm-1
                     ptmp(nf:nm,lm+1) = ptmp(nf:nm,lm+1) + ptmp(nm+1,lm+2)*br_T(nm+1,lm+2,nf:nm,lm+1) &
                        + ptmp(nm+1,lm)*br_T(nm+1,lm,nf:nm,lm+1)
!                     write(*,*) ni,li,nm, lm, nf,lf,ptmp(nm,lm+1),ptmp(nf,lf+1)
                  END DO
               END DO
               gbr_T(ni,li+1,nf,lf+1) = ptmp(nf,lf+1)
            END DO
         END DO
      END DO
   END DO


   ! Write generalized branching ratio in a file
   ! Singlet
   OPEN(UNIT=22,file='gen_br_ratio_S.dat', status='unknown')
   DO ni=1,nmax
      DO li=0,ni-1
         DO nf=1,nmax-1
            DO lf=0,nf-1
               IF(gbr_S(ni,li+1,nf,lf+1).GT.0.) THEN
                  WRITE(22,*) ni, li, nf, lf, gbr_S(ni,li+1,nf,lf+1)
               END IF
            END DO
         END DO
      END DO
   END DO
   CLOSE(22)
   ! Triplet
   OPEN(UNIT=222,file='gen_br_ratio_T.dat', status='unknown')
   DO ni=1,nmax
      DO li=0,ni-1
         DO nf=1,nmax-1
            DO lf=0,nf-1
```

```
            IF(gbr_T(ni,li+1,nf,lf+1).GT.0.) THEN
               WRITE(222,*) ni, li, nf, lf, gbr_T(ni,li+1,nf,lf+1)
            END IF
         END DO
      END DO
   END DO
END DO
CLOSE(22)



! Read the initial population file
OPEN(UNIT=13,file='initial_population.dat', status='old')
DO i=1, imax
   READ(13,*,END=99) ni, li, ip(ni,li+1)
END DO
99 CLOSE(13)

! Distribute the intensity statistically between singlet and triplet
ip_S=ip/4.
ip_T=ip*3/4.

! Choose a specific transition
!WRITE(*,*) 'Please choose the transition. Enter ni li nf lf'
!READ(*,*) nit, lit, nft, lft
!WRITE(*,*) 'Please choose the transition. Enter ni li'
!READ(*,*) nit, lit


! Calculate all the transition intensity
! Singlet
! Step 0: Initial population of the levels are the initial population given
pp_S=ip_S
DO nit=2,nmax
   DO lit=0,nit-1
      ! Step 1: calculation of the relative population of the initial level
      DO ni=nit+1, nmax
         DO li=0, nmax-1
            IF(ip_S(ni,li+1).GT.0.) THEN
               pp_S(nit,lit+1)= pp_S(nit,lit+1) + gbr_S(ni,li+1,nit,lit+1)*ip_S(ni,li+1)
            END IF
            !write(*,*) ni, li, nit, lit, gbr(ni,li+1,nit,lit+1),ip(ni,li+1),gbr(ni,li+1,nit,lit+1)*ip(ni,li+1)
         END DO
      END DO

      ! Step 2: calculate the transition intensity using the branching ratio
      DO nft=1,nit-1
         DO lft=0,nft-1
            ti_S(nit,lit+1,nft,lft+1) = pp_S(nit,lit+1)*br_S(nit,lit+1,nft,lft+1)
            !IF(ti_S(nit,lit+1,nft,lft+1).GT.0.) THEN
               !write(*,*) nit, lit, nft, lft, ti(nit,lit+1,nft,lft+1), &
               !   pp(nit,lit+1),br(nit,lit+1,nft,lft+1), gbr(10,10,nit,lit+1)
            !END IF
         END DO
      END DO
   END DO
END DO
! Triplet
! Step 0: Initial population of the levels are the initial population given
pp_T=ip_T
DO nit=2,nmax
   DO lit=0,nit-1
      ! Step 1: calculation of the relative population of the initial level
      DO ni=nit+1, nmax
         DO li=0, nmax-1
            IF(ip_T(ni,li+1).GT.0.) THEN
               pp_T(nit,lit+1)= pp_T(nit,lit+1) + gbr_T(ni,li+1,nit,lit+1)*ip_T(ni,li+1)
            END IF
            !write(*,*) ni, li, nit, lit, gbr(ni,li+1,nit,lit+1),ip(ni,li+1),gbr(ni,li+1,nit,lit+1)*ip(ni,li+1)
         END DO
      END DO

      ! Step 2: calculate the transition intensity using the branching ratio
      DO nft=1,nit-1
         DO lft=0,nft-1
            ti_T(nit,lit+1,nft,lft+1) = pp_T(nit,lit+1)*br_T(nit,lit+1,nft,lft+1)
            !IF(ti_T(nit,lit+1,nft,lft+1).GT.0.) THEN
               !write(*,*) nit, lit, nft, lft, ti(nit,lit+1,nft,lft+1), &
               !   pp(nit,lit+1),br(nit,lit+1,nft,lft+1), gbr(10,10,nit,lit+1)
```

```
            !END IF
         END DO
      END DO
   END DO
END DO


IF (yn_n2.EQ.'y') THEN
! Calculate the population of the 1s2, 1s2s levels
   ! Singlet
   fpp_S(2,1) = ip_S(2,1)
   DO ni=2, nmax
      DO li=0, nmax-1
         IF(ip_S(ni,li+1).GT.0.) THEN
            fpp_S(1,1)= fpp_S(1,1) + gbr_S(ni,li+1,1,1)*ip_S(ni,li+1)
            fpp_S(2,1)= fpp_S(2,1) + gbr_S(ni,li+1,2,1)*ip_S(ni,li+1)
         END IF
      END DO
   END DO
   ! Triplet foundameltal
   fpp_T(2,1) = ip_T(2,1)
   fpp_T(2,2) = ip_T(2,2)


   DO ni=2, nmax
      DO li=0, nmax-1
         IF(ip_T(ni,li+1).GT.0.) THEN
            fpp_T(1,1)= fpp_T(1,1) + gbr_T(ni,li+1,1,1)*ip_T(ni,li+1)
            fpp_T(2,1)= fpp_T(2,1) + gbr_T(ni,li+1,2,1)*ip_T(ni,li+1)
            fpp_T(2,2)= fpp_T(2,2) + gbr_T(ni,li+1,2,2)*ip_T(ni,li+1)
         END IF
      END DO
   END DO

   ! Triplet 1s2s 3S1, the only intrashell transition admited here and never considerated before
   fpp_T(2,1)=fpp_T(2,1)+fpp_T(2,2)*br_T(2,2,2,1)


ELSE
! Calculate the population of the 1s2, 1s2s and 1s2p levels
   ! Singlet
   fpp_S(2,1) = ip_S(2,1)
   fpp_S(2,2) = ip_S(2,2)
   DO ni=3, nmax
      DO li=0, nmax-1
         IF(ip_S(ni,li+1).GT.0.) THEN
            fpp_S(1,1)= fpp_S(1,1) + gbr_S(ni,li+1,1,1)*ip_S(ni,li+1)
            fpp_S(2,1)= fpp_S(2,1) + gbr_S(ni,li+1,2,1)*ip_S(ni,li+1)
            fpp_S(2,2)= fpp_S(2,2) + gbr_S(ni,li+1,2,2)*ip_S(ni,li+1)
         END IF
      END DO
   END DO
   ! To eliminate the influence of the 2p->1s transition and just looks for the np->1s transitions
   IF(fpp_S(1,1).GT.fpp_S(2,2)) fpp_S(1,1) =  fpp_S(1,1) - fpp_S(2,2)
   ! Triplet foundameltal
   fpp_T(2,1) = ip_T(2,1)
   fpp_T(2,2) = ip_T(2,2)
   DO ni=3, nmax
      DO li=0, nmax-1
         IF(ip_T(ni,li+1).GT.0.) THEN
            fpp_T(2,1)= fpp_T(2,1) + gbr_T(ni,li+1,2,1)*ip_T(ni,li+1)
            fpp_T(2,2)= fpp_T(2,2) + gbr_T(ni,li+1,2,2)*ip_T(ni,li+1)
         END IF
      END DO
   END DO
END IF


! Write the populations
! Singlet
OPEN(UNIT=11,file='populations_S.dat', status='unknown')
DO ni=1, nmax
   DO li=0, nmax-1
      IF(pp_S(ni,li+1).GT.0.) THEN
         WRITE(11,*) ni, li, pp_S(ni,li+1)
      END IF
   END DO
END DO
CLOSE(11)
```

```
! Triplet
OPEN(UNIT=111,file='populations_T.dat', status='unknown')
DO ni=1, nmax
   DO li=0, nmax-1
      IF(pp_T(ni,li+1).GT.0.) THEN
         WRITE(111,*) ni, li, pp_T(ni,li+1)
      END IF
   END DO
END DO
CLOSE(111)

! Write on the screen the population of the 1s and 2s levels for the given initial population
! (1s is calculated from the 2p)
! Change the writing mode if you choose yn_n2='n'
IF (yn_n2.EQ.'y') THEN
   WRITE(*,*) '#####################################################'
   WRITE(*,*) 'Final population of the 1s and 2s levels (SINGLET)'
   WRITE(*,*) '1s_S: ', fpp_S(1,1)
   WRITE(*,*) '2s_S: ', fpp_S(2,1)
   WRITE(*,*) '1s_S+2s_S: ', fpp_S(1,1)+fpp_S(2,1)
   WRITE(*,*) '-----------------------------------------------------'
   WRITE(*,*) 'Final population of the 2s and 2p levels (TRIPLET)'
   WRITE(*,*) '1s_T: ', fpp_T(1,1)
   WRITE(*,*) '2s_T: ', fpp_T(2,1)
   WRITE(*,*) '1s_T+2s_T: ', fpp_T(1,1)+fpp_T(2,1)
   WRITE(*,*) 'Singlet plus Triplet --------------------------------'
   WRITE(*,*) '1s_S+1s_T: ', fpp_S(1,1)+fpp_T(1,1)
   WRITE(*,*) '1s_S+2s_S+1s_T+2s_T: ', fpp_S(1,1)+fpp_S(2,1)+fpp_T(1,1)+fpp_T(2,1)
   WRITE(*,*) '3P/1P ratio: ',ti_T(2,2,1,1)/ti_S(2,2,1,1)
ELSE
   WRITE(*,*) '#####################################################'
   WRITE(*,*) '!!!!!!!! NO n=2->2,1 TRANSITION ACTIVATED !!!!!!!!'
   WRITE(*,*) 'Final population of the 2s and 2p levels (SINGLET)'
   WRITE(*,*) '1s_S: ', fpp_S(1,1)
   WRITE(*,*) '2s_S: ', fpp_S(2,1)
   WRITE(*,*) '2p_S: ', fpp_S(2,2)
   WRITE(*,*) '1s_S+2s_S+2p_S: ', fpp_S(1,1)+fpp_S(2,1)+fpp_S(2,2)
   WRITE(*,*) '-----------------------------------------------------'
   WRITE(*,*) 'Final population of the 2s and 2p levels (TRIPLET)'
   WRITE(*,*) '2s_T: ', fpp_T(2,1)
   WRITE(*,*) '2p_T: ', fpp_T(2,2)
   WRITE(*,*) '2s_T+2p_T: ', fpp_T(2,1)+fpp_T(2,2)
   WRITE(*,*) 'Singlet plus Triplet --------------------------------'
   WRITE(*,*) '1s_S+1s_T: ', fpp_S(1,1)+fpp_T(1,1)
   WRITE(*,*) '1s_S+2s_S+2p_S+S+2s_T+2p_T: ', fpp_S(1,1)+fpp_S(2,1)+fpp_S(2,2)+fpp_T(2,1)+fpp_T(2,2)
END IF
WRITE(*,*) '#####################################################'



! Write the transition intensities
OPEN(UNIT=33,file='trans_int_S.dat', status='unknown')
DO nit=1,nmax
   DO lit=0,nit-1
      DO nft=1,nmax-1
         DO lft=0,nft-1
            IF(ti_S(nit,lit+1,nft,lft+1).GT.0.) THEN
               WRITE(33,*) nit, lit, nft, lft, ti_S(nit,lit+1,nft,lft+1)
            END IF
         END DO
      END DO
   END DO
END DO
CLOSE(33)
OPEN(UNIT=333,file='trans_int_T.dat', status='unknown')
DO nit=1,nmax
   DO lit=0,nit-1
      DO nft=1,nmax-1
         DO lft=0,nft-1
            IF(ti_T(nit,lit+1,nft,lft+1).GT.0.) THEN
               WRITE(333,*) nit, lit, nft, lft, ti_T(nit,lit+1,nft,lft+1)
            END IF
         END DO
      END DO
   END DO
END DO
CLOSE(333)
```

```
   ! Calculate the sum of the transition intensities level per level
   DO nit=1,nmax
      DO lit=0,nit-1
         DO nft=1,nmax-1
            DO lft=0,nft-1
               IF(ti_S(nit,lit+1,nft,lft+1).GT.0.) THEN
                  tisum_S(nit,nft) = tisum_S(nit,nft)+ ti_S(nit,lit+1,nft,lft+1)
               END IF
            END DO
         END DO
      END DO
   END DO
   DO nit=1,nmax
      DO lit=0,nit-1
         DO nft=1,nmax-1
            DO lft=0,nft-1
               IF(ti_T(nit,lit+1,nft,lft+1).GT.0.) THEN
                  tisum_T(nit,nft) = tisum_T(nit,nft)+ ti_T(nit,lit+1,nft,lft+1)
               END IF
            END DO
         END DO
      END DO
   END DO

   ! Write the sum of the transition intensities level per level
   ! Singlet
   OPEN(UNIT=44,file='trans_int_sum_S.dat', status='unknown')
   DO nit=1,nmax
      DO nft=1,nmax-1
         IF(tisum_S(nit,nft).GT.0.) THEN
            WRITE(44,*) nit, nft, tisum_S(nit,nft)
         END IF
      END DO
   END DO
   CLOSE(44)
   ! Triplet
   OPEN(UNIT=444,file='trans_int_sum_T.dat', status='unknown')
   DO nit=1,nmax
      DO nft=1,nmax-1
         IF(tisum_T(nit,nft).GT.0.) THEN
            WRITE(444,*) nit, nft, tisum_T(nit,nft)
         END IF
      END DO
   END DO
   CLOSE(444)
   ! Sum
   OPEN(UNIT=55,file='trans_int_sum_ST.dat', status='unknown')
   DO nit=1,nmax
      DO nft=1,nmax-1
         IF(tisum_S(nit,nft).GT.0.OR.tisum_T(nit,nft).GT.0) THEN
            WRITE(55,*) nit, nft, tisum_S(nit,nft)+tisum_T(nit,nft)
         END IF
      END DO
   END DO
   CLOSE(55)

END PROGRAM CASCADE_HE
```

Appendix E

Article about Bayesian data analysis methods

Nuclear Instruments and Methods in Physics Research B xxx (2017) xxx–xxx

Contents lists available at ScienceDirect

Nuclear Instruments and Methods in Physics Research B

journal homepage: www.elsevier.com/locate/nimb

Bayesian data analysis tools for atomic physics

Martino Trassinelli *

Institut des NanoSciences de Paris, CNRS, Sorbonne Universités, UPMC Univ Paris 06, F-75005 Paris, France

ARTICLE INFO

Article history:
Received 29 November 2016
Received in revised form 13 May 2017
Accepted 15 May 2017
Available online xxxx

Keywords:
Bayesian data analysis
Atomic physics
Nested sampling
Model testing

ABSTRACT

We present an introduction to some concepts of Bayesian data analysis in the context of atomic physics. Starting from basic rules of probability, we present the Bayes' theorem and its applications. In particular we discuss about how to calculate simple and joint probability distributions and the Bayesian evidence, a model dependent quantity that allows to assign probabilities to different hypotheses from the analysis of a same data set. To give some practical examples, these methods are applied to two concrete cases. In the first example, the presence or not of a satellite line in an atomic spectrum is investigated. In the second example, we determine the most probable model among a set of possible profiles from the analysis of a statistically poor spectrum. We show also how to calculate the probability distribution of the main spectral component without having to determine uniquely the spectrum modeling. For these two studies, we implement the program `Nested_fit` to calculate the different probability distributions and other related quantities. `Nested_fit` is a Fortran90/Python code developed during the last years for analysis of atomic spectra. As indicated by the name, it is based on the nested algorithm, which is presented in details together with the program itself.

1. Introduction

Commonly, a data analysis is based on the comparison between a function $F(\boldsymbol{a})$ used to model the data that depends on a set of parameters $\boldsymbol{a}$ (ex. $a_1 \rightarrow$ amplitude, $a_2 \rightarrow$ position, etc.) and the data them-self that consist in recorded number of counts y_i at each channel x_i. The estimation of the parameter values describing at best the data is generally obtained by the maximum likelihood method (and its lemma, the method of the least squares), which consists to find the values $\boldsymbol{a}^{best}$ that maximize the product of the probabilities for each channel x_i to observe y_i counts for a given expected value $F(x_i, \boldsymbol{a}^{best})$.

Even if very successfully in many cases, this method has some limitations. If some function parameter is subject to constraints on its values (as ex. one model parameter could be a mass of a particle, which cannot be negative), the corresponding boundary conditions cannot be taken into account in a well defined manner. With the likelihood function we are in fact calculating the probabilities to observe the data $\{x_i, y_i\}$ for given parameter values and not the probability to have certain parameter values for given experimental data.

An additional difficulty for the maximum likelihood method arises when different hypotheses are compared, represented for example by two possible modeling functions F_A and F_B, in view of the acquired data. The determination of the most adapted model describing the data generally done with goodness-of-fit tests like the χ^2-test, the likelihood-ratio test, etc. [1–6]. In the unfortunate case where there is no clear propensity to a unique model and we are interested on the value of a parameter common to all models (as the position of the a peak with undefined shape), no sort of weighted average can be computed from goodness-of-fit test outcomes. To do this, the assignment of a probability $P(\mathcal{M})$ to each model is mandatory, which cannot be calculated in the classical statistics framework.

Another important and fundamental problem of the common data analysis approach is the requirement of repeatability for the definition of *probability* itself. In classic data analysis manuals we can find sentences as:

> *"Suppose we toss a coin in the air and let it land. There is 50% probability that it will land heads up and a 50% probability that it will land tails up. By this we mean that if we continue tossing a coin repeatedly, the fraction of times that it lands with heads up will asymptotically approach 1/2 ..."* [3].

This definition is completely inadequate to rare processes as those encountered for example in cosmology, where several models are considered to describe one unique observation, our universe, and more recently in gravitational-wave astronomy, where at present only two observations are available [7,8].

* Corresponding author.
E-mail address: trassinelli@insp.jussieu.fr

http://dx.doi.org/10.1016/j.nimb.2017.05.030
0168-583X/

To overcome these problems, a different approach has to be implemented with a new and more general definition of probability. This approach is the result of the work of Th. Bayes, P.-S. Laplace, H. Jeffreys and of many others [9–12] and is commonly called *Bayesian statistics*.

Bayesian methods are routinely used in many fields: cosmology [13–15], particle physics [16], nuclear physics, ... In atomic physics their implementation is still limited (e.g. in atomic interferometry [17,18], quantum information [19], ion trapping [20], ion–matter interaction [21], etc.) with almost no use in atomic spectroscopy, even if in some cases it would be strongly required. For example, when we want to determine the correct shape of a instrumental response function we are actually testing hypotheses, as in the case of the determination of the presence or not of possible line contributions in a complex or statistically poor spectrum.

The goal of this article is to present a basic introduction of Bayesian data analysis methods in the context of atomic physics spectroscopy and to introduce the program `Nested_fit` for the calculation of distribution probabilities and related quantities (mean values, standard deviation, confidence intervals, etc.) from the application of these methods. The introduction to Bayesian statics is based in the extended literature on this domain, and in particular on Refs. [11,14,22–24]. For a clear and practical presentation, we will present two simple applications of data analysis where we implemented a Bayesian approach using the `Nested_fit` program. The first example is about the probability evaluation of the presence of a satellite peak in a simple atomic spectrum. The second one deals with the analysis of a statistically poor spectrum in which one or multiple peaks contributions has to be considered and where possible aberrations in the response function have also to be taken into account. We will in particular show how to assign probabilities to the different models from the experimental data analysis and compare them to classical goodness-of-fit tests. Moreover, we will see how to extract the probability distribution of the main peak position without the need to uniquely choose between the different models.

The article is organized as following. A general definition of probability and Bayesian statistic concepts as the Bayes' theorem and *Bayesian evidence* are present in Section 2, together with a very general and axiomatic definition of probability deduced from simple logic arguments. In Section 3 we present in details the nested algorithm for the calculation of the Bayesian evidence and in Section 4 we will see its implementation in the program `Nested_fit`, which is also presented. These two sections are quite technical and they could be skipped in a first reading. Section 5 is dedicated to the Bayesian data analysis applications to two real data sets and Section 6 is our conclusion. Two appendixes are also proposed: one about the introduction of information and complexity concepts in the context of Bayesian statistics, and a second about the evaluation of the uncertainty of the Bayesian evidence calculated by the nested sampling method.

2. Probability

2.1. Probability axioms

A very general definition of probability $P(X)$ can be obtained by trying to assign real numbers to a certain degree of plausibility or believe than assertions X, Y, etc., would be true. X and Y assertions are very general. They can be assertions of specific statements (ex. "In the next toss the coin will land heads") or implying values (ex. the parameter b is in a certain range $[b_{min}, b_{max}]$). When basic logic and consistency are required, the form of the probability P is ensured by the axioms [22,25,12,24,23]

$$0 \leqslant P(X|I) \leqslant 1, \tag{1}$$

$$P(X|X,I) = 1, \tag{2}$$

$$P(X|I) + P(\bar{X}|I) = 1, \tag{3}$$

$$P(X,Y|I) = P(X|Y,I) \times P(Y|I). \tag{4}$$

In the equations above, $\bar{X}$ indicates the negation of the assertion X (not-X); the vertical bar "|" means "given" and where I represents the current state of knowledge. For example, I can represent the ensemble of the physics laws describing a certain phenomenon, e.g. the thermodynamics laws, and X, Y can represent two quantitative measurements related to this phenomenon, e.g. two temperature measurements at different times of a cooling body. The joint probability $P(X,Y|I)$ means that both "X AND Y" are true (equivalent to the logical conjunction '$\wedge$'). The deduction of these axioms have been obtained for the first time in 1946 by Richard Cox using Boolean logic [22]. The first three axioms are compatible with the usual probability rules. Here we have an additional axiom that, as we will see, plays a very important role.

From these axioms the following rule (sum rule) is deduced [23]

$$P(X+Y|I) = P(X|I) + P(Y|I) - P(X,Y|I). \tag{5}$$

Here the symbol '+' in the notation $X+Y$ means the logical disjunction ($X+Y \equiv X \vee Y \equiv$ "X OR Y is true").

The fourth axiom determines the rule for inference probabilities (product rule) for conditional cases. If X and Y are independent assertions, this is reduced to the classical probability property

$$P(X,Y|I) = P(X|I) \times P(Y|I). \tag{6}$$

When a set of mutual exclusive assertions are considered $\{Y_i\}$, with $P(Y_i|Y_{j\neq i}) = 0$, we have the so-called *marginalization rule*

$$P(X|I) = \sum_i P(X,Y_i|I) \tag{7}$$

that in the limit of continuous case $Y_{i+1} - Y_i \to dY$ becomes

$$P(X|I) = \int_{-\infty}^{\infty} P(X,Y|I)dY. \tag{8}$$

2.2. Bayes' theorem and posterior probability

Another important corollary can be derived from the fourth axiom (Eq. (4)) and the similar expression with exchange between X and Y:

$$P(X|Y,I) = \frac{P(Y|X,I) \times P(X|I)}{P(Y|I)}. \tag{9}$$

This is what is called the Bayes' Theorem, named after Rev. Thomas Bayes, who first [9] formulated theorems of conditional probability, and rediscovered in 1774 and further developed by Pierre-Simon Marquis de la Laplace [10].

For a better insight in the implication of this theorem, we consider the case where X represent the hypothesis that the parameter values set $\boldsymbol{a}$ truly describes the data (via the function $F(x,\boldsymbol{a})$) and where Y correspond to the recorded data $\{x_i, y_i\}$. In this case Eq. (9) becomes

$$P(\boldsymbol{a}|\{x_i,y_i\},I) = \frac{P(\{x_i,y_i\}|\boldsymbol{a},I) \times P(\boldsymbol{a}|I)}{P(\{x_i,y_i\}|I)} = \frac{L(\boldsymbol{a}) \times P(\boldsymbol{a}|I)}{P(\{x_i,y_i\}|I)}, \tag{10}$$

where I includes our available background information and where $P(\{x_i,y_i\}|\boldsymbol{a},I)$ is by definition the likelihood function $L(\boldsymbol{a})$ for the given set of data. Differently from the common statistical approach where only the likelihood function is considered, we have here the additional term $P(\boldsymbol{a}|I)$ that includes the prior knowledge on the parameters $\boldsymbol{a}$ or its possible boundaries. The denominator term $P(\{x_i,y_i\}|I)$ can be considered for the moment as a normalization factor but it plays an important role when different hypotheses are considered and compared (see next section).

Please cite this article in press as: M. Trassinelli, Bayesian data analysis tools for atomic physics, Nucl. Instr. Meth. B (2017), http://dx.doi.org/10.1016/j.nimb.2017.05.030

The priors can look as an unsuitable input due to the possible subjectivity in their choice; this is actually the main critics to *Bayesian statistics*. On the contrary, the priors reflects our knowledge or ignorance in a quantify way. If two scientists have different choices of priors, and uses some common experimental data, the posterior probability distributions are generally not significantly different. If the posteriors are different because of the different choice of priors, this means that the data are not sufficient to analyze the problem.

From $P(\boldsymbol{a}|\{x_i,y_i\},I)$, the probability distribution of each parameter $P(a_j|\{x_i,y_i\},I)$ or joint probabilities $P(a_j,a_k|\{x_i,y_i\},I)$ can be obtained from the marginalization (Eq. (8)), i.e. the integration of the posterior probability on the unconcerned parameters.

For a more in-deep introduction to Bayesian statistics, we invite the reader to consult Refs. [11,14,24]. In the following paragraphs, we will present more specific examples adapted to cases commonly encountered in atomic physics and related to the problem of hypotheses testing.

2.3. Model testing and Bayesian evidence

An important consequence of the Bayes' theorem is to have the possibility to assign probabilities to different hypotheses (models) with a simple and well-defined procedure. In this case, X in Eq. (9) represents the hypothesis that the model $\mathcal{M}$ describes well the observations and Y represents the data, as in the previous section. From Bayes' theorem we have that the posterior probability of the model $\mathcal{M}$ is [12,24,14]

$$P(\mathcal{M}|\{x_i,y_i\},I) \propto P(\{x_i,y_i\}|\mathcal{M},I) \times P(\mathcal{M}|I), \tag{11}$$

where the first term of the right part is the so-called *Bayesian evidence* E of the model and the second term is the prior probability assigned to the model from our background knowledge. Using the marginalization rule to the parameter values and the probability properties (Eqs. (1)–(4)), we have

$$\begin{aligned} E \equiv P(\{x_i,y_i\}|\mathcal{M},I) &= \\ &= \int P(\{x_i,y_i\}|\boldsymbol{a},\mathcal{M},I)P(\boldsymbol{a}|\mathcal{M},I)d^J\boldsymbol{a} = \\ &= \int L^{\mathcal{M}}(\boldsymbol{a})P(\boldsymbol{a}|\mathcal{M},I)d^J\boldsymbol{a}, \end{aligned} \tag{12}$$

where J is the number of the parameters of the considered model, and where we explicitly show the likelihood function $L^{\mathcal{M}}(\boldsymbol{a})$ relative to the model $\mathcal{M}$. The Bayesian evidence, also called *marginal likelihood* or *model likelihood*, is the integral of the likelihood function over the J-dimensional parameter space under the priors constraints for a specific model choice. The evidence is also the denominator of Eq. (9), which now assumes a clearer signification than a simple normalization factor (with $\mathcal{M}$ included in I). Considering equal priors, the probability of a model is higher if the evidence is higher, which means that the average of the likelihood function over the model parameter space is higher. To note, this does not implies that the maximum of the likelihood function is larger, as in the case of the likelihood ratio test used to compare the goodness of fit of two models (where however we do not assign probabilities to the models themselves but where we define only a criterion to choose between two models). Models with higher number of parameters are generally penalized because of the higher dimensionality of the integral that corresponds to a larger parameter volume $V_{\boldsymbol{a}}$ (and then to a lower average value of the likelihood function). In fact, the calculation of the model probability via the Bayesian evidence includes, in some sense, the Ockham's razor[1] favoring simpler models when the values of the likelihood function are similar.

If we have to choose among only two different models $\mathcal{M}_1,\mathcal{M}_2$, the comparison between model probabilities is related to the calculation of the simple ratio

$$\frac{P(\mathcal{M}_1|\{x_i,y_i\},I)}{P(\mathcal{M}_2|\{x_i,y_i\},I)} = \frac{P(\{x_i,y_i\}|\mathcal{M}_1,I)}{P(\{x_i,y_i\}|\mathcal{M}_2,I)} \times \frac{P(\mathcal{M}_1|I)}{P(\mathcal{M}_2|I)}. \tag{13}$$

If the prior probabilities of the models are equal, this probability ratio is given by the *Bayes factor* $B_{12} = E_1/E_2$ that is nothing else than the ratio of the evidences [11,24,14]. Values of B_{12} larger or smaller than one indicate a propensity for $\mathcal{M}_1$ or $\mathcal{M}_2$, respectively. In the literature several tables are available to assign, in addition to probabilities, degrees of propensity of favor to one or other model [11,26] with a correspondence to the p-value and the standard deviation [27].

For models with similar values of evidence, another criterium to decide between them is the Bayesian complexity $\mathcal{C}$, which measures the number of model parameters that the data can support [14]. This quantity is related to the gain of information (in the Shannon sense) and it is discussed in Appendix A. When E values are similar, we should favor the simplest model, i.e. the model with the smallest $\mathcal{C}$.

The possibility to assigning probabilities to models has another important advantage. In the case we are interested to determine the probability distribution of a common parameter a_j without the need to identify the correct model among the available choices $\mathcal{M}_\ell$, we can obtain the probability distribution $P(a_j|\{x_i,y_i\},I)$ from the weighted sum

$$P(a_j|\{x_i,y_i\},I) = \sum_\ell P(a_j|\{x_i,y_i\},\mathcal{M}_\ell,I) \times P(\mathcal{M}_\ell|,I), \tag{14}$$

where $P(a_j|\{x_i,y_i\},\mathcal{M}_\ell,I)$ are the probability distributions of a_j for each model and $P(\mathcal{M}_\ell|,I)$ are the probabilities of the different models. As we will see in Section 5.2, this capability plays an important role in the case where models have comparable probabilities.

3. The nested sampling algorithm

3.1. The evidence calculation problem

The major difficulty to calculate hypothesis probabilities is the substantial computational power required for the evaluation of the Bayesian evidence. Contrary to the maximum likelihood method, where only the maximum of a function has to be found, we have to calculate an integral over the J-dimensional space of parameters $V_{\boldsymbol{a}}$. Except in very few cases, there is not analytical solution of Eq. (12). Numerical integration by quadrature is not efficient due to the span of different order of magnitude of the likelihood function and the high dimensionality of the problem. The calculation of the evidence is then generally done via the Monte Carlo sampling of the product $P(\{x_i,y_i\}|\boldsymbol{a},\mathcal{M},I)P(\boldsymbol{a}|\mathcal{M},I)$.

A common approach to produce good sampling is the use of the Markov chain Monte Carlo (MCMC) technique. A Markov chain is a sequence of random variables such that the probability of the nth element in the chain only depends on the value of the $(n-1)$th element. The purpose of the Markov chain is to construct a sequence of points $\boldsymbol{a}_n$ in the parameter space whose density is proportional to the posterior probability distribution. Different probabilistic algorithms are applied to build these chains like Metropolis-Hasting algorithm, Gibbs sampling, Hamiltonian Monte Carlo, etc. (see as example Ref. [28] and references their-in).

Another method is the *nested sampling*, originally developed by John Skilling in 2004 [29,24,30]. On this method is based the program `Nested_fit`, the Bayesian data analysis program we present

[1] *"Non sunt multiplicanda entia sine necessitate"*, "Entities must not be multiplied beyond necessity" from William of Ockham's (1287–1347), which can be interpreted in a more modern form as "Among competing hypotheses, the one with the fewest assumptions should be selected".

in this article. The method algorithm is based on the subdivision of the parameters space volume $V_{\boldsymbol{a}}$, delimited by the parameters prior probabilities, into J-dimensional nested volumes that get closer and closer to the maxima of the likelihood function. With this method, the calculation of the evidence (Eq. 12) is reduced to a one-dimensional integral from the original J-dimensional problem.

To reduce to a one-dimensional integral, we define the variable X (real and positive) corresponding to the volume of the parameter space, weighted by the priors, for which the likelihood function is larger than a certain value $\mathcal{L}$:

$$X(\mathcal{L}) = \int_{L(\boldsymbol{a})>\mathcal{L}} P(\boldsymbol{a}|I)d^J\boldsymbol{a}. \tag{15}$$

A schematic visualisation of this relation is presented in Fig. 1. $X(\mathcal{L})$ is by construction monotonic and invertible, with $\mathcal{L} = \mathcal{L}(X)$. When $\mathcal{L} = 0$, the whole parameter volume $V_{\boldsymbol{a}}$ is considered and then $X = 1$ because of the prior probability normalization. When $\mathcal{L} \geqslant \max[L(\boldsymbol{a})], X$ is equal to zero. The infinitesimal volume dX is

$$dX = P(\boldsymbol{a}|I)d^J\boldsymbol{a}, \tag{16}$$

where $P(\boldsymbol{a}|I)d^J\boldsymbol{a}$ corresponds to the infinitesimal weighted volume of the parameter space where $\mathcal{L}(X) < L(\{x_i, y_i\}, \boldsymbol{a}) < \mathcal{L}(X + dX)$.

With the above definitions, we can then rewrite Eq. (12) as a simpler one-dimensional integral in X:

$$E = \int_0^1 \mathcal{L}(X)dX. \tag{17}$$

3.2. The algorithm for the numerical integration

The one-dimensional integral in the above equation and represented on the left part of Fig. 1 can be numerically calculated using the rectangle integration method subdividing the $[0, 1]$ interval in $M + 1$ segments with an ensemble $\{X_m\}$ of M ordered points $0 < X_M < \ldots < X_2 < X_1 < X_0 = 1$. Eq. (17) is approximated by the sum

$$E \approx \sum_m \mathcal{L}_m \Delta X_m, \tag{18}$$

where $\mathcal{L}_m = \mathcal{L}(X_m)$ and $\Delta X_m = X_m - X_{m+1}$. The difficulty is now the determination of $\mathcal{L}_m$ and ΔX_m because we do not know a priori the relation between X and $\mathcal{L}$.

The evaluation of $\mathcal{L}_m$ values is obtained by the exploration of the likelihood function with a Monte Carlo sampling via a subsequence of steps. For this, we use a collection of K parameter values $\{\boldsymbol{a}_k\}$ that we call *live points*. At the beginning, these values are randomly chosen from the prior probability distribution $P(\boldsymbol{a}_k|I)$ and they evolve during the computation steps described in the following paragraphs.

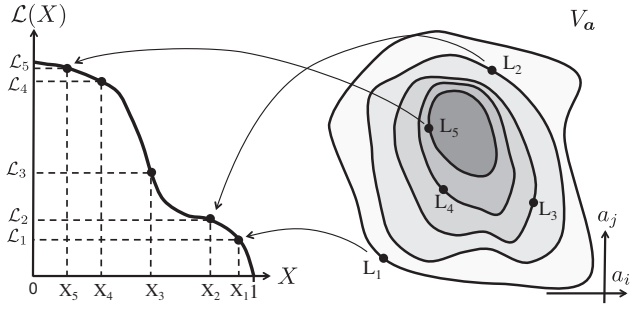

Fig. 1. Visualisation of the integral of $\mathcal{L}(X)$ and corresponding volumes on the parameter space (two parameters only, a_i, a_j are considered with a 2D representation).

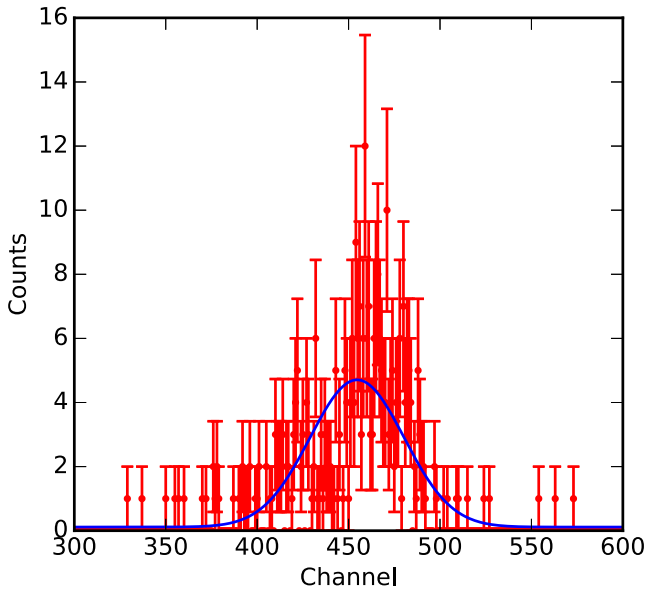

Fig. 2. High-resolution X-ray spectrum of the helium-like uranium $1s2p\ ^3P_2 \rightarrow 1s2s\ ^3S_1$ intrashell transition from Ref. [31] and corresponding fit with one Gaussian peak (plus a flat background).

To clearly present the different stages of the algorithm, we consider a real analysis of a very simple case. We assume a Gaussian peak plus a flat background (four parameters in total) as model and a very statistical poor data set. The data refer to a high-resolution X-ray spectrum of the helium-like uranium $1s2p\ ^3P_2 \rightarrow 1s2s\ ^3S_1$ intrashell transition obtained by Bragg diffraction from a curved crystal [31]. The data and the best guess (maximum likelihood) of Gaussian peak profile are shown in Fig. 2.

For each computation step m of the algorithm we indicate with $\{\boldsymbol{a}_{m,k}\}$ the live points of the step, with $k = 1, \ldots, K$. The corresponding likelihood function values are indicated by $\mathcal{L}_{m,k} = L(\boldsymbol{a}_{m,k})$ and we define $\mathcal{L}_m = \min(\mathcal{L}_{m,k})$. The related X values are indicated by $\xi_{m,k} = X(\mathcal{L}_{m,k})$ and we define $X_m = \max(\xi_{m,k})$. Considering Eq. (15) and Fig. 1, we see that X_m is equal to the integral of the volume where all $\{\boldsymbol{a}_{m,k}\}$ are contained. In other words, the volume $V_{L\geqslant\mathcal{L}_m}$ in the parameter space corresponds to the segment $[0, X_m]$ in the X axis. Let us see the different steps of the algorithm in details.

Step 1: The initial $\{\boldsymbol{a}_{1,k}\}$ live points are sorted considering $P(\boldsymbol{a}_k|I)$ and $\mathcal{L}_1 = \min(\mathcal{L}_{1,k})$ is found. From $\xi = X(\mathcal{L})$ relationship, we have $X_1 = \max(\xi_{1,k})$ and the $\Delta X_1 = X_0 - X_1$, where $X_0 = 1$. We have now our first pair of values for the sum in Eq. (18).

Step 2: We built now a new ensemble of live points $\{\boldsymbol{a}_{2,k}\}$, which is the same as $\{\boldsymbol{a}_{1,k}\}$ but where we remove the k'-th element with the lower value of likelihood (corresponding to the higher value of X, i.e. where $\mathcal{L}_1 = L(\boldsymbol{a}_{1,k'})$ with $X_1 = \xi_{1,k'}$, and we store its value with the name $\tilde{\boldsymbol{a}}_1 = \boldsymbol{a}_{1,k'}$. We replace this point with a new $\boldsymbol{a}$ value, randomly chosen with the only condition $L(\boldsymbol{a}) > \mathcal{L}_1$. With this requirement we impose that this point is inside the volume $V_{L\geqslant\mathcal{L}_1}$. From this new ensembles $\{\xi_{2,k}\}$ and $\{\mathcal{L}_{2,k}\}$ we define $X_2 = \max(\xi_{2,k})$. The interval $[0, X_2]$ corresponds to the volume of the parameter space $V_{L\geqslant\mathcal{L}_2}$ nested in the volume $V_{L\geqslant\mathcal{L}_1}$ (see Fig. 1). We have then the elements $\mathcal{L}_2, \Delta X_2$ of the sum in Eq. (18) and we store the value of the discarded live point $\tilde{\boldsymbol{a}}_1$.

Step m: We continue the iteration as in the step 2, storing at each step the values $\mathcal{L}_m, \Delta X_m$ and $\tilde{\boldsymbol{a}}_m$. All new live points $\{\boldsymbol{a}_{m,k}\}$ are enclosed in smaller and smaller parameter volumes defined by $L(\boldsymbol{a}) > \mathcal{L}_m$ that correspond to $[0, X_m]$ intervals (see Fig. 1) with $X_m = \max(\xi_{m,k})$.

Please cite this article in press as: M. Trassinelli, Bayesian data analysis tools for atomic physics, Nucl. Instr. Meth. B (2017), http://dx.doi.org/10.1016/j.nimb.2017.05.030

Step M, the end: After M iterations, the estimated error Err_M on the evidence E evaluation due to the truncation of the sum in Eq. (18) is less than the target accuracy ΔE and the calculation stops. For each step m, Err_m is upper limited by the product $L_{max}X_m$ where $L_{max} = \max[L(\boldsymbol{a}_{m,k})]$. When $L_{max}X_m < \Delta E$, we have $Err_m < \Delta E$, the main iteration loop of the nested algorithm stops and the main calculation is finalized. The likelihood function value associated to the last live points is the average $\mathcal{L}_M = \langle L(\boldsymbol{a}_{M,k})\rangle$.

In addition to the final live points $\{\boldsymbol{a}_{M,k}\}$ and their likelihood function values, all intermediate $\mathcal{L}_m, \Delta X_m, \tilde{\boldsymbol{a}}_m$ are stored and used for the calculation of the posterior probability distributions as presented in Section 3.3.

For the specific example where we consider the analysis of the data in Fig. 2 and a Gaussian peak as model, we show in Fig. 3 the evolution of the values of the $\tilde{\boldsymbol{a}}_m$, corresponding in this example to the peak position, as function of the algorithm step number. Starting from a sampling range corresponding to our priors (here a flat distribution between channel 300 and 600), the algorithm explores smaller and smaller ranges corresponding to nested volumes of the parameter space. The product $\mathcal{L}_m\Delta X_m$ relative to each steps are shown in both plots of Fig. 4 via the value $weight = \mathcal{L}_m\Delta X_m/E$ (see next section for further explanation).

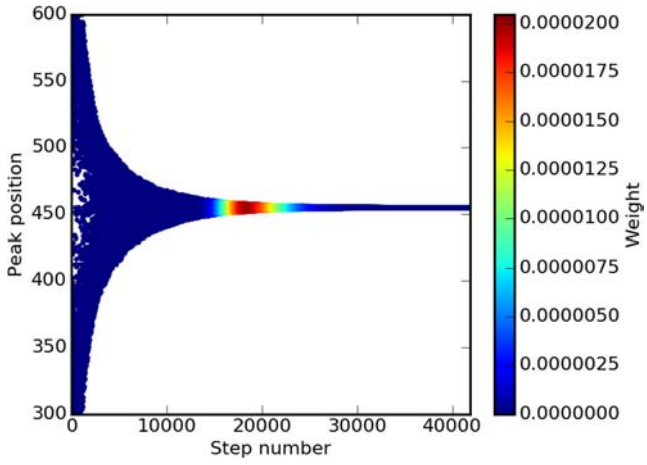

Fig. 3. Evolution of the sampled parameter value relative to the peak over the algorithm step.

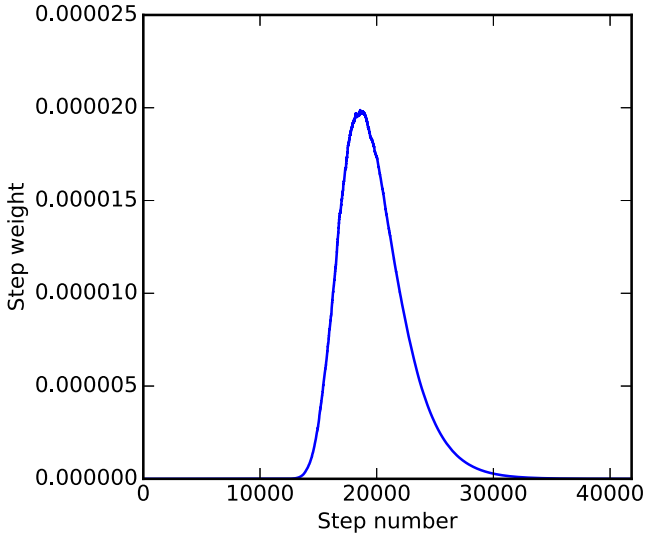

Fig. 4. Weights associated to discarded value at each step, which are proportional to the product $\mathcal{L}_m\Delta X_m)$].

We have now a recipe for calculating $\mathcal{L}_m$ values but not the X_m. In the previous paragraphs we defined $X_m = \max[X(\mathcal{L}_{m,k})]$ using Eq. (15). But we do not know the function $X(\mathcal{L})$ and neither its inverse $\mathcal{L}(X)$. We can, however, estimate the values of X_m from some statistical consideration. The extraction of a set of K live points $a_{m,k}$ in the parameter volume $V_{L(a)>\mathcal{L}_m}$ correspond to sort K random numbers in the interval $[0, X_m]$ (with $\xi_{m,k} = X[L(a_{m,k})]$). For each step, when we pass from the $[0, X_{m-1}]$ interval to the $[0, X_m]$ interval, we shrink the volume (one-dimensional here) by a factor $t_m = X_m/X_{m-1}$. The probability distribution for each t_m is equal to the probability for having a maximum value t given K random numbers $\in [0, 1]$. The statistical distribution of t is (see Appendix B for more details)

$$P(t) = Kt^{K-1}, \quad \text{with} \quad \langle \ln t\rangle = -1/K. \tag{19}$$

For the first and second step we have $X_1 = t_1$ ($X_0 = 1$) and $X_2 = t_2X_1 = t_1t_2$. For a generic step, considering Eq. (19), X_m is given by the product

$$X_m = \prod_i^m t_i \quad \text{and then} \quad X_m \approx e^{-m/K}. \tag{20}$$

From this equation, the values of ΔX_m can be estimated, with $\Delta X_M = e^{-M/K}$ for the last live points. This approximation introduces an error in the evidence calculation that is proportional to $1/\sqrt{K}$, where K is the number of the employed live points. A detailed discussion of the evidence uncertainty is presented in Appendix B.

We note that for the final calculation of the evidence, the terms $\mathcal{L}_m, \Delta X_m$ in Eq. (18) are not equally important. ΔX_m values are monotonically decreasing with m where $\mathcal{L}_m$ values are increasing. As we can see from Fig. 3, the product $\mathcal{L}_m\Delta X_m$ (which defines the step weight as we will see next section) has a maximum. $\tilde{a}_m$ corresponding to this maximum will strongly influence the posterior probability distributions and the value of the evidence.

The bottleneck of the nested sampling algorithm is the search of new points within the J-dimensional volume defined by $L > \mathcal{L}_m$. Different methods are commonly employed to accomplish this difficult task. One efficient method is the ellipsoidal nested sampling [32]. It is based for each step on the approximation of the iso-likelihood contour defined by $L = \mathcal{L}_m$ by a J-dimensional ellipsoid calculated from the covariance matrix of the live points. The new point is then selected within the ellipsoidal volume (times an user-defined enlargement factor). This methods, well adapted for unimodal posterior distribution has been also extended to multimodal problems [33,15], i.e. with the presence of distinguished regions of the parameter space with high values of the likelihood function. Other search algorithms are based on Markov chain Monte Carlo (MCMC) methods [34], as in particular the *lawn mower robot* method, developed by L. Simons [35], and the recent *Galilean Monte Carlo* [36,37], particularly adapted to explore the regions close to the boundary of $V_{L>\mathcal{L}_m}$ volumes. `Nested_fit` program is based in an evolution of Simons' algorithm and is presented in Section 4.

Additional material on the nested sampling can be found in Refs. [29,24,30,32,15,34]. In particular in Ref. [38], the different search algorithms, their efficiency and accuracy are discussed.

3.3. Posterior probability distributions

The posterior probability distributions are built from the discarded live points $\tilde{a}_m$, the final set of K live points $a_{M,k}$ and their associated $\mathcal{L}_m, \Delta X_m$ values.

Once the evidence $E \equiv P(\{x_i, y_i\}|I)$ is determined, posterior inference can be easily generated from the $\{\tilde{a}_m\}$ and $\{a_k\}_M$ values. Each $\tilde{a}_m$ is in the infinitesimal parameter volume $\Delta V_{\mathcal{L}_m<L(\tilde{a}_m)<\mathcal{L}_{m+1}}$

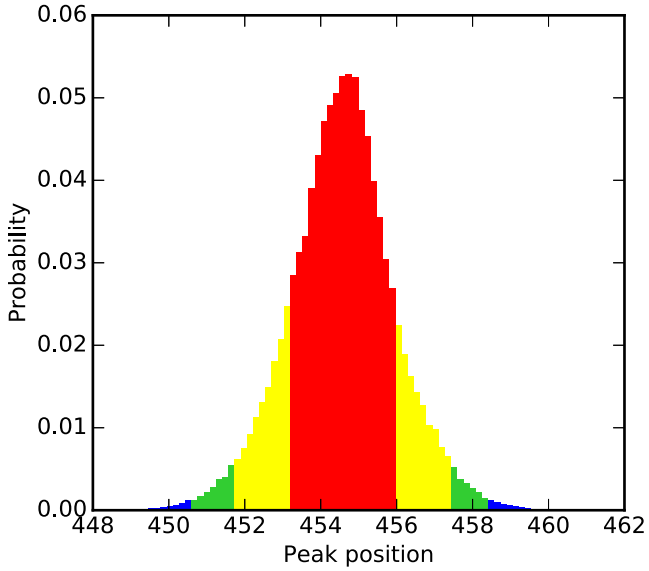

Fig. 5. Histogram of the Gaussian peak position built from the values $\mathcal{L}_m, \Delta X_m$, and $\tilde{a}_m$ (see text). Red, yellow and green regions indicate 68%, 95% and 99% confidence intervals (credible intervals). (For interpretation of the references to colour in this figure caption, the reader is referred to the web version of this article.)

that correspond to the interval ΔX_m. Considering the discrete form of Eq. (16) and Eq. (10), we can calculate the probability associated to the parameter values $\tilde{a}_m$, in other words the step *weight* named in the previous sections:

$$P(\tilde{a}_m|\{x_i, y_i\}, I) = P(X_m) \approx \frac{\mathcal{L}_m \Delta X_m}{E}. \tag{21}$$

From Eq. (21), the probability distribution of any single parameter a_j is obtained by marginalization Eq. ((8)), i. e. integrating of the posterior probability $P(a|\{x_i, y_i\}, I)$ over the other parameters.

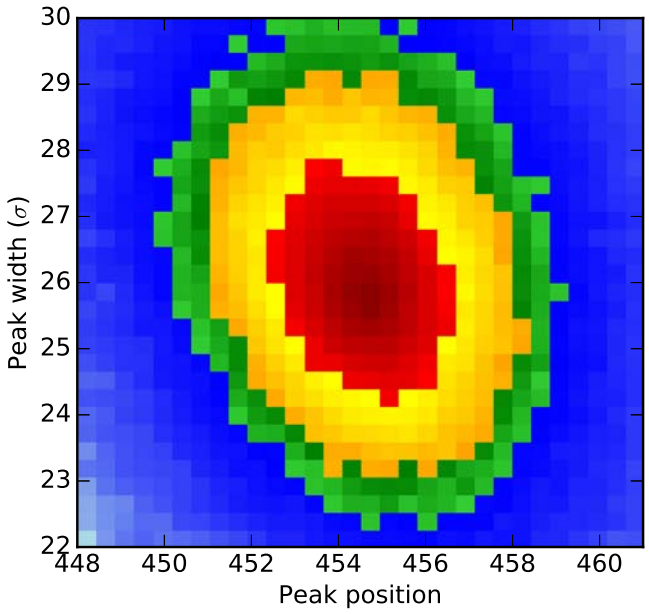

Fig. 6. Joint probability distribution of the parameters relative to the peak position and width (in terms of sigmas of the Gaussian profile). Red, yellow and green regions indicate 68%, 95% and 99% confidence intervals (credible intervals). (For interpretation of the references to colour in this figure caption, the reader is referred to the web version of this article.)

In our case, if the parameter of interest corresponds to the j^{th} component, its probability distribution can be built from $(\tilde{a}_m)_j$ values and their corresponding weights defined by Eq. (21).

For our specific example with a Gaussian distribution as a model, this corresponds to take $(\tilde{a}_m)_j$ values showed in Fig. 3 (top) and built a weighted histogram (with the weights $\mathcal{L}_m \Delta X_m / E$ showed by the different color intensities in Fig. 3 and in Fig. 4). From the marginalization on $J - 2$ parameters, also joint probabilities can be built, as that one presented in Fig. 6 corresponding to the position and width distribution of the peak.

4. The `Nested_fit` program

4.1. General considerations

`Nested_Fit` has been developed in Fortran90 for the calculation of the Bayesian evidence and posterior parameters probability distributions for a given set of data and selected model. The core of `Nested_Fit` is the algorithm used for the calculation of the Bayesian evidence which is, as indicated by its name, the nested sampling developed by Skilling and presented in Section 3, but with an original method to find new live points.

Due to the large span of the values of the different quantities (likelihood function, evidence, X_m, etc.), all computations are done with respect to their logarithms, as many programs based on the nested sampling. The data inputs are provided in the form $\{x_i, y_i\}$, where x_i are real numbers and y_i are necessarily counts detected at the channels x_i. To analyze statistically poor (but also not-poor) data sets, the likelihood function is built considering a Poissonian statistics for each channel (which tend to the normal distribution for large number of counts), leading to

$$L(a) = \prod_i \frac{F(x_i, a)^{y_i} e^{-F(x_i,a)}}{y_i!}, \tag{22}$$

where for each channel, y_i is the recorded number of counts and $F(x_i, a)$ is the expected value of the modeling function that depends on the parameters a. A large library of functions is available and new *ad hoc* functions can easily be added.

Outputs of `Nested_Fit` include the evaluation of the Bayesian evidence, the corresponding information gain and complexity, and the information to build parameter probability distributions. The different probability histograms and other plots are produced via a series of functions of a dedicated Python library. The figures of this article are examples of their typical outcomes. In addition to the graphic outputs, Python library functions can be used to recursively modify the input file `nf_input.dat` and to read the results in the output files. These functions are particularly useful for automated analysis and systematic surveys.

Several set of data can be analyzed at the same time by `Nested_Fit` program. For example, distinct spectra with a same response function can be analyzed, and common parameters such as the profile width can be extracted by correctly taking into account the correlations between data sets.

4.2. Computation algorithm of the Bayesian evidence

The calculation of the Bayesian evidence is made with the nested sampling following the steps presented in Section 3, similarly to other programs based to the same algorithm [24,32,33,15,34]. Even if the basic structure is practically identical to existing codes, the algorithm for the search of new live points is substantially different. The searching algorithm is a Markov chain Monte Carlo method to explore the parameter volume $V_{L>\mathcal{L}_m}$ and it is an evolution of the *lawn mower robot* method, developed by

Please cite this article in press as: M. Trassinelli, Bayesian data analysis tools for atomic physics, Nucl. Instr. Meth. B (2017), http://dx.doi.org/10.1016/j.nimb.2017.05.030

L. Simons [35]. To cancel the correlation between the starting point and the final point, a series of N jumps are done in this volume. The different stages of the algorithm are.

1. Choose randomly a starting point $a_{n=0} = a_0$ from the available live points $\{a_{m,k}\}$ as starting point of the Markov chain where n is the number of the jump. The number of tries n_t (see below) is set to zero.
2. From the values a_{n-1}, find a new parameter sets a_n where each j^{th} parameter is calculated by $(a_n)_j = (a_{n-1})_j + f\ r\ \sigma_j$, where σ_j is the standard deviation of the live points $\{a_{m,k}\}$ relative to the j^{th} parameter, $r \in [-1, 1]$ is a sorted random number and f is a factor defined by the user.
   (a) If $L(a_n) > \mathcal{L}_m$ and $n < N$, go to the beginning of step 2 with an increment of the jump number $n = n + 1$.
   (b) If $L(a_n) > \mathcal{L}_m$ and $n = N, a_{n=N}$ is new *live point* to be included in the new set $\{a_{m+1,k}\}$.
   (c) If $L(a_n) < \mathcal{L}_m$ and $n < N$ and the number of tries n_t is less than the maximum allowed number N_t, go back to beginning of step 2 with an increment of the number of tries $n_t = n_t + 1$.
   (d) If $L(a_n) < \mathcal{L}_m$ and $n < N$ and $n_t = N_t$ a new parameter set a_0 has to be selected. Instead than choosing one of the existing live points, a_0 is built from distinct j^{th} components from different live points: $(a_0)_j = (a_{m,k})_j$ where k is randomly chosen between 1 and K for each j. Then $a_{n=0} = a_0$ and go to the beginning of step 2.

The last step makes the algorithm well adapted to problems with multimodal parameter distributions allowing to easily jump between high-likelihood regions. An example of presence of several maximal likelihood regions is presented in Fig. 7 where we plot the joint probability of the position and amplitude of one of the four Gaussian peaks of the considered model. The value of N_t is fixed in the code ($N_t = 10,000$ in the present version). The other parameters can be provided by the input file.

4.3. Inputs

All input parameter required by `Nested_fit` are provided in the file `nf_input.dat`. The most important inputs are:

The maximum number of jumps N and the real number f: These parameters are important for efficiency of the search of the new live points and for the non-correlated and efficient exploration of the parameter space. A higher value of f guarantees a better independence between the current live points and the new point but also a minor efficiency for finding it because of the higher probability to jump in the volume region $L < \mathcal{L}_m$. The same reasoning applies for the total number of jumps N.

The number of live points K: The choice of K influence directly the expected accuracy of the evidence $\delta E \propto 1/\sqrt{K}$, and also provides a better sampling of the parameter volume. As counterpart, an increasing of K increases the computation time.

The required final evidence accuracy ΔE: A too large value of the accuracy will bias the evidence calculation. A too small value can make the evidence computation significantly long. For a given problem, the optimal value is obtained by looking a posteriori at the evolution of $\mathcal{L}_m \Delta X_m$. The calculation has to stop significantly far from the region where the product $\mathcal{L}_m \Delta X_m$ is large, i. e. far from the most influent values of $X \sim \exp(-\mathcal{H})$ where $\mathcal{H}$ is the extracted information (in the sense of Shannon, see Appendies A and B). Good and efficient values are generally between 10^{-3} and 10^{-5} as also discussed in Ref. [34].

The number of trials sets of live points N_{LPS}: Besides theoretical considerations, the best strategy to estimate the evidence accuracy is to calculate E several times with different starting sets of live points (with different seed for the random generator) and to extract the mean and standard deviation of the logarithmic values of the computed evidence, which is the pertinent quantity for the uncertainty evaluation (see Appendix B). In addition this method provides more sampling points of the parameter space for a better evaluation of the posterior probability distributions, especially important when multimodal distributions are present.

The parameter priors Priors of the different parameters can be selected between two options: (i) an uniform prior where the parameter value boundaries have to be provided or (ii) a normal distribution where a main value and the associated standard deviation have to be provided (as example from a past experiment).

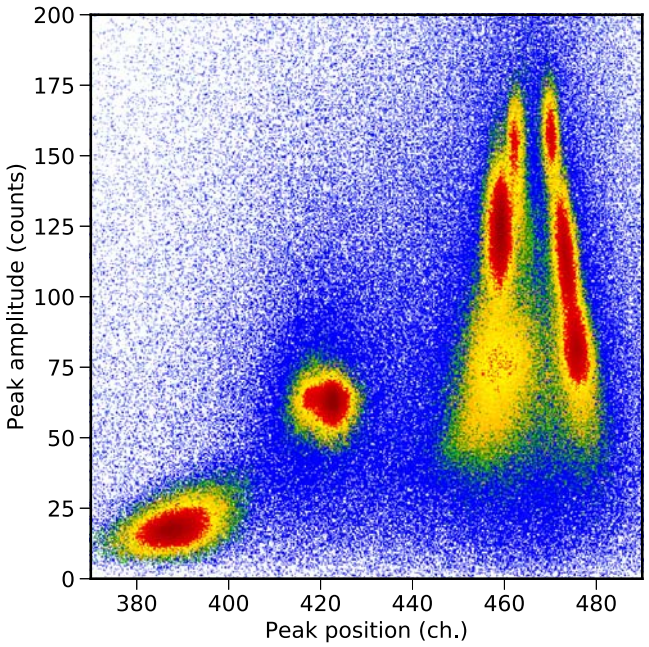

Fig. 7. Joint probability distribution of the parameters relative to the position and amplitude of one peak in four Gaussian peaks model. Eight distinct likelihood maxima can be identified. Red, yellow and green regions indicate 68%, 95% and 99% confidence intervals.

Except for the priors, each parameter has to be tuned by looking the output in order to have valuable results (to uniformly and randomly cover the entire parameter space) but also to have a fast calculation (a good efficiency to find new live points). For this goal, the most sensitive parameters are the number of live points K, the number of jumps N and the real number f.

4.4. Outputs

Once ended, the program provides four major output files described below.

- `nf_output_res.dat` contains the details of the computation (n. of live points trials, n. of total iteration), the final evidence value and its uncertainty $E \pm \delta E$, the parameter values $\hat{a}$

corresponding to the maximum of the likelihood function, the mean, the median, the standard deviation and the confidence intervals (68%, 95% and 99%) of the posterior probability distribution of each parameter. Moreover, the information gain $\mathcal{H}$, the Bayesian complexity $\mathcal{C}$ and the theoretical minimal value of the required iteration number deduced from the computed information gain $\mathcal{H}$, also provided in the output. δE is calculated only if $N_{LPS} > 2$.

- `nf_output_data.dat` contains the original input data together with the model function values corresponding to the parameters $\hat{a}$ with the highest likelihood function value, the residuals and the uncertainty associated to the data.
- `nf_output_tries.dat` is present only if $N_{LPS} > 2$. For each live points trial, it contains the final evidence, the number of iterations and the maximum value of the likelihood function.
- `nf_output_points.dat` contains all discarded and final live points values $\tilde{a}_m$ and $\{a_{M,k}\}$, their associated likelihood values $L(a)$ and posterior probabilities $P(a|\{x_i, y_i\}, I) \approx \mathcal{L}_m \Delta X_m / E$. From them, the different parameter probability distributions, as shown in Fig. 5, or joint probabilities, as shown in Figs. 6 and 7, can be built from the marginalization Eq. (8) of the unretained parameters.

5. Two examples

In this section we will present two practical applications of the statistical analysis methods described above. In the first one, we calculate the probability of the presence or not of a satellite line in a spectrum at a well defined position but with unknown intensity. The second, more complex, consists in the analysis of a statistically poor set of data for which we would like to determine the most probable model among different possibilities and to extract the position of the main component.

5.1. Satellite line contamination

We consider a common case in spectroscopy where we would like to test the presence or not of an unresolved weak spectral line close to a intense line. In this specific example, we consider the $5g - 4f$ transition in pionic nitrogen, an hydrogen-like atom formed by a nitrogen nucleus and a negatively charged pion. During the formation of the pionic atoms, all electrons are expected to be ejected. The presence of a remaining electron in the K shell cannot completely be excluded. Its presence can cause a shift of the main tradition energy due to the Coulomb screening and then an appearance of a new component in the spectrum. To determine the probability of such a scenario, we have to calculate the evidence for the two possible models: Model 1 without remaining electrons (a pure hydrogen-like pionic atom) and Model 2 with the possible presence of one remaining electron. More details on the physics case can be found in Refs. [39,40].

The examined data consist in seven distinct spectra similar to the one represented in Fig. 8 with a total of about 60000 recorded counts. Each spectra is obtained by a Bragg spectrometer equipped by a spherically bent crystal. The evidence and probability distributions of both models are computed with `Nested_fit` taking into account all seven spectra at the same time. For this specific propose we used $K = 1000$ live points and an accuracy requirement $\delta E = 10^{-5}$. For the search of the new points we choose the values $J = 20$ jumps and $f = 0.1$. These parameters insure an efficient and complete exploration of the parameter space and an accurate evaluation of the evidence. For a rough estimation of the evidence uncertainty we consider $N_{LPS} = 8$ different live point trial sets. For both models, we chose flat prior probability distributions for the different parameters. Compared to model 1, model 2 has only as additional free parameter the satellite line intensity whose relative position with respect to the main line has been fixed by the theory.

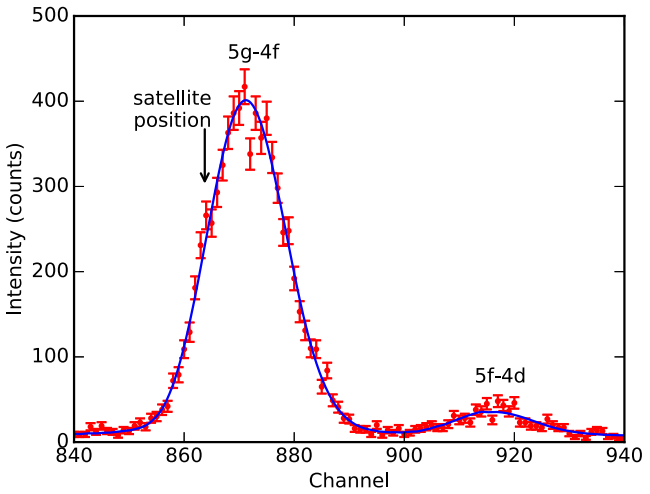

Fig. 8. Pionic nitrogen $5 - 4$ transitions. Possible additional transitions from the presence of one remaining electron in the K shell are indicated.

Since we have to choose among two models only, the relevant quantity to calculate is the Bayes factor B_{12}, defined in Section 2.3, from which we can determine the criterium in favor to one of the two hypothesis.

From the output of `Nested_fit`, we obtain $\ln B_{12} = 6.6 \pm 1.8$, which correspond to a probability of 99.98% in favor to the model without remaining electrons (between 99.86% and 100% when the Bayes factor uncertainty is taken into account). This Bayes factor value indicates a decisive support for the Model 1 hypothesis considering any considered scale ("decisive" in the Jeffreys scale [11], "very strong" in the Kass scale [26] or "strong" in the Gordon-Trotta scale [27]) with an equivalent p-value of about 10^{-5} for Model 2 [27].

In conclusion, the presence of remaining electrons can be safely excluded and the main line position can be reliably evaluated. Additional discussion on this analysis can be found in Ref. [40].

5.2. A nasty peak

In this second example we consider the experimental data already presented in Section 4 corresponding to the helium-like uranium $1s2p\ ^3P_2 \rightarrow 1s2s\ ^3S_1$ intrashell transition obtained from a Bragg diffraction spectrometer equipped by a curved crystal [31]. As can be seen in Fig. 9, the experimental peak is statistically poor, quite broad and asymmetric. We do not know where this asymmetry comes from. Eventually, it might be related to the presence of several spectral components or from spectrometer's aberrations. From the Bayesian analysis we would like i) to determine the most probable model that describes the data and ii) to determine the probability distribution of the main spectral component position, independently on the choice of the model.

For each model, we calculate with `Nested_fit` the evidence, the probability distributions and the complexity using the same parameters as in the previous example except for the number of live points and the number of trial sets. Here we use $K = 2000$ live points and N_{LPS} between 8 and 32 depending on the model. For all models, we chose flat prior probability distributions.

First we consider the simple case where we can have only Gaussian peaks, between one and four, with the same width σ, which we know to be a priori between 10 and 30 channels, and a flat background. From these working hypotheses, we would like to determine which model is the most probable. i.e. how many peaks

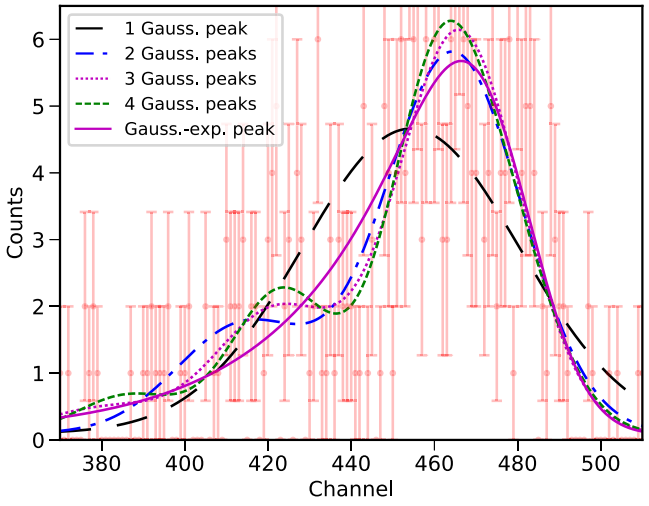

Fig. 9. Profile curves corresponding to the likelihood maxima of the different models (1–4 Gaussian peaks and Gaussian-exponential peak).

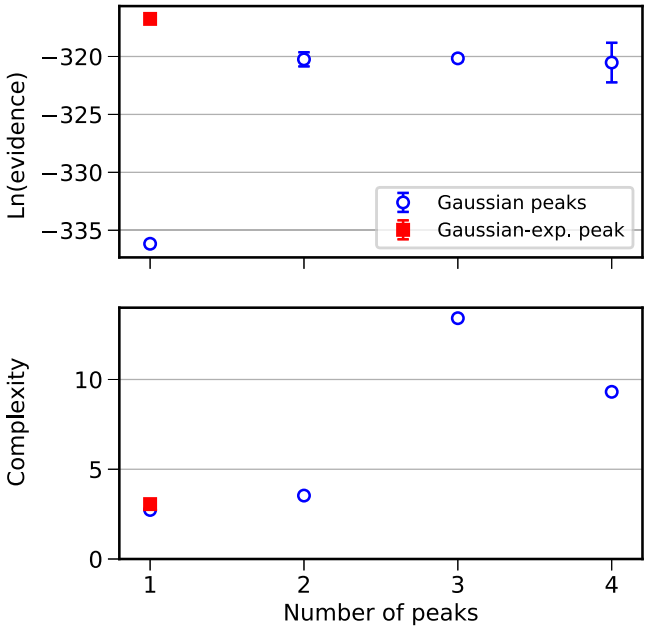

Fig. 10. Evidence and complexity of the different considered models.

are present, and what is the position of the main peak. To note, the model with four Gaussian peaks requires for any single trial set much more computation time than the single peak due to the presence of several high-value likelihood regions (see Fig. 7). This is in fact the practical reason why we consider a maximum of four components. Similar examples have been presented in the past by Sivia [41,24]. With respect to these works, here we consider the analysis of a statistically poor data set from a real experiment instead of a simulation, where we do not know the real nature of the spectra.

To visually compare the outcome of the different models, we present in Fig. 9 the corresponding curves relative to each likelihood function maximum. As it can be observe, the profile maxima are close to each other except for the single Gaussian peak profile. In the particular case of the 4-peak model, two Gaussian component are unresolved (as suggested by Fig. 11).

The quantitative results obtained from `Nested_fit` are summarized in Table 1 and Fig. 10 where we report values of the evidence (in the logarithmic scale), of the model complexity and the probability of the model (in the table only). The model with a single Gaussian peak results to have a very low probability. From the results of the other hypotheses, we cannot clearly determine how many peaks are present because models with 2, 3 and 4 components have the same evidence (within the associated uncertainty). As suggested by Trotta [14], a criterium to choose between different models with similar evidence is the Bayesian complexity $\mathcal{C}$ value (see Section 2.3 and Appendix A). When different hypotheses have similar evidence values, we should choose the model with the lower value of $\mathcal{C}$ to favor once more simple models versus complex models, in agreement to the Ockham's razor principle. In our case, the two-peak model is the favorite with a low complexity value, only slightly higher than the one-peak model complexity, and high probability.

If we are not interested to determine the number of peaks, but only to the main peak position component μ_0, we can built the correspondent probability distribution $P(\mu_0|\{x_i, y_i\}, I)$ from the output of the each model analysis. As in Eq. (14), we can build $P(\mu_0|\{x_i, y_i\}, I)$ from the different $P(\mu_0|\{x_i, y_i\}, \mathcal{M}_\ell, I)$ distributions using as weight the model probabilities summarized in Table 1. The final probability distribution of the main peak position (around channels 450–480) is presented in Fig. 11. It is quite complex, with the presence of several maxima mainly due to the four-peak model contribution. These maxima correspond in fact to the high-likelihood regions visible in Fig. 7. Because of the low probability, the one-peak model does not contribute significantly to the final distribution. As comparison its contribution is presented in Fig. 11 with a strong magnification factor.

Alternatively to the presence of several Gaussian peaks, a valid hypothesis is the presence of some kind of aberration due to the spectrometer characteristics. A spectrometer with cylindrically bent crystal in the Johann geometry is in fact used. To take into account this possibility, we model the aberration effect by a line profile resulting from the convolution between a Gaussian and an exponential function [42]. As we can see in Fig. 9, the curve corresponding to the likelihood maximum reproduces well the data, with a maximum very close to the multi-Gaussian peaks models (with exclusion of the single peak model). From Table 1 and Fig. 10, we can observe more quantitatively that the associated

Table 1
For each model, the different probability values $P(\mathcal{M}|I)$ and related quantities are reported. In addition to the evidence value (in natural log), we report the model probability considering only Gaussian peaks ($P_{\text{G. models}}(\mathcal{M}|,I)$), a two-model probability with the two-Gaussian peak model as reference ($P_{\text{Two-models}}(\mathcal{M}|,I)$), the Bayesian complexity, the minimum value of reduced chi-square χ^2_{red} and the related probabilities (P_χ and P_F) from χ^2- and F-test.

Model	$\ln E$	$P_{\text{G. models}}$	$P_{\text{Two-models}}$	Complexity	χ^2_{red}	P_χ	P_F
1 Gauss. peak	-336.17 ± 0.19	4.3×10^{-8}	0.00001 %	2.7	0.8213	0.38885 %	10.1 %
2 Gauss. peaks	-320.25 ± 0.61	35.1%	–	3.5	0.7224	0.00081 %	–
3 Gauss. peaks	-320.16 ± 0.25	38.2%	52.1 %	13.4	0.7009	0.00014 %	61.7 %
4 Gauss. peaks	-320.52 ± 1.71	26.6%	43.1 %	9.3	0.7022	0.00017 %	61.0 %
1 Gauss.-exp. peak	-316.76 ± 0.12	–	97.0 %	3.1	0.7190	0.00060 %	48.1 %

Please cite this article in press as: M. Trassinelli, Bayesian data analysis tools for atomic physics, Nucl. Instr. Meth. B (2017), http://dx.doi.org/10.1016/j.nimb.2017.05.030

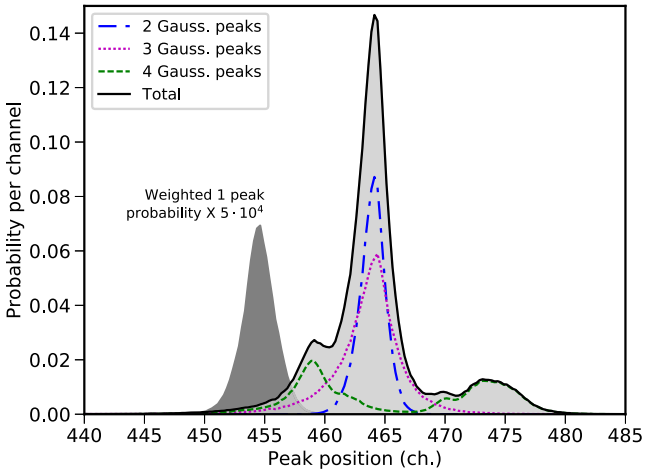

Fig. 11. Probability distribution of the main peak position from the single probabilities of the models with one-to-four Gaussian peaks. For the single peak model, we magnify its weighted probability (in grey) to compare the distributions.

evidence is significantly higher than any other model. With respect to the two-Gaussian peaks, the probability for the Gaussian-exponential profile is in fact $P_{\text{Two-models}}(\mathcal{M}|, I) = 97.0\%$. At the same time the associated complexity remains small, intermediate between single and double Gaussian peak models, indicating that, together with the high model probability value, the presence of an aberration as explanation of the asymmetry experimental data distribution is the most valid hypothesis.

To compare the results from the evidence analysis to classical goodness-of-fit tests such the χ^2-test and the F-test, for each model, we find the minimal χ^2 value using Minuit CERN library [43]. Due to the low statistics, we use a modified form of the χ^2 derived from the Poisson distribution [44] in a homemade Fortran program (called *Minuit_fit*) that uses Minuit library. For the χ^2-test, we compute the probability P_χ for obtaining a higher value of the reduced chi-square χ^2_{red}. The low statistics causes low values of χ^2_{red} (significantly less than one) and accordingly small values of P_χ for all models. For the F-test, we compute the probability P_F for obtaining higher values of the χ^2_{red} ratio between the selected model and the two-Gaussian model considered as reference. All values are reported in Table 1. For completeness, in the table we report in addition the two-model probability $P_{\text{Two-models}}(\mathcal{M}|, I)$ computed from the evidence of the selected model and the two-Gaussian model. When only Gaussian profiles are considered, both χ^2- and the F-test outcomes indicate that the single Gaussian peak model should be excluded, without a net preference of one of the multi-Gaussian peak models, similarly to the Bayesian analysis results. When the Gaussian-exponential model is considered in addition, the two approaches do not agree. In the comparison between Bayesian evidence values, the Gaussian-exponential has the highest probability. In opposite, the F-test indicates an unclear preference between the two-Gaussian and the Gaussian-exponential models. To note that the F-test as well as the χ^2 test are based on the probability for having a certain minimal value χ^2_{red} (i.e. maximum values of the likelihood function). In opposite, $P_{\text{Two-models}}(\mathcal{M}|, I)$ consider the ensemble of the likelihood function over the parameter space, which includes much more information. In addition we note that $P(\mathcal{M}|, I)$ are probabilities assigned to the different hypotheses calculated from the experimental data. P_χ and P_F are in contrary only probabilities linked to the statistical distribution of χ^2_{red} values that are used as criteria to favor one model with respect another. For this reason, they cannot be used to extract an average of a common parameter to the different models without selecting one precise model, which is possible from $P(\mathcal{M}|, I)$ values.

In the previous paragraphs we show how evidence and complexity evaluations can help to determine the most plausible model to describe a set of data. In this specific example, we remember that we consider a strong assumption on the number of the possible Gaussian peaks to mainly limit the computational time. Other hypotheses could be considered but always taking into account our prior knowledge coming from previous experiments or general physical considerations. Formally this prior knowledge should be included in the model prior probability that, once multiplied to the evidence, gives the final probability for the different models. For this point, critics could be addressed about the objectivity. But again, the meaning of such dependency on the priors should be pragmatically be interpreted as a message saying that the data quality is not sufficient to correctly analyze the problem and choose among different hypotheses. Nevertheless, this approach provide a well defined procedure to exclude unrealistic models with the comparison with the data via the evidence computation (as for the single-peak model) or, via prior probabilities, models that are not consistent with our present knowledge of physics and simply common sense, on which our logic is based.

6. Conclusions

The main intent of this article is to provide an useful starting point for the atomic physics community to use Bayesian methods for data analysis. For this propose, we provide a very synthetic and basic introduction to Bayesian statistics. We show how, from basic logic reasoning with requirement of consistency, a very general definition of probability can be constructed. This definition automatically implies the Bayes' theorem, which plays the central role for the prior probability inclusion. From this approach, we see how posterior probabilities can be simply calculated as well as probabilities for different hypotheses.

To visualize the practical consequences of the use of these new concepts, we show two atomic spectra analysis examples. In the first one we see how we can determine the presence or not of an unresolved spectral line. In the second, more complex, we calculate the probability of different possible models (different number of peaks and shapes) and we see how to extract valuable information (the main peak position in our case) from equiprobable hypotheses.

For hypotheses testing, the calculation of the Bayesian evidence from the experimental data is essential. Different methods are available in the literature to evaluate the Bayesian evidence. In this article we present in detail the nested sampling technique developed originally by J. Skilling in 2004 based on a particular for of Monte Carlo sampling of the model parameter space. We also present the newly developed program `Nested_fit` based on such a method but with a new parameter exploration algorithm. We show its capabilities and typical inputs and outputs.

As final general comment, we invite to use Bayesian methods to all cases where (i) hypotheses/models testing are involved and (ii) where constraints or prior knowledge on the model parameters are involved. As we saw, classical criteria based on goodness-of-fit tests can also be used. In this case only the minimal values of χ^2 are considered, and not their dependency on the entire possible range of parameter values. This can be dangerous for statistically poor data sets where small quantity of information is available. In addition, from goodness-of-fit test outputs, the average of a parameter common to the different models is impossible to

Please cite this article in press as: M. Trassinelli, Bayesian data analysis tools for atomic physics, Nucl. Instr. Meth. B (2017), http://dx.doi.org/10.1016/j.nimb.2017.05.030

compute without selecting one precise model. This issue is trivial with Bayesian statistics methods.

Acknowledgments

First of all we would like to express our deep gratitude to Leopold M. Simons who introduced us to the Bayesian data analysis and without whom this work could not have been started. We would like to sincerely thank also Nicolas Winckler for the numerous discussions about statistics and data analysis, and, together with Robert Grisenti, for the careful reading of the manuscript. This work has been developed in the context of several experiments; we would like to thank all members of the Pionic Hydrogen, FOCAL and GSI Oscillation collaborations and the ASUR group at the Institute of NanoSicence of Paris for support and discussions.

Appendix A. Information and complexity

The gain of knowledge we obtain from the analysis of experimental data can be quantified in terms of information $\mathcal{H}$, in the Shannon sense [45,46], comparing the posterior probability $P(a|\{x_i,y_i\},I)$ with the prior probability $P(a|I)$. The information gain, in units of nat,[2] is given by the so-called Kullback–Leibler divergence [47]

$$\mathcal{H} \equiv D_{KL} = \int P(a|\{x_i,y_i\},I) \ln\left[\frac{P(a|\{x_i,y_i\},I)}{P(a|I)}\right] d^D a. \tag{A.1}$$

Considering Eq. (10), D_{KL} can be written as

$$D_{KL} = -\ln E + \int P(a|\{x_i,y_i\},I) \ln L(a) d^D a, \tag{A.2}$$

which is nothing else that the negative logarithm of the evidence plus the average of the logarithmic value of the likelihood function.

From D_{KL} an interesting quantity can be derived that provides an additional criterion to compare models: the *Bayesian complexity* $\mathcal{C}$. $\mathcal{C}$ is calculated from the difference between D_{KL} and the "expected surprise" [14] from the data represented by the value $\hat{D}_{KL}$, with

$$\hat{D}_{KL} = -\ln E + \ln L(\hat{a}), \tag{A.3}$$

where $\hat{a}$ usually correspond to the posterior parameter mean values, or other possible estimators (ex. the likelihood function maximum or the posterior distribution medians) depending on the details of the problem.[3] The complexity is then defined as [6,14]

$$\mathcal{C} = -2(D_{KL} - \hat{D}_{KL}) = -2[\langle \ln L(a)\rangle - \ln L(\hat{a})], \tag{A.4}$$

where the symbol $\langle\ \rangle$ indicates the mean value. $\mathcal{C}$ gives in practice a measurement of the number of parameters that the data can support for a certain model $\mathcal{M}$ for a defined parameter priors [6,48].

For equiprobable models (similar evidence values), the comparison of Bayesian complexity can be used to choose in favor to one hypothesis or another. Considering two different models $\mathcal{M}_1$ and $\mathcal{M}_2$ with $E_1 \approx E_2$ and different number of parameters $J_1 < J_2$, we can have to cases [14]:

> $\mathscr{C}_1 < \mathscr{C}_2$: The quality of the data is sufficient to measure the additional parameters of the more complicated model, but they do not improve its evidence by much. We should prefer model with less parameters.
>
> $\mathscr{C}_1 \approx \mathscr{C}_2$: The quality of the data is not sufficient to measure the additional parameters of the more complicated model and we cannot draw any conclusions as to whether extra parameters are needed.

Appendix B. Theoretical uncertainty of the evidence calculation by nested sampling

The main uncertainty of the final evaluation of the evidence calculated by the nested sampling is, as stated by the author of this method J. Skilling, related to the probabilistic nature of the terms ΔX_m in Eq. (18) [24,30,49,34]. The choice of numerical integration of Eq. (17) (rectangle method, trapezoidal rule, etc.) does not influence very much the final result. Instead, the statistical glittering of ΔX_m in Eq. (18) introduces a significant error.

The interval values are calculated from $X_m = \prod_i^m t_i$ (Eq. (20)), where t_i are the shrinking of the considered interval of X. The statistical distribution of the shrinking values t_i can be obtained from simple probabilistic considerations. For each step m, the shrinking value is derived from the $\{\xi_{m,k}\}$ values of X that correspond to the K considered live points. The K randomly sorted live points correspond the K values $\{\xi_{m,k}\}$ that are uniformly distributed in the interval $[0, X_m]$. To pass to the $m+1$ step, we have to identify the maximum value of $\{\xi_{m,k}\}$ to determine the shrinking factor $t_{m+1} = \max(\xi_{m,k}/X_m)$. This correspond to find the maximum of K values $\{x_k\}$ uniformly distributed in the interval $[0,1]$ (where $x_k = \xi_{m,k}/X_m$).

Considering a certain $x_{k'} = t$, the probability that all other values are less than t is $\prod_{k\neq k'} P(x_k \in [0,t]) = t^{K-1}$. Because this is valid for any $x_{k'} \in \{x_k\}$, we have

$$P(t = \max\{x_k\}) = K t^{K-1}. \tag{B.1}$$

This probability distribution has the following properties. The average and standard deviation of $\ln t$ are

$$\langle \ln t\rangle = -\frac{1}{K} \quad \text{and} \quad \sigma_{\ln t} = \frac{1}{K}. \tag{B.2}$$

From the above equation and Eq. (20), we have

$$\ln X_m = -\frac{m}{K} \pm \frac{\sqrt{m}}{K}. \tag{B.3}$$

If the main value of X_m is taken into account (as in Section 3), we introduce an error of the order of $\sqrt{m}/K$ in the evidence evaluation via ΔX_m.

As we see in Fig. 4, not all m steps contribute equally to for the final value of E. The calculated evidence is dominated by the region where the product $\mathcal{L}_m \Delta X_m$ is maximal. The maximum position can correlate to the information gain $\mathcal{H}$ associated to the data (and the model) by Eq. (A.1).

To estimate this position, we have to make some approximation. Considering Eqs. (A.1), (16) and (17), we have that the information in terms of $\mathcal{L}(X)$ is

$$\mathcal{H} = \int_0^1 \frac{\mathcal{L}(X)}{E} \ln\left[\frac{\mathcal{L}(X)}{E}\right] dX = \int_0^1 P(X) \ln P(X) dX. \tag{B.4}$$

If we assume the extreme case of a likelihood function with a core with a constant value $\mathcal{L}(X) = \hat{\mathcal{L}}$ for $X < \hat{X}$ and zero elsewhere [49], we have that $E = \hat{L}\hat{X}$ and then $P(X) = 1/\hat{X}$ for $X < \hat{X}$ and zero otherwise. In this simple case we have

$$\mathcal{H} = \int_0^{\hat{X}} \frac{1}{\hat{X}} \ln\left(\frac{1}{\hat{X}}\right) dX = -\ln \hat{X} \tag{B.5}$$

and then $\hat{X} = e^{-\mathcal{H}}$ (see also Refs. [24,30,49,34] for further considerations).

[2] *nat* is the unit of information when the normal logarithm is used, similarly to the *bit*, the unit where the base-2 logarithm is employed.

[3] For multimode posterior probability distributions, the likelihood function maximum is more adapted. In fact the mean value can easily be far from the parameter region corresponding to high values of the likelihood function.

Please cite this article in press as: M. Trassinelli, Bayesian data analysis tools for atomic physics, Nucl. Instr. Meth. B (2017), http://dx.doi.org/10.1016/j.nimb.2017.05.030

From Eqs. (B.3) and (B.5), we see that the m value associated to this region, the most influent region for the value of E, is $m = K\mathcal{H}$ and

$$\ln \hat{X} = \mathcal{H} \pm \sqrt{\frac{\mathcal{H}}{K}}. \tag{B.6}$$

The dominant uncertainty associated to the evidence is then

$$\delta(\ln E) \approx \delta\left[\ln\left(\sum_m \Delta X_m\right)\right] \approx \sqrt{\frac{\mathcal{H}}{K}}. \tag{B.7}$$

Many approximations in this evaluation have been done but the dependency of $\delta(\ln E) \propto 1/\sqrt{K}$ emerges. This dependency has been confirmed by computational studies [34] that also investigate the influence of the search algorithm parameters for the new live points in the nested sampling.

A more pragmatic and practical way to evaluate the accuracy of E, which is employed in `Nested_Fit` program (see Section 4), is to calculate the evidence for different trials with different sets of live points and calculate then the average and the standard deviation of the different values of $\ln E$. From the consideration above, this is in fact the natural estimation to study the uncertainty of E [49,50].

References

[1] J. Neyman, E. Pearson, On the problems of the most efficient tests of statistical hypotheses, Philos. Trans. R. Soc. 231 (1933) 289–337.
[2] F. Yates, Contingency tables involving small numbers and the χ^2 test, Suppl. J. R. Stat. Soc. 1 (2) (1934) 217–235.
[3] P. Bevington, D. Robinson, Data Reduction and Error Analysis for the Physical Sciences, McGraw-Hill, 2003.
[4] F.J. Massey, The Kolmogorov-Smirnov test for goodness of fit, J. Am. Stat. Assoc. 46 (253) (1951) 68–78.
[5] H. Akaike, A new look at the statistical model identification, IEEE Trans. Automat. Contr. 19 (6) (1974) 716–723.
[6] D.J. Spiegelhalter, N.G. Best, B.P. Carlin, A. Van Der Linde, Bayesian measures of model complexity and fit, J. R. Stat. Soc. B 64 (4) (2002) 583–639.
[7] B.P. Abbott et al., (LIGO Scientific Collaboration and Virgo Collaboration), Observation of gravitational waves from a binary black hole merger, Phys. Rev. Lett. 116 (6) (2016) 061102.
[8] B.P. Abbott et al., (LIGO Scientific Collaboration and Virgo Collaboration), Gw151226: Observation of gravitational waves from a 22-solar-mass binary black hole coalescence, Phys. Rev. Lett. 116 (24) (2016) 241103.
[9] M. Bayes, M. Price, An essay towards solving a problem in the doctrine of chances. by the late rev. mr. Bayes, f. r. s. communicated by mr. price, in a letter to john canton, a. m. f. r. s, in: 418, Philos. Trans. 53 (1763) 370.
[10] P. Laplace, Essai philosophique sur les probabilités, Bachelier, 1825.
[11] H. Jeffreys, Theory of Probability, third ed., Oxford University Press, Oxford, U. K., 1961.
[12] E. Jaynes, G. Bretthorst, Probability Theory: The Logic of Science, Cambridge University Press, 2003.
[13] A. Lewis, S. Bridle, Cosmological parameters from CMB and other data: a Monte Carlo approach, Phys. Rev. D 66 (10) (2002) 103511.
[14] R. Trotta, Bayes in the sky: Bayesian inference and model selection in cosmology, Contemp. Phys. 49 (2) (2008) 71–104.
[15] F. Feroz, M.P. Hobson, M. Bridges, Multinest: an efficient and robust bayesian inference tool for cosmology and particle physics, Mon. Not. R. Astron. Soc. 398 (4) (2009) 1601–1614.
[16] C. Patrignani, G. Particle, Data, Review of particle physics, Chin. Phys. B 40 (10) (2016) 100001.
[17] J.K. Stockton, X. Wu, M.A. Kasevich, Bayesian estimation of differential interferometer phase, Phys. Rev. A 76 (3) (2007) 033613.
[18] D. Calonico, F. Levi, L. Lorini, G. Mana, Bayesian inference of a negative quantity from positive measurement results, Metrologia 46 (3) (2009) 267.
[19] N. Wiebe, C. Granade, Efficient bayesian phase estimation, Phys. Rev. Lett. 117 (1) (2016) 010503.
[20] A. Mooser, H. Kracke, K. Blaum, S.A. Bräuninger, K. Franke, C. Leiteritz, W. Quint, C.C. Rodegheri, S. Ulmer, J. Walz, Resolution of single spin flips of a single proton, Phys. Rev. Lett. 110 (14) (2013) 140405.
[21] N.P. Barradas, C. Jeynes, M. Jenkin, P.K. Marriott, Bayesian error analysis of Rutherford backscattering spectra, Thin Solid Films 343 (1999) 31–34.
[22] R.T. Cox, Probability, frequency and reasonable expectation, Am. J. Phys. 14 (1) (1946) 1–13.
[23] L.E. Ballentine, Probability theory in quantum mechanics, Am. J. Phys. 54 (10) (1986) 883–889.
[24] D.S. Sivia, J. Skilling, Data Analysis: A Bayesian Tutorial, 2nd Edition., Oxford University Press, 2006.
[25] R. Cox, Algebra of Probable Inference, Johns Hopkins University Press, 1961.
[26] R.E. Kass, A.E. Raftery, Bayes factors, J. Am. Stat. Assoc. 90 (430) (1995) 773–795.
[27] C. Gordon, R. Trotta, Bayesian calibrated significance levels applied to the spectral tilt and hemispherical asymmetry, Mon. Not. R. Astron. Soc. 382 (4) (2007) 1859–1863.
[28] C. Robert, G. Casella, Monte Carlo Statistical Methods, Springer, New York, 2013.
[29] J. Skilling, Nested sampling, AIP Conf. Proc. 735 (1) (2004) 395–405.
[30] J. Skilling, Nested sampling for general bayesian computation, Bayesian Anal. 1 (4) (2006) 833–859.
[31] M. Trassinelli, A. Kumar, H.F. Beyer, P. Indelicato, R. Märtin, R. Reuschl, Y.S. Kozhedub, C. Brandau, H. Bräuning, S. Geyer, A. Gumberidze, S. Hess, P. Jagodzinski, C. Kozhuharov, D. Liesen, U. Spillmann, S. Trotsenko, G. Weber, D. F.A. Winters, T. Stöhlker, Observation of the $2p_{3/2} \rightarrow 2s_{1/2}$ intra-shell transition in He-like uranium, Eur. Phys. Lett. 87 (6) (2009) 63001.
[32] P. Mukherjee, D. Parkinson, A.R. Liddle, A nested sampling algorithm for cosmological model selection, Astrophys. J. Lett. 638 (2) (2006) L51.
[33] F. Feroz, M.P. Hobson, Multimodal nested sampling: an efficient and robust alternative to Markov chain Monte Carlo methods for astronomical data analyses, Mon. Not. R. Astron. Soc. 384 (2) (2008) 449–463.
[34] J. Veitch, A. Vecchio, Bayesian coherent analysis of in-spiral gravitational wave signals with a detector network, Phys. Rev. D 81 (6) (2010) 062003.
[35] M. Theisen, Analyse der Linienform von Röntgenübergängen nach der Bayesmethode, Diplomarbeit, Fakultät für Mathematik, Informatik uns Naturwisssenschaften der RWTH Aachen, 2013.
[36] J. Skilling, Bayesian computation in big spaces-nested sampling and galilean Monte Carlo, AIP Conf. Proc. 1443 (1) (2012) 145–156.
[37] F. Feroz, J. Skilling, Exploring multi-modal distributions with nested sampling, AIP Conf. Proc. 1553 (1) (2013) 106–113.
[38] J. Buchner, A statistical test for nested sampling algorithms, Stat. Comp. 26 (1) (2016) 383–392.
[39] M. Trassinelli, D.F. Anagnostopoulos, G. Borchert, A. Dax, J.P. Egger, D. Gotta, M. Hennebach, P. Indelicato, Y.W. Liu, B. Manil, N. Nelms, L.M. Simons, A. Wells, Measurement of the charged pion mass using X-ray spectroscopy of exotic atoms, Phys. Lett. B 759 (2016) 583–588.
[40] M. Trassinelli, D.F. Anagnostopoulos, G. Borchert, A. Dax, J.P. Egger, D. Gotta, M. Hennebach, P. Indelicato, Y.W. Liu, B. Manil, N. Nelms, L.M. Simons, A. Wells, Measurement of the charged pion mass using a low-density target of light atoms, EPJ web conf. 130 (2016), 01022.
[41] D.S. Sivia, C.J. Carlile, Molecular spectroscopy and bayesian spectral analysis - how many lines are there?, J Chem. Phys. 96 (1) (1992) 170–178.
[42] Y. Kalambet, Y. Kozmin, K. Mikhailova, I. Nagaev, P. Tikhonov, Reconstruction of chromatographic peaks using the exponentially modified gaussian function, J. Chemometr. 25 (7) (2011) 352–356.
[43] F. James, M. Roos, MINUIT-A system for function minimization and analysis of the parameter errors and correlations, in: 367, Comp. Phys. Comm. 10 (6) (1975) 343.
[44] S. Baker, R.D. Cousins, Clarification of the use of chi-square and likelihood functions in fits to histograms, Nucl. Instrum. Methods 221 (2) (1984) 437–442.
[45] C.E. Shannon, A mathematical theory of communication, Bell Syst. Tech. J. 27 (4) (1948) 623–656.
[46] C.E. Shannon, A mathematical theory of communication, Bell Syst. Tech. J. 27 (3) (1948) 379–423.
[47] S. Kullback, R.A. Leibler, On information and sufficiency, Ann. Math. Stat. 22 (1951) 79–86.
[48] D.J. Spiegelhalter, N.G. Best, B.P. Carlin, A. Van Der Linde, The deviance information criterion: 12 years on, J. R. Stat. Soc. B 76 (3) (2014) 485–493.
[49] J. Skilling, Nested sampling's convergence, AIP Conf. Proc. 1193 (1) (2009) 277–291.
[50] N. Chopin, C.P. Robert, Properties of nested sampling, Biometrika 97 (3) (2010) 741–755.

Please cite this article in press as: M. Trassinelli, Bayesian data analysis tools for atomic physics, Nucl. Instr. Meth. B (2017), http://dx.doi.org/10.1016/j.nimb.2017.05.030

Appendix F

Article about the pion mass measurement

Physics Letters B 759 (2016) 583–588

Contents lists available at ScienceDirect

Physics Letters B

www.elsevier.com/locate/physletb

Measurement of the charged pion mass using X-ray spectroscopy of exotic atoms

M. Trassinelli [a,*], D.F. Anagnostopoulos [b], G. Borchert [c,1], A. Dax [d], J.-P. Egger [e], D. Gotta [c], M. Hennebach [c,2], P. Indelicato [f], Y.-W. Liu [d,3], B. Manil [f,4], N. Nelms [g,5], L.M. Simons [d], A. Wells [g]

[a] Institut des NanoSciences de Paris, CNRS-UMR 7588, Sorbonne Universités, UPMC Univ. Paris 06, 75005, Paris, France
[b] Dept. of Materials Science and Engineering, University of Ioannina, GR-45110 Ioannina, Greece
[c] Institut für Kernphysik, Forschungszentrum Jülich GmbH, D-52425 Jülich, Germany
[d] Laboratory for Particle Physics, Paul Scherrer Institut, CH 5232-Villigen PSI, Switzerland
[e] Institut de Physique de l' Université de Neuchâtel, CH-2000 Neuchâtel, Switzerland
[f] Laboratoire Kastler Brossel, UPMC-Sorbonne Universités, CNRS, ENS-PSL Research University, College de France, 4, place Jussieu, 75005 Paris, France
[g] Dept. of Physics and Astronomy, University of Leicester, Leicester LEI7RH, England, United Kingdom

ARTICLE INFO

Article history:
Received 10 May 2016
Received in revised form 10 June 2016
Accepted 12 June 2016
Available online 15 June 2016
Editor: V. Metag

Keywords:
Charged pion mass
Exotic atoms
X-ray spectroscopy

ABSTRACT

The $5g-4f$ transitions in pionic nitrogen and muonic oxygen were measured simultaneously by using a gaseous nitrogen–oxygen mixture at 1.4 bar. Due to the precise knowledge of the muon mass the muonic line provides the energy calibration for the pionic transition. A value of $(139.57077 \pm 0.00018)\,\mathrm{MeV/c^2}$ (± 1.3 ppm) is derived for the mass of the negatively charged pion, which is 4.2 ppm larger than the present world average.

X-ray spectroscopy of exotic atoms allows the determination of the mass of captured negatively charged particle like muons, pions, and antiprotons from the energies of the characteristic X-radiation. X-ray transitions occur during the de-excitation cascade of the exotic atom which is formed at principal quantum numbers of $n \approx 16$ in the case of pions [1,2]. The precise determination of the pion mass requires the use of X-ray lines which are not affected either by strong-interaction effects nor by collisions with surrounding atoms. Such conditions are found in the intermediate part of the cascade for exotic atoms formed in gases.

The most recent X-ray measurements were performed at the Paul Scherrer Institute (PSI) and used either a DuMond [3–5] or a Johann-type crystal spectrometer [6]. In the case of the DuMond spectrometer, the energy calibration for the pionic magnesium $(4f-3d)$ transition was performed with a nuclear γ-ray, while for the Johann set-up Kα fluorescence radiation from copper was used to determine the energy of the pionic nitrogen $(5g-4f)$ transition.

In the πMg experiment, electron refilling is unavoidable due to the use of a solid state target. Different assumptions on the K electron population lead to differences in the pion mass up to 16 ppm [5]. The previous πN experiment, as well as the present one, used a nitrogen gas target at pressures around 1 bar, where electron refilling is unlikely [7,8], *i.e.* the de-excitation cascade is decoupled from the environment. The absence of refilling of the electrons ejected already during the upper part of the cascade by internal Auger effect manifests in the appearance of X-ray lines at $n \geq 5$, which otherwise would be converted into Auger transitions [9–11]. Furthermore, a large Doppler broadening was measured for $(5-4)$ transitions [12]. It originates from Coulomb explosion during the formation process of the exotic atom with molecules and indicates that the velocity at the time of X-ray emission is essentially unchanged since the breakup of the molecule. Thus, the

* Corresponding author.
E-mail address: martino.trassinelli@insp.jussieu.fr (M. Trassinelli).
[1] Present address: TU Munich, D-85747 Garching, Germany.
[2] Present address: DAHER NUCLEAR TECHNOLOGIES GmbH, D-63457 Hanau, Germany.
[3] Present address: Phys. Depart., National Tsing Hua Univ., Hsinchu 300, Taiwan.
[4] Present address: Lab. de Physique des Lasers, Université Paris 13, Sorbonne Paris Cité, CNRS, France.
[5] Present address: ESA-ESTEC, PO Box 299, 2200 AG, Noordwijk, The Netherlands.

http://dx.doi.org/10.1016/j.physletb.2016.06.025

Table 1
Calculated contributions to the total QED transition energy of μO and πN($5g-4f$) lines (in eV) [17]. For the pionic transition, the world average pion mass value as given in [14] is used. The μO line constitutes a triplet due to the muon spin. The total uncertainty of the QED calculation (excluding the uncertainty of the pion mass) is ±1 meV.

Transition	μ^{16}O			π^{14}N
	$(5g_{9/2}-4f_{7/2})$	$(5g_{7/2}-4f_{7/2})$	$(5g_{7/2}-4f_{5/2})$	$(5g-4f)$
Coulomb	4022.8625	4022.6188	4023.4124	4054.1180
self energy	−0.0028	−0.0013	−0.0013	−0.0001
vac. pol. (Uehling)	0.8800	0.8800	0.8807	1.2485
vac. pol. Wichman–Kroll	−0.0007	−0.0007	−0.0007	−0.0007
vac. pol. two-loop Uehling	0.0003	0.0004	0.0004	0.0008
vac. pol. Källén–Sabry	0.0084	0.0084	0.0084	0.0116
relativistic recoil	0.0025	0.0025	0.0025	0.0028
hyperfine structure	–	–	–	−0.0008
Total	4023.7502	4023.5079	4024.2983	4055.3801

absence of screening effects from remaining electrons in the intermediate part of the atomic cascade leads to a unique solution for the mass [6]. In addition, in dilute targets the line intensity is already mostly collected in the circular transitions $(n, \ell = n-1) \rightarrow (n-1, \ell = n-2)$, where corrections owing to the hadronic potential are still tiny.

From the πN experiment $m_{\pi^-} = (139.57071 \pm 0.00053)\,\mathrm{MeV/c^2}$ [6] is obtained which suggests that both K electrons are present when the πMg($4f-3d$) transition occurs (solution B: $m_{\pi^-} = (139.56995 \pm 0.00035)\,\mathrm{MeV/c^2}$ [5]). This is corroborated by the fact that the result, assuming 1 K electron only (solution A: $m_{\pi^-} = (139.56782 \pm 0.00037)\,\mathrm{MeV/c^2}$), is in conflict with the measurement of the muon momentum for charged pion decay at rest $\pi^+ \rightarrow \mu^+\nu_\mu$ [13]. For solution A, the mass squared of the muon neutrino becomes negative by six standard deviations, whereas the average of solution B and the result of the πN($5g-4f$) measurement ($m_{\pi^-} = (139.57018 \pm 0.00035)\,\mathrm{MeV/c^2}$ [14]) yields the upper limit $m_{\mu_\nu} < 190\,\mathrm{keV/c^2}$ (90% c.l.).

The experiment described here resumes the strategy of the gas target, but exploits (i) the high precision of 0.033 ppm for the mass of the positively charged muon being $m_{\mu^+} = (105.6583715 \pm 0.0000035)\,\mathrm{MeV/c^2}$ [14] and (ii) the unique feature that in πN and μO transition energies almost coincide (Table 1). Using a N_2/O_2 gas mixture in the target allows the simultaneous measurement of πN and μO lines, with the muonic transition serving as an on-line calibration. Hence, systematic shifts during the unavoidably long measuring periods are minimised.

In the case of nitrogen and oxygen, ($6h-5g$), ($5g-4f$), and ($4f-3d$) transitions meet the operating conditions of the crystal spectrometer. Finally, the ($5g-4f$) transition was chosen because: (i) for the ($6h-5g$) lines (2.2 keV) absorption in the target gas itself and windows significantly reduces the count rate and (ii) the $3d$-level energy in πN requires a substantial correction because of the strong interaction. Electromagnetic transition energies (Tables 1 and 2) were calculated using a multi-configuration Dirac–Fock approach [15,16] to a precision of ±1 meV and include relativistic and quantum electrodynamics contribution (relativistic recoil, self-energy, vacuum polarisation) as well as the hyperfine structure of pionic nitrogen [17].

Energy shifts due to nuclear finite size are found to be as small as 4 aeV and 2 peV for the $5g$ and $4f$ levels in πN. Values for nuclear masses, radii, and moments were taken from recent compilations [18–20]. The strong-interaction shifts of the πN levels were estimated from interpolating the measured hadronic $2p$-level shifts in πC and πO [21] and by using scaling relations based on the overlap of nucleus and a hydrogen-like wave function for the pion orbit (see Table 3). Details on the calculation of the transition energies may be found elsewhere [22].

The measurement was performed at the high-intensity pion beam line πE5 of the Paul Scherrer Institute (PSI) using a set-up

Table 2
Transition energies E_{QED} [17] and Bragg angles Θ_{B} of the μO and πN lines used in the fit to the spectrum. The relative intensities within the fine structure multiplets of μO (FS int.) have been fixed in the fit to the statistical weight. The Bragg angle includes the index of refraction shift calculated with the code XOP [32]. For twice the lattice distance $2d = 0.768\,062\,286\,(13)$ nm is assumed at a temperature of 22.5°C [34]. The conversion constant used is $hc = 1.239\,841\,930\,(28)$ nm keV [14]. The πN($5g-4f$) and πN($5f-4d$) transition energies include the strong-interaction shift (see Table 3).

Transition	FS int.	E_{QED}/eV	Θ_{B}
μ^{16}O($5g_{7/2}-4f_{7/2}$)	1	4023.5079	53°21′51.48″
μ^{16}O($5g_{9/2}-4f_{7/2}$)	35	4023.7503	53°21′34.77″
μ^{16}O($5g_{7/2}-4f_{5/2}$)	27	4024.2984	53°20′57.01″
μ^{16}O($5f_{5/2}-4d_{5/2}$)	1	4025.3956	53°19′41.47″
μ^{16}O($5f_{7/2}-4d_{5/2}$)	20	4025.8031	53°19′13.44″
μ^{16}O($5f_{5/2}-4d_{3/2}$)	14	4026.9922	53°17′51.70″
μ^{16}O($5d_{5/2}-4p_{3/2}$)	9	4028.5625	53°16′3.90″
μ^{16}O($5d_{3/2}-4p_{1/2}$)	5	4033.5273	53°10′24.10″
μ^{18}O($5g_{7/2}-4f_{7/2}$)	1	4026.6692	53°18′13.90″
μ^{18}O($5g_{9/2}-4f_{7/2}$)	35	4026.9132	53°17′57.13″
μ^{18}O($5g_{7/2}-4f_{5/2}$)	27	4027.4642	53°17′19.28″
π^{14}N($5g-4f$)		4055.3802	52°45′46.76″
π^{14}N($5f-4d$)		4057.6984	52°43′11.81″
π^{14}N($5d-4p$)	*QED only*	4061.9460	52°38′28.76″
π^{15}N($5g-4f$)		4058.2394	52°42′35.67″
π^{15}N($5f-4d$)		4060.5605	52°40′ 0.95″

similar to the one used by Lenz et al. [6]. Major improvements are: (i) The use of cyclotron trap II [23] having a larger gap between the magnet coils yielding a substantially increased muon stop rate, (ii) a Bragg crystal of superior quality and (iii) a large-area X-ray detector in order to simultaneously cover the reflections of the muonic and pionic transitions (see Fig. 1). In addition, the average proton current of the accelerator was about 1.4 mA, which is 40% higher than in the previous experiment.

The N_2/O_2 gas mixture was enclosed in a cylindrical target cell placed at the centre of the cyclotron trap. The cell wall was made of a 50 µm thick Kapton® foil. Towards the crystal spectrometer a circular 7.5 µm Mylar® window was used supported by a stainless steel honeycomb structure with a free area of 90%. The target was operated at 1.4 bar and room temperature.

The muons used originate from the decay of slow pions inside the cyclotron trap, because the stop density for muons at the high-intensity pion beam is still superior to the one at a dedicated muon channel. For the simultaneous measurement comparable count rates are required for the πN and the μO line. This was achieved with a N_2/O_2 mixture of 10%/90% by adapting the set of polyethylene degraders inside the magnet gap and optimised by

Table 3
Corrections to the measured angle difference between the $\pi^{14}\mathrm{N}(5g-4f)$ and the $\mu^{16}\mathrm{O}(5g_{9/2}-4f_{7/2})$ transitions and associated uncertainties. A 1 ppm change in the pion mass corresponds to 4.055 meV in transition energy, to 0.27 arcsec in diffraction angle, or to a displacement of 3.2 µm in the detector plane. Contributions to the mass uncertainty from lattice and conversion constant cancel in leading order because the measurement principle is based on the angular difference. For more details see text.

Type of uncertainty	μO / arcsec	πN / arcsec	Total / arcsec	Uncertainty / ppb
index of refraction shift	13.22	12.94	−0.28	±20
silicon lattice constant				±2
bending correction	14.01	13.71	0.30	±20
penetration depth correction	−0.07	−0.07	0	±4
focal length				±670
temperature correction				±30
CCD alignment				±340
pixel distance				±120
alignment of detector normal				$^{+\ 0}_{-30}$
detector height offset				$^{+\ 0}_{-35}$
shape of target window				±100
shape of reflection				±225
individual curvature correction				±150
response function and Doppler broadening				$^{+290}_{-350}$
line pattern modelling				$^{+190}_{-290}$
fit interval				±15
muon mass				±30
QED energy				±350
conversion constant hc				±2
$4f$ strong interaction 45 µeV		0.003	−0.003	±10
$5g$ strong interaction 0.2 µeV		0.000	0.000	±0
K electron screening				±0
total systematic error				$^{+\ 960}_{-1000}$
statistical error				±820

means of an X-ray measurement using a Si(Li) semiconductor detector.

The crystal spectrometer is set up in Johann geometry [24] using a spherically bent Bragg crystal and optimised to the needs of exotic-atom X-ray spectroscopy [25]. Such a configuration allows the simultaneous measurement of two different energies within an energy interval, the limits of which are given by the extension of the target in the direction of dispersion and correspondingly by the size the detector. Spherical bending leads to a partial vertical focusing [26] which increases the count rate.

The Bragg crystal was made from a silicon crystal disk of 290 µm thickness and of a diameter of 100 mm. The disk is attached to a high-quality polished glass lens defining a spherical segment. The average radius of curvature of the crystal surface was measured to $R_\mathrm{c} = (2981.31 \pm 0.33)$ mm by sampling 500 points at the surface with a mechanical precision sensor (performed by Carl Zeiss AG, D-73447 Oberkochen, Germany). An upper limit for the cut angle (angle between crystal surface and reflecting lattice planes) was determined in a dedicated measurement to be 120 seconds of arc [27]. Hence, the focal condition corresponds to the symmetric Bragg case being $R_\mathrm{c} \cdot \sin\Theta_\mathrm{B}$. The measurement uses the second order reflection at the (110) planes. An aluminium aperture of 90 mm diameter covered the boundary region of the Si disk in order to avoid edge effects. For source geometry as given here, the overall efficiency of the crystal set-up is $\approx 5 \cdot 10^{-8}$. About 85% of the reflected intensity is covered by the sensitive area of the detector.

The detector with a total sensitive area of about $48\times72\,\mathrm{mm}^2$ (width×height) was built up by a 2×3 array of charge-coupled devices (CCDs) of 24 mm×24 mm (600×600 pixels) with frame storage option [28]. Having a depletion depth of about 30 µm these CCDs reach their maximum in detection efficiency of almost 90% at 4 keV. The detector surface is oriented perpendicular to the direction of the incoming X-rays. Excellent background conditions are achieved (i) by using an especially tailored concrete shielding of at least 1 m thickness between the X-ray detector and the target region and (ii) by exploiting the different pixel topology of low-energy X-rays and background events, which are mainly caused by neutron induced high energetic nuclear γ rays [2,6].

The Bragg angle for the $\pi\mathrm{N}(5g-4f)$ transition and thereby its energy is determined from the position difference to the $\mu\mathrm{O}(5g-4f)$ line. The positions are determined from the projection of the pattern on the CCD onto the direction of dispersion after correction for curvature by means of a parabola fit (Fig. 1). The main transitions $\mu\mathrm{O}(5g-4f)$ and $\pi\mathrm{N}(5g-4f)$ are separated by about 25 mm.

About 9000 events for each element were collected in each of the $(5g-4f)$ transitions during 5 weeks of data taking. The count rates for the πN and μO transitions were about 15 events per hour each. Only a common small drift was observed for the line positions of less than one pixel in total. Because of the simultaneous measurement the position difference is not affected. Bragg angle dependent corrections are small because the leading order cancels in such a difference measurement performed in the same order of reflection.

In fourth order, the Bragg angles of the Cu Kα lines are very close to the ones of the $\mu\mathrm{O}(5g-4f)$ transitions. Therefore, in addition Cu X-rays were repeatedly recorded as a stability monitor

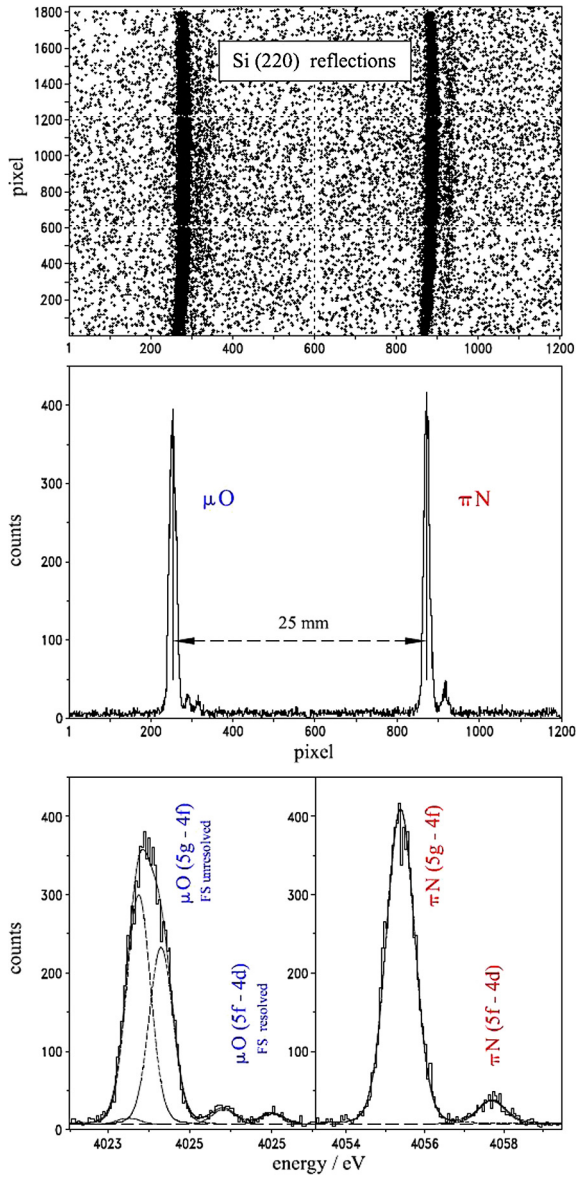

Fig. 1. Simultaneously measured $(5g-4f)$ transitions in muonic oxygen (calibration) and pionic nitrogen. Top: Distribution of the Bragg reflections on the surface of the 2×3 CCD array. The binning corresponds to the pixel size of the CCDs (note the different scales vertically and horizontally). Straight dashed lines indicate CCD boundaries. Middle: Projection on the axis of dispersion after correction for curvature (see text). Bottom: Details of the fit to line patterns.

corroborating the amount of the small common drift observed for the μO/πN pair.

Various parameters of the analysis and of the set-up enter in the determination of the line positions and their difference. These contributions and their uncertainties are summarised in Table 3 and are discussed in detail below.

Index of refraction shift. The systematic uncertainty of the index shift correction is assumed to be about 5% [29,30], *i.e.* the uncertainty of the difference is negligibly small.

Silicon lattice constant and wavelength conversion. Both the silicon lattice constant $2d$ and the conversion constant hc are known to an accuracy of $\approx 10^{-8}$.

Bending and penetration depth corrections. The energy dependent penetration depths of the X-rays lead to different corrections for the lattice constant of the Bragg crystal due to its curvature. The difference of the shift due to the average penetration depths itself turns out to be negligible. The primary extinction lengths including absorption were calculated both with the codes XOP [32] and DIXI [33], where results were found to coincide perfectly. We assume that the crystal behaves like an ideal one for such large bending radii [35]. The corrections for the Bragg angle were calculated following the approach of [36,37] using for the Poisson number the value $\nu = 0.208$ obtained from [38,39].

Focal length. Because of the different focal lengths for the πN and μO lines of 18.4 mm, the detector was placed in an intermediate position, which was determined by a survey measurement to be (2388.27 ± 0.20) mm. The uncertainty of the distance crystal-to-detector represents the largest contribution to the systematic error.

Temperature correction. The temperature during the measurement varied between 19°C and 21°C during the measurement. All periods were rescaled to 22.5°C by using the appropriate thermal expansion coefficient. The main correction comes from the change of the lattice constant. A smaller contribution arises from the variation of the distance crystal detector.

CCD alignment and pixel distance. In the CCD array small gaps of the order of 0.3 mm emerge between the individual devices. Secondly, the nominal pixel size of the CCDs, reported to be $40\,\mu\text{m}\times 40\,\mu\text{m}$ at room temperature, changes for the operating temperature of -100°C. Both the relative orientations of the six CCD devices and the average pixel distance have been measured precisely in a separate experiment using a nanometric quartz mask [31]. The average pixel distance was found to be $(39.9775 \pm 0.0006)\,\mu$m, substantially different from the nominal value.

Alignment of detector normal. The surface of the CCD array was set-up perpendicular to the direction crystal-detector to better than $\pm 0.14°$. The uncertainty also includes the imperfectness of the vacuum tubes, of their connections, and of the support structures of the CCDs.

Detector height offset. A possible offset in height of the detector from the ideal geometry defined by the plane through the centres of X-ray source, crystal, and detector leads to a distortion of the reflections. The size of such an effect was quantified by means of a Monte-Carlo simulation.

Shape of the target window. The circular shape of the target window leads to boundaries of different inclination for the πN and μO reflections. The corresponding possible uncertainty for the position difference was determined from a Monte-Carlo simulation.

Shape of reflection. The curvature of the πN and μO reflections is determined from a parabola fit to the hit pattern of the circular transitions. The assumption of a parabolic shape for the curvature is valid only close to the above-mentioned central plane. In addition, the curvature fit assumes a constant width of the reflection. A possible effect on the position difference over the height of the CCD array, which principally increases with increasing distance from the central plane, was studied by restricting the detector surface in height. The deviations are found to be far below the statistical error of the line positions.

Individual curvature correction. The parabola parameters for the πN and μO reflections are slightly different because of different

focal lengths. No difference could be verified from the fits which, however, is expected within the available statistics. The uncertainty is therefore given by the error of the fit to the curvature. For curvature correction, the average values were taken of the πN and μO reflection.

Response function and Doppler broadening. The response is found by a convolution of the intrinsic crystal response with the aberration caused by the imaging properties of a spherically bent crystal. The crystal response was calculated with the code XOP [32], and the geometry was taken into account by means of Monte-Carlo ray-tracing [25]. The resulting response shows a significant asymmetry having a width of 450 meV (FWHM).

Measured line widths of πN and μO transitions, however, are dominated by Doppler broadening due to Coulomb explosion [12], which was underestimated in the analysis reported by Lenz et al. [6] because of an inferior quality of the Bragg crystal. The line shapes are almost symmetric having a width of about 750 meV (FWHM). The Doppler broadening was accounted for best by folding in an additional Gaussian of about 40 seconds of arc. The Gaussian was determined from the analysis of a dedicated measurement optimised for pion stops, where in total 60000 events were accumulated in the πN$(5g-4f)$ transition.

The defocusing due to the different focal lengths is included in the Monte-Carlo based response, which is calculated for the appropriate distance in each case. In addition, it was verified that the parameters found in the curvature fit to the data are reproduced for the Monte-Carlo result.

Line pattern. The total line pattern to be considered is a superposition of the circular $(5g-4f)$ and the inner transitions $(5f-4d)$ and $(5d-4p)$ together with the corresponding contributions from the other isotopes (Table 2). The isotope abundances are fixed as tabulated (^{16}O/^{18}O: 99.76%/0.21%, ^{14}N/^{15}N: 99.64%/0.36%). The relative intensities of the inner transitions are due to the cascade dynamics and, therefore, free parameters of the fit.

The line positions within the πN and μO$(5g-4f)$ patterns were fixed according to the QED energies. In the case of μO, all fine structure components were included in the fit. For a proper description of the background, the two strong components of the μ^{16}O$(5d-4p)$ triplet and the πN$(5d-4p)$ transition were included in the fit. For the pionic line, position and width were free parameters, because it is shifted and broadened by about 1 eV compared to the electromagnetic value by the strong interaction [6].

Fit interval. Changing the interval used in the fit of the line positions does affect the result insignificantly.

K electron screening. From the analysis of the high-statistics πN$(5g-4f)$ data, we exclude the influence of satellites lines due to remaining K electrons. The energy shift of the pionic transition is calculated to be -456 (-814) meV in the case of one (two) K electron(s). Two hypothesis (presence of satellites or not) are compared via the Bayes factor [40–43] yielding an upper limit of less than $3\cdot10^{-6}$ for the relative intensity of possible satellites.

The measured energy of the πN$(5g-4f)$ transition was found to be $(4055.3970 \pm 0.0033_{stat} \pm 0.0038_{sys})$ eV. Basically two facts limit the accuracy of the method of a simultaneous measurement as described here: (i) The low rate obtainable from the muonic transitions hinders to accumulate as high statistics as would be achievable when using a set-up optimised for pionic atoms. For pionic transitions, count rates being a factor of 20 larger than for muonic X-rays can be achieved. (ii) The large Doppler broadening induced by Coulomb explosion when using diatomic gases, which approximately doubles the line width as expected from the spectrometer response.

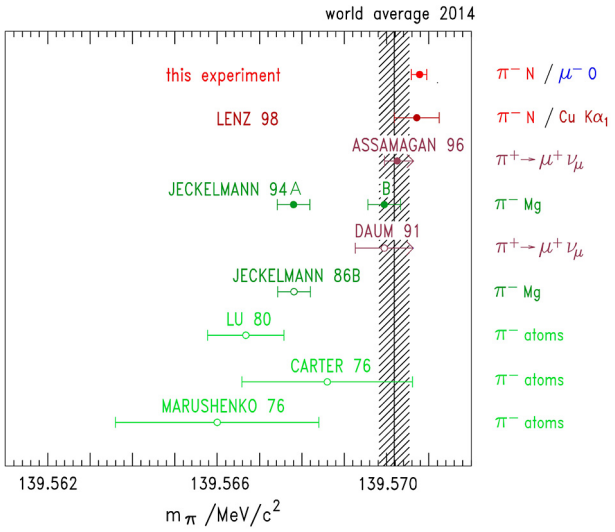

Fig. 2. Results for the mass of the charged pion. Also shown are previous exotic-atom results (Jeckelmann et al. (86B [3,4]), Lu et al. [44], Carter et al. [45], Marushenko et al. [46]) and π^+ decay at rest (Daum et al. [47]). The shaded region indicates the world average before this experiment [14].

To summarise, the mass of the negatively charged pion has been measured by means of equivalent X-ray transitions in hydrogen-like pionic nitrogen and muonic oxygen, where the muonic line serves as energy calibration. The value of (139.57077 ± 0.00018) MeV/c^2 is 4.2 ppm larger than the present world average [14]. Repeating the procedure as described in ref. [6] by using the Cu Kα_1 line for calibration, yields a value of $m_\pi = (139.57090 \pm 0.00056)$ MeV/c^2. The accuracy of $\pm$4.0 ppm represents the limit for a calibration with broad X-ray fluorescence lines. Both results are in good agreement with the mass obtained by [6], but 5.4 ppm and 6.8 ppm, respectively, above the result of the pionic magnesium experiment (solution B [5]) using a nuclear γ ray for calibration (Fig. 2).

The analysis shows no evidence for any satellite lines from remaining electrons at the time of X-ray emission of the $(5g-4f)$ transition. This corroborates strongly our assumption for a complete depletion of the electron shell during the preceding steps of the atomic cascade.

In conclusion, the present study demonstrates the potential of crystal spectroscopy with bent crystals in the field of exotic atoms. Its limits are given, on one hand, by statistics for the present beam and detector technologies. On the other hand, the systematic uncertainties discussed at length above illustrate the level of sophistication which must be applied.

Facing the fact that pion beams at PSI provide a flux of about 10^9/s, the use of double-flat crystal spectrometers may be considered allowing for absolute angle calibrations without a (muonic or X-ray) reference line. Choosing pionic transitions not affected by Coulomb explosion, *e.g.* from pionic neon, a precision for the pion mass determination of the order of 0.5 ppm is feasible which, however, may be regarded to be the maximum achievable by means of exotic-atom X-ray spectroscopy.

As a result, X-rays of hydrogen-like pionic atoms are useful to provide calibration standards in the few keV range, where suitable radioactive sources are not available [22,49]. At present, the accuracy is given by the uncertainty of the pion mass [50]. The quality of such standards may benefit substantially from laser spec-

troscopy of metastable high-lying pionic states which is proposed to be performed in pionic helium also at PSI [51].

Combined with the measurement of the muon momentum after pion decay at rest [13], a non-zero value for the muon neutrino mass is obtained of $m_{\nu_\mu} = 183\,^{+62}_{-83}$ keV/c^2 (c.l. 90%) when using the statistical approach of [48]. The result is far above the cosmological limit of at least 11 eV/c^2 for the sum of all neutrino flavours [14]. However, extending the error limits to 3σ either for the pion mass or the muon momentum yields values for m_{ν_μ} consistent with zero.

Acknowledgements

We are grateful to N. Dolfus, H. Labus, B. Leoni and K.-P. Wieder for solving numerous technical problems. We thank the PSI staff for providing excellent beam conditions and appreciate the support by the Carl Zeiss AG, Oberkochen, Germany, which fabricated the Bragg crystals. We thank Prof. Dr. E. Förster and his collaborators at the University of Jena, and A. Freund and his group at ESRF, for the help in characterising the crystal material as well as A. Blechmann for a careful study of the CCD performance. We are indebted to PSI for supporting the stay during the run periods (D.F.A.). This work is part of the PhD thesis of B.M. (Université Pierre et Marie Curie, 2001), N.N. (University of Leicester, 2002) and M.T. (Université Pierre et Marie Curie, 2005).

References

[1] L.M. Simons, D. Horvâth, G. Torelli (Eds.), Proc. of the Fifth Course of the International School of Physics of Exotic Atoms, May 14–20, 1989, Erice, Italy, Plenum Press, New York, 1990, and references therein.
[2] D. Gotta, Prog. Part. Nucl. Phys. 52 (2004) 133.
[3] B. Jeckelmann, et al., Phys. Rev. Lett. 56 (1986) 1444.
[4] B. Jeckelmann, et al., Nucl. Phys. A 457 (1986) 709.
[5] B. Jeckelmann, P.F.A. Goudsmit, H.J. Leisi, Phys. Lett. B 335 (1994) 326.
[6] S. Lenz, et al., Phys. Lett. B 416 (1998) 50.
[7] R. Bacher, et al., Phys. Rev. A 39 (1989) 1610.
[8] K. Kirch, et al., Phys. Rev. A 59 (1999) 3375.
[9] G.R. Burbidge, A.H. de Borde, Phys. Rev. 89 (1953) 189.
[10] P. Vogel, Phys. Rev. A 22 (1980) 1600.
[11] R. Bacher, et al., Phys. Rev. Lett. 54 (1985) 2087.
[12] T. Siems, et al., Phys. Rev. Lett. 84 (2000) 4573.
[13] K. Assamagan, et al., Phys. Rev. D 53 (1996) 6065.
[14] K.A. Olive, et al., Particle Data Group, Chin. Phys. C 38 (9) (2014) 090001.
[15] J. Desclaux, et al., Computational Approaches of Relativistic Models in Quantum Chemistry, vol. 10, Elsevier, 2003.
[16] J.P. Santos, et al., Phys. Rev. A 71 (2005) 032501.
[17] M. Trassinelli, P. Indelicato, Phys. Rev. A 76 (2007) 012510.
[18] G. Audi, A. Wapstra, C. Thibault, Nucl. Phys. A 729 (2003) 337.
[19] I. Angeli, At. Data Nucl. Data Tables 87 (2004) 185.
[20] P. Raghavan, At. Data Nucl. Data Tables 42 (1989) 189.
[21] G. de Chambrier, et al., Nucl. Phys. A 442 (1985) 637.
[22] M. Trassinelli, PhD thesis, Univ. Piere et Marie Curie, Paris, 2005, http://tel.ccsd.cnrs.fr/tel-00067768.
[23] L.M. Simons, Phys. Scr. T 22 (1988) 90;
L.M. Simons, Hyperfine Interact. 81 (1993) 253.
[24] H.H. Johann, Z. Phys. 69 (1931) 185.
[25] D.E. Gotta, L.M. Simons, Spectrochim. Acta, Part B 120 (2016) 9, http://dx.doi.org/10.1016/j.sab.2016.03.006.
[26] J. Eggs, K. Ulmer, Z. Angew. Phys. 20 Band (Heft 2) (1965) 118.
[27] D.S. Covita, et al., Rev. Sci. Instrum. 79 (2008) 033102.
[28] N. Nelms, et al., Nucl. Instrum. Methods, Sect. A 484 (2002) 419.
[29] B.L. Henke, E.M. Gullikson, J.C. Davies, At. Data Nucl. Data Tables 54 (1993) 181.
[30] C.T. Chantler, J. Phys. Chem. Ref. Data 24 (1995) 71.
[31] P. Indelicato, et al., Rev. Sci. Instrum. 77 (2006) 043107.
[32] M. Sanchez del Rio, R.J. Dejus, XOP version 2.4: recent developments of the X-ray optics toolkit, SPIE Proc. 8141 (2011) 814115.
[33] G. Hölzer, O. Wehrhan, E. Förster, Cryst. Res. Technol. 33 (1998) 555.
[34] P.J. Mohr, B.N. Taylor, D.B. Newell, CODATA2010, Rev. Mod. Phys. 84 (2012) 1527.
[35] I. Uschmann, et al., J. Appl. Crystallogr. 26 (1993) 405.
[36] F. Cembali, et al., J. Appl. Crystallogr. 25 (1992) 424.
[37] C.T. Chantler, R.D. Deslattes, Rev. Sci. Instrum. 66 (1995) 5123.
[38] J.J. Wortman, R.A. Evans, J. Appl. Phys. 36 (1965) 153.
[39] F.N. Chukhovskii, et al., J. Appl. Crystallogr. 29 (1996) 438.
[40] E.T. Jaynes, G.L. Bretthorst, Probability Theory: The Logic of Science, Cambridge University Press, 2003.
[41] D.S. Sivia, J. Skilling, Data Analysis: A Bayesian Tutorial, second ed., Oxford University Press, 2006.
[42] R.E. Kass, A.E. Raftery, J. Am. Stat. Assoc. 90 (1995) 773.
[43] C. Gordon, R. Trotta, Mon. Not. R. Astron. Soc. 382 (2007) 1859.
[44] D.C. Lu, et al., Phys. Rev. Lett. 45 (1980) 1066.
[45] A.L. Carter, et al., Phys. Rev. Lett. 37 (1976) 1360.
[46] V.N. Marushenko, et al., JETP Lett. 23 (1976) 72.
[47] M. Daum, et al., Phys. Lett. B 265 (1991) 425.
[48] G.J. Feldman, R.D. Cousins, Phys. Rev. D 57 (1998) 3873.
[49] D.F. Anagnostopoulos, et al., Phys. Rev. Lett. 91 (2003) 240801.
[50] S. Schlesser, et al., Phys. Rev. C 84 (2011) 015211.
[51] M. Hori, V.I. Korobov, Anna Sótér, Phys. Rev. A 89 (2014) 042515, http://dx.doi.org/10.1103/PhysRevA.89.042515.

Appendix G

Article about ion–atom collisions

J. Phys. B: At. Mol. Opt. Phys. **45** (2012) 085202 (11pp) doi:10.1088/0953-4075/45/8/085202

Investigation of slow collisions for (quasi) symmetric heavy systems: what can be extracted from high resolution x-ray spectra

M Trassinelli[1,2], C Prigent[1,2], E Lamour[1,2], F Mezdari[1,2,3], J Mérot[1,2], R Reuschl[1,2,4], J-P Rozet[1,2], S Steydli[1,2] and D Vernhet[1,2]

[1] CNRS, INSP, UMR7588, 4 Place Jussieu, 75005 Paris, France
[2] Université Pierre et Marie Curie, INSP, UMR7588, 4 Place Jussieu, 75005 Paris, France

E-mail: martino.trassinelli@insp.jussieu.fr

Received 16 December 2011, in final form 14 February 2012
Published 15 March 2012
Online at stacks.iop.org/JPhysB/45/085202

Abstract

We present a new experiment on (quasi) symmetric collision systems at low velocity, namely Ar^{17+} ions ($v = 0.53$ au) on gaseous Ar and N_2 targets, using low- and high-resolution x-ray spectroscopy. Thanks to an accurate efficiency calibration of the spectrometers, we extract absolute x-ray emission cross sections combining low-resolution x-ray spectroscopy and a complete determination of the ion beam–gas jet target overlap. Values with improved uncertainty are found in agreement with previous results (Tawara *et al* 2001 *Phys. Rev.* A **64** 042712). Resolving the whole He-like Ar^{16+} Lyman series from $n = 2$–10 with our crystal spectrometer enables us to determine precisely the distribution $\{\mathcal{P}_n\}$ of the electron capture probability and the preferential n_{pref} level of the selective single-electron capture. Evaluation of cross sections for this process as well as for the contribution of multiple-capture is carried out. Their sensitivity to the ℓ-distribution of n levels populated by single-electron capture is clearly demonstrated, providing a stringent benchmark for theories. In addition, the hardness ratio is extracted and the influence of the decay of the metastable 1s2s $^3S_1$ state on this ratio is discussed.

(Some figures may appear in colour only in the online journal)

1. Introduction

The interaction between low velocity ions and atoms or molecules has been extensively investigated in the past decades. At the low velocity regime (0.4–1 atomic units (au)), the dominant process is electron capture that occurs in selective projectile excited states, the collisional system behaving like a quasi-molecule. It leads to an energy gain of the projectile ion and the populated excited states decay by emission of photons and/or electrons, both carrying information on the collision dynamics. During the 1980s, many experiments have been performed with light ions, like C, N, Ne, ... interacting with light targets as H_2 and He leading to a quite complete understanding of the mechanisms involved in the collision. Besides total cross sections determination, the n- and ℓ-population distributions ($\{\mathcal{P}_n\}$ and $\{\mathcal{P}_\ell\}$, respectively) of the single capture process have been characterized as well as the role of rotational versus radial couplings while for double-capture, the $n\ell n'\ell'$ channels have been identified. For such studies, different detection techniques have been applied, as the kinetic energy gain of the projectile ([2] and references therein) or the electron and the radiative emission detection [3–7]. At the same time, extended theoretical investigations have been developed. They include simple approaches such

[3] Present address: Department of Physics, Faculty of Sciences of Gabes Cité Erriadh 6072, Zrig, Gabes, Tunisia.
[4] Present address: ExtreMe Matter Institute EMMI, GSI Helmholtzzentrum, 64291 Darmstadt, Germany.

Appendix H

Article about irradiation-induced modifications in magnetocaloric thin films

Suppression of the thermal hysteresis in magnetocaloric MnAs thin film by highly charged ion bombardment

M. Trassinelli,[1,2,a)] M. Marangolo,[1,2] M. Eddrief,[1,2] V. H. Etgens,[1,2,b)] V. Gafton,[1,2] S. Hidki,[1,2] E. Lacaze,[1,2] E. Lamour,[1,2] C. Prigent,[1,2] J.-P. Rozet,[1,2] S. Steydli,[1,2] Y. Zheng,[1,2] and D. Vernhet[1,2]

[1]*CNRS, UMR 7588, Institut des NanoSciences de Paris (INSP), F-75005 Paris, France*
[2]*Sorbonne Universités, UPMC Univ. Paris 06, UMR 7588, INSP, F-75005 Paris, France*

(Received 6 November 2013; accepted 9 February 2014; published online 24 February 2014)

We present the investigation on the modifications of structural and magnetic properties of MnAs thin film epitaxially grown on GaAs induced by slow highly charged ions bombardment under well-controlled conditions. The ion-induced defects facilitate the nucleation of one phase with respect to the other in the first-order magneto-structural MnAs transition, with a consequent suppression of thermal hysteresis without any significant perturbation on the other structural and magnetic properties. In particular, the irradiated film keeps the giant magnetocaloric effect at room temperature opening new perspective on magnetic refrigeration technology for everyday use.
 [http://dx.doi.org/10.1063/1.4866663]

At present, the application of the magnetocaloric effect (MCE) as an alternative method for refrigeration is one of the great technological challenges. Compared to the common gas-compression/expansion method, MCE has a higher efficiency with absence of moving parts and a consequently small environmental impact and maintenance. Materials showing conventional MCE are characterized by a second-order magnetic transition. In giant-MCE (GMCE) materials, a magneto-structural first-order transition generally occurs. The search of materials with a GMCE close to room temperature is of great interest, and it is mainly obtained by varying material composition[1–7] or, more recently, by applying an external strain to bulk[8] or to thin films.[9–11] However, first-order transitions exhibit a considerable thermal hysteresis ΔT_{hys}, which makes GMCE materials difficult to handle in applications for real refrigerators that work cyclically. Much effort has been made for reducing this hysteresis. In the past years, this reduction has been obtained by doping bulk manganese arsenide (MnAs),[5–7] where a suppression of the thermal hysteresis has been reached but only for low intensity magnetic field[6,7] ($H = 0.01$ T).

Another interesting way to change the magnetic properties of thin films is the bombardment and implantation of ions. Nevertheless, up to present, only monocharged ions have been used to irradiate materials exhibiting a second-order transition exclusively.[12–18]

Here, we investigate the modifications of MnAs thin film epitaxially grown on a GaAs substrate submitted to the bombardment of highly charged ions. MnAs is one of the more promising GMCE materials. It exhibits a large change of magnetic entropy in proximity of the phase transition close to room temperature ($T_C = 313$ K), typically[3,19] $\Delta S(T_c) \approx -30$ J Kg^{-1} K^{-1} corresponding to a large refrigeration power (that depends on the ΔS integral over a temperature interval) up to 200 J Kg^{-1}. This ferromagnetic–non-ferromagnetic transition is associated with the magneto-structural phase transition from hexagonal (α-phase, NiAs-type) to orthorhombic (β-phase, MnP-type). Compared to bulk materials, in MnAs thin films, the strain of the substrate disturbs the phase transition that leads to the $\alpha - \beta$ phase coexistence. This is characterized by a self-organization with longitudinal alternating regions over a large range of temperatures (290–320 K), generating a consequent modification of the magnetic properties of the film.[20] In particular, the phase coexistence reduces the maximum value of ΔS(T) but keeps the same refrigeration power. Indeed the ΔS per mole of material portion passing from one phase to another is still very high, which characterizes the giant MCE materials.[9] The period λ of the self-organization depends linearly on the MnAs film thickness t with the relationship[21,22] $\lambda \approx 4.8\,t$.

MnAs epilayers investigated here are grown by molecular beam epitaxy (MBE) on GaAs(001) substrate. The deposed MnAs is oriented with the α-MnAs[0001] and β-MnAs[001] axis parallel to GaAs[$\bar{1}$10]. At the end of the growth process, 150 ± 10 nm thick samples are capped *in situ* with an amorphous As layer in order to prevent the MnAs oxidation before the ion bombardment. More details on the growth process can be found in Ref. 23.

The ion irradiation is performed at the SIMPA facility[24] (French acronym for highly charged ion source of Paris) that includes an electron-cyclotron resonance ion source coupled to a dedicated ultra-high vacuum beam line. The different samples, with a surface of about 4×5 mm^2 obtained from the same wafer, are irradiated with a beam of Ne^{9+} ions with a kinetic energy of 90 keV (4.5 keV/u). The incidence angle between the ion beam and the sample surface is set at 60°, for having an average penetration depth of the ions corresponding to the half-thickness of the MnAs film[25] with a consequent maximization effect of ion irradiation.[15] The ion—sample collision zone is continuously monitored with a visible-light sensitive CCD camera and a X-ray solid-state detector during the irradiation. Only a negligible fraction of ions is deposited in the GaAs substrate excluding the

[a)]martino.trassinelli@insp.jussieu.fr
[b)]Also at Université de Versailles Saint-Quentin en Yvelines, 55 Avenue de Paris, 78035 Versailles, France.

possibility of MnAs-GaAs mixing.[17] Different ion beam bombardment durations at 0.5 μA beam intensity, from 5 to several thousands of seconds, and corresponding to a fluence between $\Phi = 1.6 \times 10^{12}$ and 1.6×10^{15} ions/cm^2, are applied on different samples coming from the same growth. The potential energy of the ions, which depends on their charge state, contributes marginally, with only 3.1 keV, making the dependency on the ion charge insignificant in the bombardment. More details about the irradiation process can be found in Ref. 26.

After highly charged ions impact, sample properties modification and their dependency on the ion fluence are studied using different techniques, namely: X-ray diffraction (XRD), magnetic force microscopy (MFM), and sample magnetometry (with a vibrating sample magnetometer, VSM, and a superconducting quantum interference device, SQUID magnetometer). With the XRD (model PANalytical XPert MRD), structural changes are investigated at room temperature ($T = 293 \pm 1$ K). From X-ray reflectivity, the MnAs layer thickness of the different samples is evaluated to the constant value of 150 nm, whatever the ion fluence, demonstrating that sputtering effects are negligible. XRD measurements at Bragg angles are used to determine the α- and β-phase crystal spacing as a function of the fluence Φ and are presented in Fig. 1. From this detailed analysis, the $\alpha - \mathrm{MnAs}(\bar{3}300)$ and β-MnAs(060) reflection peaks are clearly identified for the non-irradiated sample (curve in the bottom), the β peaks being much less intense at 293 K. At low fluence, the α and β diffraction reflections are well separated. At the highest fluence, they merge resulting to a unique diffraction reflection. From the angle difference between the MnAs and the substrate GaAs reflections, the lattice constants of the two phases are measured. We use here the orthorhombic crystallographic system (shown in the inset of Fig. 2), which is more appropriate since the residual strain breaks off the hexagonal symmetry of the α-phase. The lattice values of the axis perpendicular to the surface, c_{orth}, are presented in Fig. 2. For the non-irradiated sample, c_{orth} values are comparable to the literature[27] values for similar sample thickness at 293 K: $c_{\mathrm{orth}}(\alpha) = 6.44$ Å and $c_{\mathrm{orth}}(\beta) = 6.37$ Å. Different to the preliminary data survey presented in Ref. 26, we can observe in Fig. 2 that the contribution from the two phases is still clearly distinguishable for any value of the fluence except for the highest. The presence of two distinguished structural phases indicates that the associated magnetic transition remains of first-order type. $c_{\mathrm{orth}}(\alpha)$ continuously decreases when increasing Φ, whilst $c_{\mathrm{orth}}(\beta)$ increases until the merging of the two diffraction peaks. This progressive bridging suggests an increasing of the strain between the zones of different phases due to their spatial fragmentation, in analogy with the theoretical results presented in Ref. 21.

A direct observation of the α- and β-phase zones layout can also be obtained with a MFM (Bruker Multimode AFM microscope equipped with a magnetic tip coated with Co/Cr, model MESP). For this survey performed at 293 K, a well-defined procedure has been applied before each measurement. The samples are demagnetized at higher temperature ($T \approx 340$ K) and then magnetized along the surface parallel to the easy axis b_{orth}. The contrast detected by the MFM corresponds to the out-of-plane component of the stray magnetic field emanating from α stripes. The resulting images are presented in Fig. 3. For the non-irradiated sample (top), the regular arrangement between α- and β-phase is well visible. The Fourier transform of a large sample area (40×40 μm) shows clearly the first and the second order maxima corresponding to $\lambda = 0.73$ μm, close to the expected periodicity. MFM images of the bombarded samples show that the stripe-type structure is more and more distorted, but not suppressed. The

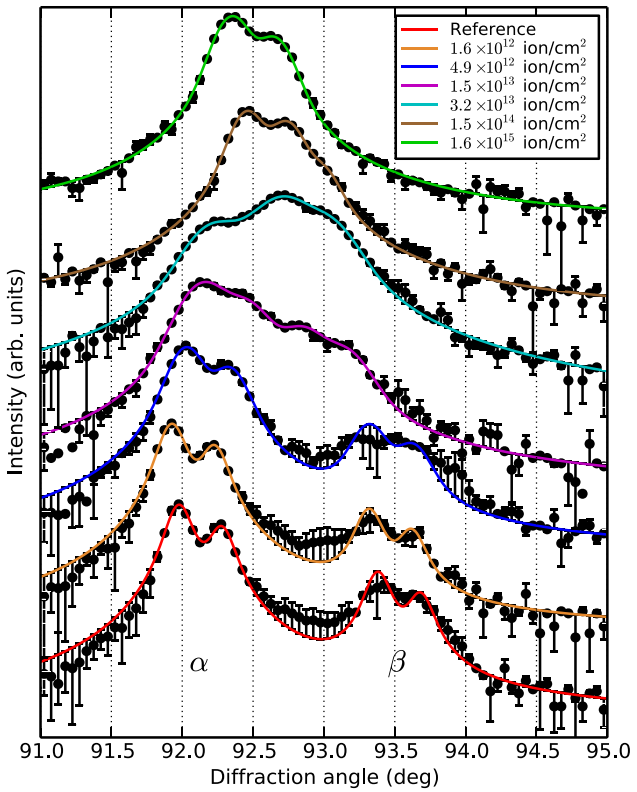

FIG. 1. $\alpha - \mathrm{MnAs}(\bar{3}300)$ (left) and $\beta - \mathrm{MnAs}(060)$ (right) reflection peaks of samples submitted to different ion fluences Φ. The double peak structure is due to the CuK$\alpha_{1,2}$ emission used in the diffractometer. The full lines represent the result of the profile fits.

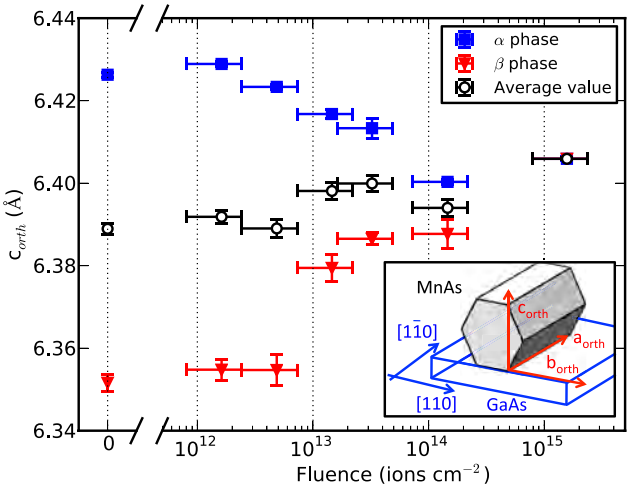

FIG. 2. Plot of the c_{orth} values of the α- and β-phases extracted from the diffraction curves as a function of the ion fluence Φ. In the inset, scheme of the MnAs film with its orientation relative to the GaAs(001) substrate.

Fourier transform of the irradiated sample with 1.5×10^{13} ions/cm^2 presents indeed maxima at the same position than for the non-irradiated sample, with simply a larger dispersion, due to the random defects produced by ion impact on the regular pattern. Quantitatively, an increase of the full width at half maximum from $0.31 \pm 0.01\ \mu\text{m}^{-1}$ to $0.83 \pm 0.08\ \mu\text{m}^{-1}$ is measured. We recall that the main periodicity λ is intrinsically related to the structural difference between the α- and β-phases,[21] and no extra phase of MnAs has to be invoked.[26] The observed increasing fragmentation of the $\alpha - \beta$ regions and the absence of modification in the λ periodicity confirm the interpretation made above for the XRD data. For $\Phi > 1.5 \times 10^{13}$ ions/cm^2, magnetic imaging becomes impossible due to the low out-of-plane magnetic field (stripes disappearance).

Even if the structural properties are not strongly modified by the ion bombardment, the presence of additional seeding defects might perturb the phase transition and then modify the transition temperature, the thermal hysteresis, and the giant magnetocaloric properties. These aspects are investigated by measuring the magnetic moment, the coercivity, and the magnetic anisotropy of the samples at different temperatures and magnetic fields. Information about the coercivity field, anisotropy, and, more generally, magnetic hysteresis cycle is extracted with a vibrating sample magnetometer (VSM, in the Quantum Design PPMS 9 T) from (H,$M(H)$) hysteresis curves of the magnetization M at different temperatures T with a variable magnetic field H. After a depolarization at 350 K and $H = 0$, each sample has been brought at a defined temperature T. Then, the magnetic moment is recorded continuously during the field H variation between +1 and −1 T. No large difference on the hysteresis cycles (H,$M(H)$) is noticeable between the reference and the irradiated sample (see Fig. 4). The presence of the ion-induced defects produces additional pinning on the mobility of the magnetic domains, visible by the presence of "wings" on the magnetic cycle. In contrast, the nucleation of the magnetic domains is unchanged. The temperature dependency of the associated coercivity field (inset in Fig. 4) shows the characteristic peak on the $\alpha - \beta$ coexisting zone.[28] A small reduction of its maximum value is noticeable for the bombarded sample, from 250 Oe to 150–200 Oe, but a constant value of about 30 Oe is found below ∼300 K, independently on the ion fluence.

The samples magnetization dependency on the temperature, with a fixed H applied, is obtained with a SQUID magnetometer (Quantum Design MPMS-XL). The measurement procedure is the following: (i) Each sample is initially brought to 350 K with $H = 0$; (ii) the sample is cooled down to 100 K, and then, a magnetic field $H = 1$ T is applied; and (iii) the magnetic moment is recorded continuously during the temperature variation from 100 to 350 K, and then back to 100 K, with a sweep rate of ±2 K/min. The results are presented in Fig. 5, where (T,$M(T)$) curves corresponding to an irradiated and the reference samples are shown. At low temperature, the saturation magnetization values M_{sat} of the reference and irradiated samples are comparable within the experimental uncertainty of 1%–2%. Similarly, the transition temperature T_C, defined here as the temperature for which $M(T_C) = M_{\text{sat}}/2$, is for both samples around 305 K. In contrast, different from the reference sample, characterized by $\Delta T_{\text{hys}} \approx 5$ K for $H = 1$ T, the thermal hysteresis disappears in the irradiated samples.

After the observation of the suppression of ΔT_{hys}, it is interesting to check whether the magnetocaloric properties

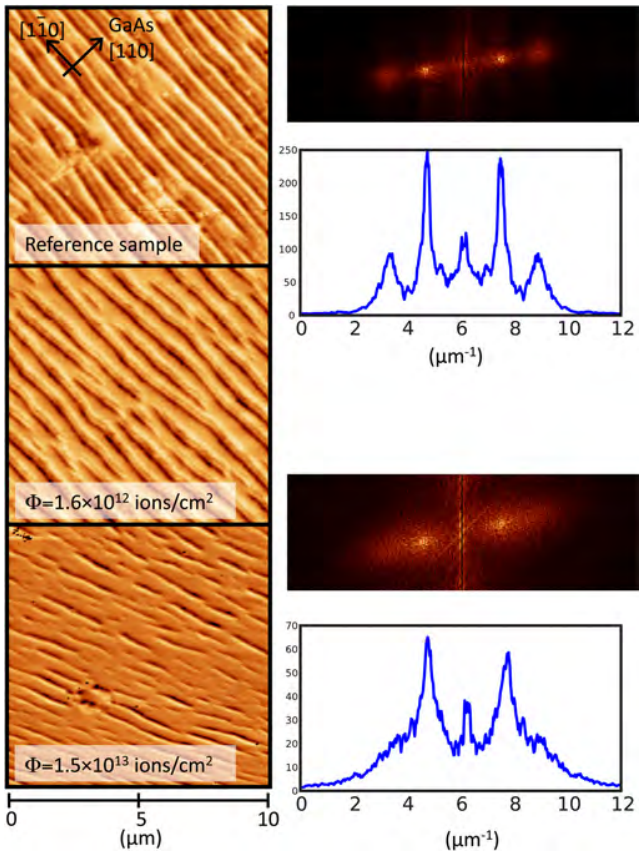

FIG. 3. On the left, MFM images of the reference sample (top) and of samples submitted to different ion fluences. The regular spacing due to the GaAs substrate constrains is visible in all images. In irradiated samples, random defects due to the ion bombardment introduce a distortion of the regular pattern. On the right, Fourier transforms and intensity profiles are presented for the reference and the most irradiate samples.

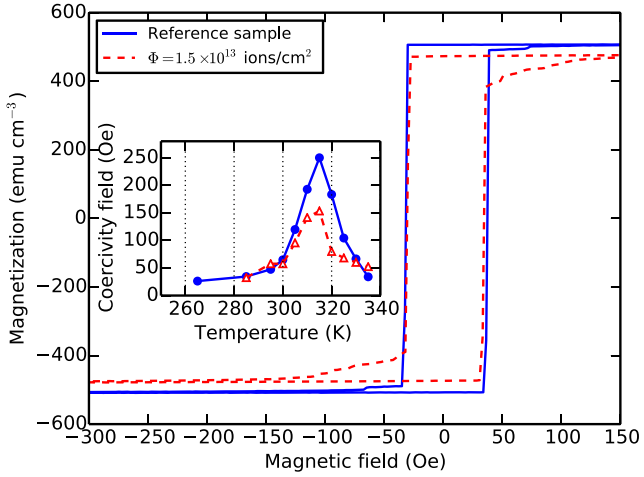

FIG. 4. Magnetization as a function of external magnetic field at the temperature of 285 K for the reference and for the irradiated samples. In the inset, the dependency of the coercivity field on the temperature is shown.

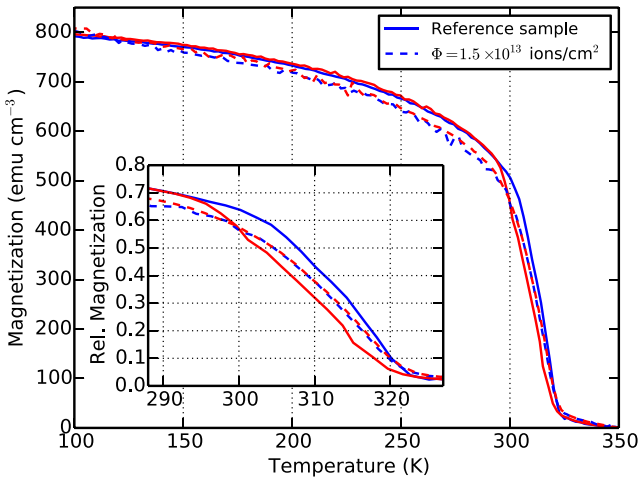

FIG. 5. Magnetization as a function of temperature for the reference (solid lines) and for the irradiated samples (dashed lines). Data obtained by a temperature increase (from colder temperatures) and decrease (from hotter temperatures) are presented in blue and red, respectively. In the inset, the magnetization relative to saturation close to the transition region is shown.

of the irradiated samples have been also modified or not. The MCE is evaluated from the dependence of the magnetization at different temperatures and external fields in the SQUID magnetometer, following a procedure similar to that described in Ref. 9: (i) Each sample is initially brought to 350 K with $H = 0$; (ii) a magnetic field H (with a starting value equal to 2 T) is applied; (iii) the sample is cooled down to 150 K; (iv) the magnetic moment is recorded continuously during the temperature variation from 150 to 350 K with a sweep rate of +2 K/min; (v) at $T = 350$ K, the magnetic field is decreased with a step of 0.2 T; and then again from (ii) to (v) is repeated until $H = 0$. At a given temperature T, the magnetic entropy change is calculated numerically by[29] $\Delta S(T, \Delta H) = \int_{H_i}^{H_f} (\partial M/\partial T)_H \, dH$, for a magnetic field variation $\Delta H = H_f - H_i$. As presented in Fig. 6, the magnetic entropy change is only weakly affected by the ion bombardment, the integrated value of ΔS between 290 and 330 K decreases only from 175 to 163 J/kg (−7%). The irradiated MnAs thin film results in keeping the giant magnetocaloric properties at room temperature accompanied by a fully reversible behavior in $M(T)$ curves.

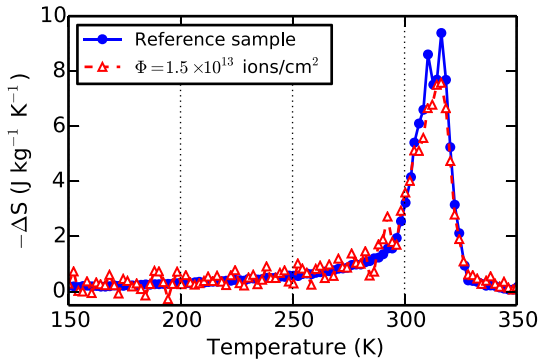

FIG. 6. Magnetic entropy change as a function of temperature determined from magnetization data of the reference and irradiated sample for a magnetic field change from 0 to 2 T.

Summarizing the different observations, we can conclude that the main effect of the highly charged ion bombardment on MnAs thin films is the disappearance of the thermal hysteresis occurring in the magneto-structural phase transition. The defects induced by the ion collision facilitate the nucleation of one phase with respect to the other during the transition, with a consequent suppression of ΔT_{hys}, but without any change on the nucleation of the magnetic domains and only a small perturbation of their mobility. In fact, contrary to the magnetic hysteresis, the other structural and magnetic properties of the film, are only slightly affected by the ion bombardment. In particular, the large refrigeration power of MnAs related to GMCE is preserved. This finding opens new perspectives on magnetic refrigeration considering even bulk materials if dealing with defects that can be induced by highly charged ions at higher velocity, taking advantage of their ballistic properties.[30]

We would like to thank P. Atkinson, M. Barturen, M. Chatelet, R. Gohier, J. Mérot, D. Mosca, and L. Thevenard for the fruitful discussion and support. This experiment is supported by a Grant from "Agence Nationale pour la Recherche (ANR)" No. ANR-06-BLAN-0223 and from Helmholtz Alliance No. HA216/EMMI.

[1]V. K. Pecharsky and J. K. A. Gschneidner, Phys. Rev. Lett. **78**, 4494 (1997).
[2]V. K. Pecharsky and J. K. A. Gschneidner, Appl. Phys. Lett. **70**, 3299 (1997).
[3]H. Wada and Y. Tanabe, Appl. Phys. Lett. **79**, 3302 (2001).
[4]A. de Campos, D. L. Rocco, A. M. G. Carvalho, L. Caron, A. A. Coelho, S. Gama, L. M. da Silva, F. C. G. Gandra, A. O. dos Santos, L. P. Cardoso, P. J. von Ranke, and N. A. de Oliveira, Nat. Mater. **5**, 802 (2006).
[5]D. L. Rocco, A. de Campos, A. M. G. Carvalho, L. Caron, A. A. Coelho, S. Gama, F. C. G. Gandra, A. O. dos Santos, L. P. Cardoso, P. J. von Ranke, and N. A. de Oliveira, Appl. Phys. Lett. **90**, 242507 (2007).
[6]N. K. Sun, W. B. Cui, D. Li, D. Y. Geng, F. Yang, and Z. D. Zhang, Appl. Phys. Lett. **92**, 072504 (2008).
[7]W. B. Cui, W. Liu, X. H. Liu, S. Guo, Z. Han, X. G. Zhao, and Z. D. Zhang, J. Alloys Compd. **479**, 189 (2009).
[8]J. Liu, T. Gottschall, K. P. Skokov, J. D. Moore, and O. Gutfleisch, Nat. Mater. **11**, 620 (2012).
[9]D. H. Mosca, F. Vidal, and V. H. Etgens, Phys. Rev. Lett. **101**, 125503 (2008).
[10]J. Y. Duquesne, J. Y. Prieur, J. A. Canalejo, V. H. Etgens, M. Eddrief, A. L. Ferreira, and M. Marangolo, Phys. Rev. B **86**, 035207 (2012).
[11]X. Moya, L. E. Hueso, F. Maccherozzi, A. I. Tovstolytkin, D. I. Podyalovskii, C. Ducati, L. C. Phillips, M. Ghidini, O. Hovorka, A. Berger, M. E. Vickers, E. Defay, S. S. Dhesi, and N. D. Mathur, Nature Mater. **12**, 52 (2013).
[12]C. Chappert, H. Bernas, J. Ferré, V. Kottler, J. P. Jamet, Y. Chen, E. Cambril, T. Devolder, F. Rousseaux, V. Mathet, and H. Launois, Science **280**, 1919 (1998).
[13]W. M. Kaminsky, G. A. C. Jones, N. K. Patel, W. E. Booij, M. G. Blamire, S. M. Gardiner, Y. B. Xu, and J. A. C. Bland, Appl. Phys. Lett. **78**, 1589 (2001).
[14]K. Zhang, R. Gupta, K. P. Lieb, Y. Luo, G. A. Müller, P. Schaaf, and M. Uhrmacher, Europhys. Lett. **64**, 668 (2003).
[15]K. Zhang, K. P. Lieb, G. A. Müller, P. Schaaf, M. Uhrmacher, and M. Münzenberg, Eur. Phys. J. B **42**, 193 (2004).
[16]G. A. Müller, E. Carpene, R. Gupta, P. Schaaf, K. Zhang, and K. P. Lieb, Eur. Phys. J. B **48**, 449 (2005).
[17]J. Fassbender, J. von Borany, A. Mücklich, K. Potzger, W. Müller, J. McCord, L. Schultz, and R. Mattheis, Phys. Rev. B **73**, 184410 (2006).
[18]P. J. Cook, T. H. Shen, P. J. Grundy, M. Y. Im, P. Fischer, S. A. Morton, and A. L. D. Kilcoyne, J. Appl. Phys. **109**, 063917 (2011).
[19]H. Wada and T. Asano, J. Magn. Magn. Mater. **290**, 703 (2005).
[20]L. Däweritz, Rep. Prog. Phys. **69**, 2581 (2006).

[21]V. M. Kaganer, B. Jenichen, F. Schippan, W. Braun, L. Däweritz, and K. H. Ploog, Phys. Rev. B **66**, 045305 (2002).
[22]M. Kastner, C. Herrmann, L. Däweritz, and K. H. Ploog, J. Appl. Phys. **92**, 5711 (2002).
[23]R. Breitwieser, F. Vidal, I. L. Graff, M. Marangolo, M. Eddrief, J. C. Boulliard, and V. H. Etgens, Phys. Rev. B **80**, 045403 (2009).
[24]A. Gumberidze, M. Trassinelli, N. Adrouche, C. I. Szabo, P. Indelicato, F. Haranger, J. M. Isac, E. Lamour, E. O. Le Bigot, J. Merot, C. Prigent, J. P. Rozet, and D. Vernhet, Rev. Sci. Instrum. **81**, 033303 (2010).
[25]J. F. Ziegler, J. P. Biersack, and M. D. Ziegler, *Stopping and Range of Ions in Matter* (SRIM Company, 2008).
[26]M. Trassinelli, V. E. Gafton, M. Eddrief, V. H. Etgens, S. Hidki, E. Lacaze, E. Lamour, X. Luo, M. Marangolo, J. Mérot, C. Prigent, R. Reuschl, J. P. Rozet, S. Steydli, and D. Vernhet, Nucl. Instrum. Methods Phys. Res., Sect. B **317**, 154 (2013).
[27]C. Adriano, C. Giles, O. D. D. Couto, M. J. S. P. Brasil, F. Iikawa, and L. Däweritz, Appl. Phys. Lett. **88**, 151906 (2006).
[28]L. B. Steren, J. Milano, V. Garcia, M. Marangolo, M. Eddrief, and V. H. Etgens, Phys. Rev. B **74**, 144402 (2006).
[29]K. A. Gschneidner, Jr., V. K. Pecharsky, and A. O. Tsokol, Rep. Prog. Phys. **68**, 1479 (2005).
[30]D. K. Avasthi and G. K. Mehta, *Swift Heavy Ions for Materials Engineering and Nanostructuring* (Springer, 2011).

Appendix I

Article about something completely different

Journal of Theoretical Biology 396 (2016) 42–52

Contents lists available at ScienceDirect

Journal of Theoretical Biology

journal homepage: www.elsevier.com/locate/yjtbi

Energy cost and optimisation in breath-hold diving

M. Trassinelli

Institut des NanoSciences de Paris, CNRS-UMR 7588, Sorbonne Universités, UPMC Univ Paris 06, 75005 Paris, France

HIGHLIGHTS

- We present a new model for calculating the locomotion cost of breath-hold divers.
- Optimal speed during dive transits is predicted to be a function of dive depth.
- Air exhalation before diving observed in phocid seals is explained.
- An upper limit to the active to passive drag ratio is given for dolphins.
- Neutral buoyancy of divers has been confirmed to be energetically advantageous.

ARTICLE INFO

Article history:
Received 11 April 2015
Received in revised form
4 February 2016
Accepted 8 February 2016
Available online 17 February 2016

Keywords:
Swimming
Cost of transport
Response to diving
Buoyancy
Dolphin

ABSTRACT

We present a new model for calculating locomotion costs in breath-hold divers. Starting from basic mechanics principles, we calculate the work that the diver must provide through propulsion to counterbalance the action of drag, the buoyant force and weight during immersion. Compared to those in previous studies, the model presented here accurately analyses breath-hold divers which alternate active swimming with prolonged glides during the dive (as is the case in mammals). The energy cost of the dive is strongly dependent on these prolonged gliding phases. Here we investigate the length and impacts on energy cost of these glides with respect to the diver characteristics, and compare them with those observed in different breath-hold diving species. Taking into account the basal metabolic rate and chemical energy to propulsion transformation efficiency, we calculate optimal swim velocity and the corresponding total energy cost (including metabolic rate) and compare them with observations. Energy cost is minimised when the diver passes through neutral buoyancy conditions during the dive. This generally implies the presence of prolonged gliding phases in both ascent and descent, where the buoyancy (varying with depth) is best used against the drag, reducing energy cost. This is in agreement with past results (Miller et al., 2012; Sato et al., 2013) where, when the buoyant force is considered constant during the dive, the energy cost was minimised for neutral buoyancy. In particular, our model confirms the good physical adaption of dolphins for diving, compared to other breath-hold diving species which are mostly positively buoyant (penguins for example). The presence of prolonged glides implies a non-trivial dependency of optimal speed on maximal depth of the dive. This extends previous findings (Sato et al., 2010; Watanabe et al., 2011) which found no dependency of optimal speed on dive depth for particular conditions. The energy cost of the dive can be further diminished by reducing the volume of gas-filled body parts in divers close to neutral buoyancy. This provides a possible additional explanation for the observed exhalation of air before diving in phocid seals to minimise dive energy cost. Until now the only explanation for this phenomenon has been a reduction in the risk of decompression sickness.

1. Introduction

During their dives, breath-hold diving animals minimise energetic cost to gain time foraging as oxygen stored in their body is limited. Besides plastic physiological adaptations to diving, like bradycardia, reduction and redistribution of the blood flow (Butler and Jones, 1997; Kooyman, 1985; Kooyman and Ponganis, 1998; Butler, 2004), dive energy cost can be lowered by reducing dive duration and/or the mechanical work necessary for propulsion. Energy cost related to the basal metabolic rate is proportional to dive duration and inversely proportional to swimming velocity. On the other side, energy spent for propulsion depends on the drag force during the dive, which increases with the square of velocity. Besides swimming optimisation and hydrodynamics, thrust work is efficiently reduced by slowing down swim speed. Optimal dive

E-mail address: trassinelli@insp.jussieu.fr

http://dx.doi.org/10.1016/j.jtbi.2016.02.009
0022-5193/

Acronyms

a.u. atomic units.

ARIBE Accélérateurs pour les Recherches avec les Ions de Basses Énergies (at GANIL).

ASUR Agrégats et surfaces sous excitations intenses.

CCD Charge-Coupled Device.

COB Classical Over-the-Barrier.

CTMC Classical Trajectory Monte Carlo.

GANIL Grand Accélérateur National d'Ions Lourds (Caen, France).

GMCE Giant MagnetoCaloric Effect.

GSI Gesellschaft für Schwerionenforschung.

HCI Highly Charged Ions.

INSP Institut des NanoSciences de Paris.

MCE MagnetoCaloric Effect.

MFM Magnetic Force Microscope.

ppm parts per million.

QED Quantum ElectroDynamics.

SDD Silicon Drift Detector.

SIMPA Source d'Ions Multichargés de Paris.

UHV Ultra-High Vacuum.

Detailed Curriculum vitæ

Martino Trassinelli

Curriculum Vitæ

Institut des NanoSciences de Paris
CNRS e Università Pierre et Marie Curie
☎ *+33 (0)1 44 27 62 30*
✉ *martino.trassinelli@insp.jussieu.fr*

Bird date 18th September

Current position Researcher at the Centre National de la Recherche Scientifique (CNRS, France) in the group "Clusters and Surfaces under Intense Excitation" at the Institut des NanoSciences de Paris

Scientific interests

- Dynamics of highly charged ion interaction with atoms (fast and slow ion velocity), whit surfaces and with clusters (slow ion velocity).
- Structure of exotic atoms (pionic atoms, highly charged ions, ...): study of quantum electrodynamics, strong and weak interactions.
- Modifications of structural and magnetic properties of thin films irradiated with ions.
- High-resolution X-ray spectroscopy based on Bragg diffraction.
- Bayesian statistics and applications to data analysis.

Teaching experience

2016-17 **Course of Ultrafast dynamics in Atoms and Molecules (part)**, *Research Master Light, Matter and Interactions*, University Pierre et Marie Curie- Paris 6, Paris, France, 11h in total.

2006 **Lecture on in *Exotic atoms* in the course Structure and Dynamics of Ions and Atoms**, *Research Master of Physics)*, Goethe University Frankfurt, Germany.

2005 **Physics tutoring in Thermodynamics**, *University Pierre et Marie Curie- Paris 6, Paris, France*, 2nd year undergraduate class, 36h plus 40h of practical work.

2003 **Physics tutoring in Mechanics and Fluido-dynamics**, *University Pierre et Marie Curie- Paris 6, Paris, France*, 1st year undergraduate class, 48h plus 24h of practical work.

Ph.D. thesis (Università Pierre et Marie Curie – Paris 6)

Title *Quantum Electrodyn. Tests and X-rays Standards using Pionic Atoms and Highly Charged Ions*

Director Paul Indelicato (Laboratoire Kastler Brossel, Paris, France)

Defence December 2005

Formation

2001–2002 **2nd year of Master's degree in Particle and Nuclear Physics (DEA Champs, Particules et Matières)**, *University Pierre et Marie Curie and E.N.S.*, Paris, France.

2000–2001 **1st year of Master's degree in Physics (Maîtrise de Physique)**, *University Pierre et Marie Curie and E.N.S.*, Paris, France.

1999–2000 **Licence de Physique**, *University Pierre et Marie Curie and E.N.S.*, Paris, France.

1999–2002 **Magistère Inter-universitaire de Physique**, *University Pierre et Marie Curie and E.N.S.*, Paris, France.

1997–1999 **Bachelor's degree in Physics (first two years)**, *Universiy of Florence*, Italy.

1996 **Maturità Artistica**, *Liceo Leon Battista Alberti*, Firenze, Italia.

Awards and recognitions

2013 **CNRS Scientific Excellence arward**.

2006–2007 **Postdoctoral Humboldt Research Fellowships**.

1999–2003 **Élève fonctionnaire stagiaire**, *École Normale Supérieure de Paris*.

Current collaboration

2011 – pres. Member of the collaboration *FISIC (Fast Ion – Slow Ion Collisions)* part of the EQUIPEX S3 (founding of the Agence Nationale de la Recherche (France)

2005 – pres. Member of the collaboration *SPARC (Stored Particles Atomic Research Collaboration)* for atomic physics at *FAIR (Facility for antiproton and ion research)*, Darmstadt, Germany

2003 – pres. Member of the collaboration *FOCAL* (FOcusing Compensated Asymmetric Laue spectrometer) for the measurement of the Lamb shift in heavy hydrogenlike ions, Darmstadt, Germani

2002 – pres. Member of the collaboration *Pionic Hydrogen et Pion Mass* for the study of strong interaction force in light pionic atoms and the measurement of the negatively charged pion mass

2005 – pres. Member of the European Physical Society

Positions in the administration of research

2013 – pres. Member of the international board (for France) of the *SPARC* collaboration

2013 – pres. Elected member of the laboratory council of the Institut des NanoSciences de Paris

2011 – pres. Coordinator of the group *Photon and X-Ray Spectrometers* of the SPARC collaboration

Participation to research projects

2013 – pres. Participation to the international ANR project *Fit-FISIC: First steps Towards atomic physics of Fast Ion – Slow Ion Collision*, inetrnational ANR/DFG founding , ANR-13-IS04-0007,(PI: E. Lamour)

2016 – pres. Leader of the project *Detector development for atomic physics at FAIR* in the program ENSAR2 No. 654002 *Transnational Access to GSI*, Horizon 2020 – EU Framework Programme for Research and Innovation –Integrated Activity, Germany

2013 – 2015 Leader of the project *Measurement of the bound-state beta decay of bare* ^{205}*Tl ions* in the program ENSAR No. 262010 *Transnational Access to GSI*, FP7 – Structuring the ERA - Integrated Activity, Germany

2007 Leader of the project *Test of Strong-Field-QED: High Resolution Detection Systems for Spectroscopy in Atomic Physics Experiments at GSI and FAIR and for Precision X-Ray Imaging*, non-recurring financing from the Helmholtz association for the promotion of young researchers, Germany

2006–2010 Participation to the ANR project *La Spectroscopie X: Métrologie et Sonde de l'Interaction avec les Ions de SIMPA*, ANR-06-BLAN-0223, Francia

Patents

rocess for obtaining a giant magnetocaloric effect material by irradiation of ions, French patent n. 1753170

Expert and referee activity

2014 – 2015 Member of the expert comity of Université Pierre et Marie Curie (atomic physics section)

2013 Referee for a Ph.D. Thesis of Oulu University (Finland)

2012 Member of the selection comity for an assistant professor position at the University Paris 13

2003 – pres. Referee in the international journals *Journal of Physics*, *Spectroscopy Letters*, *Physica Scripta*, *Nuclear Instruments and Methods A and B* et *Nanoscales Letters*

Organization of seminars and conferences

2016–pres. Member of the seminar comity of the Institut des NanoSciences de Paris

2017 Co-organizer of the workshop *MPBT platform scientific day*

2016–2017 Member of the scientific comity of the conference *Precision Physics, Quantum Electrodynamics and Fundamental Interactions*

Supervision of students

Ph.D. students

2014 – prés. Co-supervision of S. Cervera Ph.D. thesis *Suppression with ion irradiation of the thermal hysteresis of giant magnetocaloric materials at room temperature*, University Pierre et Marie Curie, Paris, France

2013 – 2016. Co-supervision of V.E. Gafton Ph.D. thesis *Contributions to the Study of Magnetic Properties of Materials in Interaction with High Energy Ionic Beams*, University of Ioan Cuza, Romania

2012 – 2016. Co-supervision of T. Gassner Ph.D. thesis *Measurement of the Lamb Shift of the Fundamental Level in Hydrogen-like Gold*, University de Jena, Germany

Master students

2017 Co-supervision of A. Kaoua, student of the Master Sciences of Materials and Nano-Objets (Univ. P. et M. Curie, Paris, Paris), 5 months

2014 Supervision of L. Bernard Carlsson, student of the Master Nansciences (ENS Cachan), 4 months

2012 Supervision of V.E. Gafton, student of the Master Nanomat (Univ. P. et M. Curie, Paris, Paris), 6 months

General public science communication

2008 – pres. Regular participation to the organization of the "Fête de la science", University Pierre et Marie Curie

March 2017 General public seminar *The physics of freediving*, Freediving club $7^{ème}$ *Apnée*

Publications in international journals with referee comity

[A1] S. Cervera, M. Trassinelli, M. Marangolo, V. Garcia, E. Jacquet, C. Carrétéro, S. Hidki, E. Lamour, A. Lévy, S. Macé, C. Prigent, J. P. Rozet, S. Steydli, and D. Vernhet, *Towards a spatial modulation of the phase transition temperature in giant magnetocaloric thin films with heavy ion irradiation*, submitted to Adv. Energy Mater.

[A2] T. Gassner, M. Trassinelli, R. Hess, U. Spillmann, D. Banas, K.-H. Blumenhagen, F. Bosch, C. Brandau, W. Chen, C. Dimopoulou, E. Förster, R. E. Grisenti, A. Gumberidze, S. Hagmann, P.-M. Hillenbrand, P. Indelicato, P. Jagodzinski, T. Kämpfer, C. Kozhuharov, M. Lestinsky, D. Liesen, Y. Litvinov, R. Loetzsch, B. Manil, R. Märtin, F. Nolden, N. Petridis, M. Sanjari, K. Schulze, M. Schwemlein, A. Simionovici, M. Steck, Th.Stöhlker, C. Szabo, S. Trotsenko, I. Uschmann, G. Weber, O. Wehrhan, N. Winckler, D. Winters, N. Winters, E. Ziegler, and H. Beyer, *Wavelength-dispersive spectroscopy in the hard x-ray regime on a heavy highly-charged ion: The 1s Lamb shift in hydrogen-like gold*, submitted to Phys. Rev. Lett.

[A3] A. Gumberidze, C. Kozhuharov, R. T. Zhang, S. Trotsenko, Y. S. Kozhedub, R. D. DuBois, H. F. Beyer, K. H. Blumenhagen, C. Brandau, A. Bräuning-Demian, W. Chen, O. Forstner, B. Gao, T. Gassner, R. E. Grisenti, S. Hagmann, P. M. Hillenbrand, P. Indelicato, A. Kumar, M. Lestinsky, Y. A. Litvinov, N. Petridis, D. Schury, U. Spillmann, C. Trageser, M. Trassinelli, X. Tu, and T. Stöhlker, *Impact parameter sensitive study of inner-shell atomic processes in the experimental storage ring*, Nucl. Instrum. Methods B, in press.

[A4] M. Trassinelli, *Bayesian data analysis tools for atomic physics*, arxiv:physics.data-an/1611.10189, Nucl. Instrum. Methods B, in press.

[A5] M. Trassinelli, L. Bernard Carlsson, S. Cervera, M. Eddrief, V. H. Etgens, E. V. Gafton, E. Lacaze, E. Lamour, A. Lévy, S. Macé, C. Prigent, J. P. Rozet, S. Steydli, M. Marangolo, and D. Vernhet, *Low energy ne ion beam induced-modifications of magnetic properties in MnAs thin films*, J. Phys. Condens. Matter **29** (2017), 055001.

[A6] M. Lestinsky, V. Andrianov, B. Aurand, V. Bagnoud, D. Bernhardt, H. Beyer, S. Bishop, K. Blaum, A. Bleile, A. Borovik, F. Bosch, C. Bostock, C. Brandau, A. Bräuning-Demian, I. Bray, T. Davinson, B. Ebinger, A. Echler, P. Egelhof, A. Ehresmann, M. Engström, C. Enss, N. Ferreira, D. Fischer, A. Fleischmann, E. Förster, S. Fritzsche, R. Geithner, S. Geyer, J. Glorius, K. Göbel, O. Gorda, J. Goullon, P. Grabitz, R. Grisenti, A. Gumberidze, S. Hagmann, M. Heil, A. Heinz, F. Herfurth, R. Heß, P.-M. Hillenbrand, R. Hubele, P. Indelicato, A. Källberg, O.

Kester, O. Kiselev, A. Knie, C. Kozhuharov, S. Kraft-Bermuth, T. Kühl, G. Lane, Y. Litvinov, D. Liesen, X. Ma, R. Märtin, R. Moshammer, A. Müller, S. Namba, P. Neumeyer, T. Nilsson, W. Nörtershäuser, G. Paulus, N. Petridis, M. Reed, R. Reifarth, P. Reiß, J. Rothhardt, R. Sanchez, M. Sanjari, S. Schippers, H. Schmidt, D. Schneider, P. Scholz, R. Schuch, M. Schulz, V. Shabaev, A. Simonsson, J. Sjöholm, O. Skeppstedt, K. Sonnabend, U. Spillmann, K. Stiebing, M. Steck, T. Stöhlker, A. Surzhykov, S. Torilov, E. Träbert, M. Trassinelli, S. Trotsenko, X. Tu, I. Uschmann, P. Walker, G. Weber, D. Winters, P. Woods, H. Zhao, and Y. Zhang, *Physics book: CRYRING@ESR*, Eur. Phys. J. Spec. Top. **225** (2016), 797–882.

[A7] M. Trassinelli, D. F. Anagnostopoulos, G. Borchert, A. Dax, J. P. Egger, D. Gotta, M. Hennebach, P. Indelicato, Y. W. Liu, B. Manil, N. Nelms, L. M. Simons, and A. Wells, *Measurement of the charged pion mass using x-ray spectroscopy of exotic atoms*, Phys. Lett. B **759** (2016), 583–588.

[A8] M. Trassinelli, *Energy cost and optimisation in breath-hold diving*, J. Theor. Biol. **396** (2016), 42–52.

[A9] E. V. Gafton, G. Bulai, O. F. Caltun, S. Cervera, S. Macé, M. Trassinelli, S. Steydli, and D. Vernhet, *Structural and magnetic properties of zinc ferrite thin films irradiated by 90 keV neon ions*, App. Surf. Sci. **379** (2016), 171–178.

[A10] E. Lamour, P. D. Fainstein, M. Galassi, C. Prigent, C. A. Ramirez, R. D. Rivarola, J. P. Rozet, M. Trassinelli, and D. Vernhet, *Extension of charge-state-distribution calculations for ion-solid collisions towards low velocities and many-electron ions*, Phys. Rev. A **92** (2015), 042703.

[A11] E. Lamour, C. Prigent, J.-M. Ramillon, J.-P. Rozet, S. Steydli, M. Trassinelli, and D. Vernhet, *High-resolution X-ray spectroscopy to probe quantum dynamics in collisions of* $Ar^{17+,18+}$ *ions with atoms and solids, towards clusters*, J. Phys. B **48** (2015), 144016.

[A12] A. Gumberidze, D. B. Thorn, C. J. Fontes, B. Najjari, H. L. Zhang, A. Surzhykov, A. Voitkiv, S. Fritzsche, D. Banaś, H. Beyer, W. Chen, R. D. DuBois, S. Geyer, R. E. Grisenti, S. Hagmann, M. Hegewald, S. Hess, C. Kozhuharov, R. Märtin, N. Petridis, R. Reuschl, A. Simon, U. Spillmann, M. Trassinelli, S. Trotsenko, G. Weber, D. F. A. Winters, N. Winters, D. Yu, and T. Stöhlker, *Ground-state excitation of heavy highly-charged ions*, J. Phys. B **48** (2015), 144006.

[A13] H. F. Beyer, T. Gassner, M. Trassinelli, R. Heß, U. Spillmann, D. Banaś, K.-H. Blumenhagen, F. Bosch, C. Brandau, W. Chen, C. Dimopoulou, E. Förster, R. E. Grisenti, A. Gumberidze, S. Hagmann, P.-M. Hillenbrand, P. Indelicato, P. Jagodzinski, T. Kämpfer, C. Kozhuharov, M. Lestinsky, D. Liesen, Y. A. Litvinov, R. Loetzsch, B. Manil, R. Märtin, F. Nolden, N. Petridis, M. S. Sanjari, K. S. Schulze, M. Schwemlein, A. Simionovici, M. Steck, T. Stöhlker, C. I. Szabo, S. Trotsenko, I. Uschmann, G. Weber, O. Wehrhan, N. Winckler, D. F. A. Winters, N. Winters, and E. Ziegler, *Crystal optics for precision X-ray spectroscopy on highly charged ions—conception and proof*, J. Phys. B **48** (2015), 144010.

[A14] M. Trassinelli, M. Marangolo, M. Eddrief, V. H. Etgens, V. Gafton, S. Hidki, E. Lacaze, E. Lamour, C. Prigent, J.-P. Rozet, S. Steydli, Y. Zheng, and D. Vernhet, *Suppression of the thermal hysteresis in magnetocaloric MnAs thin film by highly charged ion bombardment*, Appl. Phys. Lett. **104** (2014), 081906.

[A15] P. Jagodziński, M. Pajek, D. Banaś, H. F. Beyer, M. Trassinelli, and T. Stöhlker, *Ray-tracing simulations of spherical johann diffraction spectrometer for in-beam X-ray experiments*, Nucl. Instrum. Methods A **753** (2014), 121–130.

[A16] M. Hennebach, D. F. Anagnostopoulos, A. Dax, H. Fuhrmann, D. Gotta, A. Gruber, A. Hirtl, P. Indelicato, Y. W. Liu, B. Manil, V. E. Markushin, A. J. Rusi el Hassani, L. M. Simons, M. Trassinelli, and J. Zmeskal, *Hadronic shift in pionic hydrogen*, Eur. Phys. J. A **50** (2014), 1–10.

[A17] P. Amaro, C. I. Szabo, S. Schlesser, A. Gumberidze, E. G. Kessler Jr, A. Henins, E. O. Le Bigot, M. Trassinelli, J. M. Isac, P. Travers, M. Guerra, J. P. Santos, and P. Indelicato, *A vacuum double-crystal spectrometer for reference-free X-ray spectroscopy of highly charged ions*, Radiat. Phys. Chem. **98** (2014), 132–149.

[A18] D. Gotta, D. S. Covita, D. F. Anagnostopoulos, H. Fuhrmann, H. Gorke, A. Gruber, A. Hirtl, T. Ishiwatari, P. Indelicato, E. O. Le Bigot, M. Nekipelov, V. Pomerantsev, M. Popov, J. M. F. dos Santos, P. Schmid, L. M. Simons, M. Trassinelli, J. F. C. A. Veloso, and J. Zmeskal, *Precision measurement of the (3p–1s) X-ray transition in muonic hydrogen*, Phys. Part. Nuclei **45** (2014), 181–183.

[A19] S. Schlesser, S. Boucard, D. S. Covita, J. M. F. dos Santos, H. Fuhrmann, D. Gotta, A. Gruber, M. Hennebach, A. Hirtl, P. Indelicato, E. O. Le Bigot, L. M. Simons, L. Stingelin, M. Trassinelli, J. F. C. A. Veloso, A. Wasser, and J. Zmeskal, *High-accuracy X-ray line standards in the 3 keV region*, Phys. Rev. A **88** (2013), 022503.

[A20] P. Kienle, F. Bosch, P. Bühler, T. Faestermann, Y. A. Litvinov, N. Winckler, M. Sanjari, D. Shubina, D. Atanasov, H. Geissel, V. Ivanova, X. Yan, D. Boutin, C. Brandau, I. Dillmann, C. Dimopoulou, R. Hess, P.-M. Hillebrand, T. Izumikawa, R. Knöbel, J. Kurcewicz, N. Kuzminchuk, M. Lestinsky, S. Litvinov, X. Ma, L. Maier, M. Mazzocco, I. M. b, C. Nociforo, F. Nolden, C. Scheidenberger, U. Spillmann, M. Steck, T. Stöhlker, B. Sun, F. Suzaki, T. Suzuki, Y. Torilov, M. Trassinelli, X. Tu, M. Wang, H. Weick, D. Winters, N. Winters, P. Woods, T. Yamaguchir, G. Zhang, and T. Ohtsubov, *High-resolution measurement of the time-modulated orbital electron capture and of the decay of hydrogen-like* $^{142}Pm^{60+}$ *ions*, Phys. Lett. B **726** (2013), 638–645.

[A21] A. Gumberidze, D. B. Thorn, C. J. Fontes, B. Najjari, H. L. Zhang, A. Surzhykov, A. Voitkiv, S. Fritzsche, D. Bans, H. Beyer, W. Chen, R. D. DuBois, S. Geyer, R. E. Grisenti, S. Hagmann, M. Hegewald, S. Hess, C. Kozhuharov, R. Märtin, I. Orban, N. Petridis, R. Reuschl, A. Simon, U. Spillmann, M. Trassinelli, S. Trotsenko, G. Weber, D. F. A. Winters, N. Winters, D. Yu, and T. Stöhlker, *Electron- and proton-impact excitation of hydrogenlike uranium in relativistic collisions*, Phys. Rev. Lett. **110** (2013), 213201.

[A22] M. Trassinelli, V. E. Gafton, M. Eddrief, V. H. Etgens, S. Hidki, E. Lacaze, E. Lamour, X. Luo, M. Marangolo, J. Mérot, C. Prigent, R. Reuschl, J. P. Rozet, S. Steydli, and D. Vernhet, *Magnetic properties of MnAs thin films irradiated with highly charged ions*, Nucl. Instrum. Methods B **317** (2013), 154–158.

[A23] R. Reuschl, T. Gassner, U. Spillmann, A. Bräuning-Demian, A. Ananyeva, H. Beyer, K. H. Blumenhagen, W. Chen, S. Hagmann, M. Hegewald, P. Indelicato, M. Schwemlein, S. Toleikis, M. Trassinelli, S. Trotsenko, D. Winters, N. Winters, and T. Stöhlker, *Lifetime measurement of the* $2\ ^3P_0$ *state in He-like uranium*, Phys. Scripta **T156** (2013), 014024.

[A24] F. Bosch, D. R. Atanasov, C. Brandau, I. Dillmann, C. Dimopoulou, T. Faestermann, H. Geissel, S. Hagmann, P. M. Hillenbrand, P. Kienle, R. Knöbel, C. Kozhuharov, J. Kurcewicz, M. Lestinsky, S. A. Litvinov, Y. A. Litvinov, X. Ma, F. Nolden, T. Ohtsubo, Z. Patyk, R. Reuschl, M. S. Sanjari, C. Scheidenberger, D. Shubina, U. Spillmann, M. Steck, S. Th, B. Sun, M. Trassinelli, S. Trotsenko, X. L. Tu, H. Weick, N. Winckler, M. Winkler, D. Winters, T. Yamaguchi, and X. L. Yan, *Beta decay of highly charged ions*, Phys. Scripta **T156** (2013), 014025.

[A25] D. R. Atanasov, D. Balabanski, L. Batist, K. Blaum, F. Bosch, D. Boutin, C. Brandau, C. Dimopoulou, H. G. Essel, T. Faestermann, H. Geissel, S. Hagmann, R. Hess, P. M. Hillenbrand, P. Kienle, R. Knöbel, C. Kozhuharov, J. Kurcewicz, M. Lestinsky, S. A. Litvinov, A. L. Yu, X. Ma, R. Märtin, M. Mazzocco, G. Münzenberg, F. Nolden, T. Ohtsubo, Z. Patyk, M. S. Sanjari, C. Scheidenberger, D. Shubina, U. Spillmann, M. Steck, S. Th, B. Sun, T. Suzuki, S. Torilov, M. Trassinelli, S. Trotsenko, X. Tu, I. Tupitsyn, H. Weick, N. Winckler, M. Winkler, D. F. A. Winters, N. Winters, H. Xu, T. Yamaguchi, X. Yan, Y. Yuan, and Y. Zhang, *Half-life measurements of highly charged radionuclides*, Phys. Scripta **2013** (2013), 014026.

[A26] M. Trassinelli, C. Prigent, E. Lamour, F. Mezdari, J. Mérot, R. Reuschl, J. P. Rozet, S. Steydli, and D. Vernhet, *Investigation of slow collisions for (quasi) symmetric heavy systems: what can be extracted from high resolution X-ray spectra*, J. Phys. B **45** (2012), 085202.

[A27] D. Atanasov, N. Winckler, D. Balabanski, L. Batist, F. Bosch, D. Boutin, C. Brandau, C. Dimopoulou, H. Essel, T. Faestermann, H. Geissel, I. Hachiuma, S. Hess, T. Izumikawa, P. Kienle, R. Knöbel, C. Kozhuharov, J. Kurcewicz, N. Kuzminchuk, S. Litvinov, Y. Litvinov, R. Mao, R. Märtin, M. Mazzocco, G. Münzenberg, K. Namihira, F. Nolden, T. Ohtsubo, Z. Patyk, R. Reuschl, M. Sanjari, C. Scheidenberger, D. Shubina, U. Spillmann, M. Steck, T. Stöhlker, B. Sun, T. Suzuki, M. Trassinelli, I. Tupitsyn, H. Weick, M. Winkler, D. Winters, and T. Yamaguchi, *Half-life measurements of stored fully ionized and hydrogen-like ^{122}I ions*, Eur. Phys. J. A **48** (2012), 1–6.

[A28] D. B. Thorn, A. Gumberidze, S. Trotsenko, D. Banas, H. Beyer, C. J. Bostock, I. Bray, W. Chen, R. DuBois, C. J. Fontes, S. Fritzsche, D. V. Fursa, R. Grisenti, S. Geyer, S. Hagmann, S. Hess, M. Hegewald, C. Kozhuharov, R. Märtin, I. Orban, N. Petridis, R. Reuschl, A. Simon, U. Spillmann, A. Surzhykov, M. Trassinelli, G. Weber, D. F. A. Winters, N. Winters, H. L. Zhang, and T. Stöhlker, *Polarization and anisotropic emission of K-shell radiation from heavy few electron ions*, Can. J. Phys. **89** (2011), 513–519.

[A29] T. Strauch, F. Amaro, D. Anagnostopoulos, P. Bühler, D. Covita, H. Gorke, D. Gotta, A. Gruber, A. Hirtl, P. Indelicato, E. Le Bigot, M. Nekipelov, J. dos Santos, P. Schmid, S. Schlesser, L. Simons, M. Trassinelli, J. Veloso, and J. Zmeskal, *Pionic deuterium*, Eur. Phys. J. A **47** (2011), 1–19.

[A30] M. Trassinelli, A. Kumar, H. F. Beyer, P. Indelicato, R. Märtin, R. Reuschl, Y. S. Kozhedub, C. Brandau, H. Bräuning, S. Geyer, A. Gumberidze, S. Hess, P. Jagodzinski, C. Kozhuharov, D. Liesen, U. Spillmann, S. Trotsenko, G. Weber, D. F. A. Winters, and T. Stöhlker, *Differential energy measurement between He- and Li-like uranium intra-shell transitions*, Phys. Scripta **T144** (2011), 014003.

[A31] S. Trotsenko, A. Kumar, A. V. Volotka, D. Banas, H. F. Beyer, H. Bräuning, S. Fritzsche, A. Gumberidze, S. Hagmann, S. Hess, P. Jagodzinski, C. Kozhuharov, R. Reuschl, S. Salem,

A. Simon, U. Spillmann, M. Trassinelli, L. C. Tribedi, G. Weber, D. Winters, and T. Stöhlker, *Spectral shape of the two-photon decay of the* 2^1S_0 *state in He-like tin*, Phys. Rev. Lett. **104** (2010), 033001.

[A32] T. Strauch, F. D. Amaro, D. F. Anagnostopoulos, P. Bühler, D. S. Covita, H. Gorke, D. Gotta, A. Gruber, A. Hirtl, P. Indelicato, E. O. Le Bigot, M. Nekipelov, J. M. F. dos Santos, S. Schlesser, P. Schmid, L. M. Simons, M. Trassinelli, J. F. C. A. Veloso, and J. Zmeskal, *Precision determination of the* $d\pi - nn$ *transition strength at threshold*, Phys. Rev. Lett. **104** (2010), 142503.

[A33] A. Gumberidze, M. Trassinelli, N. Adrouche, C. I. Szabo, P. Indelicato, F. Haranger, J. M. Isac, E. Lamour, E. O. Le Bigot, J. Merot, C. Prigent, J. P. Rozet, and D. Vernhet, *Electronic temperatures, densities, and plasma X-ray emission of a 14.5 GHz electron-cyclotron resonance ion source*, Rev. Sci. Instrum. **81** (2010), 033303–10.

[A34] J. Kurcewicz, F. Bosch, H. Geissel, Y. A. Litvinov, N. Winckler, K. Beckert, P. Beller, D. Boutin, C. Brandau, L. Chen, C. Dimopoulou, H. G. Essel, B. Fabian, T. Faestermann, A. Fragner, B. Franzke, E. Haettner, M. Hausmann, S. Hess, P. Kienle, R. Knobel, C. Kozhuharov, S. A. Litvinov, L. Maier, M. Mazzocco, F. Montes, A. Musumarra, C. Nociforo, F. Nolden, Z. Patyk, W. R. Plass, A. Prochazka, R. Reda, R. Reuschl, C. Scheidenberger, M. Steck, T. Stohlker, B. Sun, K. Takahashi, S. Torilov, M. Trassinelli, H. Weick, and M. Winkler, *Studies of two-body* β *-decays at the FRS-ESR facility*, Acta Phys. Pol. B **41** (2010), 525–536.

[A35] N. Winckler, H. Geissel, Y. A. Litvinov, K. Beckert, F. Bosch, D. Boutin, C. Brandau, L. Chen, C. Dimopoulou, H. G. Essel, B. Fabian, T. Faestermann, A. Fragner, E. Haettner, S. Hess, P. Kienle, R. Knˆbel, C. Kozhuharov, S. A. Litvinov, M. Mazzocco, F. Montes, G. M¸nzenberg, C. Nociforo, F. Nolden, Z. Patyk, W. R. Plafl, A. Prochazka, R. Reda, R. Reuschl, C. Scheidenberger, M. Steck, T. Stöhlker, S. Y. Torilov, M. Trassinelli, B. Sun, H. Weick, and M. Winkler, *Orbital electron capture decay of hydrogen- and helium-like* ^{142}Pm *ions*, Phys. Lett. B **679** (2009), 36–40.

[A36] M. Trassinelli, A. Kumar, H. F. Beyer, P. Indelicato, R. Märtin, R. Reuschl, Y. S. Kozhedub, C. Brandau, H. Bräuning, S. Geyer, A. Gumberidze, S. Hess, P. Jagodzinski, C. Kozhuharov, D. Liesen, U. Spillmann, S. Trotsenko, G. Weber, D. F. A. Winters, and T. Stöhlker, *Observation of the* $2p_{3/2} \to 2s_{1/2}$ *intra-shell transition in He-like uranium*, Eur. Phys. Lett. **87** (2009), 63001.

[A37] A. Kumar, S. Trotsenko, A. V. Volotka, D. Banaś, H. F. Beyer, H. Bräuning, A. Gumberidze, S. Hagmann, S. Hess, C. Kozhuharov, R. Reuschl, U. Spillmann, M. Trassinelli, G. Weber, and T. Stöhlker, *Spectral shape of the 2E1 decay from 2s state in He-like tin*, Eur. Phys. J. Spec. Top. **169** (2009), 19–22.

[A38] D. S. Covita, D. F. Anagnostopoulos, H. Gorke, D. Gotta, A. Gruber, A. Hirtl, T. Ishiwatari, P. Indelicato, E. O. Le Bigot, M. Nekipelov, J. M. F. dos Santos, P. Schmid, L. M. Simons, M. Trassinelli, J. F. C. A. Veloso, and J. Zmeskal, *Line shape of the mu H(3p-1s) hyperfine transitions*, Phys. Rev. Lett. **102** (2009), 023401–4.

[A39] H. F. Beyer, D. Attia, D. Banas, E. O. Le Bigot, F. Bosch, J. C. Dousse, E. Förster, A. Gumberidze, S. Hagmann, S. Hefl, J. Hoszowska, P. Indelicato, P. Jagodzinski, C. Kozhuharov, T. Krings, D. Liesen, X. Ma, B. Manil, I. Mohos, M. Pajek, D. Protic, R. Reuschl, J. Rzadkiewicz, A. Simionovici, U. Spillmann, Z. Stachura, T. Stöhlker, M. Trassinelli, S. Trotsenko, A. Warczak,

O. Wehrhan, and E. Ziegler, *Crystal optics for hard-X-ray spectroscopy of highly charged ions*, Spectrochim. Acta, Part B **64** (2009), 736–743.

[A40] E. O. Le Bigot, S. Boucard, D. S. Covita, D. Gotta, A. Gruber, A. Hirtl, H. Fuhrmann, P. Indelicato, J. M. F. d. Santos, S. Schlesser, L. M. Simons, L. Stingelin, M. Trassinelli, J. F. C. A. Veloso, A. Wasser, and J. Zmeskal, *High-precision x-ray spectroscopy in few-electron ions*, Phys. Scripta **T134** (2009), 014015.

[A41] Y. A. Litvinov, F. Bosch, N. Winckler, D. Boutin, H. G. Essel, T. Faestermann, H. Geissel, S. Hess, P. Kienle, R. Knöbel, C. Kozhuharov, J. Kurcewicz, L. Maier, K. Beckert, P. Beller, C. Brandau, L. Chen, C. Dimopoulou, B. Fabian, A. Fragner, E. Haettner, M. Hausmann, S. A. Litvinov, M. Mazzocco, F. Montes, A. Musumarra, C. Nociforo, F. Nolden, W. Plaß, A. Prochazka, R. Reda, R. Reuschl, C. Scheidenberger, M. Steck, T. Stöhlker, S. Torilov, M. Trassinelli, B. Sun, H. Weick, and M. Winkler, *Observation of non-exponential orbital electron capture decays of hydrogen-like ^{140}Pr and ^{142}Pm ions*, Phys. Lett. B **664** (2008), 162–168.

[A42] V. Andrianov, K. Beckert, P. Beller, A. Bleile, P. Egelhof, A. Gumberidze, S. Ilieva, O. Kiselev, C. Kilbourne, H. J. Kluge, S. Kraft-Bermuth, D. McCammon, J. Meier, R. Reuschl, T. Stöhlker, and M. Trassinelli, *First experiments aiming for precise Lamb shift measurements on hydrogen-like heavy ions with low temperature calorimeters*, J. Low Temp. Phys. **151** (2008), 1049–1054.

[A43] M. Trassinelli and P. Indelicato, *Relativistic calculations of pionic and kaonic atoms' hyperfine structure*, Phys. Rev. A **76** (2007), 012510–7.

[A44] M. Trassinelli, D. Banas, H. F. Beyer, P. Jagodzinski, A. Kumar, M. Pajek, and T. Stöhlker, *High accuracy crystal spectroscopy of the $n = 2$ energy level of helium-like uranium*, Can. J. Phys. **85** (2007), 441–451.

[A45] Y. A. Litvinov, F. Bosch, H. Geissel, J. Kurcewicz, Z. Patyk, N. Winckler, L. Batist, K. Beckert, D. Boutin, C. Brandau, L. Chen, C. Dimopoulou, B. Fabian, T. Faestermann, A. Fragner, L. Grigorenko, E. Haettner, S. Hess, P. Kienle, R. Knobel, C. Kozhuharov, S. A. Litvinov, L. Maier, M. Mazzocco, F. Montes, G. Munzenberg, A. Musumarra, C. Nociforo, F. Nolden, M. Pfutzner, W. R. Plass, A. Prochazka, R. Reda, R. Reuschl, C. Scheidenberger, M. Steck, T. Stohlker, S. Torilov, M. Trassinelli, B. Sun, H. Weick, and M. Winkler, *Measurement of the β^+ and orbital electron-capture decay rates in fully ionized, hydrogenlike, and heliumlike ^{140}Pr ions*, Phys. Rev. Lett. **99** (2007), 262501–4.

[A46] P. Indelicato, S. Boucard, D. S. Covita, D. Gotta, A. Gruber, A. Hirtl, H. Fuhrmann, E. O. Le Bigot, S. Schlesser, J. M. F. dos Santos, L. M. Simons, L. Stingelin, M. Trassinelli, J. Veloso, A. Wasser, and J. Zmeskal, *Highly charged ion X-rays from Electron-Cyclotron Resonance ion sources*, Nucl. Instrum. Methods A **580** (2007), 8–13.

[A47] J. Rzadkiewicz, T. Stöhlker, D. Banas, H. F. Beyer, F. Bosch, C. Brandau, C. Z. Dong, S. Fritzsche, A. Gojska, A. Gumberidze, S. Hagmann, D. C. Ionescu, C. Kozhuharov, T. Nandi, R. Reuschl, D. Sierpowski, U. Spillmann, A. Surzhykov, S. Tashenov, M. Trassinelli, and S. Trotsenko, *Selective population of the $[1s2s]\ ^1S_0$ and $[1s2s]\ ^3S_1$ states of He-like uranium*, Phys. Rev. A **74** (2006), 012511–7.

[A48] P. Indelicato, E.-O. Le Bigot, M. Trassinelli, D. Gotta, M. Hennebach, N. Nelms, C. David, and L. M. Simons, *Characterization of a charge-coupled device array for Bragg spectroscopy*, Rev. Sci. Instrum. **77** (2006), 043107.

[A49] S. Chatterjee, H. F. Beyer, D. Liesen, T. Stohlker, A. Gumberidze, C. Kozhuharov, D. Banas, D. Protic, K. Beckert, P. Beller, T. Krings, F. Bosch, B. Franzke, S. Hagmann, J. Hoszowska, P. Indelicato, H.-J. Kluge, X. Ma, B. Manil, I. Mohos, F. Nolden, U. Popp, A. Simionovici, D. Sierpowski, M. Steck, U. Spillmann, C. Brandau, E. Förster, Z. Stachura, S. Tashenov, M. Trassinelli, A. Warczak, O. Wehrhan, E. Ziegler, S. Trotsenko, and R. Reuschl, *The FOCAL spectrometer for accurate x-ray spectroscopy of fast heavy ions*, Nucl. Instrum. Methods B **245** (2006), 67–71.

[A50] H. F. Beyer, T. Stöhlker, D. Banas, D. Liesen, D. Protić, K. Beckert, P. Beller, J. Bojowald, F. Bosch, E. Förster, B. Franzke, A. Gumberidze, S. Hagmann, J. Hoszowska, P. Indelicato, O. Klepper, H.-J. Kluge, S. Köig, C. Kozhuharov, X. Ma, B. Manil, I. Mohos, A. Oršic-Muthig, F. Nolden, U. Popp, A. Simionovici, D. Sierpowski, U. Spillmann, Z. Stachura, M. Steck, S. Tachenov, M. Trassinelli, A. Warczak, O. Wehrhan, and E. Ziegler, *FOCAL: X-ray optics for accurate spectroscopy*, Spectrochim. Acta, Part B **59** (2004), 1535–1542.

[A51] D. Gotta, M. Hennebach, Y. W. Liu, V. E. Markushin, L. M. Simons, M. Cargnelli, H. Fuhrmann, M. Giersch, A. Gruber, A. Hirtl, J. Marton, J. Zmeskal, P. Indelicato, B. Manil, M. Trassinelli, D. F. Anagnostopoulos, and N. Nelms, *Precision measurements in pionic hydrogen Paul Scherrer Institut*, Phys. Scripta **T104** (2003), 94–95.

[A52] D. F. Anagnostopoulos, M. Cargnelli, H. Fuhrmann, M. Giersch, D. Gotta, A. Gruber, M. Hennebach, A. Hirtl, P. Indelicato, Y. W. Liu, B. Manil, V. E. Markushin, J. Marton, N. Nelms, L. M. Simons, M. Trassinelli, and J. Zmeskal, *Precision measurements in pionic hydrogen*, Nucl. Phys. A **721** (2003), 849C–852C.

Book chapters

[B1] T. Stöhlker, A. Gumberidze, M. Trassinelli, V. Andrianov, H. Beyer, S. Kraft-Bermuth, A. Bleile, P. Egelhof, and F. collaboration, *Quantum electrodynamics in extreme fields: Precision spectroscopy of high- z h-like systems*, in Precision Physics of Simple Atoms and Molecules, Vol. 745 of *Lecture Notes in Physics*, Springer, Berlin / Heidelberg, 2008, pp. 157–163.

[B2] P. Indelicato, M. Trassinelli, D. F. Anagnostopoulos, S. Boucard, D. S. Covita, G. Borchert, A. Dax, J. P. Egger, D. Gotta, A. Gruber, A. Hirtl, M. Hennebach, H. Fuhrmann, E. O. Le Bigot, Y. W. Liu, B. Manil, N. Nelms, S. Schlesser, J. M. F. dos Santos, L. M. Simons, L. Stingelin, J. Veloso, A. Wasser, A. Wells, and J. Zmeskal, *Experiments on highly charged heavy ions in conjunction with exotic atoms*, in Current Trends in Atomic Physics, (S. Salomonson and E. Lindroth, eds.), Vol. 53 of *Advances in Quantum Chemistry*, Academic Press, 2008, pp. 217–235.

[B3] T. Stöhlker, A. Gumberidze, A. Kumar, R. Reuschl, and M. Trassinelli, *Quantum electrodynamics in one- and two-electron high-z ions*, in Current Trends in Atomic Physics, (S. Salomonson and E. Lindroth, eds.), Vol. 53 of *Advances in Quantum Chemistry*, Academic Press, 2008, pp. 57–65.

[B4] D. Gotta, F. Amaro, D. F. Anagnostopoulos, S. Biri, D. S. Covita, H. Gorke, A. Gruber, M. Hennebach, A. Hirtl, T. Ishiwatari, P. Indelicato, T. Jensen, E. O. Le Bigot, J. Marton, M. Nekipelov, J. M. F. dos Santos, S. Schlesser, P. Schmid, L. M. Simons, T. Strauch, M. Trassinelli, J. F. C. A. Veloso, and J. Zmeskal, *Pionic hydrogen*, in Precision Physics of Simple Atoms and Molecules, Vol. 745 of *Lecture Notes in Physics*, Springer, Berlin / Heidelberg, 2008, pp. 165–186.

Proceedings with referee comity

[C1] M. Trassinelli, D. Anagnostopoulos, G. Borchert, A. Dax, J.-P. Egger, D. Gotta, M. Hennebach, P. Indelicato, Y.-W. Liu, B. Manil, N. Nelms, L. Simons, and A. Wells, *Measurement of the charged pion mass using a low-density target of light atoms*, EPJ web conf. **130** (2016), 01022.

[C2] L. Bernard Carlsson, C. Prigent, E. Lamour, S. Macé, J. P. Rozet, S. Steydli, M. Trassinelli, and D. Vernhet, *X-ray spectroscopy as a tool to enlighten the growth of Van der Waals nanoparticles in a supersonic jet*, J. Phys. CS **635** (2015), 032030.

[C3] E. Lamour, P. D. Fainstein, M. Galassi, C. Prigent, C. A. Ramirez, R. D. Rivarola, J. P. Rozet, M. Trassinelli, and D. Vernhet, *Improvement of the ETACHA code towards low velocities and many-electron ions*, J. Phys. CS **635** (2015), 032022.

[C4] S. Cervera, M. Trassinelli, M. Marangolo, L. B. Carlsson, M. Eddrief, V. H. Etgens, V. Gafton, S. Hidki, E. Lamour, A. Lévy, S. Macé, C. Prigent, J. P. Rozet, S. Steydli, Y. Zheng, and D. Vernhet, *Hints on the origin of the thermal hysteresis suppression in giant magnetocaloric thin films irradiatied with highly charged ions*, J. Phys. CS **635** (2015), 012028.

[C5] S. Cervera, M. Trassinelli, M. Marangolo, L. Bernard-Carlsson, M. Eddrief, V. H. Etgens, V. Gafton, S. Hidki, E. Lacaze, E. Lamour, C. Prigent, J. P. Rozet, S. Steydli, Y. Zheng, and D. Vernhet, *Impacts of highly charged ions as seeds in a magneto-structural phase transition of magnetocaloric thin films*, J. Phys. CS **635** (2015), 032021.

[C6] D. Gotta, F. D. Amaro, D. F. Anagnostopoulos, P. Bühler, H. Gorke, D. S. Covita, H. Fuhrmann, A. Gruber, M. Hennebach, A. Hirtl, T. Ishiwatari, P. Indelicato, T. S. Jensen, E. O. Le Bigot, V. E. Markushin, J. Marton, M. Nekipelov, V. N. Pomerantsev, V. P. Popov, J. M. F. dos Santos, S. Schlesser, P. Schmid, L. M. Simons, T. Strauch, M. Theisen, M. Trassinelli, J. F. C. A. Veloso, and J. Zmeskal, *Pionic hydrogen and friends*, Hyperfine Interact. **234** (2015), 105–111.

[C7] X. Fléchard, L. Adoui, G. Ban, P. Boduch, A. Cassimi, J. Y. Chesnel, D. Durand, F. Frémont, S. Guillous, J. P. Grandin, D. Hennecart, E. Jacquet, P. Jardin, E. Lamour, E. Liénard, D. Lelièvre, L. Maunoury, A. Méry, O. Naviliat-Cuncic, C. Prigent, J. M. Ramillon, J. Rangama, J. P. Rozet, S. Steydli, M. Trassinelli, and D. Vernhet, *Primary processes: from atoms to diatomic molecules and clusters*, J. Phys. CS **629** (2015), 012001.

[C8] H. Yin, G. Wachter, C. Deiss, C. Lemell, J. Burgdörfer, E. Lamour, C. Prigent, C. Ramond, J. P. Rozet, S. Steydli, M. Trassinelli, and D. Vernhet, *keV electron heating in laser-cluster interaction probed by X-ray and electron spectroscopy*, J. Phys. CS **488** (2014), 132033.

[C9] A. Salehzadeh, M. Trassinelli, C. Prigent, E. Lamour, J. P. Rozet, S. Steydli, D. Vernhet, and T. Kirchner, *X-ray emission from highly-charged ions after electron transfer in slow collisions: the role of multiple capture processes*, J. Phys. CS **488** (2014), 082006.

[C10] C. Prigent, E. Lamour, J.-P. Rozet, S. Steydli, M. Trassinelli, and D. Vernhet, *Electron capture at low velocity in the collision of Ar^{17+} ions with atoms, clusters and solids*, J. Phys. CS **488** (2014), 012029.

[C11] C. Prigent, M. Comte, O. Gobert, D. Guillaumet, J. Habib, E. Lamour, M. Perdrix, C. Ramond, J.-P. Rozet, S. Steydli, M. Trassinelli, and D. Vernhet, *Role of the laser wavelength in the x-ray production for clusters under intense laser pulses*, J. Phys. CS **488** (2014), 132021.

[C12] S. Trotsenko, A. Kumar, D. Banas, A. V. Volotka, A. Gumberidze, C. Kozhuharov, D. B. Thorn, H. F. Beyer, S. Fritzsche, S. Hagmann, S. Hess, P. Jagodzinski, R. Reuschl, S. Salem, A. Simon, U. Spillmann, M. Trassinelli, L. C. Tribedi, G. Weber, D. Winters, and T. Stöhlker, *Novel approach for studying two-photon transitions in heavy HCI*, J. Phys. CS **388** (2012), 082001.

[C13] M. Trassinelli, C. Ramond, E. Lamour, J. Mérot, C. Prigent, J. P. Rozet, S. Steydli, and D. Vernhet, *Determining clustering properties through the selectivity of collision dynamics*, J. Phys. CS **388** (2012), 082009.

[C14] M. Trassinelli, T. Kirchner, E. Lamour, L. Maunoury, J. Mérot, J. Y. Pacquet, C. Prigent, J. M. Ramillon, R. Reuschl, J. P. Rozet, S. Steydli, and D. Vernhet, *Interaction of slow HCI with gaseous targets: absolute x-ray emission cross sections and contribution of multi-capture processes*, J. Phys. CS **388** (2012), 082010.

[C15] C. Ramond, E. Lamour, J. Mérot, C. Prigent, R. Reuschl, J. P. Rozet, G. Schiwietz, S. Steydli, M. Trassinelli, and D. Vernhet, *Correlation between X-ray yield and electron spectra in laser-cluster interaction*, J. Phys. CS **388** (2012), 032081.

[C16] A. Gumberidze, D. B. Thorn, S. Trotsenko, D. Banas, H. Beyer, W. Chen, R. D. DuBois, S. Geyer, R. Grisenti, S. Hagmann, M. Hegewald, S. Hess, P. Indelicato, C. Kozhuharov, R. Märtin, I. Orban, N. Petridis, R. Reuschl, A. Simon, U. Spillmann, A. Surzhykov, M. Trassinelli, G. Weber, D. F. A. Winters, N. Winters, D. Yu, and Th.Stöhlker, *Electron- and proton-impact excitation in stored hydrogenlike uranium ions*, J. Phys. CS **388** (2012), 082035.

[C17] D. Gotta, F. D. Amaro, D. F. Anagnostopoulos, P. Bühler, H. Gorke, D. S. Covita, H. Fuhrmann, A. Gruber, M. Hennebach, A. Hirtl, T. Ishiwatari, P. Indelicato, E. O. Le Bigot, J. Marton, M. Nekipelov, J. M. F. Santos, S. Schlesser, P. Schmid, L. M. Simons, T. Strauch, M. Trassinelli, J. F. C. A. Veloso, and J. Zmeskal, *Pionic hydrogen and deuterium*, Hyperfine Interact. **209** (2012), 57–62.

[C18] A. Kumar, S. Trotsenko, A. V. Volotka, D. Banas, H. F. Beyer, H. Brauning, S. Fritzsche, A. Gumberidze, S. Hagmann, S. Hess, C. Kozhuharov, R. Reuschl, U. Spillmann, M. Trassinelli, G. Weber, and T. Stohlker, *Spectral distribution of the $2s \to 1s$ two-photon transition in atoms and few-electron ions*, Pramana-J. Phys **76** (2011), 331–337.

[C19] A. Gumberidze, T. Stöhlker, D. Banaś, H. Beyer, C. Brandau, H. Bräuning, S. Geyer, S. Hagmann, S. Hess, P. Indelicato, P. Jagodziński, C. Kozhuharov, A. Kumar, D. Liesen, R.

Märtin, R. Reuschl, S. Salem, A. Simon, U. Spillmann, M. Trassinelli, S. Trotsenko, G. Weber, and D. Winters, *Precision studies of fundamental atomic structure with heaviest few-electron ions*, Hyperfine Interact. **199** (2011), 59–69.

[C20] D. Gotta, F. D. Amaro, D. F. Anagnostopoulos, A. Bühler, D. S. Covita, H. Gorke, A. Gruber, M. Hennebach, A. Hirtl, P. Indelicato, T. Ishiwatari, E. O. Le Bigot, J. Marton, M. Nekipelov, J. M. F. dos Santos, S. Schlesser, P. Schmid, L. M. Simons, T. Strauch, M. Trassinelli, J. F. C. A. Veloso, and J. Zmeskal, *Pionic hydrogen*, Phys Procedia **17** (2011), 69–76.

[C21] T. Strauch, F. D. Amaro, D. F. Anagnostopoulos, P. Bühler, D. S. Covita, H. Gorke, D. Gotta, A. Gruber, A. Hirtl, P. Indelicato, E. O. Le Bigot, M. Nekipelov, J. M. F. dos Santos, P. Schmid, S. Schlesser, L. M. Simons, M. Trassinelli, J. F. C. A. Veloso, and J. Zmeskal, *Pionic deuterium*, EPJ web conf. **3** (2010), 03006.

[C22] M. Trassinelli, A. Kumar, H. F. Beyer, P. Indelicato, R. Märtin, R. Reuschl, and T. Stöhlker, *Doppler-tuned Bragg spectroscopy of excited levels in He-like uranium: A discussion of the uncertainty contributions*, J. Phys. CS **163** (2009), 012026.

[C23] M. Trassinelli, S. Bari, H. M. Dang, S. Geyer, E. Lamour, L. Maunoury, H. Merabet, J. Merot, F. Mezdari, J. Y. Pacquet, B. Pascal, C. Prigent, J. M. Ramillon, R. Reuschl, J. P. Rozet, T. Schlatholter, S. Steydli, and D. Vernhet, *Collisions of Ar^{17+} ions with gaseous and solid targets at a few tens of kev/q probed by X-ray spectroscopy*, J. Phys. CS **194** (2009), 132005.

[C24] C. Prigent, E. Lamour, J. Merot, B. Pascal, J. P. Rozet, M. Trassinelli, D. Vernhet, J. Y. Pacquet, L. Maunoury, F. Noury, and J. M. Ramillon, *X-ray spectroscopy characterization of Ar^{17+} produced by an ecris in the afterglow mode*, J. Phys. CS **163** (2009), 012111.

[C25] A. Kumar, S. Trotsenko, A. V. Volotka, D. Banas, H. F. Beyer, H. Brauning, S. Fritzsche, A. Gumberidze, S. Hagmann, S. Hess, C. Kozhuharov, G. Plunien, R. Reuschl, U. Spillmann, M. Trassinelli, G. Weber, and T. Stöhlker, *Two-photon decay in highly charged heavy ions: Spectral shape of the 2e1 ($2\ ^1S_0 \to 1\ ^1S_0$) in He-like tin*, J. Phys. CS **163** (2009), 012027.

[C26] A. Hirtl and f. t. P. H. collaboration, *Determination of the hadronic width of the ground state in pionic hydrogen*, Hyperfine Interact. **193** (2009), 153–157.

[C27] S. Hess, H. Brauning, U. Spillmann, C. Brandau, S. Geyer, S. Hagmann, M. Hegewald, C. Kozhuharov, T. Krings, A. Kumar, R. Martin, D. Protic, B. O'Rourke, R. Reuschl, M. Trassinelli, S. Trotsenko, G. Weber, D. F. A. Winters, and T. H. Stohlker, *Polarization studies of radiative electron capture into highly-charged uranium ions*, J. Phys. CS **163** (2009), 012072.

[C28] D. Covita, D. Anagnostopoulos, H. Gorke, D. Gotta, A. Gruber, A. Hirtl, T. Ishiwatari, P. Indelicato, E. Le Bigot, M. Nekipelov, J. dos Santos, P. Schmid, L. Simons, M. Trassinelli, J. Veloso, and J. Zmeskal, *Line shape of the $\mu H(3p-1s)$ transition*, Hyperfine Interact. **193** (2009), 61–67.

[C29] S. Trotsenko, S. Th, D. Banas, C. Z. Dong, S. Fritzsche, A. Gumberidze, S. Hagmann, S. Hess, P. Indelicato, C. Kozhuharov, M. Nofal, R. Reuschl, J. Rzadkiewicz, U. Spillmann, A. Surzhykov, M. Trassinelli, and G. Weber, *Investigation of the decay properties of the $1s(2s)^2$ state in Li-like uranium*, J. Phys. CS **58** (2007), 141.

[C30] M. Trassinelli, S. Boucard, D. S. Covita, D. Gotta, A. Hirtl, O. Indelicato, P. andLe Bigot, J. M. F. d. Santos, L. M. Simons, L. Stingelin, J. F. C. A. Veloso, A. Wasser, and J. Zmeskal, *He-like argon, chlorine and sulfur spectra measurement from an electron cyclotron resonance ion trap*, J. Phys. CS **58** (2007), 129.

[C31] T. Stöhlker, H. Beyer, A. Gumberidze, A. Kumar, D. Liesen, R. Reuschl, U. Spillmann, and M. Trassinelli, *Ground state Lamb-shift of heavy hydrogen-like ions: status and perspectives*, Hyperfine Interact. **172** (2007), 135–140.

[C32] R. Reuschl, D. Banas, H. F. Beyer, S. Chatterjee, A. Gumberidze, S. Hess, T. Krings, D. Liesen, D. Protic, U. Spillmann, S. Th, M. Trassinelli, S. Trotsenko, Gweber, and F. collaboration, *Recent experimental developments for the lamb shift investigation in heavy ions*, J. Phys. CS **58** (2007), 407.

[C33] D. Banas, P. Jagodzinski, M. Pajek, S. Th, M. Trassinelli, H. F. Beyer, R. Reuschl, and U. Spillmann, *Development of a bragg spectrometer for experiments with highly charged ions at storage rings*, J. Phys. CS **58** (2007), 415.

Patents

[D1] M. Trassinelli, S. Cervera, D. Vernhet, M. Marangolo, and V. Garcia *Procédé d'obtention d'un matériau à effet magnétocalorique géant par irradiation d'ions*, Patent FR 1753170 (2017).

Conferences and seminars

Below are reported all the conferences personally presented by the author.

Invited oral contributions at conferences

[E1] *Light pionic and muonic atoms: investigation of hadron physics at low energy and atomic physics in exotic bound systems*, **Precision Physics, Quantum Electrodynamics and Foudamental Interactions**, 30 April - 5 Mai 2017, Cargèse, France.

[E2] *Measurement of the pion mass from X-ray spectroscopy of exotic atoms*, **14th International Workshop on Meson Production, Properties and Interaction**, 2-7 June 2016, Krakow, Poland.

[E3] *Symmetric heavy collision systems at low energy investigated by high resolution X-ray spectroscopy*, **23rd International Symposium on Ion Atom Collisions**, 19-22 July 2013, Beijing, China.

[E4] *Accurate Spectroscopy of Excited Levels in He-like Uranium*, **International Conference on the Physics of Highly Charged Ions**, 30 August - 3 September 2010, Shanghai, China.

[E5] *Correlations and Quantum Electrodynamics effects in He-like uranium*, **DPG Spring Meeting**, 10-14 March 2008, Darmstadt, Germany.

Selected oral contributions at conferences

[F1] M. Trassinelli, *HCI collisions to suppress the thermal hysteresis in magnetocaloric thin films*, **18th International Conference on the Physics of Highly Charged Ions**, 11-16 September 2016, Kielce, Poland.

[F2] *Suppression of the Thermal Hysteresis in Magnetocaloric Materials by Highly Charged Ion Bombardment*, **MMM Intermag 2016 Joint Conference**, 11-15 January 2016, San Diego, United States.

[F3] *Slow highly charged ion colliding with atoms, clusters and solid*, **26th International Conference on Atomic Collisions in Solids**, 13-18 July 2014 2014, Debrecen, Hungary.

[F4] *Contribution of multiple capture processes in slow collisions of highly charged ions with a many electrons target*, **46th Conference of the European Group on Atomic Systems**, 1-4 July 2014 2014, Lille, France.

[F5] *Investigation of (quasi) symmetric slow collisions between highly charged ions and free atoms*, **16th International Conference on the Physics of Highly Charged Ions**, 2-7 September 2012, Heidelberg, Germany.

[F6] *Investigation of (quasi) symmetric slow collisions between highly charged ions and free atoms* , **44th Conference of the European Group on Atomic Systems**, 9-13 July 2012, Gothenburg, Sweden.

[F7] *Determining clustering properties through the selectivity of collision dynamics*, **XXVII International Conference on Photonic, Electronic and Atomic Collisions**, 27 July - 2 August 2011, Belfast, Northern Ireland, UK (**selected topic**).

[F8] *Measurement of the Lamb shift in hydrogen-like lead using crystal spectroscopy methods*, **European Group on Atomic Systems Conference (EGAS 38)**, June 7-10 2006, Ischia, Italy.

[F9] *Precision spectroscopy of pionic atoms: from pion mass evaluation to tests of chiral perturbation theory*, **4th DAΦNE 2004: Physics at meson factories**, June 7-11 2004, Frascati, Italy.

Invited oral contributions at workshops

[G1] *Highly charged ions impact, a promising route to exploit the refrigeration power of giant magnetocaloric thin films*, **Journéees annuelles de la SF2M**, 26 - 28 October 2015, Paris, France.

[G2] *Images MFM de couches minces d'arséniure de manganèse irradié par des ions multichargés*, **Microscopie en champ proche à l'INSP**, 3 December 2015, Paris, France.

[G3] *Highly charges ions impact, a promising route to exploit the refrigeration power of giant magnetocaloric thin films*,**11th Topical Workshop of the SPARC collaboration**, 22-27 September 2015, Fodele, Greece.

[G4] *High-accuracy X-ray spectroscopy: a unique tool for studying atomic structure and dynamical processes in high Coulomb fields*, **X-ray Physics Workshop**, 24-26 February 2014, Jena, Germany.

[G5] *Astrophysics in lab via slow highly charged ion collisions with multi-electron targets*, **EMMI Physics Days 2013**, 18-19 November 2013, Darmstadt, Germany.

[G6] $n = 2 \rightarrow 2$ *transitions in highly charged two-electron ions.* **10th Topical Workshop of the SPARC collaboration**. 28-29 October 2013, Jena, Germany.

[G7] $n = 2 \rightarrow 2$ *transitions in highly charged two-electron ions*, **Mini workshop: Wavelength standards in the x-ray region Helmholtz-Institut Jena**, 19 April 2013, Jena, Germany.

[G8] M. Trassinelli, E. Lamour, S. Macé, C. Prigent, J.-P. Rozet, S. Steydli and D. Vernhet, *Experiments at the SIMPA ECR ion source in Paris: ion collisions*, **Micro-calorimeters applied for precision x-ray experiments: x-ray spectroscopy towards FAIR**, 31 January 2013, Jena, Germany.

[G9] *Interaction of slow HCI with gaseous targets: absolute x-ray emission cross sections and contribution of multi-capture processes*, **8th International Topical SPARC Workshop**, 5-10 September 2011, Moscow, Russia.

[G10] *Accurate Spectroscopy of Excited Levels in He-like Uranium*, **Physics Prospects at the ESR and HITRAP, EMMI Institute Workshop**, June 27-30 2010, Eisenach, Germany.

[G11] *Accurate Spectroscopy of Excited Levels in He-like Uranium*, **26th Wilhelm and Else Heraeus Seminar, Atomic Theory for Fundamental Interactions and Simple Systems in Strong Fields**, January 18-21 2009, Bad Honnef, Germany.

[G12] *Accurate Spectroscopy of Excited Levels in He-like Uranium*, **5th SPARC Workshop**, September 23-28 2008, Predeal, Romania.

[G13] *Low X-ray spectroscopy of highly charged ions*, **Topical Workshop of the SPARC Collaboration: Novel Research Opportunities for Atomic Physics with Heavy Ions: Facilities and Instrumentation**, February 12-15 2007, Paris, France.

[G14] *Atomic Physics with Highly Charged Ions at Storage Rings*, **XXXVIII. Arbeitstreffen Kernphysik**, February 22 - March 1 2007. Schleching.

[G15] *X-ray spectroscopy at HITRAP*, **HITRAP and Cave-A Topic workshop**, November 20-21 2006, Darmstadt, Germany.

[G16] *X-ray spectroscopy with HCI's at MAXEBIS and HITRAP*, **Workshop on "Charge breeding and related topic"**, May 22-24, 2006 Darmstadt, Germany.

Selected oral contributions at workshops

[H1] *Highly charged ions impact, a promising route to exploit the refrigeration power of giant magnetocaloric thin films*, **21th International Workshop on Inelastic Ion-Surface Collisions**, 18 - 23 October 2015, Donostia–San Sebastián, Spain.

[H2] M. Trassinelli, V.E. Gafton, M. Eddrief, V.H. Etgens, E. Lamour, X. Luo, M. Marangolo, C. Prigent, R. Reuschl, J.-P. Rozet, S. Steydli and D. Vernhet, *Magnetic properties changes of MnAs thin films irradiated with highly charged ions*, **19th International Workshop on Inelastic Ion-Surface Collisions**, 16-21 September 2012, Frauenchiemsee , Germany.

[H3] *High Resolution He-like Argon and Sulfur Spectra from the PSI ECRIT*, **Electron Cyclotron Resonance Ion Sources: 16th International Workshop on ECR Ion Sources ECRIS'04**, September 26-30 2004, Berkeley, California (USA).

Invited seminars

[I1] *Un gros souffle pour aller à 200 m de profondeur : la physique de la plongée en apnée*, Séminaire générale de l'Institut des NanoSciences de Paris, 29 June 2017, Paris, France.

[I2] *Un gros souffle pour aller à 200 m de profondeur : la physique de la plongée en apnée*, Séminaires de la Licence de Physique, Université Pierre et Marie Curie, 31 January 2017, Paris, France

[I3] *One deep breath to go 200 m deep in the sea: the physics of freedivers*, Maxwell lectures, King's College London, November 2016, London, United Kingdom.

[I4] *Light pionic and muonic atoms: investigation of hadron physics at low energy and atomic physics in exotic bound systems*, 26 September 2012, Helmholtz Institute Jena, Jena, Germany.

[I5] *Quantum Electrodynamics Tests and X-rays Standards using Pionic Atoms and Highly Charged Ions* 26 June 2006, Gesellschaft für Schwerionenforschung. Darmstadt, Germany

[I6] *Tests d'Électrodynamique Quantique et étalons de Rayons-X à l'Aide des Atomes Pioniques et des Ions Multichargés*, 9 January 2006, Institut des NanoSciences de Paris, Paris, France.

Bibliography

[1] R. Pohl, A. Antognini, F. Nez, F. D. Amaro, F. Biraben, J. M. R. Cardoso, D. S. Covita, A. Dax, S. Dhawan, L. M. P. Fernandes, A. Giesen, T. Graf, T. W. Hänsch, P. Indelicato, L. Julien, C.-Y. Kao, P. Knowles, E.-O. L. Bigot, Y.-W. Liu, J. A. M. Lopes, L. Ludhova, C. M. B. Monteiro, F. Mulhauser, T. Nebel, P. Rabinowitz, J. M. F. dos Santos, L. A. Schaller, K. Schuhmann, C. Schwob, D. Taqqu, J. F. C. A. Veloso, and F. Kottmann, *The size of the proton*, Nature **466** (2010), 213–216.

[2] A. Antognini, F. Nez, K. Schuhmann, F. D. Amaro, F. Biraben, J. M. R. Cardoso, D. S. Covita, A. Dax, S. Dhawan, M. Diepold, L. M. P. Fernandes, A. Giesen, A. L. Gouvea, T. Graf, T. W. Hänsch, P. Indelicato, L. Julien, C.-Y. Kao, P. Knowles, F. Kottmann, E.-O. L. Bigot, Y.-W. Liu, J. A. M. Lopes, L. Ludhova, C. M. B. Monteiro, F. Mulhauser, T. Nebel, P. Rabinowitz, J. M. F. dos Santos, L. A. Schaller, C. Schwob, D. Taqqu, J. F. C. A. Veloso, J. Vogelsang, and R. Pohl, *Proton structure from the measurement of 2S-2P transition frequencies of muonic hydrogen*, Science **339** (2013), 417–420.

[3] J. Ullmann, Z. Andelkovic, C. Brandau, A. Dax, W. Geithner, C. Geppert, C. Gorges, M. Hammen, V. Hannen, S. Kaufmann, K. König, Y. A. Litvinov, M. Lochmann, B. Maaß, J. Meisner, T. Murböck, R. Sánchez, M. Schmidt, S. Schmidt, M. Steck, T. Stöhlker, R. C. Thompson, C. Trageser, J. Vollbrecht, C. Weinheimer, and W. Nörtershäuser, *High precision hyperfine measurements in bismuth challenge bound-state strong-field QED*, Nat. Commun. **8** (2017), 15484.

[4] P. Beiersdorfer, *Testing qed and atomic-nuclear interactions with high- z ions*, J. Phys. B **43** (2010), 074032.

[5] V. A. Yerokhin and V. M. Shabaev, *Lamb shift of n = 1 and n = 2 states of hydrogen-like atoms,* $1 \leq z \leq 110$, J. Phys. Chem. Ref. Data **44** (2015), 033103.

[6] S. Deser, M. L. Goldberger, K. Baumann, and W. Thirring, *Energy level displacements in pi-mesonic atoms*, Phys. Rev. **96** (1954), 774–776.

[7] D. Gotta, *Precision spectroscopy of light exotic atoms*, Progress in Particle and Nuclear Physics **52** (2004), 133–195.

[8] J. Gasser, V. E. Lyubovitskij, and A. Rusetsky, *Hadronic atoms in qcd+qed*, Phys. Rep. **456** (2008), 167–251.

[9] P. J. Mohr, D. B. Newell, and B. N. Taylor, *Codata recommended values of the fundamental physical constants: 2014*, Rev. Mod. Phys. **88** (2016), 035009.

[10] U. D. Jentschura, A. Matveev, C. G. Parthey, J. Alnis, R. Pohl, T. Udem, N. Kolachevsky, and T. W. Hänsch, *Hydrogen-deuterium isotope shift: From the 1s-2s-transition frequency to the proton-deuteron charge-radius difference*, Phys. Rev. A **83** (2011), 042505.

[11] C. Brandau, C. Kozhuharov, Z. Harman, A. Muller, S. Schippers, Y. S. Kozhedub, D. Bernhardt, S. Bohm, J. Jacobi, E. W. Schmidt, P. H. Mokler, F. Bosch, H. J. Kluge, T. Stohlker, K. Beckert, P. Beller, F. Nolden, M. Steck, A. Gumberidze, R. Reuschl, U. Spillmann, F. J. Currell, I. I. Tupitsyn, V. M. Shabaev, U. D. Jentschura, C. H. Keitel, A. Wolf, and Z. Stachura, *Isotope shift in the dielectronic recombination of three-electron* $^a nd^{57+}$, Phys. Rev. Lett. **100** (2008), 073201–4.

[12] K. P. Gall, E. Austin, J. P. Miller, F. O'Brien, B. L. Roberts, D. R. Tieger, G. W. Dodson, M. Eckhause, J. Ginkel, P. P. Guss, D. W. Hertzog, D. Joyce, J. R. Kane, C. Kenney, J. Kraiman, W. C. Phillips, W. F. Vulcan, R. E. Welsh, R. J. Whyley, R. G. Winter, R. J. Powers, R. B. Sutton, and A. R. Kunselman, *Precision measurements of the* K^- *and* Σ^- *masses*, Phys. Rev. Lett. **60** (1988), 186–189.

[13] M. Gur'ev, A. Denisov, A. Zhelamkov, Y. M. Ivanov, P. Levchenko, V. Malakhov, A. Petrunin, Y. P. Platonov, A. Sergeev, and A. Smirnov, *First measurement of the x-ray emission of* σ^- *atoms by means of a crystal-diffraction spectrometer*, JETP Lett. **57** (1993), 400–400.

[14] S. Lenz, G. Borchert, H. Gorke, D. Gotta, T. Siems, D. F. Anagnostopoulos, M. Augsburger, D. Chatellard, J. P. Egger, D. Belmiloud, P. El-Khoury, P. Indelicato, M. Daum, P. Hauser, K. Kirch, and L. M. Simons, *A new determination of the mass of the charged pion*, Phys. Lett. B **416** (1998), 50–55.

[15] G. Beer, A. M. Bragadireanu, W. Breunlich, M. Cargnelli, C. Curceanu (Petrascu), J.-P. Egger, H. Fuhrmann, C. Guaraldo, M. Giersch, M. Iliescu, T. Ishiwatari, K. Itahashi, B. Lauss, V. Lucherini, L. Ludhova, J. Marton, F. Mulhauser, T. Ponta, A. C. Sanderson, L. A. Schaller, D. L. Sirghi, F. Sirghi, and J. Zmeskal, *A New Method to Obtain a Precise Value of the Mass of the Charged Kaon*, Phys. Lett. B **535** (2002), 52–58.

[16] H. Ryufuku, K. Sasaki, and T. Watanabe, *Oscillatory behavior of charge transfer cross sections as a function of the charge of projectiles in low-energy collisions*, Phys. Rev. A **21** (1980), 745.

[17] R. Mann, F. Folkmann, and H. F. Beyer, *Selective electron capture into highly stripped Ne and N target atoms after heavy-ion impact*, J. Phys. B **14** (1981), 1161.

[18] W. Fritsch and C. D. Lin, *Atomic-orbital-expansion studies of electron transfer in bare-nucleus* $Z(Z = 2, 4 - 8)$ *hydrogen-atom collisions*, Phys. Rev. A **29** (1984), 3039–3051.

[19] T. G. Winter and C. D. Lin, *Triple-center treatment of electron transfer and excitation in p-H collisions*, Phys. Rev. A **29** (1984), 567–582.

[20] M. Kimura and C. D.Lin, *A unified atomic-orbital and molecular- orbital matching method for ion-atom and atom-atom collisions*, Comments on Atomic and Mol. Phys. **20**.

[21] L. F. Errea, J. M. Gomez-Llorente, L. Mendez, and A. Riera, *Convergence study of* $He^{2+} + H$ *and* $He^+ + H^+$ *charge exchange cross sections using a molecular approach with an optimised common translation factor*, J. Phys. B **20** (1987), 6089.

[22] J. Eichler and T. Stöhlker, *Radiative electron capture in relativistic ion-atom collisions and the photoelectric effect in hydrogen-like high-z systems*, Phys. Rep. **439** (2007), 1–99.

[23] M. Theisen *Analyse der Linienform von Röntgenübergängen nach der Bayesmethode* Diplomarbeit, Fakultät für Mathematik, Informatik uns Naturwisssenschaften der RWTH Aachen, 2013.

[24] F. James and M. Roos, *MINUIT-A system for function minimization and analysis of the parameter errors and correlations*, Comp. Phys. Comm. **10** (1975), 343–67.

[25] W. H. Press, S. A. Teukolsky, W. T. Vetterling, and B. P. Flannery, *Numerical Recipes in Fortran 77: The Art of Scientific Computing*, second edition, Cambridge University Press, New York, 2001.

[26] D. S. Sivia and J. Skilling, *Data analysis: a Bayesian tutorial*, Second edition, Oxford University Press, 2006.

[27] S. Baker and R. D. Cousins, *Clarification of the use of chi-square and likelihood functions in fits to histograms*, Nucl. Instrum. Methods **221** (1984), 437–442.

[28] T. Hauschild and M. Jentschel, *Comparison of maximum likelihood estimation and chi-square statistics applied to counting experiments*, Nucl. Instrum. Methods A **457** (2001), 384–401.

[29] K. J. Mighell, *Parameter estimation in astronomy with poisson-distributed data. i. the chi(2)(gamma) statistic*, Astrophys. J. **518** (1999), 380–393.

[30] D. Protic, T. Stöhlker, H. F. Beyer, J. Bojowald, G. Borchert, A. Gumberidze, A. Hamacher, C. Kozhuharov, X. Ma, and I. Mohos, *A microstrip germanium detector for position-sensitive X-ray spectroscopy*, IEEE Trans. Nucl. Sci. **48** (2001), 1048–1052.

[31] D. Protic, T. Stöhlker, T. Krings, I. Mohos, and U. Spillmann, *Two-dimensional microstrip germanium detector for the spectroscopy of hard X-ray transitions*, IEEE Trans. Nucl. Sci. **52** (2005), 3194–3198.

[32] U. Spillmann, H. Brauning, S. Hess, H. Beyer, T. Stohlker, J. C. Dousse, D. Protic, and T. Krings, *Performance of a ge-microstrip imaging detector and polarimeter*, Rev. Sci. Instrum. **79** (2008), 083101–8.

[33] T. Gaß ner, *High precision x-ray spectroscopy of highly charged heavy ions*, Thesis, 2017.

[34] J. Neyman and E. Pearson, *On the problems of the most efficient tests of statistical hypotheses*, Phil. Trans. R. Soc. **231** (1933), 289–337.

[35] F. Yates, *Contingency tables involving small numbers and the χ^2 test*, Sup. J. R. Stat. Soc. **1** (1934), 217–235.

[36] P. Bevington and D. Robinson, *Data reduction and error analysis for the physical sciences*, McGraw-Hill, 2003.

[37] F. J. Massey, *The kolmogorov-smirnov test for goodness of fit*, J. Am. Stat. Assoc. **46** (1951), 68–78.

[38] H. Akaike, *A new look at the statistical model identification*, IEEE Trans. Automat. Contr. **19** (1974), 716–723.

[39] D. J. Spiegelhalter, N. G. Best, B. P. Carlin, and A. Van Der Linde, *Bayesian measures of model complexity and fit*, J. R. Stat. Soc. B **64** (2002), 583–639.

[40] M. Bayes and M. Price, *An essay towards solving a problem in the doctrine of chances. by the late rev. mr. bayes, f. r. s. communicated by mr. price, in a letter to john canton, a. m. f. r. s*, Philosophical Transactions **53** (1763), 370–418.

[41] P. Laplace, *Essai philosophique sur les probabilités*, Bachelier, 1825.

[42] H. Jeffreys, *Theory of Probability*, 3th ed. edition, Oxford University Press, Oxford, U.K., 1961.

[43] E. Jaynes and G. Bretthorst, *Probability Theory: The Logic of Science*, Cambridge University Press, 2003.

[44] A. Lewis and S. Bridle, *Cosmological parameters from cmb and other data: A monte carlo approach*, Phys. Rev. D **66** (2002), 103511.

[45] R. Trotta, *Bayes in the sky: Bayesian inference and model selection in cosmology*, Contemp. Phys. **49** (2008), 71–104.

[46] F. Feroz, M. P. Hobson, and M. Bridges, *Multinest: an efficient and robust bayesian inference tool for cosmology and particle physics*, Mon. Not. R. Astron. Soc. **398** (2009), 1601–1614.

[47] C. Patrignani and G. Particle Data, *Review of particle physics*, Chinese Phys. B **40** (2016), 100001.

[48] J. K. Stockton, X. Wu, and M. A. Kasevich, *Bayesian estimation of differential interferometer phase*, Phys. Rev. A **76** (2007), 033613.

[49] D. Calonico, F. Levi, L. Lorini, and G. Mana, *Bayesian inference of a negative quantity from positive measurement results*, Metrologia **46** (2009), 267.

[50] N. Wiebe and C. Granade, *Efficient bayesian phase estimation*, Phys. Rev. Lett. **117** (2016), 010503.

[51] A. Mooser, H. Kracke, K. Blaum, S. A. Bräuninger, K. Franke, C. Leiteritz, W. Quint, C. C. Rodegheri, S. Ulmer, and J. Walz, *Resolution of single spin flips of a single proton*, Phys. Rev. Lett. **110** (2013), 140405.

[52] N. P. Barradas, C. Jeynes, M. Jenkin, and P. K. Marriott, *Bayesian error analysis of Rutherford backscattering spectra*, Thin Solid Films **343** (1999), 31–34.

[53] R. T. Cox, *Probability, frequency and reasonable expectation*, Am. J. Phys. **14** (1946), 1–13.

[54] R. Cox, *Algebra of Probable Inference*, Johns Hopkins University Press, 1961.

[55] L. E. Ballentine, *Probability theory in quantum mechanics*, Am. J. Phys. **54** (1986), 883–889.

[56] R. E. Kass and A. E. Raftery, *Bayes factors*, J. Am. Stat. Assoc. **90** (1995), 773–795.

[57] C. Gordon and R. Trotta, *Bayesian calibrated significance levels applied to the spectral tilt and hemispherical asymmetry*, Mon. Not. R. Astron. Soc. **382** (2007), 1859–1863.

[58] C. E. Shannon, *A mathematical theory of communication*, Bell Syst. Tech. J. **27** (1948), 623–656.

[59] C. E. Shannon, *A mathematical theory of communication*, Bell Syst. Tech. J. **27** (1948), 379–423.

[60] S. Kullback and R. A. Leibler, *On information and sufficiency*, Ann. Math. Stat. **22** (1951), 79–86.

[61] D. J. Spiegelhalter, N. G. Best, B. P. Carlin, and A. Van Der Linde, *The deviance information criterion: 12 years on*, J. R. Stat. Soc. B **76** (2014), 485–493.

[62] C. Robert and G. Casella, *Monte Carlo Statistical Methods*, Springer New York, 2013.

[63] J. Skilling, *Nested sampling*, AIP Conf. Proc. **735** (2004), 395–405.

[64] J. Skilling, *Nested sampling for general bayesian computation*, Bayesian Anal. **1** (2006), 833–859.

[65] J. Skilling, *Nested sampling's convergence*, AIP Conf. Proc. **1193** (2009), 277–291.

[66] J. Veitch and A. Vecchio, *Bayesian coherent analysis of in-spiral gravitational wave signals with a detector network*, Phys. Rev. D **81** (2010), 062003.

[67] N. Chopin and C. P. Robert, *Properties of nested sampling*, Biometrika **97** (2010), 741–755.

[68] P. Mukherjee, D. Parkinson, and A. R. Liddle, *A nested sampling algorithm for cosmological model selection*, Astrophys. J. Lett. **638** (2006), L51.

[69] R. S. Hayano, M. Hori, D. Horváth, and E. Widmann, *Antiprotonic helium and cpt invariance*, Rep. Prog. Phys. **70** (2007), 1995.

[70] K. A. Olive and G. Particle Data, *Review of particle physics*, Chinese Phys. B **38** (2014), 090001.

[71] B. Jeckelmann, P. F. A. Goudsmit, and H. J. Leisi, *The mass of the negative pion*, Phys. Lett. B **335** (1994), 326–329.

[72] M. Daum, R. Frosch, D. Heter, M. Janousch, and P.-R. Kettle, *New precision measurement of the muon momentum in pion decay at rest*, Phys. Lett. B **265** (1991), 425–429.

[73] K. Assamagan, C. Brnnimann, H. F. M. Daum, R. Frosch, P. Gheno, R. Horisberger, M. Janousch, P. R. Kettle, T. Spirig, and C. Wigger, *Upper limit of the muon-neutrino mass and charged-pion mass from momentum analysis of a surface muon beam*, Phys. Rev. D **53** (1996), 6065–6077.

[74] L. M. Simons, *Recent results on antiprotonic atoms using a cyclotron trap at lear*, Phys. Scripta **T22** (1988), 90–95.

[75] L. M. Simons, *The cyclotron trap for antiprotons*, Hyperfine Interact. **81** (1993), 253–262.

[76] J. S. Cohen, *Capture of negative exotic particles by atoms, ions and molecules*, Rep. Prog. Phys. **67** (2004), 1769.

[77] T. Siems, D. F. Anagnostopoulos, G. Borchert, D. Gotta, P. Hauser, K. Kirch, L. Simons, P. El-Khoury, P. Indelicato, M. Augsburger, D. Chatellard, and J.-P. Egger, *First direct observation of coulomb explosion during the formation of exotic atoms*, Phys. Rev. Lett. **84** (2000), 4573–4576.

[78] G. R. Burbidge and A. H. de Borde, *The mesonic auger effect*, Phys. Rev. **89** (1953), 189–193.

[79] H. B. Bethe and E. E. Salpeter, *Quantum Mechanics of One- and Two-Electron Atoms*, first edition, Springer-Verlag, 1957.

[80] P. Vogel, *Muonic cascade: General discussion and application to the third-row elements*, Phys. Rev. A **22** (1980), 1600–1609.

[81] R. Bacher, D. Gotta, L. M. Simons, J. Missimer, and N. C. Mukhopadhyay, *Muonic atoms with vacant electron shells*, Phys. Rev. Lett. **54** (1985), 2087–2090.

[82] R. Bacher, P. Blüm, D. Gotta, K. Heitlinger, M. Schneider, J. Missimer, and L. M. Simons, *Relevance of ionization and electron refilling to the observation of the $m1$ transition ($\gamma m1 : 2s-1s$) in light muonic atoms*, Phys. Rev. A **39** (1989), 1610–1620.

[83] K. Kirch, D. Abbott, B. Bach, P. Hauser, P. Indelicato, F. Kottmann, J. Missimer, P. Patte, R. T. Siegel, L. M. Simons, and D. Viel, *Muonic cascades in isolated low-z atoms and molecules*, Phys. Rev. A **59** (1999), 3375–3385.

[84] T. S. Jensen and V. E. Markushin, *Scattering of light exotic atoms in excited states*, Eur. Phys. J. D **19** (2002), 165–181.

[85] T. S. Jensen and V. E. Markushin, *Collisional deexcitation of exotic hydrogen atoms in highly excited states. i. cross-sections*, Eur. Phys. J. D **21** (2002), 261–270.

[86] S. Kilic, J.-P. Karr, and L. Hilico, *Coulombic and radiative decay rates of the resonances of the exotic molecular ions $pp\mu, pp\pi, dd\mu, dd\pi$, and $dt\mu$*, Phys. Rev. A **70** (2004), 042506.

[87] V. N. Pomerantsev and V. P. Popov, *Coulomb deexcitation of pionic hydrogen within the close-coupling method*, Phys. Rev. A **73** (2006), 040501.

[88] T. Jensen, V. Popov, and V. Pomerantsev, *Atomic cascade in muonic and hadronic hydrogen atoms*, arXiv preprint arXiv:0712.3010.

[89] V. Popov and V. Pomerantsev, *Scattering processes of excited exotic atoms: Close-coupling approach*, arXiv preprint arXiv:0712.3111.

[90] H. H. Johann, *Die erzeugung lichtstarker röntgenspektren mit hilfe von konkavkristallen.*, Z. Physik **69** (1931), 185–206.

[91] D. E. Gotta and L. M. Simons, *Remarks on a johann spectrometer for exotic-atom research and more*, Spectrochim. Acta, Part B **120** (2016), 9–18.

[92] J. Eggs and K. Ulmer, *Roentgenspektroskopie mit sphaerisch gekruemmten kristallen*, Zf. angew. Phys. **20** (1965), 118–128.

[93] N. Nelms, D. F. Anagnostopoulos, O. Ayranov, G. Borchert, J.-P. Egger, D. Gotta, M. Hennebach, P. Indelicato, B. Leoni, Y. W. Liu, B. Manil, L. M. Simons, and A. Wells, *A large area CCD X-ray detector for exotic atom spectroscopy*, Nucl. Instrum. Methods A **484** (2002), 419–31.

[94] M. Sanchez del Rio and J. Dejus, *XOP: Recent development*, in SPIE proceedings, 1998, p. 3448.

[95] M. Sánchez del Río and R. J. Dejus, *Xop v2.4: recent developments of the x-ray optics software toolkit*, SPIE proceedings **8141** (2011), 814115–814115–5.

[96] S. Biri, L. Simons, and D. Hitz, *Electron cyclotron resonance ion trap: a hybrid magnetic system with very high mirror ratio for highly charged ion production and trapping*, Rev. Sci. Instrum. **71** (2000), 1116–18.

[97] D. F. Anagnostopoulos, S. Biri, V. Boisbourdain, M. Demeter, G. Borchert, J.-P. Egger, H. Fuhrmann, D. Gotta, A. Gruber, M. Hennebach, P. Indelicato, Y. W. Liu, B. Manil, V. E. Markushin, H. Marton, N. Nelms, A. Rusi El Hassani, L. M. Simons, L. Stingelin, A. Wasser, A. Wells, and J. Zmeskal, *Highly charged ions in exotic atoms research at PSI*, Nucl. Instrum. Methods B **205** (2003), 9–14.

[98] D. F. Anagnostopoulos, S. Biri, H. Fuhrmann, D. Gotta, A. Gruber, P. Indelicato, B. Leoni, L. M. Simons, L. Stingelin, A. Wasser, and J. Zmeskal, *On the characterisation of a Bragg spectrometer with X-rays from an ECR source*, Nucl. Instrum. Methods A **545** (2005), 217–224.

[99] D. S. Covita, *High Precision Spectroscopy of the 3p – 1s X-Ray Transition in Muonic Hydrogen*, PhD thesis, University of Coimbra, 2008.

[100] J. D. Jackson, *Classical Electrodynamics*, second edition, Jhon Wiley and Sons, 1975.

[101] J. Desclaux, J. Dolbeault, M. Esteban, P. Indelicato, and E. Séré, *Computational approaches of relativistic models in quantum chemistry*, in Computational Chemistry, (C. Le Bris and M. De Franceschi, eds.), Vol. X of *Handbook of Numerical Analysis*, Elsevier, Amsterdam, 2003, p. 1032.

[102] J. P. Santos, F. Parente, S. Boucard, P. Indelicato, and J. P. Desclaux, *X-ray energies of circular transitions and electron screening in kaonic atoms*, Phys. Rev. A **71** (2005), 032501.

[103] B. Jeckelmann, W. Beer, G. De Chambrier, O. Elsenhans, K. L. Giovanetti, P. F. A. Goudsmit, H. J. Leisi, T. Nakada, O. Piller, A. Rüetschi, and W. Schwitz, *New precision determination of the π^- mass from pionic x-rays*, Nucl. Phys. A **457** (1986), 709–730.

[104] B. Jeckelmann, T. Nakada, W. Beer, G. de Chambrier, O. Elsenhans, K. L. Giovanetti, P. F. A. Goudsmit, H. J. Leisi, A. Rüetschi, O. Piller, and W. Schwitz, *New precision determination of the π^- mass from pionic x rays*, Phys. Rev. Lett. **56** (1986), 1444–1447.

[105] R. Abela, M. Daum, G. H. Eaton, R. Frosch, B. Jost, P. R. Kettle, and E. Steiner, *Precision measurement of the muon momentum in pion decay at rest*, Phys. Lett. B **146** (1984), 431–436.

[106] D. C. Lu, D. Delker, G. Dugan, C. S. Wu, A. J. Caffrey, Y. T. Cheng, and Y. K. Lee, *New high-accuracy measurement of the pionic mass*, Phys. Rev. Lett. **45** (1980), 1066–1069.

[107] A. L. Carter, M. S. Dixit, M. K. Sundaresan, J. S. Wadden, F. J. Watson, C. K. Hargrove, E. P. Hincks, R. J. McKee, H. Mes, H. L. Anderson, and A. Zehnder, *New determination of the π^- mass from pionic-atom transition energies*, Phys. Rev. Lett. **37** (1976), 1380–1383.

[108] V. N. Marushenko, A. F. Mezentsev, A. A. Petrunin, S. G. Skornyakov, and A. I. Smirnov, *New measurement of the π^--meson mass*, JETP Lett. **23** (1976), 72–74.

[109] R. E. Shafer, *Pion-mass measurement by crystal diffraction of mesonic x rays*, Phys. Rev. **163** (1967), 1451–1461.

[110] W. H. Barkas, W. Birnbaum, and F. M. Smith, *Mass-ratio method applied to the measurement of l-meson masses and the energy balance in pion decay*, Phys. Rev. **101** (1956), 778–795.

[111] M. Stearns, M. B. Stearns, S. DeBenedetti, and L. Leipuner, *Limits on π^- meson mass from mesonic X-rays*, Phys. Rev. **95** (1954), 1353–1354.

[112] K. M. Crowe and R. H. Phillips, *Precision measurement of the negative pion mass from its radiative absorption in hydrogen*, Phys. Rev. **96** (1954), 470–483.

[113] F. M. Smith, W. Birnbaum, and W. H. Barkas, *Measurements of meson masses and related quantities*, Phys. Rev. **91** (1953), 765–766.

[114] W. H. Barkas, F. M. Smith, and E. Gardner, *Meson to proton mass ratios*, Phys. Rev. **82** (1951), 102–103.

[115] Joint Committee for Guides in Metrology, *Evaluation of measurement data — guide to the expression of uncertainty in measurement*, JCGM 100, ISO/IEC Guide 98-3.

[116] G. D'Agostini, *Bayesian Reasoning in Data Analysis: A Critical Introduction*, 2003.

[117] G. D'Agostini and M. Raso, *Uncertainties due to imperfect knowledge of systematic effects: general considerations and approximate formulae.*

[118] C. Patrignani and G. Particle Data *Review of particle physics, 2017 update* `http://pdg.lbl.gov`.

[119] G. J. Feldman and R. D. Cousins, *Unified approach to the classical statistical analysis of small signals*, Phys. Rev. D **57** (1998), 3873–3889.

[120] C. M. Lisse, K. Dennerl, J. Englhauser, M. Harden, F. E. Marshall, M. J. Mumma, R. Petre, J. P. Pye, M. J. Ricketts, J. Schmitt, J. Trümper, and R. G. West, *Discovery of x-ray and extreme ultraviolet emission from comet C/Hyakutake 1996 B2*, Science **274** (1996), 205–209.

[121] V. Krasnopolsky, *On the nature of soft x-ray radiation in comets*, Icarus **128** (1997), 368–385.

[122] M. J. Mumma, V. A. Krasnopolsky, and M. J. Abbott, *Soft x-rays from four comets observed with EUVE*, Astrophys. J. Lett. **491** (1997), L125.

[123] C. M. Lisse, D. J. Christian, K. Dennerl, K. J. Meech, R. Petre, H. A. Weaver, and S. J. Wolk, *Charge exchange-induced x-ray emission from comet C/1999 S4 (linear)*, Science **292** (2001), 1343–1348.

[124] T. E. Cravens, *X-ray emission from comets*, Science **296** (2002), 1042–1045.

[125] V. A. Krasnopolsky, J. B. Greenwood, and P. C. Stancil, *X-ray and extreme ultraviolet emissions from comets*, Space Sci. Rev. **113** (2004), 271–373.

[126] K. Dennerl, *Charge transfer reactions*, Space Sci. Rev. **157** (2010), 57–91.

[127] K. Dennerl, C. M. Lisse, A. Bhardwaj, D. J. Christian, S. J. Wolk, D. Bodewits, T. H. Zurbuchen, M. Combi, and S. Lepri, *Solar system x-rays from charge exchange processes*, Astron. Nachr. **333** (2012), 324–334.

[128] J. Liu, Q. D. Wang, Z. Li, and J. R. Peterson, *X-ray spectroscopy of the hot gas in the M31 bulge*, Mon. Not. R. Astron. Soc. **404** (2010), 1879–1885.

[129] Q. D. Wang and J. Liu, *Spectroscopic evidence of charge exchange x-ray emission from galaxies*, Astron. Nachr. **333** (2012), 373–377.

[130] E. Bulbul, M. Markevitch, A. Foster, R. K. Smith, M. Loewenstein, and S. W. Randall, *Detection of an unidentified emission line in the stacked x-ray spectrum of galaxy clusters*, Astrophys. J. **789** (2014), 13.

[131] M. Bitter, K. W. Hill, B. Stratton, A. L. Roquemore, D. Mastrovito, S. G. Lee, J. G. Bak, M. K. Moon, U. W. Nam, G. Smith, J. E. Rice, P. Beiersdorfer, and B. S. Fraenkel, *Spatially resolved spectra from a new x-ray imaging crystal spectrometer for measurements of ion and electron temperature profiles*, Rev. Sci. Instrum. **75** (2004), 3660–3665.

[132] O. Marchuk, G. Bertschinger, H.-J. Kunze, N. R. Badnell, and S. Fritzsche, *Cascades between doubly excited levels in helium-like argon*, J. Phys. B **37** (2004), 1951.

[133] P. Beiersdorfer, M. Bitter, M. Marion, and R. E. Olson, *Charge-exchange-produced k-shell x-ray emission from* ar^{16+} *in a tokamak plasma with neutral-beam injection*, Phys. Rev. A **72** (2005), 032725.

[134] H. P. Winter, *HCI issues in tokamak fusion plasmas*, J. Phys. CS **58** (2007), 33.

[135] A. Barany, G. Astner, H. Cederquist, H. Danared, S. Huldt, P. Hvelplund, A. Johnson, H. Knudsen, L. Liljeby, and K. G. Rensfelt, *Absolute cross sections for multi-electron processes in low energy* $Ar^{q+} - Ar$ *collisions: Comparison with theory*, Nucl. Instrum. Methods B **9** (1985), 397–399.

[136] M. Barat and P. Roncin, *Multiple electron capture by highly charged ions at kev energies*, J. Phys. B **25** (1992), 2205.

[137] M. Mack, J. H. Nijland, P. v. d. Straten, A. Niehaus, and R. Morgenstern, *Correlation in double electron capture in collisions of fully stripped ions on He and* H_2, Phys. Rev. A **39** (1989), 3846.

[138] D. Vernhet, A. Chetioui, J. P. Rozet, C. Stephan, K. Wohrer, A. Touati, M. F. Politis, P. Bouisset, D. Hitz, and S. Dousson, *Characteristics of single capture nl distributions and double capture probabilities in slow collisions of* Al^{13+}, Al^{12+} *and* Ne^{9+} *ions with two-electron targets (He,* H_2*)*, J. Phys. B **21** (1988), 3949.

[139] A. Chetioui, F. Martin, J. P. Rozet, A. Touati, L. Blumendeld, D. Vernhet, K. Wohrer, C. Stephan, M. Barat, M. N. Gbouriaud, H. Laurent, and P. Roncin, *Doubly excited states populated in collisions of* O^{8+} *ions with He and* H_2 *at 1.24 keV* amu^{-1}, J. Phys. B **23** (1990), 3659.

[140] N. Stolterfoht, R. D. DuBois, and R. D. Rivarola, *The Physics of Multiply and Highly Charged Ions: Interactions with matter*, Springer Series on Atoms and Plasmas, Springer, 1997.

[141] F. J. Currel, *The Physics of Multiply and Highly Charged Ions: Interactions with matter*, Kluwer Academic Publisher, 2003.

[142] R. Ali, C. L. Cocke, M. L. A. Raphaelian, and M. Stockli, *Multielectron processes in 10-keV/u Ar^{q+} ($5 \leq q \leq 17$) on Ar collisions*, Phys. Rev. A **49** (1994), 3586.

[143] P. Beiersdorfer, R. E. Olson, G. V. Brown, H. Chen, C. L. Harris, P. A. Neill, L. Schweikhard, S. B. Utter, and K. Widmann, *X-ray emission following low-energy charge exchange collisions of highly charged ions*, Phys. Rev. Lett. **85** (2000), 5090.

[144] J. B. Greenwood, I. D. Williams, S. J. Smith, and A. Chutjian, *Measurement of charge exchange and x-ray emission cross sections for solar wind-comet interactions*, Astrophys. J. Lett. **533** (2000), L175.

[145] D. Fischer, B. Feuerstein, R. D. DuBois, R. Moshammer, J. R. C. López-Urrutia, I. Draganic, H. Lörch, A. N. Perumal, and J. Ullrich, *State-resolved measurements of single-electron capture in slow Ne^{7+} - and Ne^{8+} - helium collisions*, J. Phys. B **35** (2002), 1369.

[146] P. Beiersdorfer, K. R. Boyce, G. V. Brown, H. Chen, S. M. Kahn, R. L. Kelley, M. May, R. E. Olson, F. S. Porter, C. K. Stahle, and W. A. Tillotson, *Laboratory simulation of charge exchange-produced x-ray emission from comets*, Science **300** (2003), 1558–1559.

[147] H. Tawara, P. Richard, U. I. Safronova, and P. C. Stancil, *K x-ray production in H-like Si^{13+}, S^{15+}, and Ar^{17+} ions colliding with various atom and molecule gas targets at low collision energies*, Phys. Rev. A **64** (2001), 042712.

[148] H. Tawara, E. Takacs, T. Suta, K. Makonyi, L. P. Ratliff, and J. D. Gillaspy, *K x rays produced in collisions of bare ions with atoms: Contribution of multiple-electron transfer in Kr^{36+}, Ar^{18+}, and $Ne^{10+} + Ar$ collisions*, Phys. Rev. A **73** (2006), 012704–5.

[149] F. I. Allen, C. Biedermann, R. Radtke, G. Fussmann, and S. Fritzsche, *Energy dependence of angular momentum capture states in charge exchange collisions between slow highly charged argon ions and argon neutrals*, Phys. Rev. A **78** (2008), 032705–7.

[150] S. Knoop and et al., *Single-electron capture in kev $Ar^{15+...18+}$ + He collisions*, J. Phys. B **41** (2008), 195203.

[151] M. A. Leutenegger, P. Beiersdorfer, G. V. Brown, R. L. Kelley, C. A. Kilbourne, and F. S. Porter, *Measurement of anomalously strong emission from the 1s-9p transition in the spectrum of H-like phosphorus following charge exchange with molecular hydrogen*, Phys. Rev. Lett. **105** (2010), 063201.

[152] W. Chen, G. Vorobyev, D. Guo, P. M. Hillenbrand, F. Herfurth, S. Hagmann, U. Spillmann, S. Trotsenko, A. Gumberidze, and T. Stöhlker, *Charge transfer of slow highly charged xenon ions in collisions with magnesium atoms*, Phys. Rev. A **88** (2013), 052703.

[153] H. Shimaya, T. Ishida, S. Ishikawa, S. Suda, H. Tanuma, H. Akamatsu, H. Ohashi, N. Ijima, M. Inoue, Y. Ezoe, Y. Ishisaki, T. Ohashi, K. Shinozaki, K. Mitsuda, L. Liu, and J. Wang, *Soft x-ray emission from solar wind charge exchange in the laboratory*, Phys. Scripta **T156** (2013), 014002.

[154] L. Liu, J. G. Wang, and R. K. Janev, *Charge-transfer-induced x-ray spectra in collisions of ne^{10+} with he and ne atoms*, Phys. Rev. A **89** (2014), 012710.

[155] R. Ali, P. Beiersdorfer, C. L. Harris, and P. A. Neill, *Charge-exchange x-ray spectra: Evidence for significant contributions from radiative decays of doubly excited states*, Phys. Rev. A **93** (2016), 012711.

[156] G. L. Betancourt-Martinez, P. Beiersdorfer, G. V. Brown, R. L. Kelley, C. A. Kilbourne, D. Koutroumpa, M. A. Leutenegger, and F. S. Porter, *Observation of highly disparate k-shell x-ray spectra produced by charge exchange with bare mid-z ions*, Phys. Rev. A **90** (2014), 052723.

[157] C. Shah, S. Dobrodey, S. Bernitt, R. Steinbrügge, J. R. C. López-Urrutia, L. Gu, and J. Kaastra, *Laboratory measurements compellingly support a charge-exchange mechanism for the 'dark matter" ∼3.5 keV x-ray line*, Astrophys. J. **833** (2016), 52.

[158] K. Taulbjerg, *Reaction windows for electron capture by highly charged ions*, J. Phys. B **19** (1986), L367.

[159] H. J. Lüdde, A. Henne, T. Kirchner, and R. M. Dreizler, *Optimized dynamical representation of the solution of time-dependent quantum problems*, J. Phys. B **29** (1996), 4423.

[160] O. J. Kroneisen, H. J. Lüdde, T. Kirchner, and R. M. Dreizler, *The basis generator method: optimized dynamical representation of the solution of time-dependent quantum problems*, J. Phys. A **32** (1999), 2141.

[161] T. Kirchner, M. Horbatsch, H. J. Ludde, and R. M. Dreizler, *Time-dependent screening effects in ion-atom collisions with many active electrons*, Phys. Rev. A **62** (2000), 042704.

[162] R. Abrines and I. C. Percival, *A generalized correspondence principle and proton-hydrogen collisions*, P. Phys. Soc. **88** (1966), 873.

[163] R. E. Olson and A. Salop, *Charge-transfer and impact-ionization cross sections for fully and partially stripped positive ions colliding with atomic hydrogen*, Phys. Rev. A **16** (1977), 531–541.

[164] S. Otranto, R. E. Olson, and P. Beiersdorfer, *X-ray emission cross sections following charge exchange by multiply charged ions of astrophysical interest*, Phys. Rev. A **73** (2006), 022723–9.

[165] R. Ali, P. A. Neill, P. Beiersdorfer, C. L. Harris, D. R. Schultz, and P. C. Stancil, *Critical test of simulations of charge-exchange-induced x-ray emission in the solar system*, Astrophys. J. Lett. **716** (2010), L95.

[166] S. Otranto and R. E. Olson, *X-ray emission cross sections following Ar^{18+} charge-exchange collisions on neutral argon: The role of the multiple electron capture*, Phys. Rev. A **83** (2011), 032710.

[167] D. Vernhet, A. Chetioui, K. Wohrer, J. P. Rozet, P. Piquemal, D. Hitz, S. Dousson, A. Salin, and C. Stephan, *Alignment of Ne^{8+} n^1P states produced by collisions of Ne^{9+} with H_2 at 4 keV/amu*, Phys. Rev. A **32** (1985), 1256.

[168] D. Vernhet, L. Adoui, J. Rozet, K. Wohrer, A. Chetioui, A. Cassimi, J. Gradin, and J. Ramillon, *Multielectron processes in heavy ion-atom collisions at intermediate velocity*, Phys. Rev. Lett. **79** (1997), 3625–3628.

[169] L. Maunoury, R. Leroy, T. Been, G. Gaubert, L. Guillaume, D. Leclerc, A. Lepoutre, V. Mouton, J. Y. Pacquet, J. M. Ramillon, and R. Vicquelin, *LIMBE: A new facility for low energy beams*, Rev. Sci. Instrum. **73** (2002), 561–563.

[170] E. Lamour, C. Prigent, B. Eberhardt, J. P. Rozet, and D. Vernhet, *2E1 Ar^{17+} decay and conventional radioactive sources to determine efficiency of semiconductor detectors*, Rev. Sci. Instrum. **80** (2009), 023103–7.

[171] I. M. Savukov, W. R. Johnson, and U. I. Safronova, *Multipole (E1, M1, E2, M2) transition wavelengths and rates between states with n_l=6 in helium-like carbon, nitrogen, oxygen, neon, silicon, and argon*, At. Data Nucl. Data Tables **85** (2003), 83–167.

[172] P. Indelicato and J. Desclaux *MCDFGME, a MultiConfiguration Dirac Fock and general matrix elements program (release 2005)* `http://dirac.spectro.jussieu.fr/mcdf`, 2005.

[173] I. Wolfram Research, *Mathematica*, Wolfram Research, Inc., Champaign, Illinois, USA, Version 10.2 edition, 2015.

[174] A. Niehaus, *A classical model for multiple-electron capture in slow collisions of highly charged ions with atoms*, J. Phys. B **19** (1986), 2925–2937.

[175] J. Burgdorfer, R. Morgenstern, and A. Niehaus, *Angular momentum distribution in the classical over-barrier model for electron capture into highly charged slow projectiles*, J. Phys. B **19** (1986), L507–L513.

[176] T. Kirchner private communication, 2011.

[177] A. Salehzadeh and T. Kirchner, *Strong multiple-capture effect in slow* Ar^{17+} – Ar *collisions: a quantum mechanical analysis*, J. Phys. B **46** (2013), 025201.

[178] S. Otranto, N. D. Cariatore, and R. E. Olson, *X-ray emission produced in charge-exchange collisions between highly charged ions and argon: Role of the multiple electron capture*, Phys. Rev. A **90** (2014), 062708.

[179] R. Ginzel, *Wechselwirkung niederenergetischer hochgeladener Ionen mit Materie*, PhD thesis, Naturwissenschaftlich-Mathematischen Gesamtfakultät der Ruprecht-Karls-Universität Heidelberg, 2010.

[180] G. H. Kinchin and R. S. Pease, *The displacement of atoms in solids by radiation*, Rep. Prog. Phys. **18** (1955), 1.

[181] F. Seitz and J. S. Koehler, *Displacement of atoms during irradiation*, Solid State Phys. **2** (1956), 305–448.

[182] J. F. Ziegler and J. P. Biersack, *The Stopping and Range of Ions in Matter*, Springer US, Boston, MA, 1985, pp. 93–129.

[183] M. Nastasi, J. Mayer, and J. Hirvonen, *Ion-Solid Interactions: Fundamentals and Applications*, Cambridge University Press, 1996.

[184] I. P. Jain and G. Agarwal, *Ion beam induced surface and interface engineering*, Surf. Sci. Rep. **66** (2011), 77–172.

[185] M. W. Thompson, *Defects and Radiation Damage in Metals*, CUP Archive, 1974.

[186] M. Toulemonde, C. Dufour, and E. Paumier, *Transient thermal process after a high-energy heavy-ion irradiation of amorphous metals and semiconductors*, Phys. Rev. B **46** (1992), 14362–14369.

[187] J. F. Ziegler, J. P. Biersack, and M. D. Ziegler, *Stopping and Range of Ions in Matter*, SRIM Company, 2008.

[188] P. Sigmund, *Sputtering by ion bombardment theoretical concepts*, Springer Berlin Heidelberg, Berlin, Heidelberg, 1981, pp. 9–71.

[189] F. Aumayr and H. Winter, *Potential sputtering*, Phil. Trans. R. Soc. A **362** (2004), 77–102.

[190] P. Sigmund, *Elements of sputtering theory*, 2012, pp. 1–40.

[191] T. Neidhart, F. Pichler, F. Aumayr, H. Winter, M. Schmid, and P. Varga, *Potential sputtering of lithium fluoride by slow multicharged ions*, Phys. Rev. Lett. **74** (1995), 5280–5283.

[192] G. Hayderer, S. Cernusca, M. Schmid, P. Varga, H. Winter, and A. F., *Kinetically assisted potential sputtering of insulators by highly charged ions*, Phys. Rev. Lett. **86** (2001), 3530–3533.

[193] H. Winter and F. Aumayr, *Interaction of slow hci with solid surfaces: What do we know, what should we know?*, Phys. Scripta **T92** (2001), 15–21.

[194] I. C. Gebeshuber, S. Cernusca, F. Aumayr, and H. Winter, *AFM search for slow MCI-produced nanodefects on atomically clean monocrystalline insulator surfaces*, Nucl. Instrum. Methods B **205** (2003), 751–757 (TY - JOUR).

[195] A. S. El-Said, W. Meissl, M. C. Simon, J. R. Crespo López-Urrutia, I. C. Gebeshuber, J. Laimer, H. P. Winter, J. Ullrich, and F. Aumayr, *Creation of surface nanostructures by irradiation with slow, highly charged ions*, Radiat. Eff. Def. Solids **162** (2007), 467–472.

[196] J. M. Pomeroy, A. C. Perrella, H. Grube, and J. D. Gillaspy, *Gold nanostructures created by highly charged ions*, Phys. Rev. B **75** (2007), 241409.

[197] S. Facsko, R. Heller, A. S. El-Said, W. Meissl, and F. Aumayr, *Surface nanostructures by single highly charged ions*, J. Phys. Condens. Matter **21** (2009), 224012.

[198] F. Aumayr, S. Facsko, A. S. El-Said, C. Trautmann, and M. Schleberger, *Single ion induced surface nanostructures: a comparison between slow highly charged and swift heavy ions*, J. Phys. Condens. Matter **23** (2011), 393001.

[199] Y. Y. Wang, C. Grygiel, C. Dufour, J. R. Sun, Z. G. Wang, Y. T. Zhao, G. Q. Xiao, R. Cheng, X. M. Zhou, J. R. Ren, S. D. Liu, Y. Lei, Y. B. Sun, R. Ritter, E. Gruber, A. Cassimi, I. Monnet, S. Bouffard, F. Aumayr, and M. Toulemonde, *Energy deposition by heavy ions: Additivity of kinetic and potential energy contributions in hillock formation on CaF_2*, Sci. Rep. **4** (2014), 5742.

[200] K. Nordlund, J. Keinonen, M. Ghaly, and R. S. Averback, *Coherent displacement of atoms during ion irradiation*, Nature **398** (1999), 49–51.

[201] A. F. Calder, D. J. Bacon, A. V. Barashev, and Y. N. Osetsky, *On the origin of large interstitial clusters in displacement cascades*, Philos. Mag. **90** (2010), 863–884.

[202] R. S. Averback and T. D. De La Rubia, *Displacement damage in irradiated metals and semiconductors*, Solid State Phys. **51** (1998), 281–402.

[203] S.-P. Kim, H. B. Chew, E. Chason, V. B. Shenoy, and K.-S. Kim, *Nanoscale mechanisms of surface stress and morphology evolution in fcc metals under noble-gas ion bombardments*, Proc. R. Soc. A **468** (2012), 2550–2573.

[204] C. Lu, K. Jin, L. K. Béland, F. Zhang, T. Yang, L. Qiao, Y. Zhang, H. Bei, H. M. Christen, R. E. Stoller, and L. Wang, *Direct observation of defect range and evolution in ion-irradiated single crystalline ni and ni binary alloys*, Sci. Rep. **6** (2016), 19994.

[205] A. Dunlop, G. Jaskierowicz, G. Rizza, and M. Kopcewicz, *Partial crystallization of an amorphous alloy by electronic energy deposition*, Phys. Rev. Lett. **90** (2003), 015503.

[206] A. Benyagoub, A. Audren, L. Thomé, and F. Garrido, *Athermal crystallization induced by electronic excitations in ion-irradiated silicon carbide*, Appl. Phys. Lett. **89** (2006), 241914.

[207] C. Chappert, H. Bernas, J. Ferré, V. Kottler, J. P. Jamet, Y. Chen, E. Cambril, T. Devolder, F. Rousseaux, V. Mathet, and H. Launois, *Planar patterned magnetic media obtained by ion irradiation*, Science **280** (1998), 1919–1922.

[208] D. Weller, J. E. E. Baglin, A. J. Kellock, K. A. Hannibal, M. F. Toney, G. Kusinski, S. Lang, L. Folks, M. E. Best, and B. D. Terris, *Ion induced magnetization reorientation in co/pt multilayers for patterned media*, J. Appl. Phys. **87** (2000), 5768–5770.

[209] W. M. Kaminsky, G. A. C. Jones, N. K. Patel, W. E. Booij, M. G. Blamire, S. M. Gardiner, Y. B. Xu, and J. A. C. Bland, *Patterning ferromagnetism in $Ni_{80}Fe_{20}$ films via Ga^+ ion irradiation*, Appl. Phys. Lett. **78** (2001), 1589–1591.

[210] D. Ozkaya, R. M. Langford, W. L. Chan, and A. K. Petford-Long, *Effect of ga implantation on the magnetic properties of permalloy thin films*, J. Appl. Phys. **91** (2002), 9937–9942.

[211] K. Zhang, R. Gupta, K. P. Lieb, Y. Luo, G. A. Müller, P. Schaaf, and M. Uhrmacher, *Xenon-ion–induced phase transition in thin Co films*, Eur. Phys. Lett. **64** (2003), 668.

[212] D. McGrouther, J. N. Chapman, and F. W. M. Vanhelmont, *Effect of ga[sup +] ion irradiation on the structural and magnetic properties of cofe/irmn exchange biased bilayers*, J. Appl. Phys. **95** (2004), 7772–7778.

[213] K. Zhang, K. P. Lieb, G. A. Müller, P. Schaaf, M. Uhrmacher, and M. Münzenberg, *Magnetic texturing of xenon-ion irradiated nickel films*, Eur. Phys. J. B **42** (2004), 193–204.

[214] G. A. Müller, E. Carpene, R. Gupta, P. Schaaf, K. Zhang, and K. P. Lieb, *Ion-beam induced changes in magnetic and microstructural properties of thin iron films*, Eur. Phys. J. B **48** (2005), 449–462.

[215] J. Fassbender, J. von Borany, A. Mücklich, K. Potzger, W. Möller, J. McCord, L. Schultz, and R. Mattheis, *Structural and magnetic modifications of Cr-implanted Permalloy*, Phys. Rev. B **73** (2006), 184410.

[216] J. Fassbender and J. McCord, *Magnetic patterning by means of ion irradiation and implantation*, J. Magn. Magn. Mater. **320** (2008), 579–596.

[217] J. McCord, L. Schultz, and J. Fassbender, *Hybrid soft-magnetic lateral exchange spring films prepared by ion irradiation*, Adv. Mater. **20** (2008), 2090–2093.

[218] N. Fujita, S. Kosugi, Y. Saitoh, Y. Kaneta, K. Kume, T. Batchuluun, N. Ishikawa, T. Matsui, and A. Iwase, *Magnetic states controlled by energetic ion irradiation in FeRh thin films*, J. Appl. Phys. **107** (2010), 09E302.

[219] K. Aikoh, S. Kosugi, T. Matsui, and A. Iwase, *Quantitative control of magnetic ordering in ferh thin films using 30 keV Ga ion irradiation from a focused ion beam system*, J. Appl. Phys. **109** (2011), 07E311.

[220] P. J. Cook, T. H. Shen, P. J. Grundy, M. Y. Im, P. Fischer, S. A. Morton, and A. L. D. Kilcoyne, *Focused ion beam patterned Fe thin films: A study by selective area Stokes polarimetry and soft x-ray microscopy*, J. Appl. Phys. **109** (2011), 063917–5.

[221] J. Sun, Z. Wang, Y. Wang, Y. Zhu, L. Pang, T. Shen, and F. Li, *Structural and magnetic properties studies on swift heavy ion (SHI) irradiated Fe_3O_4 thin films*, Nucl. Instrum. Methods B **286** (2012), 277–281.

[222] D. Oshima, T. Kato, S. Iwata, and S. Tsunashima, *Control of magnetic properties of MnGa films by Kr^+ ion irradiation for application to bit patterned media*, IEEE Trans. Magn. **49** (2013), 3608–3611.

[223] V. K. Pecharsky and K. A. Gschneidner Jr, *Magnetocaloric effect and magnetic refrigeration*, J. Magn. Magn. Mater. **200** (1999), 44–56.

[224] H. Wada and Y. Tanabe, *Giant magnetocaloric effect of $mnas_{1-x}sb_x$*, Appl. Phys. Lett. **79** (2001), 3302–3304.

[225] O. Gutfleisch, M. A. Willard, E. Brück, C. H. Chen, S. G. Sankar, and J. P. Liu, *Magnetic materials and devices for the 21st century: Stronger, lighter, and more energy efficient*, Adv. Mater. **23** (2011), 821–842.

[226] A. Chirkova, K. P. Skokov, L. Schultz, N. V. Baranov, O. Gutfleisch, and T. G. Woodcock, *Giant adiabatic temperature change in ferh alloys evidenced by direct measurements under cyclic conditions*, Acta Mater. **106** (2016), 15–21.

[227] P. Weiss and A. Piccard, *Le phénomène magnétocalorique*, J. Phys. Theor. Appl. **7** (1917), 103–109.

[228] A. Smith, *Who discovered the magnetocaloric effect?*, Eur. Phys. J. H **38** (2013), 507–517.

[229] P. Debye, *Einige bemerkungen zur magnetisierung bei tiefer temperatur*, Ann. Phys. (Berlin) **386** (1926), 1154–1160.

[230] W. F. Giauque, *A thermodynamic treatment of certain magnetic effects. a proposed method of producing temperatures considerably below 1° absolute*, J. Am. Chem. Soc. **49** (1927), 1864–1870.

[231] W. F. Giauque and D. P. MacDougall, *Attainment of temperatures below 1° absolute by demagnetization of $Gd_2(SO_4)_3 \cdot 8\ H_2O$*, Phys. Rev. **43** (1933), 768–768.

[232] G. V. Brown, *Magnetic heat pumping near room temperature*, J. Appl. Phys. **47** (1976), 3673–3680.

[233] N. A. de Oliveira and P. J. von Ranke, *Theoretical aspects of the magnetocaloric effect*, Phys. Rep. **489** (2010), 89–159.

[234] G. Urbain, P. Weiss, and F. Trombe, *Un nouveau métal ferromagnétique, le gadolinium*, C. R. Acad. Sci. **200** (1935), 2132–2134.

[235] C. Chilowsky *Method and apparatus for refrigeration*, Patent US 2589775 (1952).

[236] C. Chilowsky *Thermomagnetic generator and refrigerator*, Patent US 2619603 (1952).

[237] W. A. Steyert, *Stirling-cycle rotating magnetic refrigerators and heat engines for use near room temperature*, J. Appl. Phys. **49** (1978), 1216–1226.

[238] J. A. Barclay, *Use of a ferrofluid as the heat-exchange fluid in a magnetic refrigerator*, J. Appl. Phys. **53** (1982), 2887–2894.

[239] J. A. Barclay and W. A. Steyert *Active magnetic regenerator*, Patent US 4332135 (1982).

[240] B. Yu, M. Liu, P. W. Egolf, and A. Kitanovski, *A review of magnetic refrigerator and heat pump prototypes built before the year 2010*, Int. J. Refrig. **33** (2010), 1029–1060.

[241] K. Engelbrecht, D. Eriksen, C. R. H. Bahl, R. Bjørk, J. Geyti, J. A. Lozano, K. K. Nielsen, F. Saxild, A. Smith, and N. Pryds, *Experimental results for a novel rotary active magnetic regenerator*, Int. J. Refrig. **35** (2012), 1498–1505.

[242] M. P. Annaorazov, S. A. Nikitin, A. L. Tyurin, K. A. Asatryan, and A. K. Dovletov, *Anomalously high entropy change in FeRh alloy*, J. Appl. Phys. **79** (1996), 1689–1695.

[243] V. K. Pecharsky and J. K. A. Gschneidner, *Tunable magnetic regenerator alloys with a giant magnetocaloric effect for magnetic refrigeration from 20 to 290 k*, Appl. Phys. Lett. **70** (1997), 3299–3301.

[244] V. K. Pecharsky and J. K. A. Gschneidner, *Giant magnetocaloric effect in $Gd_5(Si_2Ge_2)$*, Phys. Rev. Lett. **78** (1997), 4494–4497.

[245] S. Jacobs, J. Auringer, A. Boeder, J. Chell, L. Komorowski, J. Leonard, S. Russek, and C. Zimm, *The performance of a large-scale rotary magnetic refrigerator*, Int. J. Refrig. **37** (2014), 84–91.

[246] *Chemistryviews 2016* `www.chemistryviews.org/details/news/7261611/Prototype_of_Magnetocaloric_Wine_Cooler.html`.

[247] E. Brück, *Developments in magnetocaloric refrigeration*, J. Phys. D **38** (2005), R381.

[248] K. A. Gschneidner, V. K. Pecharsky, and A. O. Tsokol, *Recent developments in magnetocaloric materials*, Rep. Prog. Phys. **68** (2005), 1479.

[249] A. Kitanovski and P. W. Egolf, *Thermodynamics of magnetic refrigeration*, Int. J. Refrig. **29** (2006), 3–21.

[250] E. Brück, O. Tegus, D. T. Cam Thanh, N. T. Trung, and K. H. J. Buschow, *A review on mn based materials for magnetic refrigeration: Structure and properties*, Int. J. Refrig. **31** (2008), 763–770.

[251] K. A. Gschneidner and V. K. Pecharsky, *Thirty years of near room temperature magnetic cooling: Where we are today and future prospects*, Int. J. Refrig. **31** (2008), 945–961.

[252] B. G. Shen, J. R. Sun, F. X. Hu, H. W. Zhang, and Z. H. Cheng, *Recent progress in exploring magnetocaloric materials*, Adv. Mater. **21** (2009), 4545–4564.

[253] A. Smith, C. R. H. Bahl, R. Bjørk, K. Engelbrecht, K. K. Nielsen, and N. Pryds, *Materials challenges for high performance magnetocaloric refrigeration devices*, Adv. Energy Mater. **2** (2012), 1288–1318.

[254] V. Franco, J. Blázquez, B. Ingale, and A. Conde, *The magnetocaloric effect and magnetic refrigeration near room temperature: Materials and models*, Annu. Rev. Mater. Res. **42** (2012), 305–342.

[255] K. G. Sandeman, *Magnetocaloric materials: The search for new systems*, Scripta Mat. **67** (2012), 566–571.

[256] L. Manosa, A. Planes, and M. Acet, *Advanced materials for solid-state refrigeration*, J. Mater. Chem. A **1** (2013), 4925–4936.

[257] X. Moya, S. Kar-Narayan, and N. D. Mathur, *Caloric materials near ferroic phase transitions*, Nature Mater. **13** (2014), 439–450.

[258] O. Gutfleisch, T. Gottschall, M. Fries, D. Benke, I. Radulov, K. P. Skokov, H. Wende, M. Gruner, M. Acet, P. Entel, and M. Farle, *Mastering hysteresis in magnetocaloric materials*, Phil. Trans. R. Soc. A **374**.

[259] J. Lyubina, *Magnetocaloric materials for energy efficient cooling*, J. Phys. D **50** (2017), 053002.

[260] L. Landau and E. Lifshitz, *Statistical Physics part 1*, Vol. 5, Third edition, Elsevier Science, 2013.

[261] M. Zemansky and R. Dittman, *Heat and Thermodynamics: An Intermediate Textbook*, McGraw-Hill, 1997.

[262] J. Sethna, *Statistical Mechanics: Entropy, Order Parameters, and Complexity*, OUP Oxford, 2006.

[263] B. K. Banerjee, *On a generalised approach to first and second order magnetic transitions*, Phys. Lett. **12** (1964), 16–17.

[264] X. Zhou, W. Li, H. P. Kunkel, and G. Williams, *Order of sequential magnetic phase transitions in Ni-Mn-Ga alloys as revealed by Arrott plots*, Phys. Rev. B **73** (2006), 012412.

[265] B. Li, H. Meng, W. Ren, and Z. Zhang, *Intrinsic magnetocaloric effect at a first-order magnetic transition*, Eur. Phys. Lett. **97** (2012), 57002.

[266] S. B. Roy, *First order magneto-structural phase transition and associated multi-functional properties in magnetic solids*, J. Phys. Condens. Matter **25** (2013), 183201.

[267] M. R. Ibarra and P. A. Algarabel, *Giant volume magnetostriction in the FeRh alloy*, Phys. Rev. B **50** (1994), 4196–4199.

[268] O. Tegus, E. Bruck, K. H. J. Buschow, and F. R. de Boer, *Transition-metal-based magnetic refrigerants for room-temperature applications*, Nature **415** (2002), 150–152.

[269] J. Liu, T. Gottschall, K. P. Skokov, J. D. Moore, and O. Gutfleisch, *Giant magnetocaloric effect driven by structural transitions*, Nature Mater. **11** (2012), 620–626.

[270] X. Moya, L. E. Hueso, F. Maccherozzi, A. I. Tovstolytkin, D. I. Podyalovskii, C. Ducati, L. C. Phillips, M. Ghidini, O. Hovorka, A. Berger, M. E. Vickers, E. Defay, S. S. Dhesi, and N. D. Mathur, *Giant and reversible extrinsic magnetocaloric effects in $La_{0.7}Ca_{0.3}MnO_3$ films due to strain*, Nature Mater. **12** (2013), 52–58.

[271] D. H. Mosca, F. Vidal, and V. H. Etgens, *Strain engineering of the magnetocaloric effect in mnas epilayers*, Phys. Rev. Lett. **101** (2008), 125503.

[272] J. Y. Duquesne, J. Y. Prieur, J. A. Canalejo, V. H. Etgens, M. Eddrief, A. L. Ferreira, and M. Marangolo, *Ultrasonic triggering of giant magnetocaloric effect in mnas thin films*, Phys. Rev. B **86** (2012), 035207.

[273] M. Marangolo, W. Karboul-Trojet, J.-Y. Prieur, V. H. Etgens, M. Eddrief, L. Becerra, and J.-Y. Duquesne, *Surface acoustic wave triggering of giant magnetocaloric effect in mnas/gaas devices*, Appl. Phys. Lett. **105** (2014), 162403.

[274] H. Wada and T. Asano, *Effect of heat treatment on giant magnetocaloric properties of $Mn_{1-\delta}As_{1-x}Sb_{\delta}$*, J. Magn. Magn. Mater. **290** (2005), 703–705.

[275] R. Breitwieser, F. Vidal, I. L. Graff, M. Marangolo, M. Eddrief, J. C. Boulliard, and V. H. Etgens, *Phase transition and surface morphology of MnAs/GaAs(001) studied with in situ variable-temperature scanning tunneling microscopy*, Phys. Rev. B **80** (2009), 045403.

[276] H. Okamoto, *The As–Mn (arsenic-manganese) system*, J. Phase. Equilib. **10** (1989), 549–554.

[277] R. W. De Blois and D. S. Rodbell, *Magnetic first-order phase transition in single-crystal MnAs*, Phys. Rev. **130** (1963), 1347–1360.

[278] C. P. Bean and D. S. Rodbell, *Magnetic disorder as a first-order phase transformation*, Phys. Rev. **126** (1962), 104.

[279] J. B. Goodenough and J. A. Kafalas, *High-pressure study of the first-order phase transition in MnAs*, Phys. Rev. **157** (1967), 389–395.

[280] N. Menyuk, J. A. Kafalas, K. Dwight, and J. B. Goodenough, *Effects of pressure on the magnetic properties of mnas*, Phys. Rev. **177** (1969), 942–951.

[281] L. Pytlik and A. Zieba, *Magnetic phase diagram of MnAs*, J. Magn. Magn. Mater. **51** (1985), 199–210.

[282] P. J. von Ranke, S. Gama, A. A. Coelho, A. de Campos, A. M. G. Carvalho, F. C. G. Gandra, and N. A. de Oliveira, *Theoretical description of the colossal entropic magnetocaloric effect: Application to MnAs*, Phys. Rev. B **73** (2006), 014415.

[283] R. Engel-Herbert, D. M. Schaadt, and T. Hesjedal, *Analytical and numerical calculations of the magnetic force microscopy response: A comparison*, J. Appl. Phys. **99** (2006), –.

[284] L. Däweritz, *Interplay of stress and magnetic properties in epitaxial MnAs films*, Rep. Prog. Phys. **69** (2006), 2581.

[285] V. M. Kaganer, B. Jenichen, F. Schippan, W. Braun, L. Däweritz, and K. H. Ploog, *Strain-mediated phase coexistence in heteroepitaxial films*, Phys. Rev. Lett. **85** (2000), 341–344.

[286] V. M. Kaganer, B. Jenichen, F. Schippan, W. Braun, L. Däweritz, and K. H. Ploog, *Strain-mediated phase coexistence in MnAs heteroepitaxial films on GaAs: An x-ray diffraction study*, Phys. Rev. B **66** (2002), 045305.

[287] M. Kastner, C. Herrmann, L. Daweritz, and K. H. Ploog, *Atomic scale morphology of self-organized periodic elastic domains in epitaxial ferromagnetic mnas films*, J. Appl. Phys. **92** (2002), 5711–5713.

[288] F. Schippan, G. Behme, L. Däweritz, K. H. Ploog, B. Dennis, K.-U. Neumann, and K. R. A. Ziebeck, *Magnetic structure of epitaxially grown mnas on gaas(001)*, J. Appl. Phys. **88** (2000), 2766–2770.

[289] L. Däweritz, M. Kästner, T. Hesjedal, T. Plake, B. Jenichen, and K. H. Ploog, *Structural and magnetic order in mnas films grown by molecular beam epitaxy on gaas for spin injection*, J. Cryst. Growth **251** (2003), 297–302.

[290] J. Mohanty, T. Hesjedal, A. Ney, Y. Takagaki, R. Koch, L. Däweritz, and K. H. Ploog, *Effect of strain on the local phase transition temperature of mnas/gaas(001)*, Appl. Phys. Lett. **83** (2003), 2829–2831.

[291] J. Mohanty, T. Hesjedal, T. Plake, M. Kästner, L. Däweritz, and K. H. Ploog, *Variable-temperature micromagnetic study of epitaxially grown mnas films on gaas(001)*, Appl. Phys. A **77** (2003), 739–742.

[292] T. Plake, T. Hesjedal, J. Mohanty, M. Kästner, L. Däweritz, and K. H. Ploog, *Temperature-dependent magnetic force microscopy investigation of epitaxial mnas films on gaas(001)*, Appl. Phys. Lett. **82** (2003), 2308–2310.

[293] L. Däweritz, L. Wan, B. Jenichen, C. Herrmann, J. Mohanty, A. Trampert, and K. H. Ploog, *Thickness dependence of the magnetic properties of mnas films on gaas(001) and gaas(113)a: Role of a natural array of ferromagnetic stripes*, J. Appl. Phys. **96** (2004), 5056–5062.

[294] J. Lindner, T. Toliński, K. Lenz, E. Kosubek, H. Wende, K. Baberschke, A. Ney, T. Hesjedal, C. Pampuch, R. Koch, L. Däweritz, and K. H. Ploog, *Magnetic anisotropy of MnAs-films on GaAs(001) studied with ferromagnetic resonance*, J. Magn. Magn. Mater. **277** (2004), 159–164.

[295] K. H. Ploog, *Epitaxial ferromagnet-semiconductor heterostructures for electrical spin injection*, J. Cryst. Growth **268** (2004), 329–335.

[296] L. Daweritz, C. Herrmann, J. Mohanty, T. Hesjedal, K. H. Ploog, E. Bauer, A. Locatelli, S. Cherifi, R. Belkhou, A. Pavlovska, and S. Heun, *Tailoring of the structural and magnetic properties of mnas films grown on gaas—strain and annealing effects*, J. Vac. Sci. Technol. B **23** (2005), 1759–1768.

[297] R. Engel-Herbert, T. Hesjedal, J. Mohanty, D. M. Schaadt, and K. H. Ploog, *Field dependence of micromagnetic domain patterns in mnas films*, J. Appl. Phys. **98** (2005), 063909.

[298] C. Adriano, C. Giles, O. D. D. Couto, M. J. S. P. Brasil, F. Iikawa, and L. Daweritz, *Strain redistribution at the phase transition of mnas/gaas(001) films*, Appl. Phys. Lett. **88** (2006), 151906–3.

[299] L. N. Coelho, B. R. A. Neves, R. Magalhães-Paniago, F. C. Vicentin, H. Westfahl, R. M. Fernandes, F. Iikawa, L. Däweritz, C. Spezzani, and M. Sacchi, *Magnetic reconfiguration of MnAs/GaAs(001) observed by magnetic force microscopy and resonant soft x-ray scattering*, J. Appl. Phys. **100** (2006), 083906.

[300] T. Manago, H. Kuramochi, and H. Akinaga, *Thickness dependence of magnetic domains of mnas films*, Surf. Sci. **600** (2006), 4155–4159.

[301] K.-S. Ryu, J. Kim, Y. Lee, H. Akinaga, T. Manago, R. Viswan, and S.-C. Shin, *Thickness-dependent magnetic domain change in epitaxial mnas films on gaas(001)*, Appl. Phys. Lett. **89** (2006), 232506.

[302] L. Däweritz and C. Herrmann, *Self-organization and finite size effects in epitaxial ferromagnetic mnas films on gaas*, Phys. Status Solidi B **244** (2007), 2936–2943.

[303] V. Garcia, Y. Sidis, M. Marangolo, F. Vidal, M. Eddrief, P. Bourges, F. Maccherozzi, F. Ott, G. Panaccione, and V. H. Etgens, *Biaxial strain in the hexagonal plane of mnas thin films: The key to stabilize ferromagnetism to higher temperature*, Phys. Rev. Lett. **99** (2007), 117205–4.

[304] B. Rache Salles, M. Marangolo, C. David, and J. C. Girard, *Cross-sectional magnetic force microscopy of mnas/gaas(001)*, Appl. Phys. Lett. **96** (2010), 052510.

[305] L. Panitzsch, M. Stalder, and R. F. Wimmer-Schweingruber, *Direct high-resolution ion beam-profile imaging using a position-sensitive Faraday cup array*, Rev. Sci. Instrum. **80** (2009), 113302–6.

[306] L. Panitzsch, M. Stalder, and R. F. Wimmer-Schweingruber, *Spatially resolved measurements of electron cyclotron resonance ion source beam profile characteristics*, Rev. Sci. Instrum. **82** (2011), 033302–7.

[307] L. Caron, Z. Q. Ou, T. T. Nguyen, D. T. Cam Thanh, O. Tegus, and E. Brück, *On the determination of the magnetic entropy change in materials with first-order transitions*, J. Magn. Magn. Mater. **321** (2009), 3559–3566.

[308] L. Tocado, E. Palacios, and R. Burriel, *Entropy determinations and magnetocaloric parameters in systems with first-order transitions: Study of MnAs*, J. Appl. Phys. **105** (2009), –.

[309] A. Ney, T. Hesjedal, C. Pampuch, A. K. Das, L. Däweritz, R. Koch, K. H. Ploog, T. Toliński, J. Lindner, K. Lenz, and K. Baberschke, *Nature of the magnetic and structural phase transition in* MnAs/GaAs(001), Phys. Rev. B **69** (2004), 081306.

[310] L. B. Steren, J. Milano, V. Garcia, M. Marangolo, M. Eddrief, and V. H. Etgens, *Magnetization reversal and anomalous dependence of the coercive field with temperature in mnas epilayers grown on gaas*, Phys. Rev. B **74** (2006), 144402.

[311] G. Liger-Belair, G. Polidori, and P. Jeandet, *Recent advances in the science of champagne bubbles*, Chem. Soc. Rev. **37** (2008), 2490–2511.

[312] N. E. Shafer and R. N. Zare, *Through a beer glass darkly*, Phys. Today **44** (1991), 48–52.

[313] B. Vonnegut, *Nucleation of supercooled water clouds by silver iodide smokes*, Chem. Rev. **44** (1949), 277–289.

[314] R. Niemann, S. Hahn, A. Diestel, A. Backen, L. Schultz, K. Nielsch, M. F.-X. Wagner, and S. Fähler, *Reducing the nucleation barrier in magnetocaloric heusler alloys by nanoindentation*, APL Mater. **4** (2016), 064101.

[315] R. Mahendiran, A. Maignan, M. Hervieu, C. Martin, and B. Raveau, *Anomalous increase of resistivity against thermal cycling in some of the phase separated manganites*, J. Appl. Phys. **90** (2001), 2422–2426.

[316] D. Khomskii and L. Khomskii, *Fine mist versus large droplets in phase separated manganites*, Phys. Rev. B **67** (2003), 052406.

[317] K. De, S. Majumdar, and S. Giri, *Memory effect and inverse thermal hysteresis in* $La_{0.87}Mn_{0.98}Fe_{0.02}O_x$, J. Appl. Phys. **101** (2007), 103909.

[318] V. Markovich, G. Jung, S. I. Khartsev, M. I. Tsindlekht, A. M. Grishin, Y. Ya, and G. Gorodetsky, *Inverse thermal hysteresis and peculiar transport properties of* $La_{0.9}MnO_{3-\delta}$ *film*, J. Phys. CS **200** (2010), 052014.

[319] Y.-Y. Zhao, J. Wang, H. Kuang, F.-X. Hu, H.-R. Zhang, Y. Liu, Y. Zhang, S.-H. Wang, R.-R. Wu, M. Zhang, L.-F. Bao, J.-R. Sun, and B.-G. Shen, *Abnormal percolative transport and colossal electroresistance induced by anisotropic strain in (011)-*$Pr_{0.7}(Ca_{0.6}Sr_{0.4})_{0.3}MnO_3$*/PMN-PT heterostructure*, Sci. Rep. **4** (2014), 7075.

[320] W. Hauptmann, M. Votsmeier, J. Gieshoff, A. Drochner, and H. Vogel, *Inverse hysteresis during the NO oxidation on Pt under lean conditions*, Appl. Catal. B Environ. **93** (2009), 22–29.

[321] M. Casapu, A. Fischer, A. M. Gänzler, R. Popescu, M. Crone, D. Gerthsen, M. Türk, and J.-D. Grunwaldt, *Origin of the normal and inverse hysteresis behavior during CO oxidation over* Pt/Al_2O_3, ACS Catal. **7** (2017), 343–355.

[322] A. Arrott, *Criterion for ferromagnetism from observations of magnetic isotherms*, Phys. Rev. **108** (1957), 1394–1396.

[323] G. Shirane, C. W. Chen, P. A. Flinn, and R. Nathans, *Mössbauer study of hyperfine fields and isomer shifts in the Fe-Rh alloys*, Phys. Rev. **131** (1963), 183–190.

[324] M. Fallot and R. Hocart, *Sur l'apparition du ferromagnétisme par élévation de température dans des alliages de fer et de rhodium*, Rev. Sci. **77** (1939), 498–500.

[325] A. Zakharov, A. Kadomtseva, R. Levitin, and E. Ponyatovskii, *Magnetic and magnetoelastic properties of a metamagnetic iron–rhodium alloy*, Sov. Phys. JETP **19** (1964), 1348–1353.

[326] O. Kubaschewski, *Fe—Rh Iron—Rhodium*, Springer Berlin Heidelberg, Berlin, Heidelberg, 1982, pp. 120–122.

[327] N. H. Dung, Z. Q. Ou, L. Caron, L. Zhang, D. T. C. Thanh, G. A. de Wijs, R. A. de Groot, K. H. J. Buschow, and E. Brück, *Mixed magnetism for refrigeration and energy conversion*, Adv. Energy Mater. **1** (2011), 1215–1219.

[328] L. Caron, M. Hudl, V. Höglin, N. H. Dung, C. P. Gomez, M. Sahlberg, E. Brück, Y. Andersson, and P. Nordblad, *Magnetocrystalline anisotropy and the magnetocaloric effect in Fe_2P*, Phys. Rev. B **88** (2013), 094440.

[329] N. Fujita, S. Kosugi, Y. Zushi, T. Matsui, Y. Saito, and A. Iwase, *Effects of energetic heavy ion irradiation on the structure and magnetic properties of FeRh thin films*, Nucl. Instrum. Methods B **267** (2009), 921–924.

[330] A. H. Compton, *A precision X-ray spectrometer and the wave length of mo $k\alpha_1$*, Rev. Sci. Instrum. **2** (1931), 365–376.

[331] D. F. Anagnostopoulos, D. Gotta, P. Indelicato, and L. M. Simons, *Low-energy X-ray standards from hydrogenlike pionic atoms*, Phys. Rev. Lett. **91** (2003), 240801.

[332] S. Okada, D. A. Bennett, C. Curceanu, W. B. Doriese, J. W. Fowler, J. D. Gard, F. P. Gustafsson, T. Hashimoto, R. S. Hayano, S. Hirenzaki, J. P. Hays-Wehle, G. C. Hilton, N. Ikeno, M. Iliescu, S. Ishimoto, K. Itahashi, M. Iwasaki, T. Koike, K. Kuwabara, Y. Ma, J. Marton, H. Noda, G. C. O'Neil, H. Outa, C. D. Reintsema, M. Sato, D. R. Schmidt, H. Shi, K. Suzuki, T. Suzuki, D. S. Swetz, H. Tatsuno, J. Uhlig, J. N. Ullom, E. Widmann, S. Yamada, J. Yamagata-Sekihara, and J. Zmeskal, *First application of superconducting transition-edge sensor microcalorimeters to hadronic atom x-ray spectroscopy*, Progr. Theor. Exp. Phys. **2016**.

[333] M. Hori, A. Soter, D. Barna, A. Dax, R. Hayano, S. Friedreich, B. Juhasz, T. Pask, E. Widmann, D. Horvath, L. Venturelli, and N. Zurlo, *Two-photon laser spectroscopy of antiprotonic helium and the antiproton-to-electron mass ratio*, Nature **475** (2011), 484–488.

[334] M. Hori, A. Sótér, and V. I. Korobov, *Proposed method for laser spectroscopy of pionic helium atoms to determine the charged-pion mass*, Phys. Rev. A **89** (2014), 042515.

[335] M. Hori, A. Sótér, H. Aghai-Khozani, D. Barna, A. Dax, R. S. Hayano, Y. Murakami, and H. Yamada, *Method for laser spectroscopy of metastable pionic helium atoms*, Hyperfine Interact. **233** (2015), 83–87.

[336] R. Alonso-Mori, J. Kern, D. Sokaras, T.-C. Weng, D. Nordlund, R. Tran, P. Montanez, J. Delor, V. K. Yachandra, J. Yano, and U. Bergmann, *A multi-crystal wavelength dispersive x-ray spectrometer*, Rev. Sci. Instrum. **83** (2012), 073114–9.

[337] J. Szlachetko, M. Nachtegaal, E. de Boni, M. Willimann, O. Safonova, J. Sa, G. Smolentsev, M. Szlachetko, J. A. van Bokhoven, J.-C. Dousse, J. Hoszowska, Y. Kayser, P. Jagodzinski, A. Bergamaschi, B. Schmitt, C. David, and A. Lücke, *A von Hamos x-ray spectrometer based on a segmented-type diffraction crystal for single-shot x-ray emission spectroscopy and time-resolved resonant inelastic x-ray scattering studies*, Rev. Sci. Instrum. **83** (2012), –.

[338] U. Zastrau, C. R. D. Brown, T. Döppner, S. H. Glenzer, G. Gregori, H. J. Lee, H. Marschner, S. Toleikis, O. Wehrhan, and E. Förster, *Focal aberrations of large-aperture HOPG von-Hàmos x-ray spectrometers*, J. Instrum. **7** (2012), P09015.

[339] D. Sokaras, T. C. Weng, D. Nordlund, R. Alonso-Mori, P. Velikov, D. Wenger, A. Garachtchenko, M. George, V. Borzenets, B. Johnson, T. Rabedeau, and U. Bergmann, *A seven-crystal johann-type hard x-ray spectrometer at the stanford synchrotron radiation lightsource*, Rev. Sci. Instrum. **84** (2013), 053102.

[340] C. Pies, S. Schäfer, S. Heuser, S. Kempf, A. Pabinger, J. P. Porst, P. Ranitsch, N. Foerster, D. Hengstler, A. Kampkötter, T. Wolf, L. Gastaldo, A. Fleischmann, and C. Enss, *maXs: Microcalorimeter arrays for high-resolution x-ray spectroscopy at GSI/FAIR*, J. Low Temp. Phys. **167** (2012), 269–279.

[341] D. Hengstler, M. Keller, C. Schötz, J. Geist, M. Krantz, S. Kempf, L. Gastaldo, A. Fleischmann, T. Gassner, G. Weber, R. Märtin, S. Th, and C. Enss, *Towards FAIR: first measurements of metallic magnetic calorimeters for high-resolution x-ray spectroscopy at GSI*, Phys. Scripta **T166** (2015), 014054.

[342] M. Unipan, A. Robin, R. Morgenstern, and R. Hoekstra, *Local spin polarization at surfaces probed by hollow atoms*, Phys. Rev. Lett. **96** (2006), 177601–4.

[343] M. Unipan, A. Robin, D. F. A. Winters, R. Morgenstern, and R. Hoekstra, *Probing local spin ordering at surfaces by He^{2+} ions*, Phys. Rev. A **74** (2006), 062901–9.

[344] E. Essers, G. Benner, T. Mandler, S. Meyer, D. Mittmann, M. Schnell, and R. Höschen, *Energy resolution of an omega-type monochromator and imaging properties of the mandoline filter*, Ultramicroscopy **110** (2010), 971–980.

[345] M. L. Swanson, *The study of lattice defects by channelling*, Rep. Prog. Phys. **45** (1982), 47.

[346] A. Fujita, Y. Akamatsu, and K. Fukamichi, *Itinerant electron metamagnetic transition in $La(Fe_xSi_{1-x})_13$ intermetallic compounds*, J. Appl. Phys. **85** (1999), 4756–4758.

[347] A. Fujita, S. Fujieda, Y. Hasegawa, and K. Fukamichi, *Itinerant-electron metamagnetic transition and large magnetocaloric effects in* $La(Fe_xSi_{1-x})_{13}$ *compounds and their hydrides*, Phys. Rev. B **67** (2003), 104416.

[348] A. Fujita and K. Fukamichi, *Enhancement of isothermal entropy change due to spin fluctuations in itinerant-electron metamagnetic* $La(Fe_{0.88}Si_{0.12})_{13}$ *compound*, J. Alloys Compd. **408–412** (2006), 62–65.

[349] G. Drake, *Theoretical energies for the n=1 and 2 states of the helium isoelectronic sequence up to Z=100*, Can. J. Phys. **66** (1988), 586.

[350] M. H. Chen, K. T. Cheng, and W. R. Johnson, *Relativistic configuration-interaction calculations of n=2 triplet states of heliumlike ions*, Phys. Rev. A **47** (1993), 3692.

[351] D. Plante, W. Johnson, and J. Sapirstein, *Relativistic all-order many-body calculations of the n=1 and n=2 states of heliumlike ions*, Phys. Rev. A **49** (1994), 3519–3530.

[352] A. N. Artemyev, V. M. Shabaev, V. A. Yerokhin, G. Plunien, and G. Soff, *QED calculation of the n = 1 and n = 2 energy levels in He-like ions*, Phys. Rev. A **71** (2005), 062104.

[353] Y. Kozhedub and V. Shabaev unpublished, 2008.

[354] P. Indelicato and J. P. Desclaux, *Multiconfiguration Dirac-Fock calculations of transition energies with QED corrections in three-electron ions*, Phys. Rev. A **42** (1990), 5139.

[355] P. Indelicato, J. P. Santos, S. Boucard, and J. P. Desclaux, *QED and relativistic corrections in superheavy elements*, Eur. Phys. J. D **45** (2007), 155–170.

[356] P. Indelicato unpublished, 2008.

[357] J. Taylor, *An Introduction to Error Analysis: The Study of Uncertainties in Physical Measurements*, University Science Books, 1997.

[358] J. Burgdörfer, P. Lerner, and F. W. Meyer, *Above-surface neutralization of highly charged ions: The classical over-the-barrier model*, Phys. Rev. A **44** (1991), 5674.

[359] F. W. Meyer, L. Folkerts, I. G. Hughes, S. H. Overbury, D. M. Zehner, P. A. Zeijlmans van Emmichoven, and J. Burgdörfer, *Work-function dependence of above-surface neutralization of multicharged ions*, Phys. Rev. A **48** (1993), 4479–4484.

[360] J. Burgdörfer, C. Reinhold, L. Hägg, and F. Meyer, *Interaction of highly charged ions with surfaces*, Am. J. Phys. **49** (1996), 527–542.

[361] H. Winter, *Collisions of atoms and ions with surfaces under grazing incidence*, Phys. Rep. **367** (2002), 387–582.

[362] J. P. Briand, L. de Billy, P. Charles, and S. Essabaa, *Production of hollow atoms by the excitation of highly charged ions in interaction with a metallic surface*, Phys. Rev. Lett. **65** (1990), 159–162.

[363] J.-P. Briand, S. Thuriez, G. Giardino, G. Borsoni, M. Froment, M. Eddrief, and C. Sébenne, *Observation of hollow atoms or ions above insulator and metal surfaces*, Phys. Rev. Lett. **77** (1996), 1452.

[364] A. S. El-Said, R. Heller, W. Meissl, R. Ritter, S. Facsko, C. Lemell, B. Solleder, I. C. Gebeshuber, G. Betz, M. Toulemonde, W. Mˆller, J. Burgdˆrfer, and F. Aumayr, *Creation of nanohillocks on CaF_2 surfaces by single slow highly charged ions*, Phys. Rev. Lett. **100** (2008), 237601.

[365] H.-D. Betz, *Charge states and charge-changing cross sections of fast heavy ions penetrating through gaseous and solid media*, Rev. Mod. Phys. **44** (1972), 465–539.

[366] J. P. Rozet, C. Stephan, and D. Vernhet, *Etacha: a program for calculating charge states at ganil energies*, Nucl. Instrum. Methods B **107** (1996), 67–70.

[367] C. Scheidenberger, T. Stöhlker, W. E. Meyerhof, H. Geissel, P. H. Mokler, and B. Blank, *Charge states of relativistic heavy ions in matter*, Nucl. Instrum. Methods B **142** (1998), 441–462.

[368] N. Winckler, A. Rybalchenko, V. P. Shevelko, M. Al-Turany, T. Kollegger, and T. Stöhlker, *Breit code: Analytical solution of the balance rate equations for charge-state evolutions of heavy-ion beams in matter*, Nucl. Instrum. Methods B **392** (2017), 67–73.

[369] J. P. Rozet, A. Chetioui, P. Bouisset, D. Vernhet, K. Wohrer, A. Touati, C. Stephan, and J. P. Grandin, *Anomalous population of deep capture states of fast ions emerging from solid foils*, Phys. Rev. Lett. **58** (1987), 337–340.

[370] J. D. Fuhr, V. H. Ponce, F. J. García de Abajo, and P. M. Echenique, *Dynamic screening of fast ions moving in solids*, Phys. Rev. B **57** (1998), 9329–9335.

[371] D. Vernhet, J. P. Rozet, I. Bailly-Despiney, C. Stephan, A. Cassimi, J. P. Grandin, and L. J. Dubé, *Observation of dynamical substate mixing of fast ions in solids*, J. Phys. B **31** (1998), 117.

[372] S. Datz, C. D. Moak, O. H. Crawford, H. F. Krause, P. F. Dittner, J. G. del Campo, J. A. Biggerstaff, P. D. Miller, P. Hvelplund, and H. Knudsen, *Resonant coherent excitation of channeled ions*, Phys. Rev. Lett. **40** (1978), 843–847.

[373] C. Kondo, S. Masugi, Y. Nakano, A. Hatakeyama, T. Azuma, K. Komaki, Y. Yamazaki, T. Murakami, and E. Takada, *Three-dimensional resonant coherent excitation of nonchanneling ions in a crystal*, Phys. Rev. Lett. **97** (2006), 135503–4.

[374] Y. Nakano, Y. Takano, T. Ikeda, Y. Kanai, S. Suda, T. Azuma, H. Bräuning, A. Bräuning-Demian, D. Dauvergne, T. Stöhlker, and Y. Yamazaki, *Resonant coherent excitation of the lithiumlike uranium ion: A scheme for heavy-ion spectroscopy*, Phys. Rev. A **87** (2013), 060501.